Homotopy and renormalization group approaches for strongly correlated systems

Dissertation
der Fakultät für Physik
der Ludwig-Maximilians-Universität München

vorgelegt von

Tobias Pfeffer
aus Deggendorf

2018

Erstgutachter: Prof. Dr. Lode Pollet
Zweitgutachter: Prof. Dr. Matthias Punk
Datum der Abgabe: 7. Dezember 2018
Datum der mündlichen Prüfung: 8. Februar 2019

Kurzfassung

Diese Dissertation beschäftigt sich mit der Entwicklung und Anwendung feldtheoretischer Methoden zur Untersuchung stark korrelierter Vielteilchensysteme. In diesen stark korrelierten Systemen treten aufgrund des kollektiven Verhaltens der einzelnen Freiheitsgrade neue physikalische Effekte auf. Das theoretische Verständnis dieser Systeme erfordert häufig computergestützte Rechenverfahren zur Lösung von interagierenden Vielteilchenmodellen frei von jedweden Approximationen. Im ersten Teil der Arbeit verwenden wir klassische Monte-Carlo-Simulationen in Kombination mit einem Renormalisierungsgruppenansatz, um die Existenz der "scratched"-XY-Universalitätsklasse eindeutig zu beweisen. Diese Universalitätsklasse beschreibt den kontinuierlichen Phasenübergang aus einer kritischen suprafluiden Phase in Systemen, welche eine zweidimensionale hydrodynamische Beschreibung erlauben, durch einen Mechanismus grundlegend verschieden von dem Berezinskii-Kosterlitz-Thouless Scenario, welches von topologischen Defekten getrieben wird. Dazu untersuchen wir den suprafluiden Phasenübergang bei endlicher Temperatur in einem modifizierten, zweidimensionalen, klassischen XY-Modell mit eindimensionalen Störstellen deren Stärken nach einem Potenzgesetz verteilt sind. Wenn der Exponent abnimmt, nimmt die Bedeutung der Störstellen zu und der Mechanismus, welcher den Phasenübergang treibt, wechselt von der Proliferation von Vortex–Anti-Vortex Paaren zu der "scratched"-XY-Kritikalität, welche durch einen nicht universellen Sprung des suprafluiden Responsekoeffizienten gekennzeichnet ist. Die Existenz der "scratched"-XY-Kritikalität bei endlicher Temperatur und ihre Beschreibung durch eine asymptotisch exakte Semi-Renormalisierungsgruppentheorie, welche zuvor für den Suprafluid-Isolator Phasenübergang in eindimensionalen Quantensystemen mit starken Störstellen entwickelt wurde, wird numerisch in einem speziell dafür entworfenen Modell bewiesen, welches minimale Korrekturen durch endliche Systemgrößen aufweist. Im zweiten Teil der Dissertation wird ein neuer analytischer sowie rechnerischer Ansatz zur Untersuchung stark korrelierter Vielteilchensysteme entwickelt. Anstatt die Lösung von Vielteilchenmodellen ausgehend von einem funktionalem Integral aufzubauen, wie z.B. in Pfadintegral-Quantum-Monte-Carlo-Simulationen und diagrammatischen Monte-Carlo-Berechnungen, schlagen wir die Verwendung funktionaler Integro-Differentialgleichungen vor, welche ausgehend von der Dyson-Schwinger-Gleichung hergeleitet werden. Diese funktionale Integro-Differentialgleichung wird ohne jedwede Approximation mit einem Homotopie-Ansatz gelöst, insbesondere wird dabei die "homotopy analysis method" eingeführt. In diesem Ansatz gibt es die Möglichkeit, die funktionalen Ableitungen exakt zu behandeln und damit leistungsfähige Reihenentwicklungen durchzuführen, welche sich grundlegend von herkömmlichen Reihenentwicklungen in der Strörungstheorie unterscheiden, d.h., die resultierende Homotopieserie überwindet die üblichen Paradigmen störungstheoretischer Ansätze in der Quantenfeldtheorie. Auf diese Weise können wir eine vollständige Lösung der Dyson-Schwinger-Gleichung für das ϕ^4 Modell auf einem zwei dimensionalem Gitter in seinem stark korrelierten Bereich nahe eines Phasenübergang zweiter Ordnung erzielen. Um zu diesem Ergebnis ohne jedwede Vereinfachung zu gelangen, entwickeln wir die Expansion der "homotopy analysis method" in Form von Baumdiagrammen, welches das Speicherproblem von Korrelationsfunktionen höherer Ordnung, wie z.B. der Vier-Punkt-Vertexfunktion, löst. In Analogie zu diagrammatischen Monte-Carlo Algorithmen führen wir einen Monte-Carlo-Algorithmus ein, um alle möglichen Baumdiagramme aufzusummieren, sodass die Homotopieserie auch zu höheren Ordungen ausgewertet werden kann.

Abstract

This thesis deals with the development and application of quantum field theoretic methods for the study of strongly correlated many-body systems. In these strongly correlated systems new physical effects arise due to the collective behavior of its individual constituents. The theoretical understanding of these systems often calls for first-principles computational approaches.
In the first part of the thesis we use classical Monte Carlo simulations together with a renormalization group approach to unambiguously establish the existence of the scratched-XY universality class. This universality class describes the destruction of the critical superfluid phase in systems which allow for a two dimensional hydrodynamic description by a mechanism fundamentally different from the proliferation of topological defects. For that we study the finite-temperature superfluid transition in a modified two dimensional classical XY model with power-law distributed "scratch"-like bond disorder. As its exponent decreases, the disorder grows stronger and the mechanism driving the superfluid transition changes from conventional vortex-pair unbinding to a strong randomness criticality (termed scratched-XY criticality) characterized by a non-universal jump of the superfluid stiffness. The existence of the scratched-XY criticality at finite temperature and its description by an asymptotically exact semi-renormalization group theory, previously developed for the superfluid-insulator transition in one-dimensional disordered quantum systems, is numerically proven by designing a model with minimal finite size effects.
In the second part of the thesis we develop a new analytical and computational approach for the study of strongly correlated many-body systems. Instead of setting up many-body calculations in a functional integral approach as, e.g., in path integral Quantum Monte Carlo simulations and diagrammatic Monte Carlo calculations, we propose the use of functional integro-differential equations obtained from the Dyson-Schwinger equation. This functional integro-differential equation is solved beyond any truncation scheme using a homotopy approach, in particular the homotopy analysis method. It gives the possibility to treat the functional derivatives exactly and provides a powerful series expansion technique fundamentally different from perturbation theory, i.e., the resulting homotopy series overcomes the usual paradigms of perturbative calculations in field theory. In that way we provide a full and unbiased solution to the Dyson-Schwinger equation beyond any truncation scheme illustrated for ϕ^4 theory on a two dimensional square lattice in its strongly correlated regime close to a second-order phase transition. In order to arrive at this result we develop the expansion of the homotopy analysis method in terms of rooted tree diagrams. This also solves the storage problem of higher-order correlation functions, e.g., the four-point vertex function. Moreover, in the same spirit as diagrammatic Monte Carlo algorithms are used to sum up all connected Feynman diagrams, we introduce a Monte Carlo algorithm to sum up all possible rooted tree diagrams which allows us to evaluate the homotopy series to higher orders.

Publications

This work is based on the following publications and preprints which are partially reprinted.

Tobias Pfeffer and Lode Pollet
A stochastic root finding approach: the homotopy analysis method applied to Dyson-Schwinger equations
New J. Phys. **19**, 043005 (2017) [1]

We present the construction and stochastic summation of rooted-tree diagrams, based on the expansion of a root finding algorithm applied to the Dyson-Schwinger equations. The mathematical formulation shows superior convergence properties compared to the bold diagrammatic Monte Carlo approach and the developed algorithm allows one to tackle generic high-dimensional integral equations, to avoid the curse of dealing explicitly with high-dimensional objects and to access non-perturbative regimes. The sign problem remains the limiting factor, but it is not found to be worse than in other approaches. We illustrate the method for ϕ^4 theory but note that it applies in principle to any model.

Tobias Pfeffer and Lode Pollet
Full and unbiased solution of the Dyson-Schwinger equation in the functional integro-differential representation
Phys. Rev. B **98**, 195104 (2018) [2]

We provide a full and unbiased solution to the Dyson-Schwinger equation illustrated for ϕ^4 theory in 2D. It is based on an exact treatment of the functional derivative $\delta\Gamma/\delta G$ of the four-point vertex function Γ with respect to the two-point correlation function G within the framework of the homotopy analysis method (HAM) and the Monte Carlo sampling of rooted tree diagrams. The resulting series solution in deformations can be considered as an asymptotic series around $G = 0$ in a HAM control parameter $c_0 G$, or even a convergent one up to the phase transition point if shifts in G can be performed (such as by summing up all ladder diagrams). These considerations are equally applicable to fermionic quantum field theories and offer a fresh approach to solving functional integro-differential equations beyond any truncation scheme.

Tobias Pfeffer, Zhiyuan Yao, and Lode Pollet
Strong randomness criticality in the scratched-XY model
arXiv:1807.09184 (2018)

We study the finite-temperature superfluid transition in a modified two-dimensional (2D) XY model with power-law distributed "scratch"-like bond disorder. As its exponent decreases, the disorder grows stronger and the mechanism driving the superfluid transition changes from conventional vortex-pair unbinding to a strong randomness criticality (termed scratched-XY criticality) characterized by a non-universal jump of the superfluid stiffness. The existence of the scratched-XY criticality at finite temperature and its description by an asymptotically exact semi-renormalization group theory, previously developed for the superfluid-insulator transition in one-dimensional disordered quantum systems, is numerically proven by designing a model with minimal finite size effects. Possible experimental implementations are discussed.

Contents

1

Introduction

In retrospect, the experimental discovery of superconductivity and superfluidity by Heike Kamerlingh Onnes in 1911[1] cannot be underestimated. Not only for the intriguing phenomenology of the effects on their own and their elusive technical applications, the discovery of superfluidity and superconductivity is a truly remarkable result. In a broader context, it is the first intriguing demonstration that a physical system with many degrees of freedom observed at low energies can show different and unexpected macroscopic behavior completely distinct from its microscopic constituents. These experimental results ignite theoretical effort to understand the phenomena of superconductivity and superfluidity, which eventually led to a radically new understanding of many-body systems. Landau [6] associated to each distinct macroscopic behavior a local order parameter classifying these macroscopic states into different phases of matter. In his phenomenological theory, transitions between different phases are described by the continuous development of a non-zero order parameter and the spontaneous breaking of the underlying symmetry group. Bogoliubov's theory of the weakly interacting Bose gas [7] was the starting point for the theoretical understanding of the microscopic mechanisms at play and the theory developed by Bardeen, Cooper, and Schrieffer (BCS) in 1957 [8] explained in detail the development of the superconducting order parameter in Onnes' experiment. These theories illustrated that the collective and coherent interplay between the microscopic constituents over long distances of a system made up of a large number of degrees of freedom leads to the development of a non-zero order parameter. Together with the concept of the renormalization group [9, 10, 11], this collection of results is now known as the theory of second-order or continuous phase transitions. These developments marked a paradigm shift: superfluidity, superconductivity, and other phenomena described by the theory of second-order phase transitions are not understood in terms of a more fundamental theory of the behavior of its constituents but by the concerted collective behavior of the individual constituents governed by already known quantum mechanical laws. Systems which necessitate such kind of understanding are called strongly correlated systems and the superconductivity observed by Onnes was just the first example of such a system. From the theoretical point of view understanding these strongly correlated systems is very challenging and first-principles computational approaches are almost indispensable. In this thesis we present two different approaches for the use of computational methods in the study of strongly correlated systems.

By the time Wilson formalized the renormalization group ideas, which have led to a unified microscopic understanding of Landau's concept of a local order parameter, the work of Berezinskii [12, 13], Kosterlitz, and Thouless [14] demonstrated that there are strongly correlated systems which demand for understanding beyond the concept of a local order parameter. Two

[1] Onnes, in his laboratory books, noted on the same day as superconductivity was discovered the unusual behavior of liquified ^{4}He below 2.2K [3]. In 1938 Pyotr Kapitsa [4] and John F. Allen together with Don Misener [5] published their experimental results on the phenomenological properties of Helium II (by that time it was already known that liquid ^{4}He enters a low temperature phase called Helium II).

dimensional Helium films [15, 16] and related systems [17, 18, 19] are experimental examples which undergo this Berezinskii-Kosterlitz-Thouless (BKT) transition, which was found by purely theoretical arguments. The most famous and simplest example for a microscopic model system hosting a BKT transition is the classical XY model in two dimensions (2D). In this model, a superfluid to normal liquid phase transition with a diverging correlation length, but without the development of a local order parameter, is predicted [20]. The transition is driven by topological defects, in particular the unbinding of vortex–anti-vortex pairs in the phase field of the 2D XY model.
The question whether there exists in these systems an alternative mechanism for the destruction of superfluidity fundamentally different from the proliferation of topological defects has been a contentious one for several decades - especially in the context of disordered critical points. In the first part of the thesis we give a final and conclusive affirmative answer to this question. For that we study the finite-temperature superfluid transition in a modified 2D XY model with power-law distributed "scratch"-like bond disorder. In this model it is possible to isolate the effective degrees of freedom, which lead to the development of strong correlations and drive the transition between distinct phases of matter. In that way we can obtain full analytic understanding and predict the behavior of different observables. In particular, we show that as the exponent of the power-law distributed "scratch"-like bond disorder decreases, the disorder grows stronger and the mechanism driving the superfluid transition changes from conventional vortex-pair unbinding to a strong randomness criticality - termed scratched-XY criticality. The scratched-XY criticality is analytically described by an asymptotically exact semi-renormalization group theory previously developed for the superfluid-insulator transition in one-dimensional disordered quantum systems. We numerically verify its predictions by designing a model with minimal finite size effects - the scratched-XY model - and use classical Monte Carlo simulations to unambiguously demonstrate the existence of the scratched-XY universality class. Therefore, the computational approach is used to check the correctness and reliability by comparing analytic results to first-principles numerical simulations. In this case numerical simulations are a tool to verify or disprove a theory. This is obviously the most powerful way to use the computational approach in the study of strongly correlated systems.
The first part of the thesis is organized as follows. In Sec. 2.1 we review the asymptotically exact renormalization group theory developed by Kosterlitz [20] for the 2D classical XY model. In this section we introduce the numerical protocols needed to demonstrate the existence of the BKT universality class. These protocols will also be used in a later section to verify the existence of the scratched-XY universality class. In Sec. 2.2 we introduce the perturbative renormalization group of Kane and Fisher describing the effect of an isolated impurity on the hydrodynamic description of one-dimensional quantum systems. This is one of the main building blocks of the semi-renormalization group theory and therefore we re-derive its main result in the context of the XY model. Finally, in Sec. 2.3 we introduce the scratched-XY model and show that it is analytically described by an asymptotically exact semi-renormalization group theory previously developed for the superfluid-insulator transition in one-dimensional disordered quantum systems. We then use classical Monte Carlo simulations together with the protocols introduced for the BKT universality class to verify the existence of the scratched-XY universality class.

Whereas in the first part of this thesis we use the computational approach to verify analytic predictions by first-principles numerical calculations, the developments presented in the second part are driven by a different motivation. There are strongly correlated experimental systems which defy any complete microscopic understanding. The fractional quantum Hall effect found in 1982 [21] in GaAs-AlGaAs heterojunctions in strong magnetic fields is described in terms of a two dimensional electron gas forming an intrinsic topological ordered state [22]. This state is described by a topological or global order parameter and is not formed due to long-range correlations of

the electrons but by long-range entanglement [23, 24]. Details about the microscopic mechanisms leading in these systems to the topological order is still under ongoing debate. Frustrated spin systems with quantum spin liquid ground states [25] are another prominent class of models where intrinsic topological order is realized. The experimental observation of these ground states such as in cesium chlorocuprate crystals (Cs_2CuCl_4) or herbertsmithite ($ZnCu_3(OH)_6Cl_2$) is very challenging [26] and under active research [27, 28]. Moreover, the high-temperature superconductivity found in 1986 by Bednorz and Müller in copper oxide compounds [29] and later on in various other types of materials is a type of superconductivity different from the one found by Onnes. Their unusual high transition temperatures cannot be explained by BCS theory. Despite decades of experimental and theoretical research much less consensus about their correct phenomenological description has been reached and the microscopic understanding of these systems in all their varieties is still subject of ongoing research.
Therefore, the second and not less important motivation for the use of computational approaches comes from these systems where no or little understanding about microscopic mechanisms driving the development of strong correlations has yet been reached. In this case the theoretical effort goes into building microscopic lattice or continuum models and first-principles numerical simulations are used to solve these models. The computational approach aims to identify the effective degrees of freedom dominating the low energy collective behavior in these models and consequently also in the experimental systems. Common to all these systems is that the strong correlations arise due to non-trivial interaction effects between the microscopic degrees of freedom. Unfortunately, for the experimental systems which are the least understood the interacting microscopic models - thought to capture the physics correctly - pushes the established computational approaches to their limits. Experimental systems, which feature intrinsic topological order, are modeled either by frustrated spin systems or interacting fermionic/bosonic systems in the presence of strong magnetic fields or non-trivial band topology. The most prominent model, which is thought to elucidate the physics of high-temperature superconductors, is the Hubbard model. In this model the interplay between a variety of effects [30] can be studied, including the unusual normal state behavior [31] of the high-T_c materials.
One of the most versatile techniques to solve these models in the strongly correlated regime is the Quantum Monte Carlo (QMC) approach. Unprecedented insight has been gained with path integral Monte Carlo methods for bosonic cold atomic systems [32, 33, 34] and even large scale ab-initio simulations of superfluid and supersolid ^{4}He [35, 36] are possible. For fermionic systems in the presence of special symmetries, e.g., particle-hole symmetry, determinant Monte Carlo simulations are a powerful tool [37, 38, 39]. However, in the absence of a positive expansion scheme, which is the case in generic situations, Quantum Monte Carlo algorithms scale exponentially and no further progress can be made. Diagrammatic Monte Carlo (diagMC) [40, 41] has been introduced to circumvent the exponential scaling of QMC algorithms on the system volume and inverse temperature in the case of a non-positive expansion. Instead of performing the calculations like QMC approaches in a finite simulation box diagMC works directly in the thermodynamic limit. It uses the perturbative Feynman diagrammatic expansion to sample the series of connected Feynman diagrams by Markov chain Monte Carlo techniques. The scaling is therefore exponential in the expansion order of the perturbative series. However, the biggest obstacle for the diagMC approach is that in general the perturbative series is asymptotic or divergent. The analytic continuation of the perturbative series into the strongly correlated regime, where the single particle picture breaks down, is an unsolved problem ever since the use of perturbation theory. Another set of techniques, which work directly in the thermodynamic limit, are self-consistent field theories based on the embedding of impurity problems. They are the true workhorse techniques for cutting edge ab-initio studies of strongly correlated systems in material science. The most prominent example is the dynamical mean field theory (DMFT) [42, 43], which is most successful in describing the local physics of the interaction driven metal-

insulator transition. In order to incorporate non-local correlations, extensions to DMFT have been proposed, e.g., the dynamical cluster approximation (DCA) [44] and the dynamical vertex approximation (DΓA) [45]. These extensions rely on the non-trivial solution of complicated impurity problems and further progress towards establishing the quality of the approximations in the strongly correlated regime relies on the development of more advanced impurity solvers. Even before the advent of large-scale computational approaches, the renormalization group ideas were used as a powerful semi-analytic tool in the form of the perturbative renormalization group [46, 47]. The development of the functional renormalization group (fRG) [48] provided a more intuitive computational framework of the renormalization group ideas. Nevertheless, in general, the resulting fRG equations are too complex to be solved without truncations and the quality of these approximations in the strongly correlated regime is a delicate issue. Common to the above methods is that they are all formulated in a functional integral approach. Another class of techniques study ground state properties of interacting quantum many-body models directly in the Hamiltonian approach, most prominently exact diagonalization (ED) techniques. In order to overcome the direct scaling of ED with the dimension of the Hilbert space, the large scale numerical optimization of ansatz wavefunctions has been introduced. It is well known that the DMRG algorithm developed by White in 1992 [49] is equivalent to the variational optimization of an ansatz wavefunction represented in terms of matrix product states (MPS) [50], a special form of tensor network states. It can be rigorously shown that the approximation quality of the matrix product states is bounded by the ground state area law of entanglement entropy and therefore encounter severe difficulties at dimensions larger than one. Further tensor network states such as projected entangled pair states (PEPS) [51] and the multi-scale entanglement renormalization ansatz (MERA) [52] have been explored to extend the variational calculations to 2D but much less is established about their approximation quality.

It may not be a coincidence that for the strongly correlated systems, which are the least understood, these established methods are very limited and one can easily argue that due to the lack of first-principles numerical methods our understanding of these systems is so poor. Therefore, despite decades of research, developing new first-principles methods for strongly correlated many-body systems remains an active field of research in theoretical physics.

The second part of this thesis is dedicated to these developments.

We first suggest to compare the computational complexity of the above established first-principles methods in terms of their scaling with respect to the physical relevant quantity in the strongly correlated regime, the correlation length. Based on this, we show that both Quantum Monte Carlo simulations and diagrammatic Monte Carlo calculations asymptotically scale exponentially in the strongly correlated regime. Nevertheless, we identify the flexibility of the quantum field theoretic approach based on perturbation theory as the major advantage to overcome the limitations of established methods. We demonstrate this flexibility but also its main limitations, the convergence properties of these series expansions, by discussing the calculation of critical properties from the quantum field theoretic method.

In order to overcome these limitations, we introduce a fundamentally different approach - both from the analytic and computational perspective - to quantum field theoretic many-body calculations. Instead of setting up many-body calculations in a functional integral approach as, e.g., in path integral Quantum Monte Carlo simulations and diagrammatic Monte Carlo calculations, we propose the use of functional integro-differential equations obtained from the Dyson-Schwinger equation (DSE) [101]. This functional integro-differential equation is solved beyond any truncation scheme by using the homotopy analysis method, which gives us the possibility to treat the functional derivatives exactly and provides a powerful series expansion technique fundamentally different from perturbation theory, i.e., the resulting homotopy series can overcome the usual paradigms of perturbative calculations in field theory. By developing various new computational techniques, we provide a full and unbiased solution to the Dyson-Schwinger equation beyond

any truncation scheme illustrated for ϕ^4 theory on a 2D square lattice in its strongly correlated regime close to a second-order phase transition. We use this non-trivial though representative microscopic model due to its simplicity as a benchmark for our new computational approach. Although we have not yet applied our method to the model systems driving our research efforts, the final result is obtained without any simplifications from first-principles and consequently we are confident that the above considerations are equally applicable to these model systems.
The development is guided by the solution of two problems in different fields of computational many-body physics. First, we point out a possible solution to the convergence issues of perturbation theory in field theory limiting, e.g., the applicability of diagrammatic Monte Carlo in the strongly correlated regime. Second, our approach shows how to handle functional integro-differential equations beyond any truncation scheme and may also be used for the functional renormalization group equation or Hedin's equations.
The second part of the thesis is organized as follows. In Ch. 3 we discuss the comparison between the computational complexity of QMC and diagMC. Ch. 4 reviews the perturbative field theory approach to strongly correlated systems for the example of the 2D ϕ^4 model in the continuum. The main developments of the second part of this thesis are discussed in Ch. 5. In Sec. 5.1, we illustrate the derivation of the functional closure of the DSE on the two-particle level first for the ϕ^4 model in 0D and in Sec. 5.2 for a field theory with general two-body interaction. In Sec. 5.3 we introduce the homotopy analysis method for the solution of the 0D toy model. Sec. 5.4 introduces the diagrammatic language of rooted trees and a Markov chain Monte Carlo algorithm to sum up all rooted tree diagrams for the example of an elementary integral equation. Finally, in Sec. 5.5, we apply the introduced methods to solve the DSE for the ϕ^4 model in 2D.

Part I.

Application of computational methods for the study of strongly correlated systems

2

Strong disorder criticality in (1+1)D and the superfluid transition

It is well known that in spatial dimensions D $\leq$ 2 long-range order is destroyed by thermal fluctuations for systems with continuous symmetry and short-range interactions [53]. However, the 2D XY model describing the superfluid to normal liquid (SF–NL) transition at finite temperature can still undergo a Berezinskii-Kosterlitz-Thouless (BKT) transition driven by the proliferation of topological defects, in particular the unbinding of vortex and anti-vortex pairs [14, 20, 12, 13]. This transition features a universal jump of the superfluid stiffness Λ at the critical temperature T_c, i.e., $\Lambda(T_c)/T_c = 2/\pi$ at the transition.

The fundamental question whether there exists an alternative mechanism for the destruction of superfluidity fundamentally different from the proliferation of topological defects has been a contentious one for several decades – especially in the context of the one-dimensional (1D) superfluid–Bose-glass (BG) quantum phase transition [54, 55, 56]. While in the weak disorder regime the transition is driven by the proliferation of instanton–anti-instanton pairs ["vertical" vortex–anti-vortex pairs in the (1 + 1)-dimensional superfluid phase field] with a universal critical Luttinger liquid parameter $K_c = 3/2$ [57, 58], the possibility of a different mechanism in the strong disorder regime can not be ruled out. Using the strong disorder renormalization group (SDRG) method, Altman et al. claimed that the Coulomb blockade physics of weak links (strong potential barriers) can give rise to a new criticality in the strong disorder regime [59, 60, 61, 62]. However, in this case the SDRG is uncontrolled as the fixed point solutions violate the assumptions under which the approximate RG equations have been derived. Based on the Kane-Fisher physics of weak links [63, 64], Pollet et al. developed an asymptotically exact theory of the 1D superfluid-insulator transition and showed that rare weak links can destroy superfluidity and give rise to a new criticality, the so-called scratched-XY (sXY) criticality [65, 66, 67]. The hallmark of the transition is the relation $K_c = 1/\zeta$, where ζ is a microscopic, irrenormalizable parameter characterizing the scaling behavior of the bare strength of the typically weakest links, $J_0^{(L)} \sim 1/L^{1-\zeta}$, in a system of size L.

However, the explicit relationship between ζ and the microscopic parameters is unknown, and extracting ζ numerically or experimentally requires great effort. Strong finite size effects in the 1D Bose-Hubbard model with diagonal disorder were so far preventing a solid numerical proof for the validity of the sXY scenario [67] – even to the extent that despite several large-scale simulations, a consensus of the nature of the superfluid-insulator transition in the strong disorder regime has not been reached [68, 69, 62, 70].

In this part of the thesis, we study the superfluid transition in a classical 2D XY model with power-law distribution of parallel "scratches". Due to its simplicity, this model shows minimal finite size effects and ζ can be determined analytically. These properties enable us to unambiguously demonstrate the existence of the sXY university class and verify the theory by Pollet et al. for 1D superfluid-insulator transitions. We also show that the theory by Altman et al. fails to describe the strong disorder critical point. Moreover, thanks to the fact that in the scratched-XY model

ζ is controlled by a microscopic parameter, an experimental verification for this new criticality for a finite temperature phase transition is feasible.
In this part of the thesis we provide a self-contained discussion of the sXY universality class in the context of the classical statistical field theory of the XY model. We do not introduce the low energy, long wavelength description of one dimensional interacting quantum systems where this new universality class was first suggested. In a first step we review the (SF–NL) transition of the classical XY model in 2D. We outline the main steps of the derivation of the coupled set of RG equations describing the BKT transition and afterwards discuss the analysis of numerical finite size data with respect to the solution of the RG equations. These protocols can be easily generalized to the strong disorder regime. Thereafter, we discuss the derivation of the Kane-Fisher RG equation, which is the main building block of the asymptotically exact renormalization group theory developed by Pollet et al. for 1D superfluid-insulator transitions. In the last part we apply the renormalization group theory of Pollet et al. to the scratched-XY model and use the fitting protocols introduced for the BKT transition to analyze the numerical data in the strong disorder regime.

2.1. The XY model and the superfluid–normal liquid transition

In this section we review the physics of the clean two dimensional classical XY model. We discuss the renormalization group analysis of the Berezinskii-Kosterlitz-Thouless (BKT) transition, which describes the unbinding of vortex–anti-vortex pairs. For later use we review how to derive from the solution of the RG equations the hallmark of the BKT transition: the universal jump of the superfluid stiffness and the exponential divergence of the correlation length at the transition. Moreover, we show how the renormalization group flow of the superfluid stiffness, which is obtained from the solution of the RG equations, can be fitted to numerical finite size data from classical Monte Carlo simulations.
The classical XY model is a model of classical planar spins $\mathbf{n} = (\cos\theta, \sin\theta)$ with Hamiltonian,

$$H_{\mathrm{XY}} = -J \sum_{\mathbf{r},\hat{\mu}} \mathbf{n}_{\mathbf{r}} \mathbf{n}_{\mathbf{r}+\hat{\mu}} = -J \sum_{\mathbf{r},\hat{\mu}} \cos\left(\theta_{\mathbf{r}} - \theta_{\mathbf{r}+\hat{\mu}}\right). \tag{2.1}$$

We consider the model on a 2D square lattice with linear size L where $\mathbf{r} = (x, y)$ is the site index and $\hat{\mu} \in \{\hat{x}, \hat{y}\}$ is the unit vector along the bond in μ-direction connecting nearest neighbour sites with a spin coupling J. This model has a global $U(1)$ symmetry as the phase field θ can be simultaneously shifted by a constant $\theta_{\mathbf{r}} \to \theta_{\mathbf{r}} + \delta$ for all $\mathbf{r}$ leaving the Hamiltonian invariant.
In order to determine the properties of the system at low temperatures we calculate the correlation function

$$G(\mathbf{r}) = \langle \mathbf{n}_{\mathbf{r}} \mathbf{n}_0 \rangle = \frac{1}{Z} \int \prod_{\mathbf{r}'} \mathrm{d}\theta_{\mathbf{r}'} \, \mathrm{Re}\left[e^{i(\theta_{\mathbf{r}} - \theta_0)}\right] e^{-\beta H_{\mathrm{XY}}}, \tag{2.2}$$

where Z is the partition function of the system, $\beta = 1/T$ the inverse temperature, and Re denotes the real part of a complex number. At low temperatures it can be assumed that the phase $\theta_{\mathbf{r}}$ is slowly varying with $\mathbf{r}$ and therefore the classical XY model may be approximated by a classical harmonic theory in the continuum,

$$H_{sw} = \frac{\Lambda(L_0)}{2} \int \mathrm{d}^2\mathbf{r} \, (\nabla\theta(\mathbf{r}))^2. \tag{2.3}$$

This theory has a high-energy cutoff determined by some small microscopic length scale L_0 measured in units of the lattice constant. At this length scale we have introduced the coarse

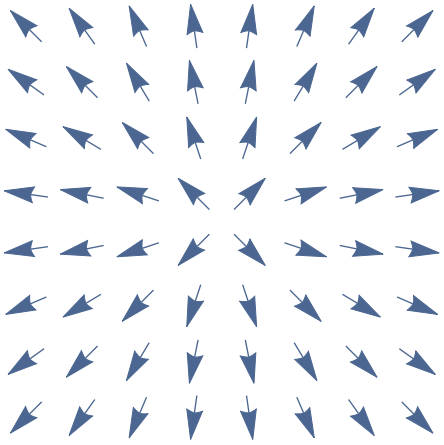

Figure 2.1.: A vortex in the phase field θ with charge $q = 1$. For the example the singular configuration in the phase field is given by $\theta(\mathbf{r}) = \phi$, where ϕ is the angle in polar coordinates.

grained continuous superfluid phase field $\theta(\mathbf{r})$ and the microscopic superfluid stiffness $\Lambda(L_0)$. Calculating the correlation function within the harmonic approximation, we obtain [71]

$$G(\mathbf{r}) \propto |\mathbf{r}|^{-\frac{1}{2K(L_0)}}. \tag{2.4}$$

We have introduced the dimensionless parameter $K(L_0) = \pi\beta\Lambda(L_0)$. This shows that for any finite temperature T the correlation function has a power law decay and therefore no long-range ordered phase can exist. This rules out any spontaneous breaking of the $U(1)$ symmetry and consequently any second-order phase transition. In a much more general context this is in agreement with the Mermin-Wagner theorem [53], which states that in spatial dimensions $D \leq 2$ long-range order is destroyed by thermal fluctuations for systems with continuous symmetry and short-range interactions. On the other hand, at high temperatures, the correlation function (2.2) can be computed within a high temperature series expansion. In this approximation an exponentially decaying correlation function is found [71],

$$G(\mathbf{r}) \propto e^{-|\mathbf{r}|/\xi}, \tag{2.5}$$

with $\xi = 1/\ln(2J^{-1})$.
These results suggest two different regimes. From the theory of second-order phase transitions it is well known that at criticality the correlation function has a power-law decay governed by the universal exponent η. For the XY model in its harmonic approximation we find a power-law decay governed by the microscopic model parameter $\eta = \frac{1}{2K(L_0)}$. This is in violation with the expectations of the renormalization group ideas, which hints that the harmonic theory is a too simplified approximation.

In the work of Berezinskii [12, 13] and Kosterlitz, Thouless [14] it was pointed out that the harmonic theory neglects the periodicity of the variable θ. Taking this periodicity into account, singular configurations in the phase field emerge as local minima. The effective degrees of freedom in these configurations are called vortices and are defined by the line integral along a closed contour $\mathcal{C}$,

$$\oint_{\mathcal{C}} \mathrm{d}\mathbf{r}\, \nabla\theta(\mathbf{r}) = 2\pi q \quad \text{where } q \in \mathbb{Z}. \tag{2.6}$$

Vortices are topological defects in the phase field as the vortex only contributes with charge q if the closed contour $\mathcal{C}$ encircles the singularity, irrespective of the shape of $\mathcal{C}$. An example of a vortex with charge $q = 1$ is shown in Fig. 2.1. Simple thermodynamic considerations show that indeed the topological defects can drive a phase transition.
The energy of a single vortex E_v in the harmonic approximation can be written as [71]

$$E_v = E^c(L_0) + \pi\Lambda(L_0)\ln\left(\frac{L}{L_0}\right). \tag{2.7}$$

The core energy $E^c(L_0)$ accounts for contributions on small length scales beyond the harmonic approximation such that E_v is independent of L_0.
Therefore, as there are $(L/L_0)^2$ positions to introduce the singular configuration, the partition function for single vortex configurations is

$$Z \approx y(L_0)\left(\frac{L}{L_0}\right)^{2-K(L_0)}, \tag{2.8}$$

where we have introduced the vortex fugacity $y(L_0) = e^{-\beta E^c(L_0)}$. The partition function grows macroscopically large for $K(L_0) < 2$ favouring free vortices for $T > \pi\Lambda(L_0)/2$ whereas for $K(L_0) > 2$ no free vortices appear.
This simple argument suggests qualitatively different regimes but raises the questions about the role of a collection of defects, especially vortex–anti-vortex pairs, i.e., pairs of defects of opposite charge. In the following we review that these pairs renormalize the superfluid stiffness such that the Nelson-Kosterlitz [72] criterion holds,

$$\Lambda_c = \frac{2}{\pi}T_c. \tag{2.9}$$

The superfluid stiffness Λ_μ on a square lattice in μ direction can be determined by the response of the free energy $F = -T\ln Z$ to twisted-boundary conditions in μ direction [73],

$$\Lambda_\mu = \lim_{L\to\infty}\Lambda_\mu(\ln L), \text{ where } \Lambda_\mu(\ln L) = \frac{2}{L^{D-2}}\frac{\mathrm{d}^2F(\varphi)}{\mathrm{d}\varphi^2}, \tag{2.10}$$

and we define $\Lambda = \sqrt{\prod_\mu \Lambda_\mu}$. The asymptotically exact renormalization group theory describing the phase transition in detail and developed in Ref. [20] is reviewed in the following.

2.1.1. Renormalization group theory of the 2D classical XY model

In order to account for the singular vortex configurations in the phase field we split the field $\theta = \theta_a + \theta_s$ in an analytic and a singular part, where the latter accounts for the vortex configurations. Parameterizing the vortex part as $\nabla\theta_s = -\hat{z}\times\nabla\phi$ the field ϕ is determined in the presence of $2n$ vortices at position $\mathbf{r}_i$ with charge q_i by [71]

$$\begin{aligned}\nabla^2\phi(\mathbf{r}) &= 2\pi\sum_{i=1}^{2n} q_i\delta(\mathbf{r}-\mathbf{r}_i),\\ \phi(\mathbf{r}) &\simeq \sum_{i=1}^{2n} q_i\ln\left(\frac{|\mathbf{r}-\mathbf{r}_i|}{L_0}\right) \text{ where } |\mathbf{r}-\mathbf{r}_i| \gg L_0.\end{aligned} \tag{2.11}$$

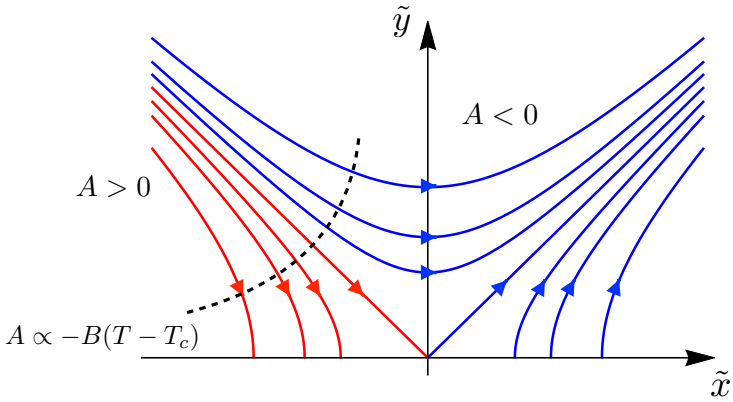

Figure 2.2.: The RG trajectories in terms of the rescaled vortex fugacity $\tilde{y}$ and $\tilde{x} = 2 - K$. The trajectories are labeled by the RG invariant $A = \tilde{x}^2 - \tilde{y}^2$ where $A > 0$ (red) corresponds to the superfluid phase and $A < 0$ (blue) to the normal liquid phase. Without loss of generality it is assumed that the system can be tuned through the transition by fixing the microscopic parameters and only varying the temperature T, i.e., $A \propto -B(T - T_c)$ (dashed line) where T_c is the critical temperature and $B > 0$ is a constant of microscopic origin.

Therefore, we can determine the energy of a field configuration in the presence of a given vortex configuration by taking into account the solution of the 2D electrostatic problem (2.11),

$$H_{XY} \approx \frac{\Lambda(L_0)}{2} \int \mathrm{d}^2\mathbf{r}\, (\nabla\theta_a(\mathbf{r}))^2 - \pi\Lambda(L_0) \sum_{i\neq j} q_i q_j \ln\left(\frac{|\mathbf{r}_i - \mathbf{r}_j|}{L_0}\right) + \sum_i E_{q_i}^{(c)}(L_0). \tag{2.12}$$

In order to arrive at this expression we have to demand charge neutrality of the vortex configuration, i.e., $\sum_i q_i = 0$, and account for self interactions of each vortex by the vortex core energies $E_{q_i}^{(c)}(L_0)$ [71]. Therefore, the partition function is split into an analytic part and a vortex part with,

$$Z_v = \sum_{N=0}^{\infty} y(L_0)^N \int \prod_{i=1}^{N} \mathrm{d}^2\mathbf{r}_i\; e^{2K(L_0)\sum_{i<j} q_i q_j \ln\left(\frac{|\mathbf{r}_i - \mathbf{r}_j|}{L_0}\right)}. \tag{2.13}$$

In the following only vortices with $|q| = 1$ are considered. Assuming that there is a low concentration of vortex pairs the contribution coming from these pairs can be integrated out perturbatively. Accounting for vortex pairs between the minimum size of L_0 and $L_0' = L_0(1 + \mathrm{d}\ell)$, K is renormalized to [73]

$$K(L_0') = K(L_0) - 4\pi K(L_0)^2 y(L_0)^2 \mathrm{d}\ell, \tag{2.14}$$

and by rescaling distances such that the original cutoff is restored the vortex fugacity is renormalized to, cf. (2.7),

$$y(L_0') = y(L_0) + (2 - K(L_0))\, y(L_0)\mathrm{d}\ell. \tag{2.15}$$

Introducing $\tilde{y} = 2\sqrt{\pi}y$ the coupled renormalization group equations can be written as

$$\frac{\mathrm{d}K(\ell)}{\mathrm{d}\ell} = -K^2\tilde{y}^2, \tag{2.16}$$

$$\frac{\mathrm{d}\tilde{y}(\ell)}{\mathrm{d}\ell} = (2 - K)\tilde{y}. \tag{2.17}$$

Although the RG equations have been derived perturbatively to order y^2, i.e., assuming that only a single vortex–anti-vortex pair renormalizes K at each length scale, the equations are asymptotically exact for $K > 2$ because in this case the vortex fugacity inevitably vanishes at large length scales.
From the coupled RG equations we obtain the previously discussed Nelson-Kosterlitz criterion,

$$K_c = 2, \tag{2.18}$$

and therefore we see that K exhibits a finite universal jump at the transition. The critical behavior can be determined by linearizing the flow equations around $K_c = 2$ by introducing $\tilde{x} = 2 - K$,

$$\frac{\mathrm{d}\tilde{x}(\ell)}{\mathrm{d}\ell} = \tilde{y}^2, \tag{2.19}$$

$$\frac{\mathrm{d}\tilde{y}(\ell)}{\mathrm{d}\ell} = \tilde{x}\tilde{y}. \tag{2.20}$$

The RG invariant is given by $A = \tilde{x}^2 - \tilde{y}^2$ and is an analytic function of the microscopic model parameters and the temperature T. Fig. 2.2 shows that for $A > 0$ the RG trajectories describe a flow which asymptotically approaches the fixed line with $y = 0$ defining the superfluid phase whereas $A < 0$ describes the normal liquid phase with $y \to \infty$ and $A = 0$ corresponds to the critical point. Without loss of generality it can be assumed that the microscopic model parameters are fixed and only the temperature is varied to tune the system through the transition. Therefore, A can be expanded as $A \propto -B(T - T_c)$ where T_c is the critical temperature and $B > 0$ is a constant of microscopic origin. The solution of the coupled RG equations for $\tilde{x}(\ell) = 2 - K(\ell)$ is

$$\tilde{x}(\ell) = -\frac{\sqrt{|A|}}{f\left(\sqrt{|A|}(\ell + C)\right)}, \tag{2.21}$$

where for $A > 0$, $f(z) = \tanh z$ and for $A < 0$, $f(z) = -\tan^{-1} z$ and C is another RG invariant. The flow at the critical point ($A = 0$) is given by

$$\tilde{x}(\ell) = -\frac{1}{\ell + C}. \tag{2.22}$$

Although the superfluid stiffness exhibits a finite jump at the transition, the RG equations (2.16) describe a continuous transition, i.e., the correlation length diverges upon approaching the transition from the normal liquid side. The correlation length is given as the length scale at which vortex–anti-vortex pairs dissociate, i.e., $y(\ell = \ln \xi) \approx 1$, and perturbation theory breaks down. From (2.21) and $y(\ell) \approx x(\ell)$ close to the transition, i.e., $A \approx 0$, one obtains [71]

$$\xi \propto e^{\frac{b}{\sqrt{\tau}}}. \tag{2.23}$$

The constant b depends on the microscopic model and we have introduced the detuning from the critical point $\tau = (T - T_c)/T_c$. Therefore, the correlation length diverges continuously at the transition point by the unusual universal behavior (2.23), which is not a power law as for second-order phase transitions. The behaviour of the correlation length is important to qualitatively understand the stability of the critical point in the presence of disorder. The limit of weak disorder can be analysed using the Harris criterion [74]. It simply states that a critical point in a clean system is stable against introducing weak disorder if the critical exponent ν

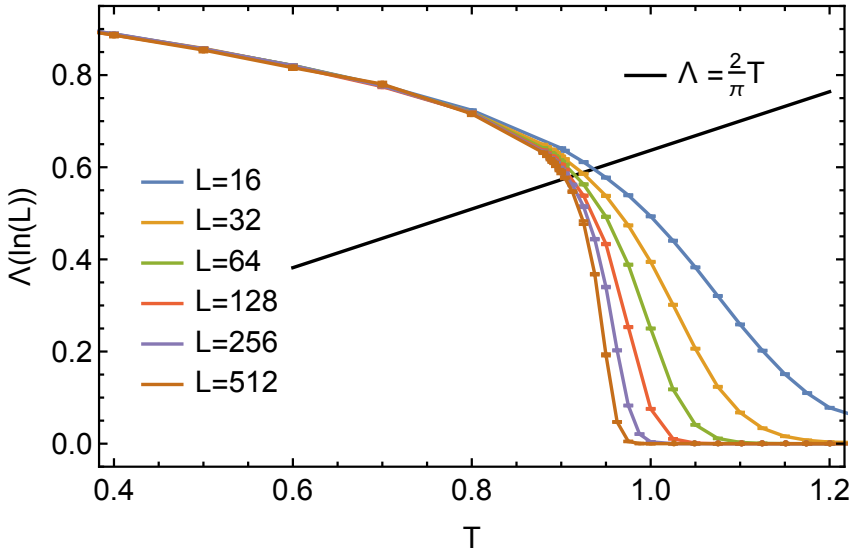

Figure 2.3.: The superfluid stiffness of the classical XY model in systems of linear size $L = 16, 32, 64, 128, 256, 512$ at various temperatures T. For $L \to \infty$ the superfluid stiffness develops a jump at the critical temperature T_c from a universal finite value $2T_c/\pi$ to zero.

determining the divergence of the correlation length, $\xi \propto \tau^{-\nu}$, satisfies

$$\nu > \frac{2}{D_r}, \tag{2.24}$$

where, as usual, the detuning from the phase transition point is denoted by τ and for uncorrelated disorder the effective dimensionality of randomness is $D_r = D$, the dimensionality of the system. For the BKT transition the correlation length diverges faster than any power law, cf. (2.23). In the context of the Harris criterion this implies $\nu = \infty$. Therefore, we conclude that for small disorder the superfluid transition is driven by the usual BKT mechanism of the unbinding of vortex–anti-vortex pairs. Nevertheless, in the following we analyze the classical XY model in the presence of "scratch"-like disorder, i.e., disorder in the form of line defects. It is known that for line defects the effective dimensionality of the randomness is reduced to $D_r = D - 1$ [75] and therefore the effect of weak disorder is already more severe. For the classical XY model Harris' criterion is still satisfied, but it is more likely that line defects can lead to a new strong randomness criticality. Before discussing the classical XY model in the presence of line defects, we introduce the fitting protocols to study the BKT transition numerically.

2.1.2. Numerical analysis

The BKT transition in the XY model can be numerically studied by measuring the superfluid stiffness $\Lambda(\ell)$ with $\ell = \ln L$ in systems of finite size L (measured in units of the microscopic lattice spacing) and fitting the data to the RG flow (2.21), (2.22). In path integral Monte Carlo simulations the superfluid stiffness in a finite square system can be easily determined by the Pollock-Ceperley formula [76] of winding number statistics,

$$\Lambda_\mu(\ell) = T\langle W_\mu^2 \rangle_{\mathrm{MC}}, \tag{2.25}$$

where $\mu \in \{x, y\}$ is the label of spatial direction, W_μ is the winding number in that direction, and $\langle \dots \rangle_{\mathrm{MC}}$ refers to statistical averaging.

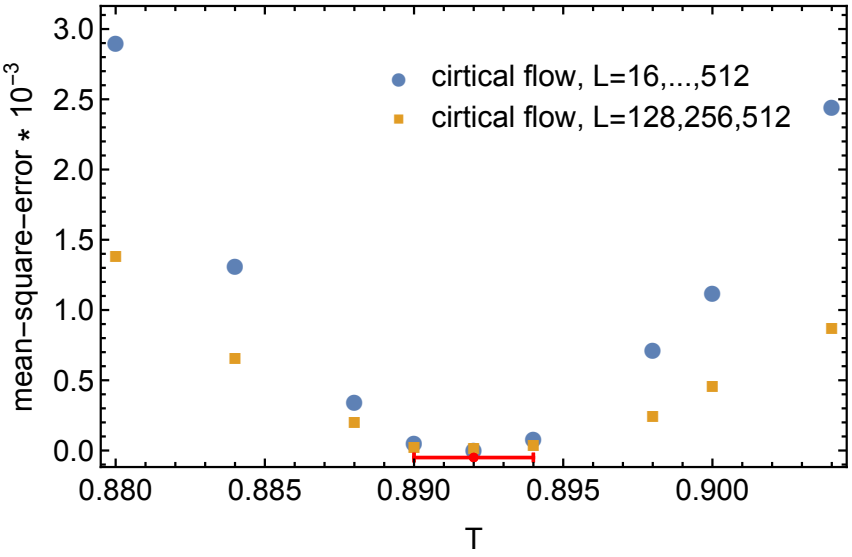

Figure 2.4.: The Weber-Minnhagen [78] mean-square-error σ by fitting the flow of $\Lambda(\ln L)$ for $L = 16, 32, 64, 128, 256, 512$ (blue dots) and $L = 128, 256, 512$ (yellow squares) to the critical flow (2.26) of the BKT universality class. The sharpe minimum of σ determines the critical temperature $T_c = 0.892(2)$ for the 2D classical XY model.

The numerical data for the superfluid stiffness at different temperatures T and for different system sizes is shown in Fig. 2.3. It can be obtained by the classical Worm algorithm [77]. The data is analyzed with the protocol introduced by Weber and Minnhagen [78]. For each temperature point T we fit the data to the critical RG flow (2.22) in the form

$$\Lambda(\ell) = \frac{2}{\pi} T + \frac{1}{\ell + C}. \tag{2.26}$$

The fit depends on a single parameter, the RG invariant C. Therefore, the mean-square-error is minimal at the critical temperature T_c. Fig. 2.4 shows that the mean-square-error has a clear minimum at $T_c = 0.892(2)$. We will use the same fitting protocol for the superfluid transition in the presence of strong disorder. This procedure is based on the fact that there is only a single parameter to fit and the accuracy is drastically reduced if two parameters have to be fitted. The result for the critical temperature can be compared with high accuracy results for the BKT transition, which report $T_c = 0.8935(1)$ [79]. To obtain this high accuracy results, higher-order corrections to the perturbative RG equations (2.16) have to be taken into account [79, 80, 81].

2.2. Kane-Fisher renormalization of a single barrier

Before studying the classical XY model in the presence of "scratch"-like bond disorder, we discuss the effect of a single barrier in the harmonic approximation of the superfluid phase field. In this section we consider the continuum model

$$\begin{aligned} Z &= \int \mathrm{d}(\theta_i)\, e^{-S[\theta_i]} \qquad \text{where} \\ S[\theta_i] &= \sum_i \frac{K}{2\pi} \int \mathrm{d}x\mathrm{d}y\, (\nabla\theta_i(\mathbf{r}))^2 - \frac{t}{T} \int \mathrm{d}y\, \cos(\theta_+(y) - \theta_-(y)) \end{aligned} \tag{2.27}$$

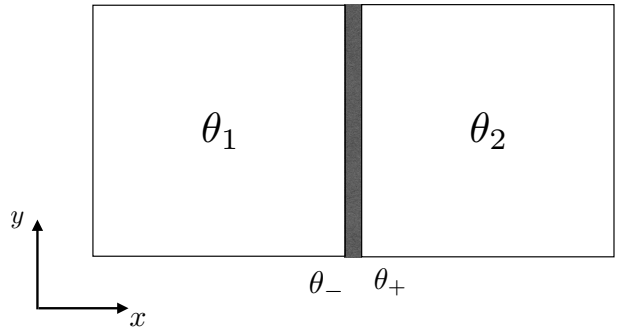

Figure 2.5.: The coupling of the harmonic modes of the superfluid phase field over a barrier described by model (2.27). $\theta_i\,(i=1,2)$ labels the phase field of the left and right superfluid and θ_- and θ_+ are the values of the left and right phase field at the barrier.

The measure of the functional integral over θ_i is denoted by $\mathrm{d}(\theta_i)$ and again $\mathbf{r}=(x,y)$.
It describes the coupling of the harmonic modes of the superfluid phase field over a barrier of bare strength t at $x=0$. Formally, we separated the infinite system into two subsystems with $\theta_i\,(i=1,2)$ labeling the phase field of the left and right superfluid, i.e., $\theta_1(\mathbf{r})=0$ for $x>0$ and $\theta_2(\mathbf{r})=0$ for $x<0$. The fields θ_- and θ_+ are the values of the left and right phase field at $x=0$, i.e., $\theta_-(y)=\theta_1(0,y)$ and $\theta_+(y)=\theta_2(0,y)$. The model is schematically illustrated in Fig. 2.5
If the y-direction is identified with the imaginary time direction for one-dimensional quantum systems in equilibrium, (2.27) is exactly the model considered by Kane and Fisher [63, 64] to describe the physics of interacting spinless fermions or bosons in 1D in the presence of a single isolated large potential barrier, i.e., the coupling of two semi-infinite Luttinger liquids over a single barrier. The main result of their analysis is presented in this section as it is one of the main building blocks in the next section. Using a RG approach, Kane and Fisher showed that for $K>1$ the barrier is irrelevant at large length scales and the phase field becomes continuous across the link whereas for $K<1$ the barrier cuts the system into two pieces such that the phase fields are independent of each other.
To show this for model (2.27), we integrate out the harmonic fluctuation of the superfluid phase field away from the barrier at $x=0$. For this we introduce the field

$$\theta(\mathbf{r})=\begin{cases}\theta_1(\mathbf{r}) & \text{for } x\le 0\\ \theta_2(\mathbf{r}) & \text{for } x>0\end{cases} \tag{2.28}$$

and the auxiliary field $\lambda(y)$. In terms of the new fields the partition function for (2.27) can be rewritten up to numerical constants as,

$$\begin{aligned} S &= \frac{K}{2\pi}\int \mathrm{d}x\mathrm{d}y\,(\nabla\theta)^2-\frac{t}{T}\int \mathrm{d}y\,\cos(\theta_0)+i\int \mathrm{d}y\,\lambda(y)\left[\theta_0(y)-\theta(\mathbf{r}^-)-\theta(\mathbf{r}^+)\right]\\ Z &\propto \int \mathrm{d}(\theta,\theta_0,\lambda)\,e^{-S} \end{aligned} \tag{2.29}$$

where we use the representation of the delta distribution to introduce the effective field $\theta_0(y)$ at $x=0$ and denote $\mathbf{r}^\pm=(0^\pm,y)$. In this representation we first integrate out the field θ and afterwards λ in order to obtain the effective action for the phase field at $x=0$

$$S_{\text{eff}}=\frac{K}{4\pi}\int_\Lambda \frac{\mathrm{d}k}{2\pi}\,|k|\left|\tilde{\theta}_0\right|^2-\frac{t}{T}\int \mathrm{d}y\,\cos(\theta_0). \tag{2.30}$$

The field $\tilde{\theta_0}$ denotes the Fourier transform of θ_0 and we explicitly indicate the high-momentum cutoff Λ of the continuum model (2.27), which holds up to some microscopic length scale, which is set to unity.
The effective model is equivalent to the Caldeira-Leggett model in a periodic potential and the RG analysis used by Fisher and Zwerger [82] to study this model is by now a textbook example for the perturbative momentum shell RG [83, 84]. We split the field θ_0 into fast and slow modes, i.e., $\theta_0 = \theta_{0,s} + \theta_{0,f}$, where, neglecting the subscript 0 from now on,

$$\theta_s(y) = \int_{|k|<\Lambda/b} e^{-iky}\tilde{\theta}(k), \qquad \theta_f(y) = \int_{\Lambda/b<|k|<\Lambda} e^{-iky}\tilde{\theta}(k). \tag{2.31}$$

The action (2.30) is split into $S_{\text{eff}}[\theta] = S_0[\theta] + t/T S_1[\theta]$ and to first order in t/T the partition function is rewritten as

$$Z = \int \mathrm{d}(\theta_s)\, e^{-S_0[\theta_s] - t/T\langle S_1[\theta]\rangle_f + \mathcal{O}\left((t/T)^2\right)}, \tag{2.32}$$

where

$$\langle S_1[\theta]\rangle_f = \int \mathrm{d}(\theta_f)\, e^{-S_0[\theta_f]} \int \mathrm{d}y\, \cos(\theta) = b^{-\frac{1}{K}} \int \mathrm{d}y\, \cos(\theta_s(y)). \tag{2.33}$$

Therefore, integrating out the fast modes rescales the bare strength of the barrier by a factor of $b^{-\frac{1}{K}}$. Restoring the high-momentum cutoff for the slow modes rescales the distances to $y' = y/b$ which yields with $b = \exp(\ell)$ the flow equation for the renormalized strength of the barrier $t(\ell)$,

$$\frac{\mathrm{d}t(\ell)}{\mathrm{d}\ell} = \left(1 - \frac{1}{K}\right) t(\ell). \tag{2.34}$$

The dimensionless quantity K is not renormalized to any order in t/T [82].
Therefore, we see that for $K < 1$ the renormalized strength of the barrier flows to 0 and therefore cuts the system into two independently fluctuating superfluid phase fields. For $K > 1$ the renormalized strength of the barrier flows to larger values and the flow has to stop at some length scale ℓ^* defined by

$$\frac{t(\ell^*)}{T} \approx 1. \tag{2.35}$$

This length scale is referred to as the clutch scale because at this length scale not only perturbation theory breaks down but also the phase field to the left and right of the barrier can be considered to be a single fluctuating superfluid phase field. As the high-momentum cutoff is fixed and all length scales are measured in units of a fixed microscopic length scale it is important to note for the next section that if we consider the model (2.27) in a finite box of size L the system size is rescaled to L/L^* when the clutch scale $L^* = \exp(\ell^*)$ is reached. With this discussion we have gathered all necessary ingredients for the discussion of the 2D classical XY model in the presence of power-law distributed "scratches", which, as we will show, hosts a new strong randomness critical point.

2.3. The scratched-XY model

Finally, in this section, we introduce the scratched-XY model and show that in this model the critical superfluid phase is destroyed by a fundamentally different mechanism from the proliferation of topological defects. The Hamiltonian of our scratched-XY model reads

$$H = -\sum_{\mathbf{r},\hat{\mu}} J_0(\mathbf{r},\hat{\mu}) \cos(\theta_{\mathbf{r}} - \theta_{\mathbf{r}+\hat{\mu}}), \tag{2.36}$$

where $\mathbf{r} = (x, y)$ is the site index of the square lattice, $\hat{\mu} \in \{\hat{x}, \hat{y}\}$ a unit vector along the bonds, and $J_0(\mathbf{r}, \hat{\mu})$ the corresponding coupling. Our units are $J_0(\mathbf{r}, \hat{y}) = 1$ and lattice spacing $a = 1$. The probability distribution of $J_0(x, \hat{x})$ is taken to be a power law distribution,

$$p(J_0)\mathrm{d}J_0 = \frac{1}{\Gamma} J_0^{1/\Gamma - 1} \mathrm{d}J_0 \,, \qquad J_0 \in [0, 1] \,, \tag{2.37}$$

where $\Gamma < 1$ is the only parameter of the model. The bare strength of the typically deepest scratch $J_0^{(L)}$ in a square lattice with linear size L can be estimated by imposing that finding at least one such deep scratch has a probability of order one,

$$L \int_0^{J_0^{(L)}} p(J_0) dJ_0 \sim 1 \,. \tag{2.38}$$

Therefore, $J_0^{(L)}$ scales with L as a power law,

$$J_0^{(L)} \sim \frac{1}{L^{1-\zeta}} \quad \text{where } \zeta = 1 - \Gamma \,. \tag{2.39}$$

Another property of the distribution is that on every new length scale the expectation value of the number of the typically deepest scratches corresponding to the new scale is just one. This follows directly from (2.38).
Without disorder, i.e., $\Gamma = 0$, we recover the clean XY model (2.1). As we have reviewed, it undergoes a BKT transition at a critical temperature $T_c(\Gamma = 0) = T_c = 0.8935(1)$. The scratched-XY model can also be seen as the generalization of the famous McCoy-Wu model [85] from $\mathcal{Z}_2$ symmetry to $U(1)$ symmetry. In contrast to the McCoy-Wu model where the Ising ($\mathcal{Z}_2$) universality in 2D with $\nu = 1$ is unstable against introducing line defects the BKT universality is stable against introducing weak "scratch"-like bond disorder, cf. Sec. 2.1. Therefore, in the limit of weak disorder, $\Gamma \to 0$, the mechanism driving the superfluid transition does not change.
In the following we will use the semi-renormalization group theory developed by Pollet et al. to show that at strong disorder the superfluid phase gets destroyed by a fundamentally different mechanism and the phase transition is described by a new universality class. It will also become clear that $T_c(\Gamma = 1) = 0$ in analogy with the diluted Ising model [86].

2.3.1. Semi-renormalization group theory of the scratched-XY model

We consider the scratched-XY model (2.36) for temperatures $T < T_c(\Gamma = 0)$. Because of the presence of deep scratches with $J_0 \ll 1$, starting from mesoscopic scales, the system can be viewed as superfluid regions joined by barriers formed by single or consecutive scratches. Therefore, in addition to the topological defects, the superfluid stiffness in the x-direction will be renormalized by the barriers connecting adjacent superfluid regions. Quantitatively, the action S that describes an otherwise homogeneous superfluid system with a barrier at $x = 0$ is

$$S = \sum_i \frac{K}{2\pi} \int dx dy \, (\nabla \theta_i)^2 - \frac{t}{T} \int dy \, \cos(\theta_+ - \theta_-) \,. \tag{2.40}$$

We have rescaled x and y and $K = \beta\pi\sqrt{\Lambda_x \Lambda_y}$. Here $\theta_i \, (i = 1, 2)$ is the phase field of the left and right superfluid, θ_- and θ_+ are the values of the left and right phase field at $x = 0$, and t is proportional to the bare strength of the barrier. The renormalization of the strength of the barrier by harmonic modes in the phase field, reviewed in Sec. 2.2, is described by the

Kane-Fisher flow equation [63, 64]

$$\frac{\mathrm{d}t(\ell)}{\mathrm{d}\ell} = \left(1 - K^{-1}\right) t(\ell)\,, \tag{2.41}$$

where $t(\ell)$ is the renormalized strength of the barrier at length scale ℓ. Since the critical value $K_c \geq 2$ (vortex–anti-vortex pairs will proliferate below $K = 2$), the bare strength t will be renormalized towards strong couplings and the RG flow (2.41) stops at the clutch scale ℓ^* where $t(\ell^*)/T \sim 1$ [66, 67]. When the clutch scale is reached, the system size has been rescaled by a factor $1/L^*$ with $L^* = \exp(\ell^*)$. At scales much bigger than the clutch scale, the effect of the barrier on renormalizing the superfluid stiffness is

$$\Lambda_x^{-1}(\ell) - \Lambda_x^{-1}(\ell_0) \propto \frac{1}{t(\ell^*)L/L^*} \propto \frac{L^*}{L}\,, \tag{2.42}$$

where ℓ_0 is some mesoscopic scale. The effect of a single weak barrier on the superfluid stiffness of a finite (1+1)D system in its harmonic approximation is discussed in more detail in App. A.

In the following we assume that the barriers are formed by single scratches and consecutive scratches play a subdominant role (numerically justified later). In the scratched-XY model with well-separated typical deepest scratches, cf. Eq. (2.38), it is possible to write down a flow equation which accounts for the renormalization effect of the scratches on different length scales successively, i.e., we set up a renormalization group flow in the system size. Moreover, the theorem of self-averaging [65] allows us to write the RG equation in terms of the median of Λ_x^{-1} instead of the full distribution. This theorem guarantees that the distribution of the superfluid stiffness (along the x direction in our case) flows towards a δ-like distribution in the superfluid phase including the critical point [65].
The flow of Λ_x^{-1} (in the median sense) due to the scratches is given by

$$\frac{\mathrm{d}\,\Lambda_x^{-1}(\ell)}{\mathrm{d}\,\ell} \propto \frac{L^*}{L}\,. \tag{2.43}$$

Rewriting Eq. (2.43) in terms of the parameter K and introducing $w(\ell) = L^*/L$ leads to

$$\frac{\mathrm{d}K(\ell)}{\mathrm{d}\ell} = -w\, K^3\,, \tag{2.44}$$

where we have rescaled w to absorb unimportant coefficients. The clutch scale implicitly depends on the system size through the strength of the typical deepest scratch. Due to the Kane-Fisher RG the typical deepest scratch picks up a renormalization factor,

$$t(\ell) = J_0(\ell) \exp\left(\int_0^{\ell^*} \mathrm{d}\ell'(1 - 1/K(\ell))\right) \approx J_0(\ell) \left(\frac{1}{L^*}\right)^{1/K(\ell^*)-1}. \tag{2.45}$$

Therefore, the condition for the clutch scale reads

$$1 \sim J_0(\ell) \left(\frac{1}{L^*}\right)^{1/K(\ell^*)-1}. \tag{2.46}$$

Differentiating this expression with respect to ℓ leads to the RG equation for $w(\ell)$,

$$\frac{\mathrm{d}w(\ell)}{\mathrm{d}\ell} = \frac{1 - \zeta K}{K - 1} w. \tag{2.47}$$

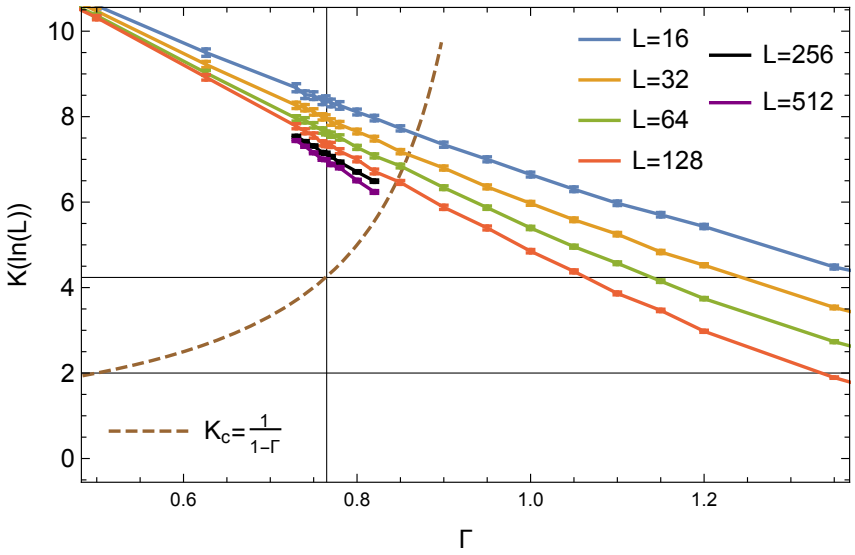

Figure 2.6.: A plot of the disorder averaged $K(\ln L)$ for $L = 16, 32, \ldots, 512$. The brown dashed line is a plot of the critical $1/\zeta$ line. We find a critical value of $\Gamma_c = 0.764(2)$ (vertical grid line) with a non-universal value of $K_c = 4.24(4)$ (upper horizontal grid line) at the transition. The non-universal value of K_c is larger than in the BKT case where $K_c = 2$ (lower horizontal grid line).

On the right-hand side we used the Taylor expansion of $K(\ell)$ together with (2.44) to substitute $K(\ell^*) = K(\ell)$ to leading order in w.
Therefore, for $1/\zeta_c > 2$, a new strong randomness criticality emerges where the superfluid transition is driven by scratches and the vortex–anti-vortex pairs play a subdominant role. Consequently, we can neglect the vortex–anti-vortex pairs in studying this new criticality, and the critical condition is given by

$$K_c = 1/\zeta_c. \tag{2.48}$$

To analyze the coupled RG-equations we perform the same analysis as for the BKT transition. Near the strong randomness critical point, it is convenient to introduce $x(\ell) = K(\ell) - \zeta_c^{-1}$ and linearize the RG equations (2.44), (2.47),

$$\frac{\mathrm{d}\tilde{x}}{\mathrm{d}\ell} = -\tilde{w} \tag{2.49}$$

$$\frac{\mathrm{d}\tilde{w}}{\mathrm{d}\ell} = -2\tilde{x}\tilde{w}\,, \tag{2.50}$$

where $\tilde{x} = x\,\zeta_c^2(1-\zeta_c)^{-1}/2$ and $\tilde{w} = w/\left(2\,\zeta_c(1-\zeta_c)\right)$ are rescaled x and w, respectively. The RG invariant $A = \tilde{w} - \tilde{x}^2$ is an analytic function of the microscopic parameters ζ and T, and $A = 0$ corresponds to the critical flow. At fixed temperature and near the critical point (T, ζ_c), $A \approx B(\zeta_c - \zeta)$ where B is a constant, and $\zeta = 1 - \Gamma$ acts as the tuning parameter. The solution $\tilde{x}(l)$ away from the critical point is given by

$$\tilde{x}(\ell) = \frac{\sqrt{|A|}}{f\left(\sqrt{|A|}(\ell + C)\right)}\,, \tag{2.51}$$

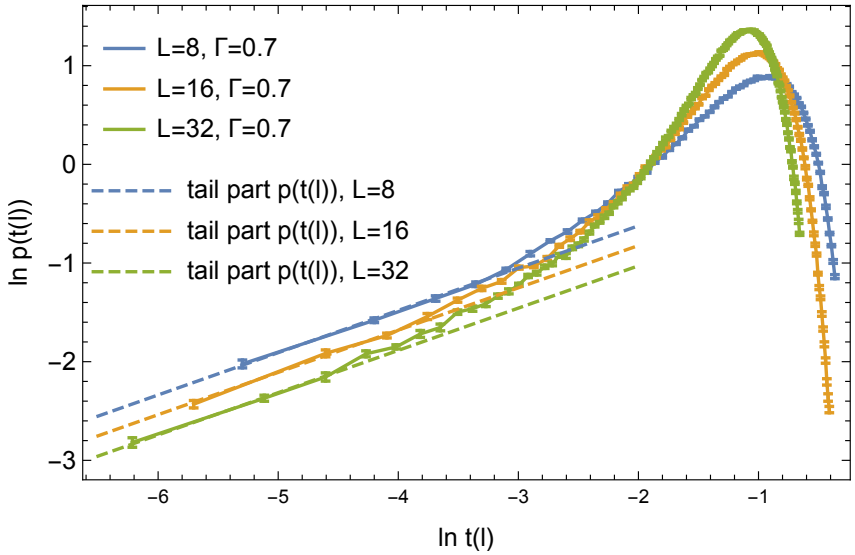

Figure 2.7.: The log-log plot of the distribution of renormalized strengths $t(\ell)$ at $\Gamma = 0.7$ for $L = 8, 16, 32$ from $8 \times 10^5, 1.2 \times 10^6, 2.0 \times 10^6$ disorder realizations (in contrast to a few thousands in [70]). The slope of the tail keeps changing until small enough $t(\ell)$ (requiring a sufficient number of disorder realizations) is reached. The tail part on the log-log scale is perfectly fitted by a linear line with a slope 0.43(1), which agrees with the exponent $1/\Gamma - 1$ within error bars. Therefore, the barriers joining adjacent superfluid regions are formed by the individual deepest scratches.

where $A > 0$, $f(z) = \tan z$ on the superfluid side, $A < 0$, $f(z) = \tanh z$ on the disordered side, and C is another RG invariant. The flow at the critical point ($A = 0$) is given by

$$\tilde{x}(\ell) = \frac{1}{\ell + C}\,. \tag{2.52}$$

The solutions of the RG equations (2.49) are used to extrapolate finite size data to infinite system size. To this end, we define the universal scaling function $F(z)$,

$$F(z) \equiv (\ln L + C)\left[K(\zeta, \ln L) - \zeta_c^{-1}\right] \tag{2.53}$$

where $z = (\zeta_c - \zeta)(\ln L + C)^2$. The universal scaling function $F(z)$ has the property $F(0) = 2(1 - \zeta_c)/\zeta_c^2$. Therefore, using the semi-renormalization group theory we have obtained full analytic control over the scratched-XY model and derived the renormalization group flow for $K(\ell)$. In the following we will use classical Monte Carlo simulations to numerically obtain the flow of $K(\ln L)$ with system size L and show that this flow is perfectly described by the one derived from the semi-renormalization group theory.

2.3.2. Numerical analysis

To numerically establish the strong randomness criticality, we study the superfluid response of the scratched-XY model at fixed temperature, $T = 0.2$, by tuning Γ. For a square lattice with linear size L, we first draw L random scratches J_0 according to the power law distribution (2.37). We then perform simulations by using the classical Worm algorithm [77]. In writing down Eq. (2.43), we assumed that the barriers joining adjacent superfluid regions are formed

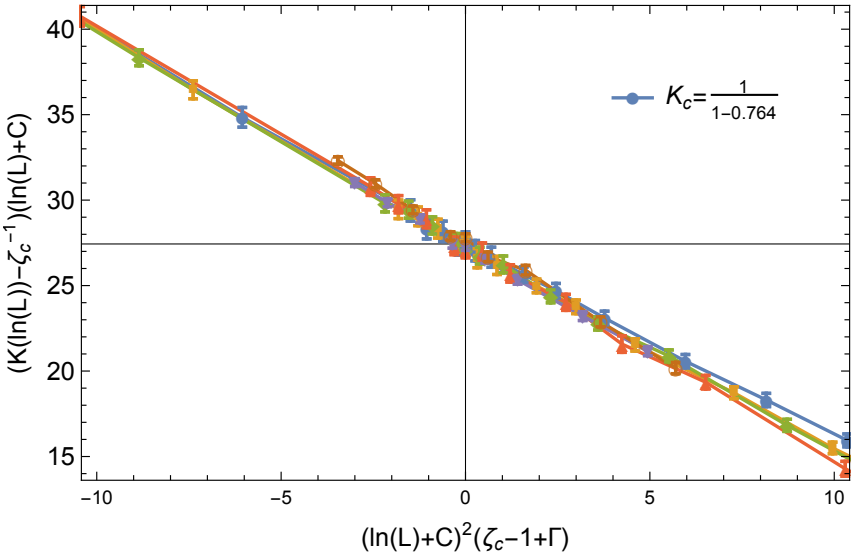

Figure 2.8.: Shown is the data collapse of $(K(\ell) - \zeta_c^{-1})\,(\ln(L) + C)$ over $(\zeta_c - \zeta)(\ln L + C)^2$. With $\zeta_c = 0.236(4)$ and $C = 3.86(5)$, all the finite size data collapse onto a single line satisfying the constraint $F(0) = 2(1 - \zeta_c)/\zeta_c^2$. The critical K_c is given by $K_c = 1/\zeta_c = 4.24(7) > 2$ as predicted by the strong randomness criticality.

by the single deepest scratches, i.e., the distribution of the bare strength of the barriers $p(t)$ at large length scales is given by (2.37). We justify this assumption by studying the distribution of the renormalized barrier strengths, $p(t(\ell))$, from a large number of disorder realizations in systems with mesoscopic system sizes L. Since strong barriers act as Josephson junctions, the supercurrent response j under a phase twist φ is given by

$$j = \frac{\partial F}{\partial \varphi} = t(\ell) \exp(-TL/2\Lambda) \sin \varphi, \tag{2.54}$$

where F is the free energy of the system under a phase twist in the x-direction, Λ is the superfluid stiffness of the left and right superfluids, $t(\ell)$ is the renormalized strength of the barrier, and $\exp(-TL/2\Lambda)$ accounts for the effect of supercurrent states at finite temperature [87]. The renormalized strength $t(\ell)$ can then be readily related to the winding number fluctuations in the x-direction by taking a second-order derivative of F with respect to φ. Since $t(\ell)$ is obtained through the supercurrent response under a phase twist across the system, $t(\ell)$ is determined irrespective of the microscopic origins. As the clutch scales of anomalously strong barriers will be much bigger than L, they will pick up a common factor due to the Kane-Fisher renormalization (2.41). Consequently, the tail of the distribution of the renormalized barrier strengths $p(t(\ell))$ will be the same as the distribution of the bare barrier strengths. As can be seen from Fig. 2.7, the tail part of the distribution of $p(t(\ell))$ is described by the same power-law distribution as (2.37). Therefore, the barriers joining adjacent superfluid regions are formed by the single deepest scratches. Moreover, the power law exponent of the tail of $p(t(\ell))$ does not flow with system size. This is in sharp contrast to the theory of Altman et al., which predicts a flow of the power law exponent governing the tail of the distribution of the renormalized strength of the barriers, i.e., strong barriers are joined to form even stronger barriers. The value of $t(\ell)$ at which this power law behaviour sets in decreases for increasing system sizes. Therefore, a large number ($> 10^6$) of disorder realizations is needed to resolve the genuine tail behavior. Moreover, it should be pointed out that although the renormalized strength of the barrier as well as the superfluid stiffness is determined through the supercurrent response under a phase twist across the system, these are distinct physical quantities. We have argued that the tail part of the distribution of

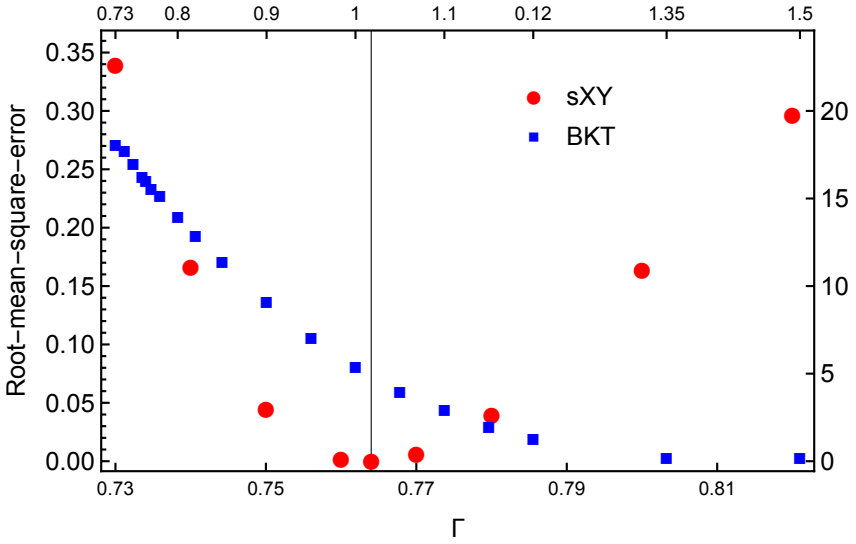

Figure 2.9.: The Weber-Minnhagen [78] root-mean-square-error σ by fitting the flow of $K(\ln L)$ for $L = 16, 32, 64, 128, 256, 512$ to the critical flow of the sXY criticality (red dots, lower and left axis) and to the BKT criticality (blue squares, upper and right axis). While σ displays a sharp minimum at $\Gamma_c = 0.764(2)$ for the sXY RG, there is no such minimum for the BKT RG.

the renormalized strengths is given by anomalously strong barriers such that the clutch scale is much bigger than the system size. Consequently, the Kane-Fisher RG flow is not yet completed and the whole system is still described by the harmonic modes of two superfluid phase fields weakly coupled to each other, cf. Sec. 2.2. Thus, a single harmonic description for the whole system does not hold at the length scales probed by the system size and therefore calculating the superfluid stiffness also has to account for this.

Having justified the key assumption in deriving the strong randomness RG equations, we continue to perform measurements for different system sizes in order to verify the sXY criticality. As already introduced the superfluid stiffness is related to the winding number statistics by the Pollock-Ceperley formula [76],

$$\Lambda_\mu = T\langle W_\mu^2 \rangle \,, \tag{2.55}$$

where $\mu \in \{x, y\}$ is the label of spatial direction, W_μ is the winding number in that direction, and $\langle \cdots \rangle$ refers to statistical averaging. Since the RG equations (2.44), (2.47) can also be understood in terms of the mean of the full distribution (medians are only needed for the inverse quantities) we average over a big number of disorder realizations (typically 5000 or more) to extract the observables. To determine the strong randomness critical point, we need to extract $K(\infty)$ from our finite size data. This is accomplished by the previously discussed data collapse technique. With the choice of $\zeta_c = 0.236(4), C = 3.86(5)$, all the finite size data fall onto a single line within error bars. From Eq. (2.48), the critical value of K is $K_c = 1/\zeta_c = 4.24(7)$, which is consistent with the condition of the strong random criticality $K_c > 2$. That the numerically obtained flow of K is described by the sXY scenario is further supported by performing a single parameter Weber-Minnhagen fit of our finite size data to the critical RG flow for different values of Γ. For the flow at the critical point, the root-mean-square-error σ is expected to show a sharp minimum [78]. As shown in Fig. 2.9, σ indeed exhibits a sharp minimum at a point, i.e., the critical point. For completeness, we also demonstrate that σ does not display a sharp minimum for a fit to the critical BKT flow in a broad region where the phase transition, if any, should occur. As we have

seen the BKT critical flow (2.22) is given by

$$K(\ell) = 2 + \frac{1}{\ell + C}\,, \tag{2.56}$$

where $K_c = 2$ from the Nelson-Kosterlitz relation [72]. As can be seen from Fig. 2.6, at $\Gamma = 1.35$, $K(\ln 128)$ is already smaller than the universal value 2. Therefore, $\Gamma_{c,\mathrm{BKT}} < 1.35$ as $K(\ln L)$ decreases monotonically along the RG flow. However, no minimum for σ can be found, cf. Fig. 2.9, implying that the RG flow can not be captured by the BKT criticality.

Therefore, we have shown that the introduced scratched-XY model hosts a new strong randomness criticality, the scratched-XY criticality, where the superfluid phase is destroyed by scale dependent scratches instead of the unbinding of vortex–anti-vortex pairs. We used the asymptotically exact semi-renormalization group theory developed for superfluid-insulator transitions in 1D disordered quantum systems to analytically obtain the RG flow of $K(\ell) = \pi\beta\sqrt{\Lambda_x(\ell)\Lambda_y(\ell)}$, which predicts a non-universal jump of $K_c = 1/\zeta_c$ at the transition, where ζ is an irrenormalizable microscopic quantity characterizing the power-law distribution of the scratches. These analytic predictions are confirmed by numerical finite size data obtained from first-principles numerical simulations of the scratched-XY model. The flow of $K(\ln L)$ with system size L can be perfectly fitted onto the one obtained from the solution of the RG equations. Therefore, we unambiguously demonstrate the existence of the scratched-XY universality class.
One of the key insights, which brought the necessary analytic control and made a solid numerical proof of the scratched-XY universality feasible, is equally well important for the design of possible experimental systems realizing this universality class. The disorder must couple directly through a power law to the phase fluctuations of the effective bosonic degrees of freedom because otherwise this power law has to be determined from measurements of a large collection of samples. A realization where such a coupling may be possible are 2D Josephson junction arrays where the individual phase fields of the superconducting islands can establish global phase coherence due to the tunneling of Cooper pairs between the islands [118], i.e., disorder can directly couple to the phase field through the strength of the tunneling barrier. Existing techniques make it possible to study the BKT-transition in 2D Josephson junction arrays [17]. In order to introduce disorder in these systems such that the power law exponent of its distribution can be determined, the strength of the tunneling barriers, i.e., the distance between the individual islands, have to be controlled to high accuracy.
From the theoretical side an interesting question is how the scratched-XY universality class is connected to the BKT universality class at weak disorder. We have established the nature of the finite-temperature phase transition in the strong disorder regime, which deep in the strong disorder regime happens at low temperatures and larges values of K. Therefore, the renormalization of the superfluid stiffness by thermally excited vortex–anti-vortex pairs, which drive the transition at weak disorder, can be neglected. At intermediate strength of disorder, where $K_c \gtrapprox 2$, this renormalization due to vortex–anti-vortex pairs has to be taken into account on the same footing as the renormalization due to scale dependent scratches. In the clean XY model, discussed in Sec. 2.1, a second order perturbative analysis for a low concentration of vortex–anti-vortex pairs leads to the flow equation (2.16)

$$\frac{\mathrm{d}K(\ell)}{\mathrm{d}\ell} = -\tilde{y}^2 K^2, \tag{2.57}$$

where $\tilde{y}$ denotes the rescaled vortex fugacity. In the presence of scratches repeating this analysis at second order of perturbation theory yields a term which describes the renormalization of $K(\ell)$ due to the interacting between single scratches and single vortices, which are thermally excited as vortex–anti-vortex pairs. The question is, if this is a relevant mechanism which leads to a

different scenario compared to the simple superposition of the two mechanisms (2.16), (2.44), e.g.,

$$\frac{\mathrm{d}K(\ell)}{\mathrm{d}\ell} = -\tilde{y}^2 K^2 - wK^3, \tag{2.58}$$

where w denotes the weak link term.
This concludes the first part of the thesis where we have used the computational approach to demonstrate and verify the analytic predictions of a theory. In the next chapter we turn to a different motivation for the use of the computational approach in the study of strongly correlated systems.

Part II.

Development of new computational methods for the study of strongly correlated systems

3

Computational Complexity

In the last decades numerous Monte Carlo techniques have been developed to simulate strongly correlated electronic or bosonic systems in the presence of the numerical sign problem. The driving force behind the current developments is that still no general method has emerged which can answer the question of how to generically simulate these systems efficiently. The larger the number of proposed methods is the harder it will be to theoretically compare a priori different methods as they all rely on different parameters which are inherent to the method and determine the accuracy of the numerical results. Currently, the performance of these algorithms is measured in terms of how fast computational time increases if these control parameters are tuned. This can lead to misdirecting conclusions in comparing different methods. Moreover, and even more important, considering the scaling of the computational time with respect to method dependent parameters makes it hard to establish the potentials and limitations of these unbiased Monte Carlo methods in the strongly correlated regime.
We suggests that the scaling of computational time has to be assessed with respect to the relevant physical quantities. We compare the computational time of different Monte Carlo algorithms, which are used in the simulation of strongly correlated systems, on the basis of the theory of second order phase transitions. Within this theory, the strong correlations develop due to the divergence of the correlation length ξ between some microscopic degrees of freedom at the phase transition point, which separates different phases with distinct macroscopic properties. Therefore, the relevant physical quantity is ξ. Fortunately, due to the theory of second order phase transitions, the thermodynamic quantify ξ can be related back to the microscopic detuning parameter τ from the phase transition point. Based on these theoretical considerations we will compare conventional quantum Monte Carlo algorithms (QMC) with diagrammatic Monte Carlo algorithms (diagMC) and in that way elucidate the role of the correlation length as an effective measure of the required system size in the analysis of the computational complexity.
The result of this comparison shows that generically for both Monte Carlo methods the computational time has to be increased exponentially with respect to the detuning from the phase transition, i.e., entering the strongly correlated regime comes at the expense of an exponential increase in computational time. Nevertheless, we want to stress that this discussion is purely based on theoretical considerations, which only describe the asymptotic scaling of the computational time. In practical applications, depending on the problem at hand, it is sometimes possible to extract the physical information before it becomes necessary to perform simulations in the asymptotic scaling regime. Based on this we identify the fundamental advantage of diagMC over QMC. Inherent to the diagrammatic language is the flexibility to set up different expansion schemes which can be adapted to the physical problem at hand and makes it possible to obtain information before the asymptotic exponential scaling barrier is reached. This flexibility is absent in QMC schemes, which rely on brute force numerical calculations of the functional integral in a finite simulation box. Therefore, in essence, the diagMC approach should be better thought of as a semi-analytic technique where an indispensable ingredient is to first choose the expansion scheme carefully.

We start with a review of the computational complexity of classical and quantum Monte Carlo simulations as it was discussed by Troyer and Wiese [88]. The expectation value of an observable A of a quantum many-body system can in equilibrium be computed as

$$\langle A \rangle = \frac{1}{Z} \mathrm{Tr} \left[A e^{-\beta H} \right], \tag{3.1}$$

with $Z = \mathrm{Tr} \left[e^{-\beta H} \right]$ the partition function of the system with Hamiltonian H at inverse temperature β and Tr denotes the summation over a complete set of many-body states.
This equation lends itself to a statistical interpretation useful for Monte Carlo simulations,

$$\langle A \rangle = \frac{\sum_{c \in \mathcal{C}} A(c) p(c)}{\sum_{c \in \mathcal{C}} p(c)} \approx \bar{A} = \frac{1}{N_{\mathrm{iid}}} \sum_{i=1}^{N_{\mathrm{iid}}} A(c_i), \tag{3.2}$$

with $p(c) = \exp\left(-\beta E(c)\right)$ the Boltzmann weight of the configuration c with energy $E(c)$ belonging to the high-dimensional configuration space $\mathcal{C}$, e.g., of Fock states, and $A(c)$ the evaluation of the operator A in configuration c. In the Monte Carlo simulation the average is replaced by the sample mean over independent and identically distributed random configurations. The stochastic error is given by

$$\Delta A = \sqrt{\frac{\mathrm{Var}(A)(2\tau_A + 1)}{N}}, \tag{3.3}$$

with $\mathrm{Var}(A)$ the variance of A and τ_A, the autocorrelation time of the time series for $A(c_i)$ of length N, accounting for possible correlation between the samples. For a large class of bosonic systems and certain fermionic systems with special symmetries all Boltzmann weights are sign definite and a Markov chain Monte Carlo process can be set up to calculate the observables stochastically. In case of sign non-definite weights, one introduces the sign $s(c) = p(c)/|p(c)|$ (or, more generally, the phase in case of complex weights) of the configuration c, and rewrites the statistical interpretation as follows,

$$\langle A \rangle = \frac{\sum_{c \in \mathcal{C}} A(c) s(c) |p(c)| / \sum_{c \in \mathcal{C}} |p(c)|}{\sum_{c \in \mathcal{C}} s(c) |p(c)| / \sum_{c \in \mathcal{C}} |p(c)|}. \tag{3.4}$$

The expectation value of A is then computed as

$$\langle A \rangle = \frac{\langle As \rangle'}{\langle s \rangle'}, \tag{3.5}$$

where the sampling takes place with respect to the bosonic system $Z' = \sum_{c \in \mathcal{C}} |p(c)|$ and is denoted by $\langle \dots \rangle'$.
Since $\langle s \rangle = Z/Z' = \exp(-\beta L^d \Delta f)$ with Δf the free energy density difference between the fermionic (Z) and bosonic (Z') system, it follows that the relative error increases exponentially,

$$\epsilon_s = \frac{\Delta s}{\langle s \rangle} = \frac{\sqrt{\left(\langle s^2 \rangle - \langle s \rangle^2 \right) / N_{\mathrm{iid}}}}{\langle s \rangle} = \frac{1}{\sqrt{N_{\mathrm{iid}}}} \frac{\sqrt{1 - \langle s \rangle^2}}{\langle s \rangle} \propto \frac{e^{\beta L^d \Delta f}}{\sqrt{N_{\mathrm{iid}}}}. \tag{3.6}$$

The number of independent and identically distributed random configurations is denoted by N_{iid}. If we fix the relative statistical error ϵ_s for a system of linear size L and assume that the computational time to collect N_{iid} samples scales at most polynomially with L, the computational time increases exponentially if the system size is doubled. QMC simulations are all performed on finite lattices and finite inverse temperatures and it is the extensiveness of the system in which the exponential scaling is usually understood.
We now assume we are interested in an accurate answer valid for (or at least extrapolated to)

the thermodynamic limit in the strongly correlated regime. Systematic errors due to the finite size of the simulation box are given by

$$\epsilon_L \sim e^{-L/\xi},\ \epsilon_\beta \sim e^{-\beta\Delta}. \tag{3.7}$$

Here Δ is the energy gap of the system, which only has to be taken into account for quantum phase transitions. The simulation time should be chosen such that the statistical error ϵ_s is of the same order as the finite size errors ϵ_L, ϵ_β. Fixing the target error $\epsilon = \epsilon_s = \epsilon_{L,\beta}$ and taking into account that the correlation length behaves like $\xi \sim \tau^{-\nu}$ and $\Delta \sim \tau^z$ close to the (quantum) phase transition, the computational time scales with the detuning τ from the transition point in the following way:

$$t_\tau \sim e^{A/\tau^{\nu d+z}}. \tag{3.8}$$

The detuning τ is defined by $\tau = |r - r_c| / r_c$ where r is some microscopic parameter, which can be used to tune the system through the second order phase transition at r_c and A is some τ independent constant.
Therefore, as expected, we find an exponential increase in computational time if we try to enter the strongly correlated regime $\tau \to 0$ for a fixed final error ϵ.

Diagrammatic Monte Carlo (diagMC) calculations use a different approach as they can be formulated for connected correlation functions directly in the thermodynamic limit. We want to determine the increase of computational time in diagMC calculations in the strongly correlated regime, i.e., with small detuning τ from a phase transition point. DiagMC calculations compute the observables automatically in the thermodynamic limit by a series expansion in terms of connected Feynman diagrams, i.e., $H = H_0 + \lambda H_1$ where H_0 is a non-interacting Hamiltonian and H_1 is the interacting part,

$$\langle A \rangle = \frac{1}{Z} \mathrm{Tr}\left[A e^{-\beta H}\right] = \sum_{n=0} A_n \lambda^n. \tag{3.9}$$

In Ref. [89] it was shown that the computational time t_M to compute M coefficients in the truncated series $A_M = \sum_{n=0}^{M} A_n \lambda^n$ scales in the best case exponentially with M,

$$t_M \propto a^M. \tag{3.10}$$

It has been argued by Rossi et al. [89] that inside the convergence radius a polynomial scaling can result as a cancellation between the exponential cost and the exponential convergence of the series, i.e., $\epsilon_M = |A_m - \langle A \rangle| / \langle A \rangle \propto b^{-M}$, with $b > 1$ a constant, from which it follows that $M \propto \log \epsilon_M^{-1}$ and finally $\log t_M \propto \log \epsilon_M^{-1}$.
The interpretation by Rossi et al. puts different nuances than the one by Troyer and Wiese [88].

We reconcile both interpretations and show that an exponential scaling of the computational time in the strongly correlated regime is unavoidable. The strongly correlated regime is defined as the regime where the correlation length between some microscopic degrees of freedom starts to diverge because the system is tuned close to a second order phase transition. In this regime the correlation length plays the role of an "effective" system size in either formulation. As we have already reviewed above this leads for QMC simulations to an exponential increase of the computational time upon entering the strongly correlated regime.
As diagMC works directly in the thermodynamic limit, from a mathematical point of view the divergence of the correlation length is caused by the presence of a non-analytic point in the free energy density, which theoretically describes the second order phase transition. Without loss of generality we assume that the critical point is determined by some critical value of the parameter

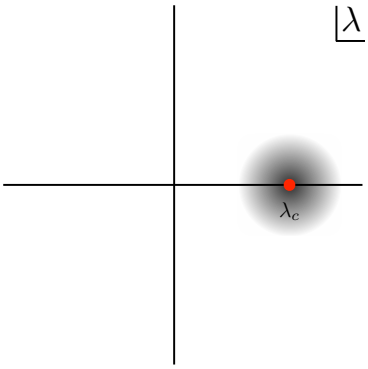

Figure 3.1.: The assumed analytic structure of the observable $A(\lambda)$ in the complex λ plane. The singularity at λ_c corresponds to the phase transition point. The precise nature of the singularity and its neighbourhood in the complex plane are unknown and unimportant for the discussion in the main text. The strongly correlated regime close to the phase transition point is indicated by the shaded region.

λ, i.e., $\tau \propto (\lambda_c - \lambda)/\lambda_c$. We furthermore assume that ultimately the convergence radius for $A(\lambda)$ is determined by the physical singularity λ_c lying on the real axis in the complex λ-plane. Therefore, all further singularities of $A(\lambda)$, which lie closer to the origin, have already been taken into account, e.g., by appropriate resummation techniques. These assumptions about the analytic structure of the observable $A(\lambda)$ are illustrated in Fig. 3.1 where the strongly correlated regime is highlighted by the shaded region.
Entering the strongly correlated regime $\tau \to 0$ comes at the expense of considering the observables $A(\lambda)$ close to a non-analytic point, i.e., close to the convergence radius of the power series in λ. Thus, the constant $b > 1$ in the exponential convergence becomes effectively λ-dependent as the series crosses over to the non-converging regime,

$$\epsilon_M = \frac{|A_M - \langle A \rangle|}{\langle A \rangle} \sim b(\lambda)^{-M} \sim \left(\frac{\lambda}{\lambda_c}\right)^M . \tag{3.11}$$

Therefore, the maximal expansion order for a fixed desired error scales with the detuning τ as

$$M \sim \frac{\log(\epsilon_M)}{\log(\lambda/\lambda_c)} \sim \frac{\log(\epsilon_M^{-1})}{\tau}. \tag{3.12}$$

This leads to an increase of the computational time in approaching the strongly correlated regime in the following form,

$$t_\tau \sim e^{B/\tau}, \tag{3.13}$$

where B is some τ independent constant. Therefore, we find an exponential increase of the computational time upon entering the strongly correlated regime.

The divergence of the truncation order in approaching the strongly correlated regime essentially leads to the exponential scaling of the computational time in the strongly correlated regime. In the following example we illustrate this behaviour. We consider the 2D Ising model where exact (or numerically exact) answers are known. The partition function for the classical 2D Ising model reads,

$$Z = \sum_{\{\sigma_i = \pm 1\}} e^{K \sum_{\langle i,j \rangle} \sigma_i \sigma_j}, \tag{3.14}$$

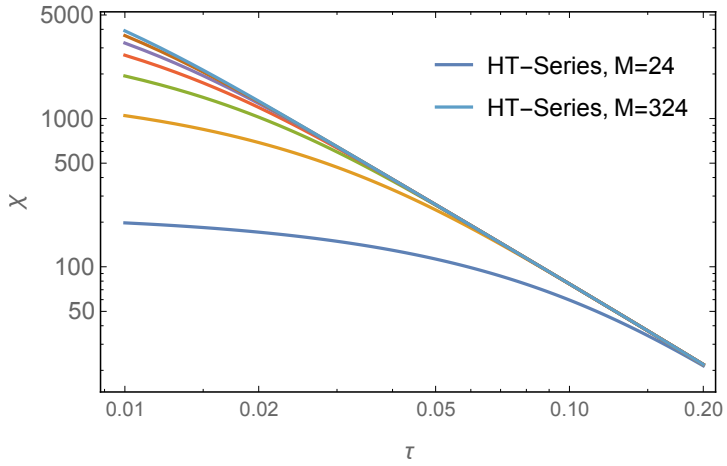

Figure 3.2.: The divergence of the susceptibility of the 2D Ising model approximated by the high temperature (HT) series for different approximation orders starting from $M = 24$ up to $M = 324$ in steps of $\Delta M = 50$.

where the lattice sum is over nearest neighbours only, and K is the product of the inverse temperature β and the spin coupling amplitude J. The coefficients for the magnetic susceptibility,

$$\chi = \frac{\beta}{V} \sum_i \langle \sigma_0 \sigma_i \rangle, \tag{3.15}$$

in the high temperature series expansion,

$$\chi = \lim_{M \to \infty} \sum_{n=0}^{M} c_n \left(\frac{\sinh(2K)}{2} \right)^n, \tag{3.16}$$

for the 2D Ising model are known up to order 324 [90]. The high-temperature series is such that the convergence is guaranteed up to the critical temperature. Therefore, the analytic structure of $\chi(K)$ is exactly as it was assumed in Fig. 3.1 with λ replaced by K.
Fig. 3.2 shows the divergence of the susceptibility for different approximation orders starting at $M = 24$ in steps of $\Delta M = 50$ up to the maximal order of $M = 324$. As can be observed in Fig. 3.2, the approximation of the high temperature series up to order $M = 324$ can be considered to be the exact analytic answer for $\tau > 0.02$. Therefore, in the following we only take detunings $\tau > 2\%$ into account and regard the high-temperature series with maximal approximation order to be the exact result.

Fig. 3.3 illustrates qualitatively how the truncation error $\epsilon = |\chi_M - \chi_{\text{exact}}| / \chi_{\text{exact}}$ decreases with larger approximation orders M for different detunings τ. It highlights that already for moderate detunings $\tau \approx 10\%$ around $M \approx 50$ expansion coefficients are needed to converge the high temperature series expansion with a truncation error $\epsilon \approx 1\%$. Moreover, the inset of Fig. 3.3 shows that by fixing the desired truncation error and looking for the minimal truncation order M_{min} such that the high temperature series drops below this truncation error we can indeed establish the relation $M_{\text{min}} \sim 1/\tau$. Together with the assumption that the computational time to calculate the M-th order truncation scales exponentially this consequently leads to an exponential increase in computational time if the strongly correlated regime is approached. To avoid misleading conclusions it should be pointed out that there are more efficient algorithms which calculate the M-th order coefficients of the high-temperature series for the 2D Ising model in $\mathcal{O}(M^6)$ time [90] instead of exponential time but this does not hold for arbitrary quantum many-body theories.

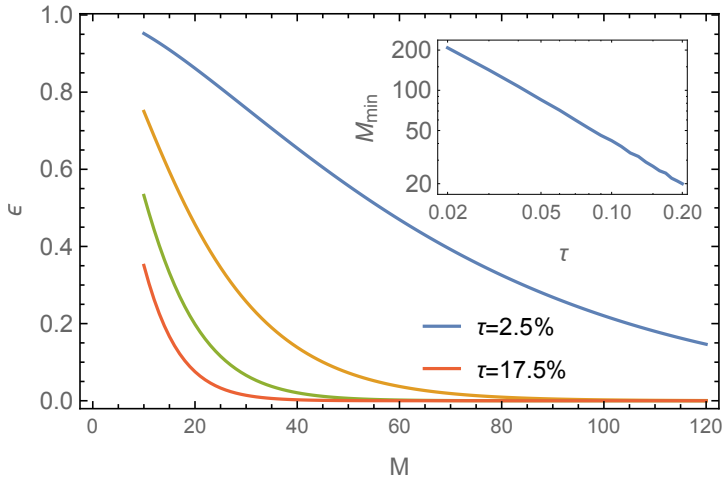

Figure 3.3.: The truncation error $\epsilon = |\chi_M - \chi_{\text{exact}}| / \chi_{\text{exact}}$ depending on the approximation order M for different detunings τ starting from $\tau = 2.5\%$ to $\tau = 17.5\%$ in steps of $\delta\tau = 5\%$. For small detunings a large number of expansion coefficients is needed in order to obtain a reasonable truncation error. The inset shows the divergence of the minimal truncation order for a target truncation error as the phase transition is approached. The inset takes just one representative example for $\epsilon = 5\%$. The slope on the log-log scale can be read off to be ≈ -1.05, i.e., $M \sim \tau^{-1}$ and thus $t_\tau \sim e^{B/\tau}$ if the computational time t_M increases exponentially with the truncation order M.

4

Perturbative field theory

In the last section we compared the computational complexity of different Monte Carlo schemes in the strongly correlated regime. The standard Quantum Monte Carlo approaches rely on the direct calculation of the functional integral in a finite simulation box. Approaching the strongly correlated regime comes at the expense of an exponentially increasing computational time. In order to identify the dominant collective long wavelength fluctuations of the system the size of the simulation box has to be increased upon approaching a transition with diverging correlation length.
On the other hand we also argued that diagrammatic Monte Carlo techniques scale generically exponentially upon approaching the strongly correlated regime. In contrast, they do not rely on a finite simulation box but on power series expansion techniques of the functional integral in the thermodynamic limit, i.e., on perturbative methods. Calculating an observable, e.g., the susceptibility of the system to an external perturbation which is coupled to the dominant long wavelength fluctuation, close to a second order phase transition, needs a large number of expansion coefficients in order to obtain controlled results.
Nevertheless, the diagrammatic language of series expansions is much more flexible than the direct brute force calculation of the functional integral in a finite simulation box. In order to predict the qualitative and quantitative behaviour of a model, series expansion techniques can be applied on top of more sophisticated calculation schemes than the direct perturbative series expansion of the functional integral. In this section we consider such perturbative calculations for the $\mathcal{Z}_2$-symmetric ϕ^4 theory in the continuum limit. The motivation for this comes from different directions. Firstly, it will demonstrate the flexibility of the diagrammatic language of series expansions. In order to calculate the critical exponents, e.g., of the correlation length, it is not strictly necessary to calculate the observables, e.g., the correlation function, directly in the strongly correlated regime and afterwards extract from their behaviour the critical exponents. Based on one particle irreducible Feynman diagrams it is possible to set up an expansion directly for the inverse of the correlation length or, using the perturbative renormalization group, even for universal quantities, to obtain accurate results with only a modest amount of expansion coefficients. Secondly, it will give an introduction to the divergence of perturbation theory for a specific example. It highlights the limitations of the perturbative approach but also its power if convergent expansions for a field theory can be found. Without the tools of resumming the perturbative series, guided by the knowledge of the analytic structure of the functional integral in the complex coupling parameter plane, no quantitatively correct results can be gained. Overcoming the convergence problems of perturbation theory is the driving force for the developments presented in this part of the thesis. Thirdly, as we use the $\mathcal{Z}_2$-symmetric ϕ^4 theory on a square lattice as a benchmark for our solution of the Dyson-Schwinger equation, we review its counterpart in the continuum - lying in the same universality class - to set the stage for the following discussions.

4.1. Perturbative series expansions

We are interested in the properties of the model

$$\begin{aligned} Z &= \int \mathrm{d}(\phi) e^{-S[\phi]} \quad \text{where} \\ S[\phi] &= \int \mathrm{d}^D x \, \frac{1}{2}(\nabla\phi_B)^2 + \frac{m_B^2}{2}\phi_B^2 + \frac{\lambda_B}{4!}\phi_B^4. \end{aligned} \tag{4.1}$$

The measure of the functional integral is denoted by $\mathrm{d}(\phi)$ and a large momentum cutoff Λ is assumed for the functional integral to be a well defined object.
We study the low energy properties of the system in $2D$ and try to establish that this model features a second order phase transition where the model is scale invariant due to the presence of a non-trivial, i.e., non-Gaussian, long wavelength fixed point of the renormalization group. This long wavelength fixed point is common to all other microscopic models within the same universality class and determines their critical properties.
Especially, we want to quantitatively describe the behaviour of the above model in the continuum limit close to that transition point. The massive continuum limit, $\Lambda \to \infty$, in 2D can be easily taken by introducing the counterterm δm_I^2 in a reparametrization

$$\phi_B = \phi_I \tag{4.2}$$

$$\lambda_B = 6 m_I^{4-D} \lambda_I \tag{4.3}$$

$$m_B^2 = m_I^2 + \delta m_I^2 \tag{4.4}$$

$$\text{where} \quad \delta m_I^2 = -\frac{\lambda_I}{2} \int_\Lambda \mathrm{d}^2\mathbf{p} \, G_0(\mathbf{p}), \tag{4.5}$$

where the non-interacting 2-point correlation function is then given by

$$G_0(\mathbf{p}) = (\mathbf{p}^2 + m_I^2)^{-1}. \tag{4.6}$$

The perturbative expansion of the 2-point correlation function $G(x_1, x_2)$ with respect to the free action

$$S_0[\phi] = \int \mathrm{d}^D x \, \frac{1}{2}(\nabla\phi_I)^2 + \frac{m_I^2}{2}\phi_I^2 \tag{4.7}$$

is given by

$$\begin{aligned} G(x_1, x_2) &= \frac{1}{Z} \int \mathrm{d}(\phi) e^{-S[\phi]} \phi(x_1)\phi(x_2) \\ &= \lim_{M\to\infty} \sum_{m=0}^{M} \frac{(-1)^m}{m!} \int \mathrm{d}y_1 \ldots \mathrm{d}y_m \langle \phi(x_1)\phi(x_2) \prod_{i=0}^{m} \left(\frac{\delta m_I}{2}\phi_I^2(y_i) + \frac{m_I^{4-D}}{4}\lambda_I \phi^4(y_i) \right) \rangle_0 \end{aligned} \tag{4.8}$$

where we denote

$$\langle \ldots \rangle_0 = \frac{1}{Z} \int \mathrm{d}(\phi) e^{-S_0[\phi]} \ldots \, . \tag{4.9}$$

The average $\langle \ldots \rangle_0$ is evaluated using Wicks theorem [91] where each generated term in this evaluation can be diagrammatically represented by standard Feynman diagrams with respect to the non-interacting 2-point correlation function G_0. Since the normalization of the functional integral in $\langle \ldots \rangle_0$ is with respect to the full partition function Z, all Feynman diagrams including vacuum bubbles are set to zero. The introduced counterterm δm_I^2 sets all Feynman diagrams including tadpole subdiagrams to zero and therefore the theory is free of any divergencies in the limit $\Lambda \to \infty$. The inverse of the 2-point correlation function is denoted by $\Gamma^{(2)}(x_1, x_2)$ and

the inverse of the correlation length ξ^{-1} can be defined by $\Gamma^{(2)}(\mathbf{p}^2 = -\xi^{-2}) = 0$. From the perturbative series expansion of $\Gamma^{(2)}$ in momentum space one finds [92]

$$\begin{aligned}\frac{\xi^{-2}}{m_I^2} &= 1 - 1.5\lambda_I^2 + 4.08599\lambda_I^3 - 14.655869(22)\lambda_I^4 + 65.97308(43)\lambda_I^5 \\ &\quad - 347.8881(28)\lambda_I^6 + 2077.703(36)\lambda_I^7 - 13771.04(54)\lambda_I^8.\end{aligned} \tag{4.10}$$

This perturbative series expansion is based on summing up all one-particle irreducible Feynman diagrams. In App. B we also review the perturbative calculation of the beta function in the fixed dimensional expansion [93], which describes the renormalization group flow of the renormalized coupling constant λ_R. Its series expansion is given by [92]

$$\begin{aligned}\frac{\beta(v)}{2} &= -v + v^2 - 0.7161736v^3 + 0.930768(3)v^4 \\ &\quad - 1.5824(2)v^5 + 3.2591(9)v^6 - 7.711(5)v^7,\end{aligned} \tag{4.11}$$

where $v = 3\lambda_R/8\pi$. Since the expansion coefficients in both cases are quickly growing, indicating zero convergence radius of the series, we can not study the behaviour of the correlation length around a possible second order phase transition nor can we conclude from a zero in the beta function that such a long wavelength fixed point exists. Therefore, in the next subsection we review resummation methods, which convert the perturbative series into a convergent expansion and consequently into a powerful tool.

4.2. Divergence of perturbation theory and resummation

Perturbation theory around some analytic solvable non-interacting model is generically only valid for small perturbations. The mathematical reason is the possible singular behaviour of the model in the complex coupling constant plane. This behaviour of perturbation theory for field theory and its physical understanding was first pointed out by Dyson in the context of quantum electrodynamics [94]. He argued that if quantum electrodynamics would be formally considered for an arbitrary small but negative fine structure constant α, any physical state would be unstable against the spontaneous creation of an arbitrary number of electron-positron pairs. Thus, any observable $F(\alpha)$ in quantum electrodynamics is ill defined for $\alpha < 0$ and thus $F(\alpha)$ can not be an analytic function around $\alpha = 0$. This implies that the convergence radius of the perturbative series in the coupling constant α is zero. Nevertheless, the series is asymptotic, i.e., the perturbative series can be controlled to exponential accuracy in α. The behaviour found for quantum electrodynamics is generic to a large class of systems although there are important exceptions such as fermionic lattice systems at finite temperature where the perturbative expansion has a finite convergence radius [95] and we comment on these systems at the end of this subsection. These systems should not be confused with lattice systems at finite temperature with a finite number of degrees of freedom, cf. the first part of this thesis, where observables are analytic functions and even physical non-analytic features, such as phase transitions, are regularized.
For calculating scattering amplitudes in quantum electrodynamics the convergence issues sets no practical limitations to the accuracy of perturbative calculations because the physical $\alpha \approx 1/137$ is indeed very small. In contrast, for strongly interacting systems, where there is no single physical small parameter, perturbative series expansions with zero convergence radius are meaningless without further additional analytic understanding of the model system. For the ϕ^4 model studied

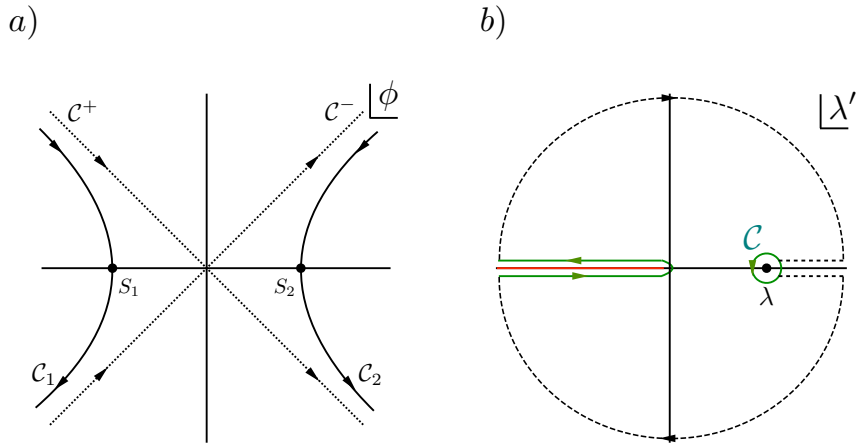

Figure 4.1.: a) The analytic continuation of the 0D toy model for $\lambda^{\pm} = -|\lambda| \pm 0^+$ by rotating the contour of integration to $\arg(\phi) = \mp\pi/4$ denoted by $\mathcal{C}^{\pm}$. The difference between the contour integrations along $\mathcal{C}^{\pm}$ can be deformed into the contour integration along $\mathcal{C}_{1/2}$ running over the subleading saddle points $S_{1/2}$ at $\phi^2 = -6/\lambda$. b) The contours of integration used in the dispersion relation approach. Through a closed contour, which avoides all singularities (symbolically indicated by the dashed black line), the contributions coming from the contour integrations, which are depicted in green, can be related to each other.

in this section Dyson's argument has been made quantitative for the first time by Bender and Wu [96, 97]. They provided the necessary analytic information to turn perturbation theory into a powerful tool in the non-perturbative regime.
We illustrate the crucial steps in understanding the perturbative series expansion of the ϕ^4 model by considering its 0D analog,

$$Z(\lambda) = \int_{-\infty}^{\infty} \mathrm{d}\phi \; e^{-\frac{1}{2}\phi^2 - \frac{\lambda}{4!}\phi^4}. \tag{4.12}$$

The above integral for $\lambda < 0$ does not converge for arbitrary small coupling constants. This implies that $Z(\lambda)$ is not analytic around $\lambda = 0$ and the power series expansion

$$Z(\lambda) = \lim_{M\to\infty} \sum_{m=0}^{M} b_m \lambda^m \tag{4.13}$$

has zero convergence radius.

We want to understand the behaviour of the singularity for $\lambda \to 0^-$ by considering the analytic continuation of $Z(\lambda)$ into the complex plane, $\lambda \in \mathbb{C}$. For $\mathrm{Re}\,(\lambda) > 0$ the integral is always convergent and the analytic continuation can be defined by rotating the contour of integration along the real line, $\phi \in \mathbb{R}$, onto a contour $\mathcal{C}$ in the complex plane on which $\mathrm{Re}\,(\lambda\phi^4) > 0$ is satisfied. Therefore, the behaviour of the integral for $\lambda \in \mathbb{R}$, $\lambda < 0$ can be studied by considering the analytic continuation for $\lambda^{\pm} = -|\lambda| \pm 0^+$, which is obtained by rotating the contour in the positive/negative direction. The discontinuity along the cut on the negative real λ-axis is given by

$$Z(-|\lambda| + 0^+) - Z(-|\lambda| - 0^+) = \int_{\mathcal{C}^+ - \mathcal{C}^-} \mathrm{d}\phi \; e^{-\frac{1}{2}\phi^2 - \frac{\lambda}{4!}\phi^4}, \tag{4.14}$$

where the contours $\mathcal{C}^{\pm}$ are along $\arg(\phi) = \mp\pi/4$ and shown in Fig. 4.1 a). The difference between the integral can be evaluated for $|\lambda| \to 0$ by saddle point techniques where the integrant has a leading order saddle point at $\phi = 0$ and two subleading saddle points at $\phi^2 = -6/\lambda$. The contribution of the leading order saddle point cancels in the difference between the contour

integrations and to leading order the discontinuity is given by the deformation of the difference of contours, $\mathcal{C}_{1/2}$, shown in Fig. 4.1 a) running over the subleading saddle points [91],

$$Z(-|\lambda| + 0^+) - Z(-|\lambda| - 0^+) = -2\sqrt{\pi} i \, e^{\frac{3}{2\lambda}}. \tag{4.15}$$

From the behaviour of the discontinuity we can determine the large order behaviour of the power series coefficients b_m from a dispersion relation approach,

$$Z(\lambda) = \frac{1}{2\pi i} \oint_{\mathcal{C}} \mathrm{d}\lambda' \frac{Z(\lambda')}{\lambda' - \lambda}. \tag{4.16}$$

The closed contour of integration in the complex coupling constant plane around $\lambda' = \lambda$ is denoted by $\mathcal{C}$, cf. Fig. 4.1 b). As $Z(\lambda)$ is analytic in the whole λ plane except for the cut along the negative real axis the contour can be deformed such that $Z(\lambda)$ can be related to the discontinuity, cf. Fig. 4.1 b). The series coefficients b_m for $m \to \infty$ are thus given by

$$b_m = \frac{1}{2\pi i} \int_{-\infty}^{0} \mathrm{d}\lambda' \frac{Z(-|\lambda'| + 0^+) - Z(-|\lambda'| - 0^+)}{\lambda'^{\,m+1}} = \frac{1}{\sqrt{\pi}} \left(-\frac{2}{3}\right)^m (m-1)!. \tag{4.17}$$

The last equality only holds in the limit $m \to \infty$ since the main contribution to the integral comes in this limit from the $\lambda \to 0^-$ behaviour of the discontinouity. Therefore, as we already argued qualitatively, the power series has zero convergence radius, which shows up quantitatively as the factorial growth of the coefficients b_m. With this analytic result it is now possible to devise powerful resummation schemes of the divergent series.
We illustrate this for the perturbative expansion of the ϕ^4 model in $2D$ where we discussed the series expansions (4.10), (4.11) in the previous subsection. Along the same line of arguments as for the $0D$ case together with advanced saddle-point techniques the large order behaviour of the perturbative series for the n-point correlation functions $G^{(n)} = \sum_m G_m^{(n)} \lambda_I^m$ is found to be [98]

$$G_m^{(n)} = \gamma_n \, (-a)^m \, \Gamma(m + \beta_n + 1) \text{ for } m \to \infty, \tag{4.18}$$

where $\beta_n = \frac{n}{2} + 1$ and from the leading saddle-point configuration the constant a, independent of the type of correlation function, can be numerically determined to be $a = 0.683708\ldots$ [98, 92]. $\Gamma(x)$ denotes the Gamma function and γ_n a constant - unimportant to the following discussion - specific to the type of correlation function and obtained in Ref. [98].
We consider as a first example the perturbative series for the inverse correlation length, $\xi^{-1}(\lambda_I) = \sum_m \xi_m^{-1} \lambda_I^m$, in units of m_I. From (4.10) we have

$$\begin{aligned} \xi^{-1}(\lambda_I) \; &= 1 - 0.75\lambda_I^2 + 2.04299\lambda_I^3 - 7.60918\lambda_I^4 + 34.5188\lambda_I^5 \\ &\quad - 181.738\lambda_I^6 + 1080.29\lambda_I^7 - 7121.29\lambda_I^8. \end{aligned} \tag{4.19}$$

The standard resummation approach for this series is to use conformal Borel resummation techniques. For that, one first defines the generalized Borel transform

$$\mathcal{B}_b(t) = \sum_{m=0}^{\infty} \frac{\xi_m^{-1}}{\Gamma(m + b + 1)} t^m = \sum_{m=0}^{\infty} \mathcal{B}_{b,m} t^m, \tag{4.20}$$

which has an inverse transformation

$$\xi^{-1}(\lambda_I) = \int_0^{\infty} \mathrm{d}t \; t^b e^{-t} \mathcal{B}_b(\lambda_I t). \tag{4.21}$$

In order to obtain $\xi^{-1}(\lambda_I)$ from (4.21) the generalized Borel transform $\mathcal{B}_b(t)$ has to be evaluated

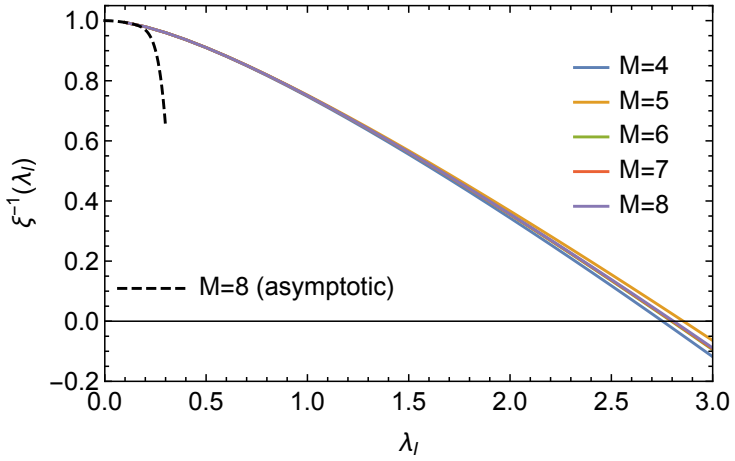

Figure 4.2.: The inverse of the correlation length as a function of λ_I. The continuum limit is taken by setting all Feynman diagrams with tadpole subdiagrams to zero. The results for different truncation orders M of the perturbative series are obtained by the resummation scheme discussed in the main text. Due to the fast convergence of the series after resummation the critical point is determined to be $\lambda_{I,c} \approx 2.80$ and the correlation length exponent $\nu \approx 1.0$. The original series is asymptotic and therefore only valid around the non-interacting limit in the weakly correlated regime.

along the complete real line $t > 0$. In the definition of the generalized Borel transform we account for the factorial growth of the coefficients ξ_m^{-1} and therefore the generalized Borel transform has a singularity at

$$t = -\frac{1}{a}, \tag{4.22}$$

which determines the convergence radius of the generalized Borel transform. In order to evaluate $\mathcal{B}_b(t)$ for arbitrary t one can use the conformal mapping

$$t(u) = \frac{4}{a}\frac{u}{1-u^2} \qquad \leftrightarrow \qquad u(t) = \frac{\sqrt{1+at}-1}{\sqrt{1+at}+1} \tag{4.23}$$

to perform the analytic continuation to arbitrary $t > 0$. It maps the complex t-plane into the unit disc of the complex u-plane where the negative real axis starting from $t < -1/a$ is mapped onto the boundary of the unit disc. Therefore,

$$(1-u)^s \mathcal{B}_b(u) = (1-u)^s \sum_{m=0}^{\infty} \mathcal{B}_{b,m} t(u)^m = \sum_{m=0}^{\infty} \tilde{\mathcal{B}}_m^{(b,s)} u^m \tag{4.24}$$

converges everywhere inside the unit disc. The additional parameter s has been added to obtain more control over the resummation results [99, 92]. From the inverse transformation (4.21) $\xi^{-1}(\lambda_I)$ can be calculated in the following way,

$$\xi^{-1}(\lambda_I) = \frac{1}{\lambda_I^{b+1}} \int_0^1 \mathrm{d}u \, \frac{\mathrm{d}u}{\mathrm{d}t} t(u)^b e^{-t(u)/\lambda_I} \frac{(1-u)^s}{(1-u)^s} \mathcal{B}_b(t(u)) \tag{4.25}$$

$$= \frac{1}{\lambda_I^{b+1}} \lim_{M\to\infty} \sum_{m=0}^{M} \tilde{\mathcal{B}}_m^{(b,s)} \int_0^1 \mathrm{d}u \, \frac{\mathrm{d}u}{\mathrm{d}t} t(u)^b e^{-t(u)/\lambda_I} \frac{u^m}{(1-u)^s}. \tag{4.26}$$

The free parameters b, s are varied such that the obtained convergence is fastest.
The result for $\xi^{-1}(\lambda_I)$ is shown in Fig. 4.2 where $b = 17/2$, $s = 5/2$ is taken and the resummed

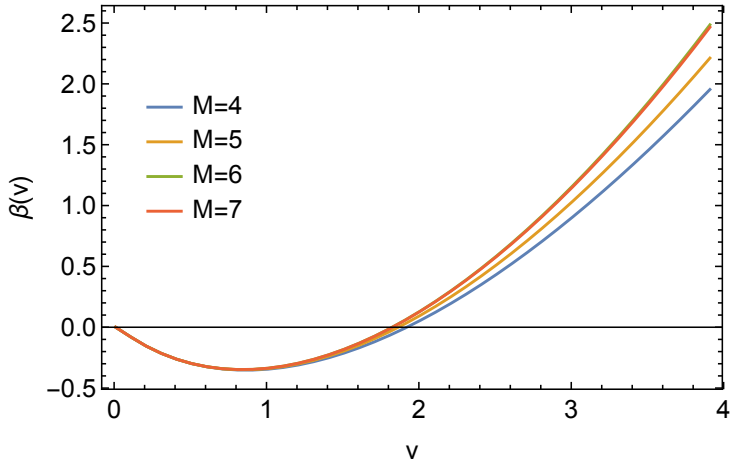

Figure 4.3.: The beta function in terms of the rescaled renormalized coupling $v = 3\lambda_R/8\pi$ after the resummation procedure discussed in the main text is used. Convergence can be observed already for a small number of perturbative coefficients used in the resummation. The beta function has a zero at $v \approx 1.83$ corresponding to a non-trivial long wavelength fixed point.

result for $\beta(v)$ is given in Fig. 4.3 where $b = 1/2$, $s = 3$ is used. The results demonstrate that it is possible to obtain with only a few number of coefficients the existence of a non-trivial universal long wavelength fixed point with $8\pi\lambda_R^\star/3 \approx 1.83$ where upon approaching the critical point of the chosen scheme, $\lambda_{I,c} \approx 2.80$, the correlation length diverges with the universal power law $\xi \propto \tau^{-\nu}$ where $\nu \approx 1.0$ and $\tau = |\lambda_I - \lambda_{I,c}|/\lambda_I$.
Nevertheless, care must be taken in discussing the generality and accuracy of the results. The result on the divergence of the correlation length has been obtained by choosing to resum the series for the inverse of the correlation length, (4.19), instead of the series for the squared inverse of the correlation length, (4.10). This is obviously guided by the prior knowledge that the considered model belongs to the 2D Ising universality class where it is known that $\nu = 1$. Although $\xi^{-1}(\lambda_I)$ has to be non-analytic at the transition point, i.e., $\xi^{-1}(\lambda_I) < 0$ for $\lambda_I > \lambda_{I,c}$ is clearly unphysical, this non-analyticity does not affect the accuracy of the resummed series (4.19) too much such that a low truncation order suffices. It can be numerically checked that resumming (4.10) does not even lead to qualitative results. Therefore, the high accuracy of the obtained results for the divergence of the correlation length is highly model specific. On the contrary, perturbative renormalization group functions were implicitly assumed to be analytic functions at the fixed point since the analytic continuation assumes that the generalized Borel transform has singularities only on the negative real axis. Consequently, under this assumption, they are the correct quantities to compute in order to obtain high accuracy results with a small number of expansion coefficients. This assumption turned out to be wrong and confluent singularities due to corrections to the leading order scaling appear in the renormalization group functions, which in 2D are worse than in, e.g., 3D. For the large amount of literature on this issue consult Sec. 2.4.3 of Ref. [100] and references therein. In particular, the universal value for the renormalized coupling strength $\lambda_R^\star$ in 2D obtained by different methods do not agree with each other and error bars of the field theory approach are underestimated. For an overview of results from different methods consult Sec. 3.2 of Ref. [100] and specific references therein. This is attributed to the singular behaviour of the renormalization group functions at the fixed point. In order to increase the reliability and accuracy of the result more series coefficients would be needed and assuming that these can only be obtained with exponential computational time the asymptotic scaling regime discussed in the first section will be quickly reached.

In conclusion, the discussion of the results shows that, in general, it is unavoidable that the required number of series coefficients grows in the strongly correlated regime, which leads - under the assumptions of the previous section - to an exponential increase in computational time. Nevertheless, due to the flexibility of series expansion techniques it is possible to obtain qualitative and quantitative results - however with a more conservative error bar - before this asymptotic scaling regime is reached.
We illustrated that, even in the strongly correlated regime, series expansion techniques are due to their flexibility a powerful computational technique. This power crucially hinges upon finding convergent series expansions and choosing the correct quantity which should be expanded. We have discussed that expansions around non-interacting limits are in general not convergent and illustrated that resumming the series is highly non-trivial. Unfortunately, resummation methods are only understood for a restricted class of systems. For models with a finite convergence radius, e.g., the 2D Hubbard model at finite temperature, the situation is even worse. Although the perturbative series is guaranteed to converge in the weakly interacting Fermi liquid regime [95], the series does not converge in the strongly correlated regime where the single particle picture breaks down and the resummation program can not be applied due to very limited understanding of the high order asymptotics of the perturbative series.
The main motivation for the following sections of this thesis is to develop a computational tool which circumvents the convergence problems of perturbative series expansion techniques but benefits from the same advantages and generality as the Feynman diagrammatic technique. We establish a method, based on the functional integro-differential representation of the Dyson-Schwinger equation, which goes beyond the usual paradigms of perturbation theory and has the potential to overcome the convergence issues without resorting to prior analytic knowledge.

5

Functional closure and solution of the Dyson-Schwinger equation

Although we found from the discussion of the computational complexity of Quantum Monte Carlo simulations and diagrammatic Monte Carlo calculations that the asymptotic scaling of the computational effort is exponential in the strongly correlated regime, we argued and illustrated in the previous section that the flexibility of the field theoretic method is the key advantage. Therefore, the most promising research directions to overcome the limitations of established computational methods in the strongly correlated regime are those which are built upon the field theoretic approach. We also discussed and illustrated that this power crucially hinges upon the convergence properties of the perturbative series. In general, the perturbative series is asymptotic or divergent and the series has to be analytically continued into the strongly correlated regime. The reliability of these resummation methods can only be guaranteed with additional analytic understanding of the many-body theory under consideration and this information has only been obtained for a very restricted class of models.

The aim of this chapter is to provide an alternative to the perturbative series expansion of the field theoretic method which enjoys the same flexibility and broad applicability. Instead of setting up field theoretic calculations within the language of functional integrals, we use functional integro-differential equations. This functional integro-differential equation is obtained from the Dyson-Schwinger equation (DSE). The prime advantage of the language of functional integro-differential equations is that series expansion methods in this formulation do not necessarily rely on the harmonic paradigm of perturbation theory in field theoretic calculations. There are powerful non-perturbative series expansion techniques for the solution of non-linear ordinary differential equations. One of these methods is the homotopy analysis method (HAM). It embeds the differential equation under consideration into a homotopy which, in that way, continuously transforms the solution of an auxiliary problem into the full solution of the non-linear differential equation. We work out the generalization of the homotopy analysis method to solve the full DSE by writing them as a closed set of functional integro-differential equations. Within this formulation there exists a semianalytic way to treat the functional derivatives and the DSE is solved without resorting to an infinite expansion of the successive n-point correlation functions. Nevertheless, we use a functional integro-differential equation for correlation functions on the two-particle level, i.e., the four-point vertex function. Such higher-order correlation functions are known to be notoriously difficult to treat numerically due to their dependence on four space-time coordinates. Therefore, the computational tools developed in this chapter moreover provide a general way to deal with such high-dimensional n-point correlation functions. The main technique we develop for that is the expansion and stochastic summation of the homotopy analysis method. We introduce rooted tree diagrams representing the expansion of the homotopy analysis method in a diagrammatic language and a Markov chain Monte Carlo algorithm that stochastically sums up all rooted tree diagrams in the same spirit as diagrammatic Monte Carlo algorithms sum up all connected Feynman diagrams. We use the developed algorithm for the full and unbiased

solution of the Dyson-Schwinger equation beyond any truncation scheme illustrated for ϕ^4 theory on a 2D square lattice in its strongly correlated regime close to a second-order phase transition. We observe the divergence of the magnetic susceptibility in the strongly correlated regime up to a maximal correlation length $\xi \approx 4$. Due to the numerical sign problem in the expansion order, discussed in general in Ch. 3, we cannot go deeper into the strongly correlated regime.
The structure of this chapter is the following. In Sec. 5.1, we discuss the derivation of the closed set of Dyson-Schwinger equations for the 0D analog of the ϕ^4 model. In Sec. 5.2 we generalize the derivation of the coupled set of equations to interacting many-body models with arbitrary two-body interaction. Sec. 5.3 introduces the homotopy analysis method and discuss the solution of the 0D toy model. In order to generalize the solution strategy presented for the 0D case, we develop in Sec. 5.4 the expansion of the homotopy analysis method in terms of rooted tree diagrams on the basis of a simple integral equations. Based on this example we introduce the Markov chain Monte Carlo algorithm for the sampling of rooted tree diagrams. Finally, in Sec. 5.5 we apply these new methods to the ϕ^4 theory in 2D.

5.1. Functional closure for a 0D toy model

The ideas developed in this chapter are most easily demonstrated for the case of a 0D field theory. In this section we derive the closed system of equations defining the field theory under consideration for a simple toy model. Consider the 1D integral

$$Z[J] = \int \mathrm{d}\phi \, e^{-S[\phi]+J\phi} \text{ with } S[\phi] = \frac{1}{2}k\phi^2 + \frac{\lambda}{4!}\phi^4, \tag{5.1}$$

where $Z[J]$ is the generating functional of the n-point correlation functions $G^{(n)}$,

$$G^{(n)} = \frac{1}{Z[0]} \int \mathrm{d}\phi \, e^{-S[\phi]} \phi^n = \frac{1}{Z[0]} \frac{\mathrm{d}^n Z[J]}{\mathrm{d}J^n}\bigg|_{J=0} = G_J^{(n)}\big|_{J=0}. \tag{5.2}$$

The n-point correlation function in the presence of a non-vanishing source field is denoted by $G_J^{(n)}$. Although in this example the generating functional $Z[J]$ is a real-valued function and the n-point correlation functions are real numbers, we will, nevertheless, use the terminology of (quantum) field theory (FT) as there will be no ambiguities. The DSE [101] can be derived by introducing an infinitesimal shift δ in the integration variable, $\phi \to \phi + \delta$, and expanding the resulting expression in powers of δ. This yields

$$\frac{\mathrm{d}S}{\mathrm{d}\phi}\left[\phi = \frac{\mathrm{d}}{\mathrm{d}J}\right] Z[J] = JZ[J]. \tag{5.3}$$

The first derivative of the action S which respect to the field ϕ is promoted to a differential operator by the substitution $\phi = \frac{\mathrm{d}}{\mathrm{d}J}$.
The DSE (5.3) is a definition of the generating functional in terms of a differential equation equivalent to the definition of $Z[J]$ through (5.1). For a realistic FT (5.3) turns into a functional integro-differential equation, whereas (5.1) turns into a functional integral. We can determine $Z[J]$ either by directly calculating the functional integral in (5.1) or solving the differential equation (5.3). The later approach is explored in this part of the thesis.
Ultimately, at the end of the calculation we are interested in determining the correlation functions $G^{(n)}$ for the model (5.1). Although $Z[J]$ encodes through is Taylor series expansion the information about all n-point correlation functions, it is not very useful in practical calculations. Starting from (5.3) we derive in the following a closed set of equations where the correlation functions are determined through the solution of this set of equations.

We first note that it is more convenient to work with connected n-point correlation functions $G_c^{(n)}$ or even one-particle irreducible n-point vertex functions $\Gamma_c^{(n)}$. Therefore, in a first step we introduce the generating functional for connected correlation functions, $F[J] = \log Z[J]$,

$$G_c^{(n)} = \left.\frac{\mathrm{d}^n F[J]}{\mathrm{d}J^n}\right|_{J=0} = \left. G_{c,J}^{(n)}\right|_{J=0}, \tag{5.4}$$

where $G_{c,J}^{(n)}$ denotes the connected correlation function in the presence of a non-vanishing source field J. After that we can perform a Legendre transform to introduce the generating functional for the n-point vertex functions, $\tilde{\Gamma}[\Phi]$,

$$\tilde{\Gamma}[\Phi] = J\Phi - F[J] \quad \text{where} \quad \frac{\mathrm{d}F[J]}{\mathrm{d}J} = \Phi. \tag{5.5}$$

We have introduced the shorthand Φ for the expectation value of ϕ in the presence of a non-vanishing source field. The n-point vertex functions are given by

$$\Gamma^{(n)} = \left.\frac{\mathrm{d}^n \tilde{\Gamma}[\Phi]}{\mathrm{d}\Phi^n}\right|_{\Phi=0} = \left. \Gamma_{\Phi}^{(n)}\right|_{\Phi=0}, \tag{5.6}$$

where $\Gamma_{\Phi}^{(n)}$ denotes the n-point vertex function in the presence of a non-vanishing Φ. Plugging the definition for $F[J]$ into the DSE for $Z[J]$ gives,

$$\frac{\mathrm{d}S}{\mathrm{d}\phi}\left[\phi = \frac{\mathrm{d}}{\mathrm{d}J} + \frac{\mathrm{d}F}{\mathrm{d}J}\right] = J. \tag{5.7}$$

In order to arrive at the DSE for the functional $\tilde{\Gamma}$ we first note the identity,

$$G_{c,J}^{(2)} = \left(\Gamma_{\Phi}^{(2)}\right)^{-1}, \tag{5.8}$$

where we have used that

$$\frac{\mathrm{d}\tilde{\Gamma}}{\mathrm{d}\Phi} = J \tag{5.9}$$

due to the definition of $\tilde{\Gamma}$ through the Legendre transform. With this we can easily rewrite the DSE for $F[J]$ to

$$\frac{\mathrm{d}S}{\mathrm{d}\phi}\left[\phi = \Phi + G_{c,J}^{(2)}\frac{\mathrm{d}}{\mathrm{d}\Phi}\right]1 = \frac{\mathrm{d}\tilde{\Gamma}}{\mathrm{d}\Phi}, \tag{5.10}$$

which for the action in (5.1) gives

$$k\Phi + \frac{\lambda}{6}\Phi^3 + \frac{\lambda}{2}\Phi G_{c,J}^{(2)} - \frac{\lambda}{6}\left(G_{c,J}^{(2)}\right)^3 \Gamma_J^{(3)} = \frac{\mathrm{d}\tilde{\Gamma}}{\mathrm{d}\Phi}. \tag{5.11}$$

This is the desired DSE for $\tilde{\Gamma}[\Phi]$, which can be used as a starting point to derive a differential equation for the vertex functions. Before discussing this derivation we want to illustrate the usual approach to solve (5.11).

The DSE (5.11) can be formally solved by deriving an infinite tower of recursion relations between the Taylor coefficients, i.e., the n-point vertex functions, of $\tilde{\Gamma}[\Phi]$,

$$\tilde{\Gamma}[\Phi] = \sum_{n=0}^{\infty} \frac{1}{n!}\,\Gamma^{(n)}\,\Phi^n. \tag{5.12}$$

Therefore, differentiating (5.11) successively with respect to Φ and setting $\Phi = 0$ afterwards yields an infinite tower of equations for the vertex functions,

$$\begin{aligned}
G^{-1} &= k + \frac{\lambda}{2} G - \frac{\lambda}{6} G^3 \Gamma^{(4)} \\
\Gamma^{(4)} &= \lambda - \frac{3\lambda}{2} G^2 \Gamma^{(4)} + \frac{3\lambda}{2} G^4 \left[\Gamma^{(4)}\right]^2 - \frac{\lambda}{6} G^3 \Gamma^{(6)} \\
\Gamma^{(6)} &= -\frac{5\lambda}{2} G^2 \Gamma^{(6)} - 30\lambda\, G^5 \left[\Gamma^{(4)}\right]^3 + \frac{5\lambda}{2} G^4 \Gamma^{(4)} \Gamma^{(6)} + 15\lambda\, G^3 \left[\Gamma^{(4)}\right]^2 - \frac{\lambda}{6} G^3 \Gamma^{(8)} \\
\Gamma^{(8)} &= \dots \\
&\dots \\
\Gamma^{(n)} &= \dots .
\end{aligned} \tag{5.13}$$

We use the shorthand notation $G = G^{(2)} = G_c^{(2)}$ for the two-point correlation function. For a classical FT or quantum FT the n-point vertex function is a rank nD or $n(D+1)$ tensor and therefore for practical reasons the infinite tower has to be truncated at some point. Various truncation schemes are studied but current computational power does not allow to generically include the four-point vertex function in untruncated form.

The differential equation derived in the following will give a practical way to go beyond any truncation scheme. The main idea to close the hierarchy is to consider the generating functional to be a functional of the inverse non-interacting two-point correlation function k, $Z[k] = Z[J = 0, k]$. Therefore, we can write,

$$G^{(4)} = -2\frac{\mathrm{d}G}{\mathrm{d}k} + G^2. \tag{5.14}$$

Using the relation between $\Gamma^{(4)}$ and $G^{(4)}$ we can rewrite (5.14) to

$$\Gamma = -2G^{-2}\frac{\mathrm{d}G^{-1}}{\mathrm{d}k} + 2G^{-2}, \tag{5.15}$$

where we use, here and in the following, the notation $\Gamma^{(4)} = \Gamma$. Therefore, the four-point vertex function can be obtained by differentiating the inverse of the two-point correlation function with respect to the inverse bare two-point correlation function k.
We can use the first equation in (5.13) to obtain

$$\Gamma = \lambda - \frac{3\lambda}{2} G^2 \Gamma^{(4)} + \frac{\lambda}{2} G^4 \left[\Gamma^{(4)}\right]^2 + \frac{\lambda}{6} G \frac{\mathrm{d}\Gamma}{\mathrm{d}k}, \tag{5.16}$$

which can be rewritten by using the chain rule,

$$\frac{\mathrm{d}\Gamma}{\mathrm{d}k} = \frac{\mathrm{d}G}{\mathrm{d}k}\Gamma' = \left(G^4\Gamma - 2G^2\right)\Gamma', \tag{5.17}$$

to

$$\Gamma[G] = \lambda - \frac{3\lambda}{2} G^2 \Gamma + \frac{\lambda}{2} G^4 \Gamma^2 - \frac{\lambda}{3} G^3 \Gamma' + \frac{\lambda}{6} G^5 \Gamma' \Gamma, \tag{5.18}$$

where we denote the derivative with respect to G as Γ'. This differential equation defines a universal functional $\Gamma[G]$.

The discussed closure of the DSE for $\tilde{\Gamma}$ gives a coupled set of equations,

$$G^{-1} = k + \frac{\lambda}{2}G - \frac{\lambda}{6}G^3\Gamma[G] \tag{5.19}$$

$$\Gamma[G] = \lambda - \frac{3\lambda}{2}G^2\Gamma + \frac{\lambda}{2}G^4\Gamma^2 - \frac{\lambda}{3}G^3\Gamma' + \frac{\lambda}{6}G^5\Gamma'\Gamma. \tag{5.20}$$

Thus the 0D toy model (5.1) can be defined in terms of a differential equation useful for practical calculations of G and Γ.
Before going into detail how to solve this coupled set of equations we discuss the derivation for a general FT.

5.2. Functional closure for an interacting field theory

In this section we derive a closed system of functional integro-differential equations for general interacting many-body models with arbitrary two-body interactions. These equations define the many-body theory under consideration in a functional integro-differential formulation.

5.2.1. Correlation functions and functional derivatives

To find a closed set of equations for correlation functions we write high order correlation functions as functional derivatives of low order correlation functions. In this section we show how we define the functional derivatives in a collective index notation.
In Sec. 5.1 the algebraic 0D field theory

$$Z[J] = \int \mathrm{d}\phi\, e^{-S[\phi]+J\phi} \text{ with } S[\phi] = \frac{1}{2}k\phi^2 + \frac{\lambda}{4!}\phi^4 \tag{5.21}$$

was considered, where $Z[J]$ is the generating functional of the n-point correlation functions

$$G^{(n)} = \frac{1}{Z[0]}\int \mathrm{d}\phi\, e^{-S[\phi]}\phi^n = \frac{1}{Z[0]}\left.\frac{\mathrm{d}^n Z[J]}{\mathrm{d}J^n}\right|_{J=0}. \tag{5.22}$$

We extend the definition of the generating functional $Z[J]$ with a 1-point source term J to a two-point source term. The inverse non-interacting two-point correlation function k can be regarded as a two-point source term. Therefore, the partition function $Z = Z[J=0]$ is considered to be a generating functional with respect to k, $Z = Z[k]$. The two-point correlation function $G = G^{(2)}$ can be obtained by differentiation with respect to the two-point source term k,

$$G = -2\left.\frac{\mathrm{d}\ln Z[k]}{\mathrm{d}k}\right|_{k_{\mathrm{phys}}}. \tag{5.23}$$

In order to practically use (5.23), $Z[k]$ has to be computed for arbitrary $k \in \mathbb{R}$ and afterwards the derivative has to be evaluated at $k = k_{\mathrm{phys}}$.
We first discuss the extension to a FT for the prototypical $\mathbb{Z}_2$ symmetric ϕ^4 model on a lattice in arbitrary dimensions D,

$$\begin{aligned} Z[J] &= \int \mathrm{d}(\phi)\, e^{-S[\phi]+\sum_i J_i\phi_i} \\ \text{with } S[\phi] &= \frac{1}{2}\sum_{i,j}\phi_i G^{-1}_{0;i,j}\phi_j + \frac{\lambda}{4!}\sum_i \phi_i^4. \end{aligned} \tag{5.24}$$

In this case $G_0^{-1} \in \mathbb{R}^{L\times L}$ with L the number of lattice sites and $G^{-1}_{0;i,j} = G^{-1}_{0;i,j;\text{phys}} = -\Box_{i,j} + m^2\delta_{i,j}$ where $\Box$ is the discretized Laplace operator in D dimensions. The measure of the functional integral is denoted by $\mathrm{d}(\phi)$. The n-point correlation function carries now additional lattice indices and is defined as

$$G^{(n)}_{i_1,\ldots,i_n} = \langle \phi_{i_1} \ldots \phi_{i_n} \rangle = \frac{1}{Z[0]} \int \mathrm{d}(\phi)\, e^{-S[\phi]} \phi_{i_1} \ldots \phi_{i_n}. \tag{5.25}$$

In analogy with the 0D case we consider $Z = Z[J=0] = Z[G_0^{-1}]$ and write the two-point correlation function as

$$G_{i,j} = -2 \left. \frac{\delta \ln Z[G_0^{-1}]}{\delta G^{-1}_{0;i,j}} \right|_{G^{-1}_{0;\text{phys}}}. \tag{5.26}$$

Therefore, $Z[G_0^{-1}]$ has to be computed for arbitrary $G_0^{-1} \in \mathbb{R}^{L\times L}$ and only after the derivative has been taken the expression is evaluated in the subspace of physical $G_0^{-1} = G^{-1}_{0;i,j;\text{phys}}$.
In particularly, although $G^{-1}_{0;i,j;\text{phys}}$ lies inside the subspace of translational invariant G_0^{-1} the calculation of $Z[G_0^{-1}]$ must not be restricted to this physical subspace. Translational invariance can only be restored after the functional derivative of $Z[G_0^{-1}]$ is evaluated at $G^{-1}_{0;\text{phys}}$.
The following argument [102] illustrates that this is indeed indispensable. The four-point correlation function $G^{(4)}_{i_1,i_2,i_3,i_4} = \langle \phi_{i_1}\phi_{i_2}\phi_{i_3}\phi_{i_4} \rangle$ can be written as

$$G^{(4)}_{i_1,i_2,i_3,i_4} = -2 \left. \frac{\delta G_{i_1,i_2}}{\delta G^{-1}_{0;i_3,i_4}} \right|_{G^{-1}_{0;\text{phys}}} + G_{i_1,i_2} G_{i_3,i_4}. \tag{5.27}$$

Model (5.24) is translational invariant and therefore $G^{(4)}$ depends on three relative distances, e.g., $i_1 - i_2$, $i_1 - i_3$, $i_1 - i_4$. If translational invariance is already restored before taking the functional derivative in (5.27), i.e., taking the functional derivative only in the restricted subspace of translational invariant G_0^{-1}, the right hand side depends only on two relative distances $i_1 - i_2$, $i_3 - i_4$. In this case the functional derivative does not provide the full information about all values of the four-point correlation function. This shows that it is crucial to consider $G_0^{-1} \in \mathbb{R}^{L\times L}$ and not perform the calculation in a restricted subspace.

We can also consider an argument based on diagrammatic reasonings which is closer to the actual computational techniques introduced in this chapter. The above result can be obtained by taking into account the following considerations. Formally, a FT can also be defined through its series expansion of correlation functions in terms of Feynman diagrams. The functional derivative with respect to G_0 (related to the one with respect to G_0^{-1} through the chain rule of functional differentiation) can be considered for each diagram. The action of this derivative on a single Feynman diagram is diagrammatically represented by removing one G_0 line in all possible ways. The result of cutting a single G_0 line is a new diagram with two additional external legs, which can be a Feynman diagram in the series expansion of a higher order correlation function. The precise relation will be derived in the following chapter. We consider this process for a specific example where translational invariance is already restored before taking the functional derivative. The functional derivative of the diagram in Fig. 5.1 a) in momentum space will give the following expression,

$$\begin{aligned} \frac{1}{3} \frac{\delta}{\delta G_0(p_3)} \int_{p_5,p_6} G_0(p_1 - p_5 - p_6) G_0(p_5) G_0(p_6) = \\ \int_{p_5} G_0(p_1 - p_3 - p_5) G_0(p_5). \end{aligned} \tag{5.28}$$

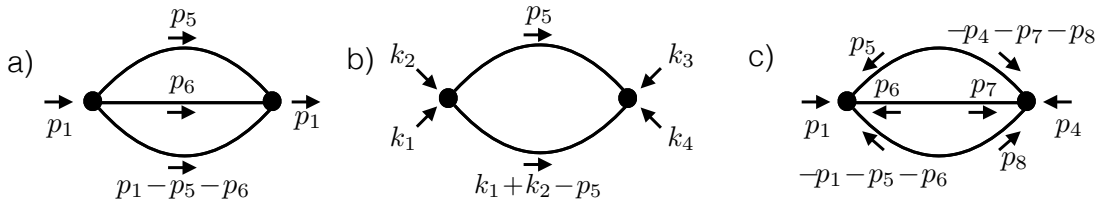

Figure 5.1.: Feynman diagrams in momentum space contributing to different correlation functions for ϕ^4 theory with action (5.24). The lines represent non-interacting two-point correlation functions G_0 whereas the interaction vertex is represented by the dot. Due to the local interaction momentum is conserved at each vertex. a) The second order contribution to the self-energy. Due to the translational symmetry of the ϕ^4 model incoming and outgoing momenta have to be equal and G_0 depends only on a single momentum variable. b) A second order contribution to the four-point vertex function depending on the four external momentum variables k_i. Due to translational symmetry, $\delta(k_1+k_2+k_3+k_4)$, the four-point vertex function effectively depends on three momentum variables. c) The second order diagram contributing to the self-energy without assuming translational symmetry. Therefore, incoming and outgoing momenta do not have to be equal and the two-point correlation function lines depend on 2-momentum variables.

Due to translational invariance G_0 is diagonal in momentum space and depends only on a single momentum variable. The resulting diagram obtained from this functional differentiation is depicted in Fig. 5.1 b). It contributes to the Feynman diagrammatic expansion of the four-point vertex function. However, as we already assumed translational invariance before taking the derivative we can obtain information only in the subspace $k_1 = -k_4 = p_1$, $k_2 = -k_3 = -p_3$.
The contribution for arbitrary external momentum variables is given by the functional derivative of the diagram in Fig. 5.1 c). Translational invariance is not taken into account yet and therefore G_0 depends on two momentum variables. In this case differentiating the diagram gives,

$$\begin{aligned}&\frac{1}{3}\frac{\delta}{\delta G_0(p_2,p_3)}\left[\int_{p_5,p_6,p_7,p_8} G_0(p_5,-p_4-p_7-p_8)G_0(p_6,p_7)G_0(-p_1-p_5-p_6,p_8)\right]\Big|_{G_0=G_{0,\mathrm{phys}}}\\ &=\delta(p_1+p_2+p_3+p_4)\int_{p_5} G_0(p_1+p_2-p_5)G_0(p_5)\end{aligned} \tag{5.29}$$

which is exactly the analytic expression for Fig. 5.1 b) with $k_i = p_i$.
This result can be generalized to more complicated symmetries such as interacting fermions with spin σ on a lattice with a translational invariant hopping matrix h and local on-site Hubbard type interaction. The free part S_0 of the action $S = S_0 + S_{\mathrm{int}}$ can then be written as

$$S_0[\bar{\psi},\psi] = \int_0^\beta \mathrm{d}\tau\mathrm{d}\tau' \sum_{\sigma,\sigma';i,j} \bar{\psi}_{i,\sigma}(\tau) G^{-1,\bar{\psi}\psi}_{0;i,j,\sigma,\sigma'}(\tau,\tau')\psi_{j,\sigma'}(\tau') \tag{5.30}$$

where $G^{-1,\bar{\psi}\psi}_{0;i,j,\sigma,\sigma'}(\tau,\tau') = G^{-1}_{0;i,j,\sigma,\sigma';\mathrm{phys}}(\tau,\tau') = \delta_{\sigma,\sigma'}\delta(\tau-\tau')\left[(\partial_\tau-\mu)\,\delta_{i,j}+h_{i,j}\right]$ and the interacting part S_{int} describes a local interaction which does not break $U(1)$ symmetry nor $SU(2)$ spin symmetry nor does it violate translational invariance in space and imaginary time.
We focus in the following on the $U(1)$ symmetry leading to particle number conservation but note that exactly the same argument can be used for $SU(2)$ spin symmetry. A second order diagram contributing to the self-energy for this model is given in Fig. 5.2 a). We only consider the labels of the diagram due to the $U(1)$ symmetry where incoming lines denote ψ and outgoing lines denote $\bar{\psi}$. Due to the $U(1)$ symmetry particle number is conserved and the number of ingoing lines

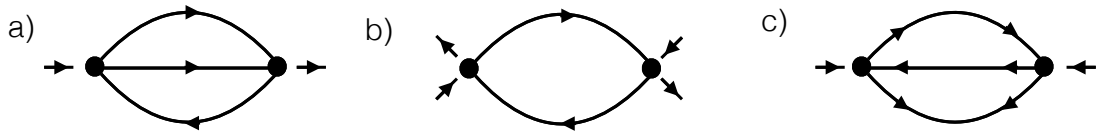

Figure 5.2.: Feynman diagrams for the fermionic model with free action (5.30) and Hubbard type interactions. The lines represent non-interacting two-point correlation functions G_0 whereas the interaction vertex is represented by the dot. The diagrams are only labeled by the arrows on the lines which corresponds to $U(1)$ symmetry. Further labels are suppressed. Incoming lines represent $\bar{\psi}$-fields and outgoing lines represent ψ-fields. As the Hubbard type density-density interaction preserves $U(1)$ symmetry the number of ingoing and the number of outgoing lines on each vertex have to be equal. a) The second order diagram contributing to the diagonal part of the self-energy. The number of incoming and outgoing lines are equal and therefore the diagram contributes to the diagonal component of the self energy. b) A second order diagram contributing to the four-point vertex function. c) The second order diagram contributing to the off-diagonal part of the self-energy. There are two incoming lines but no outgoing lines therefore the diagram contributes only in the case of broken $U(1)$ symmetry.

equals the number of outgoing lines. Taking the derivative of this diagram with respect to $G_0^{\bar{\psi}\psi}$, we obtain the diagram in Fig. 5.2 b) which contributes to the four-point correlation function. The diagram in Fig. 5.2 a) is not the only diagram which upon cutting a single propagator line leads to the diagram in Fig. 5.2 b). If we allow for $U(1)$ symmetry breaking we can also consider the diagram in Fig. 5.2 c) which contributes to the off-diagonal part of the self-energy. The particle number is not conserved for this diagram as there are two incoming lines but no outgoing lines. The diagram includes an off-diagonal G_0 line, $G_0^{\bar{\psi}\bar{\psi}}$, which is indicated by two arrows on that line pointing in different directions. Cutting this G_0 line also leads to the diagram in Fig. 5.2 b) which preserves particle number conservation. This example shows, in analogy with translational invariance, that at an intermediate stage of the calculation $U(1)$ symmetry can be broken and only after the derivative has been taken all symmetries of the action have to be respected.
Concluding, we showed that in general G_0^{-1} has to be defined outside the subspace of physical inverse non-interacting two-point correlation functions. The full space is given by a collective index space such that the free part of the action can be written as

$$S_0[\phi] = \frac{1}{2}\sum_{i,j} \phi_i G^{-1}_{0;i,j}\phi_j. \tag{5.31}$$

The collective index i summarizes all possible field labels of the considered model. For (5.30) $i = (\pm, \tau, x_i, \sigma)$ where $i = (+, \tau, x_i, \sigma)$ labels $\bar{\psi}_{x_i,\sigma}(\tau)$ and $i = (-, \tau, x_i, \sigma)$ labels $\psi_{x_i,\sigma}(\tau)$. The inverse non-interacting two-point correlation function $G^{-1}_{0;i,j}$ is therefore defined in this collective index space with properties discussed in the following.

5.2.2. Dyson-Schwinger equation for interacting many-body systems

We start with the most general form of the action of a many-body system with arbitrary two-body interactions,

$$\begin{aligned} S[\phi] &= \frac{1}{2}\phi_{i_1} G^{-1}_{0;i_1,i_2}\phi_{i_2} + \frac{1}{4!}V_{i_1,\ldots,i_4}\phi_{i_1}\phi_{i_2}\phi_{i_3}\phi_{i_4}. \\ Z &= \int d(\phi)\, e^{-S[\phi]} \end{aligned} \tag{5.32}$$

The fields ϕ_i are either complex numbers if they represent bosonic degrees of freedom or anti-commuting Grassmann numbers for fermionic degrees of freedom. They are labeled by a single collective index i which summarizes all possible labels for the fields as introduced in Sec. 5.2.1. The action can be formally defined on a lattice or in continuous space where $\mathbf{x}$ is taken to be a discrete variable or a continuous variable respectively. The inverse of the non-interacting Greens function G_0^{-1} should be thought of as a symmetric/antisymmetric matrix (for bosons/fermions) in the space of the collective index i and the matrix elements of the two-body interaction are given by a fully symmetric/antisymmetric tensor V. Summation over repeated indices is implicitly assumed.
The Dyson-Schwinger equation for model (5.32) can be derived by introducing the generating functional of the n-point correlation functions,

$$Z[J] = \int \mathrm{d}(\phi)\, e^{-S[\phi]+\sum_i J_i\phi_i}. \tag{5.33}$$

For bosons the source fields J_i are complex numbers while for fermions they are Grassmann numbers anti-commuting with itself and with the fields ϕ_i. The measure of the functional integral is denoted by $d(\phi)$. All n-point correlation functions can be generated by functional derivatives of the generating functional with respect to the source fields,

$$G^{(n)}_{i_1,\ldots,i_n} = \langle \phi_{i_1} \ldots \phi_{i_n} \rangle = \frac{1}{Z} \left. \frac{\delta^{(n)} Z[J]}{\delta J_{i_1} \ldots \delta J_{i_n}} \right|_{J=0}. \tag{5.34}$$

The Dyson-Schwinger equation is derived by considering a linear shift Δ of a single field variable in the functional integral for the generating functional. For fermions Δ has to be a Grassmann number while for bosons Δ is a complex number. The elements in the functional integral for the generating functional transform under this shift as

$$\begin{aligned} \phi_{i_1} &\to \phi_{i_1} + \Delta \\ \mathrm{d}(\phi) &\to \mathrm{d}(\phi) \\ S[\phi] &\to S[\phi] + \Delta \frac{\delta S[\phi]}{\delta \phi_{i_1}} + \mathcal{O}(\Delta^2). \end{aligned} \tag{5.35}$$

Therefore, the generating functional is given by

$$\begin{aligned} Z[J] &= \int d(\phi)\, e^{-S[\phi]+\sum_i J_i\phi_i - \Delta \frac{\delta S[\phi]}{\delta \phi_{i_1}} \pm \Delta J_{i_1} + \mathcal{O}(\Delta^2)} \\ &= \int d(\phi) \left(1 + \Delta \left[\pm J_{i_1} - \frac{\delta S[\phi]}{\delta \phi_{i_1}}\right] + \mathcal{O}(\Delta^2)\right) e^{-S[\phi]+\sum_i J_i\phi_i}. \end{aligned} \tag{5.36}$$

Here and in the following the upper sign in $\pm$ or $\mp$ is for the bosonic case where the lower sign is for the fermionic case. The differential form of the Dyson-Schwinger equation is obtained by equating the above expression in powers of Δ,

$$\left(\pm J_{i_1} - \frac{\delta S}{\delta \phi_{i_1}} \left[\frac{\delta}{\delta J}\right]\right) Z[J] = 0. \tag{5.37}$$

This is a functional integro-differential equation for the generating functional $Z[J]$. This equation can be formally solved by using the Taylor series expansion of the generating functional in terms of the source fields J_i around $J_i = 0$,

$$Z[J] = \sum_n \frac{1}{n!} \sum_{i_1,\ldots,i_n} G^{(n)}_{i_1,\ldots,i_n} J_{i_n} \ldots J_{i_1}. \tag{5.38}$$

The relations between the expansion coefficients, i.e., the n-point correlation functions, can be obtained by successive differentiation of (5.37) with respect to the source fields J_i and setting the sources to $J_i = 0$ afterwards. This yields an infinite tower of integral equations for the n-point correlation functions. The equation obtained by differentiating (5.37) once is given by

$$\pm G^{-1}_{0;i_1,i_3} G_{i_3,i_2} + \frac{1}{6} V_{i_1,i_3,i_4,i_5} G^{(4)}_{i_5,i_4,i_3,i_2} = \pm \delta_{i_1,i_2}. \tag{5.39}$$

This equation relates the two-point correlation function with the four-point correlation function. The four-point correlation function can be split into a disconnected part and a connected part which on the other hand can be factorised into a contribution coming from the two-point correlation function and a genuine four-point contribution, the four-point vertex function. Therefore, we rewrite (5.39) such that it relates the two-point correlation function G with the four-point vertex function Γ. In principle this can be done by introducing further generating functionals for one-particle irreducible correlation functions but as we only need the connection between correlation functions on the four-point level we will directly introduce the relations between them.
The connected four-point correlation function $G^{(4)}_c$ is given by

$$G^{(4)}_{c;i_1,i_2,i_3,i_4} = G^{(4)}_{i_1,i_2,i_3,i_4} - G_{i_1,i_2} G_{i_3,i_4} \mp G_{i_1,i_3} G_{i_2,i_4} - G_{i_1,i_4} G_{i_2,i_3} \tag{5.40}$$

and the four-point vertex function is related to $G^{(4)}_c$ by

$$\Gamma_{1,2,3,4} = -G^{-1}_{1,5} G^{-1}_{2,6} G^{-1}_{3,7} G^{-1}_{4,8} G^{(4)}_{c;5,6,7,8}. \tag{5.41}$$

Here and in the following we use the short hand notation $i_n = n$ for the collective index i_n.
Plugging these relations into (5.39) and solving for the inverse of the two-point correlation function, we obtain

$$\begin{aligned} G^{-1}_{1,2} =& G^{-1}_{0;1,2} - \Sigma_{1,2} \\ \Sigma_{1,2} =& \mp \frac{1}{2} V_{1,2,3,4} G_{4,3} + \frac{1}{6} V_{1,3,4,5} G_{5,6} G_{4,7} G_{3,8} \Gamma_{6,7,8,2}. \end{aligned} \tag{5.42}$$

The self-energy $\Sigma_{1,2}$ has been introduced as a short hand notation for the contributions coming from the interaction part. The above equation is a single equation for two unknown correlation functions and therefore constitutes an underdetermined set of equations. In the following section we derive a closed set of equations.

5.2.3. Closed Dyson-Schwinger equation for interacting many-body systems

Based on the Dyson-Schwinger equation (5.42) which relates the inverse two-point correlation function with the four-point vertex function we derive a closed set of functional integro-differential equations. The solution of this set of differential equations gives direct access to the two-point correlation function G and to the four-point vertex function Γ.
We start the derivation with the identity

$$\begin{aligned} \frac{\delta G_{1,2}}{\delta G^{-1}_{0;3,4}} &= \frac{\delta}{\delta G^{-1}_{0;3,4}} \left[\frac{1}{Z[G_0^{-1}]} \int d(\phi)\, e^{-S[\phi, G_0^{-1}]} \phi_2 \phi_1 \right] \\ &= \frac{1}{2} G_{3,4} G_{1,2} - \frac{1}{2} G^{(4)}_{1,2,3,4}. \end{aligned} \tag{5.43}$$

We have used that

$$\frac{\delta G^{-1}_{0;1,2}}{\delta G^{-1}_{0;3,4}} = \frac{1}{2}\left(\delta_{1,3}\delta_{2,4} \pm \delta_{1,4}\delta_{2,3}\right). \tag{5.44}$$

This functional derivative identity together with the relation between the correlation functions (5.40) yields

$$G^{(4)}_{1,2,3,4} = -2\frac{\delta G_{1,2}}{\delta G^{-1}_{0;3,4}} + G_{1,2}G_{3,4}. \tag{5.45}$$

The four-point vertex function can also be written as a functional derivative with respect to G_0^{-1} by plugging the above identity (5.45) into the definition of the four-point vertex function (5.41). The final result is

$$\Gamma_{1,2,3,4} = 2\, G^{-1}_{3,5}\frac{\delta \Sigma_{1,2}}{\delta G^{-1}_{0,5,6}} G^{-1}_{6,4} \tag{5.46}$$

where we have used the functional chain rule,

$$\frac{\delta G_{1,2}}{\delta G^{-1}_{0;3,4}} = -G_{1,5}\frac{\delta G^{-1}_{5,6}}{\delta G^{-1}_{0;3,4}} G_{6,2}. \tag{5.47}$$

Up to now all identities are only based on the general rules of functional differentiation and are not specific to any form of the action $S[\phi]$. To make the connection to the considered model (5.32), we can in principle use the identity (5.46) in the Dyson-Schwinger equation (5.42) to define a coupled set of equations for a functional $G[G_0]$. Numerically more favourable is a universal function $\Gamma[G]$. Therefore, in the following we will use the self-energy $\Sigma_{1,2}$ obtained from the Dyson-Schwinger equation (5.42) and plug this expression into the identity (5.46).
We obtain the following expression after a long but straightforward calculation

$$\begin{aligned}
\Gamma_{1,2,3,4} \;=\; & V_{1,2,3,4} - \frac{1}{2}V_{1,2,5,6}G_{5,8}G_{6,7}\Gamma_{7,8,3,4} \\
& \mp\frac{1}{2}V_{1,3,5,6}G_{5,8}G_{6,7}\Gamma_{7,8,2,4} \\
& \mp\frac{1}{2}V_{1,4,5,6}G_{5,8}G_{6,7}\Gamma_{7,8,3,2} \\
& +\frac{1}{2}V_{1,5,6,7}G_{7,10}\Gamma_{10,12,3,4}G_{12,11}G_{5,8}G_{6,9}\Gamma_{8,2,11,9} \\
& +\frac{1}{3}V_{1,7,8,9}G_{9,10}G_{8,11}G_{7,12}G^{-1}_{3,5}\frac{\delta\Gamma_{10,2,11,12}}{\delta G^{-1}_{0,5,6}}G^{-1}_{6,4}.
\end{aligned} \tag{5.48}$$

The last term can be simplified by noting that second order functional derivatives commute. The following commutator identity can be derived using this property,

$$\begin{aligned}
&\left[G^{-1}_{11,5}G^{-1}_{6,12}\frac{\delta\Gamma_{10,2,3,4}}{\delta G^{-1}_{0,5,6}} - G^{-1}_{3,5}G^{-1}_{6,4}\frac{\delta\Gamma_{10,2,11,12}}{\delta G^{-1}_{0,5,6}}\right] = \\
&2G^{-1}_{11,5}G^{-1}_{6,12}\frac{\delta}{\delta G^{-1}_{0;5,6}}\left[G^{-1}_{3,9}\frac{\delta\Sigma_{10,2}}{\delta G^{-1}_{0;9,13}}G^{-1}_{13,4}\right] - \\
&2G^{-1}_{3,5}G^{-1}_{6,4}\frac{\delta}{\delta G^{-1}_{0;5,6}}\left[G^{-1}_{11,9}\frac{\delta\Sigma_{10,2}}{\delta G^{-1}_{0;9,13}}G^{-1}_{13,12}\right] = \\
&-\frac{1}{2}\Gamma_{3,\alpha,11,12}G_{\alpha,\beta}\Gamma_{10,2,\beta,4} - \frac{1}{2}\Gamma_{11,4,\alpha,12}G_{\alpha,\beta}\Gamma_{10,2,3,\beta} \\
&+\frac{1}{2}\Gamma_{11,\alpha,3,4}G_{\alpha,\beta}\Gamma_{10,2,\beta,12} + \frac{1}{2}\Gamma_{12,\alpha,3,4}G_{\alpha,\beta}\Gamma_{10,2,11,\beta}.
\end{aligned} \tag{5.49}$$

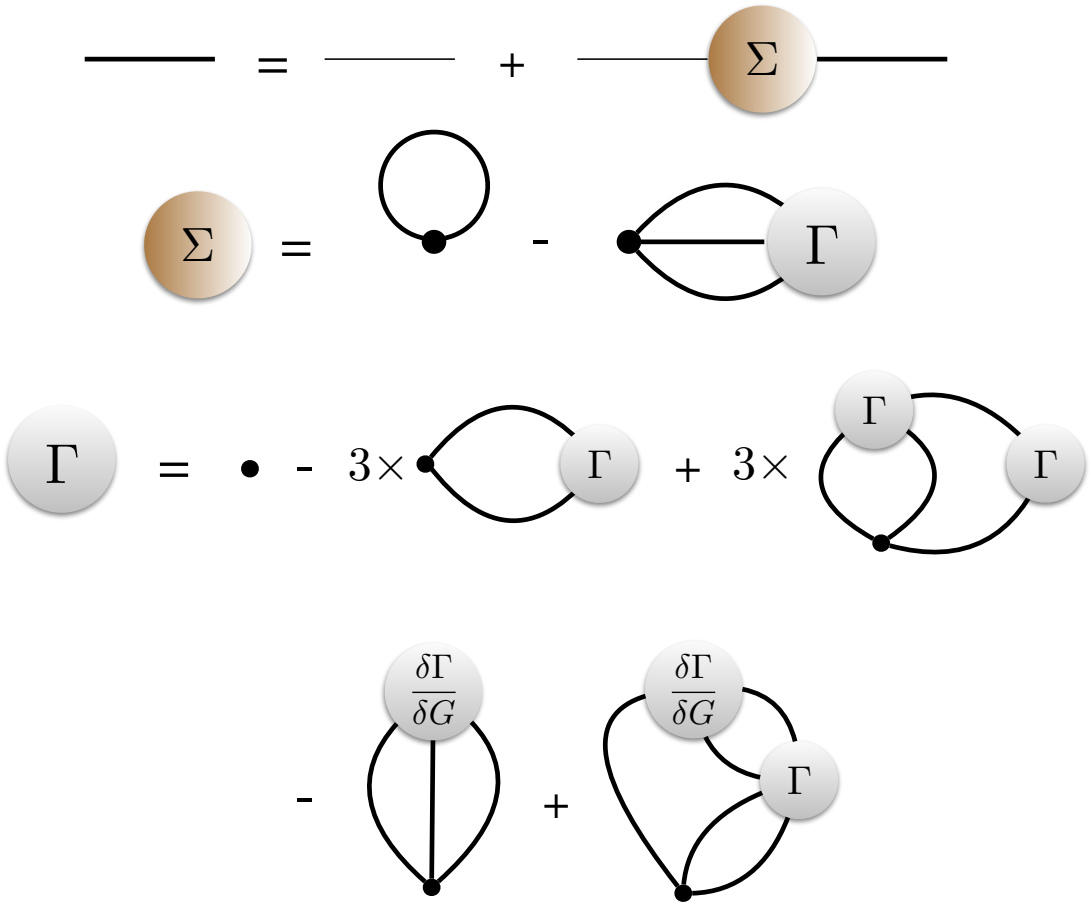

Figure 5.3.: The coupled set of equations defining model (5.32) is closed through a functional integro-differential equation. Each diagram is in one-to-one correspondence with the terms in (5.53), (5.54). The non-interacting two-point correlation function $G_{0;i,j}$ is denoted by a thin line, the two-point correlation function $G_{i,j}$ by a bold line, and the bare vertex by a dot. The correct convolution of lattice indices can be obtained by standard diagrammatic rules. The terms without functional derivatives involve the permutation of external indices and is denoted by the factor 3.

This identity is used to rewrite the last term in (5.48) such that the four-point vertex is given by

$$\begin{aligned}
\Gamma_{1,2,3,4} \;=\; & V_{1,2,3,4} - \frac{1}{2} V_{1,2,5,6} G_{5,8} G_{6,7} \Gamma_{7,8,3,4} \\
& \mp \frac{1}{2} V_{1,3,5,6} G_{5,8} G_{6,7} \Gamma_{7,8,2,4} \\
& \mp \frac{1}{2} V_{1,4,5,6} G_{5,8} G_{6,7} \Gamma_{7,8,3,2} \\
& + \frac{1}{3} V_{1,5,6,7} G_{5,8} \frac{\delta \Gamma_{8,2,3,4}}{\delta G^{-1}_{0;6,7}} \\
& + \frac{1}{6} V_{1,5,6,7} G_{7,10} \Gamma_{10,12,3,4} G_{12,11} G_{5,8} G_{6,9} \Gamma_{8,2,11,9} \\
& \pm \frac{1}{6} V_{1,5,6,7} G_{7,10} \Gamma_{10,12,2,4} G_{12,11} G_{5,8} G_{6,9} \Gamma_{8,3,11,9} \\
& \pm \frac{1}{6} V_{1,5,6,7} G_{7,10} \Gamma_{10,12,3,2} G_{12,11} G_{5,8} G_{6,9} \Gamma_{8,4,11,9}.
\end{aligned} \tag{5.50}$$

Formally (5.42), (5.50) form a closed set of equations where the four-point vertex function should be thought of as a functional of the inverse of the non-interacting two-point correlation function. It is much more desirable to define the four-point vertex function as a functional of the two-point correlation function. This functional is obtained by using again the functional chain rule,

$$\frac{\delta}{\delta G^{-1}_{0;6,7}} = \left(\frac{\delta G_{9,10}}{\delta G^{-1}_{0;6,7}}\right) \frac{\delta}{\delta G_{9,10}}. \tag{5.51}$$

With (5.45) the first term in the product can be expanded to

$$\frac{\delta G_{9,10}}{\delta G^{-1}_{0;6,7}} = \frac{1}{2} G_{9,a} G_{10,b} G_{6,c} G_{7,d} \Gamma_{a,b,c,d} - \frac{1}{2} G_{7,9} G_{6,10} \mp \frac{1}{2} G_{7,10} G_{6,9}. \tag{5.52}$$

This relation transforms (5.50) into a definition of the four-point vertex function as a universal functional $\Gamma[G]$ in the language of a functional integro-differential equation. The complete set of closed Dyson-Schwinger equations is given by

$$\begin{aligned}
G^{-1}_{1,2} &= G^{-1}_{0;1,2} - \Sigma_{1,2} \\
\Sigma_{1,2} &= \mp\frac{1}{2} V_{1,2,3,4} G_{4,3} + \\
&\quad \frac{1}{6} V_{1,3,4,5} G_{5,6} G_{4,7} G_{3,8} \Gamma_{6,7,8,2}, \qquad (5.53) \\
\Gamma_{1,2,3,4} &= V_{1,2,3,4} - \frac{1}{2} V_{1,2,5,6} G_{5,8} G_{6,7} \Gamma_{7,8,3,4} \\
&\quad \mp\frac{1}{2} V_{1,3,5,6} G_{5,8} G_{6,7} \Gamma_{7,8,2,4} \\
&\quad \mp\frac{1}{2} V_{1,4,5,6} G_{5,8} G_{6,7} \Gamma_{7,8,3,2} \qquad (5.54) \\
&\quad + \frac{1}{6} V_{1,5,6,7} G_{7,10} \Gamma_{10,12,3,4} G_{12,11} G_{5,8} G_{6,9} \Gamma_{8,2,11,9} \\
&\quad \pm\frac{1}{6} V_{1,5,6,7} G_{7,10} \Gamma_{10,12,2,4} G_{12,11} G_{5,8} G_{6,9} \Gamma_{8,3,11,9} \\
&\quad \pm\frac{1}{6} V_{1,5,6,7} G_{7,10} \Gamma_{10,12,3,2} G_{12,11} G_{5,8} G_{6,9} \Gamma_{8,4,11,9} \\
&\quad \mp\frac{1}{3} V_{1,5,6,7} G_{5,8} G_{6,9} G_{7,10} \frac{\delta \Gamma_{8,2,3,4}}{\delta G_{9,10}} \\
&\quad + \frac{1}{6} V_{1,5,6,7} G_{5,8} G_{6,11} G_{7,14} \Gamma_{11,12,13,14} G_{12,9} G_{13,10} \frac{\delta \Gamma_{8,2,3,4}}{\delta G_{9,10}}.
\end{aligned}$$

The equations are diagrammatically depicted in Fig. 5.3.

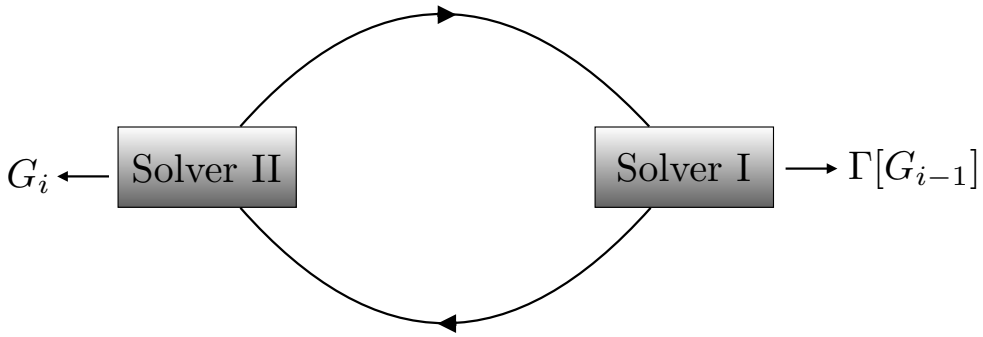

Figure 5.4.: The self-consistency loop to solve the closed set of DSEs (5.55), (5.56) for the 0D toy model, which can also be generalized to the FT case of (5.53), (5.54). "Solver I" denotes the method used to solve the differential equation (5.56). "Solver II" denotes the method used to solve the auxiliary problem (5.57). In each self-consistency step the solution to the differential equation $\Gamma[G]$ is used and evaluated at G_{i-1}, the approximation of the two-point correlation function obtained in the previous step. This yields an approximation of the four-point vertex function needed for the auxiliary problem (5.57). The auxiliary problem is solved resulting in an approximation of the two-point correlation function at step i, G_i.

5.3. Solution of the Dyson-Schwinger equation for the 0D toy model

In this section we solve the 0D toy model defined through the set of equations (5.19), (5.20) and repeated here for convenience,

$$G^{-1} = k + \frac{\lambda}{2}G - \frac{\lambda}{6}G^3\Gamma[G] \tag{5.55}$$

$$\Gamma[G] = \lambda - \frac{3\lambda}{2}G^2\Gamma + \frac{\lambda}{2}G^4\Gamma^2 - \frac{\lambda}{3}G^3\Gamma' + \frac{\lambda}{6}G^5\Gamma'\Gamma. \tag{5.56}$$

For the 0D toy model Eq. (5.56) is an ordinary differential equation (ODE) instead of a functional integro-differential equation. There are well established methods to solve ODE but in general these methods can not be generalized to functional integro-differential equations. Therefore, the aim of this chapter is to solve the set of equations (5.55), (5.56) and to develop a method which can be carried over to the FT defined through (5.53) and (5.54).
We begin the discussion by assuming that we have a method, called "Solver I", which gives the solution of the ODE (5.56) for arbitrary G and another method, called "Solver II", which gives the solution to the auxiliary problem

$$G^{-1} = k + \frac{\lambda}{2}G - \frac{\lambda}{6}G^3\Gamma[\tilde{G}]. \tag{5.57}$$

This problem is a simplified version of the DSE (5.55) as the universal functional $\Gamma[G]$ is evaluated at some arbitrary $\tilde{G}$. The full solution of the coupled set of equations can then be obtained by establishing the self-consistency loop

$$G_i^{-1} = k + \frac{\lambda}{2}G_i - \frac{\lambda}{6}G_i^3\Gamma[\tilde{G}_{i-1}], \tag{5.58}$$

where G_i, $\Gamma[G_i]$ denotes the solution after the i-th self-consistent iteration step. Therefore, at each iteration step i we have to evaluate $\Gamma[G]$ at $G = G_{i-1}$ and solve the auxiliary problem (5.57)

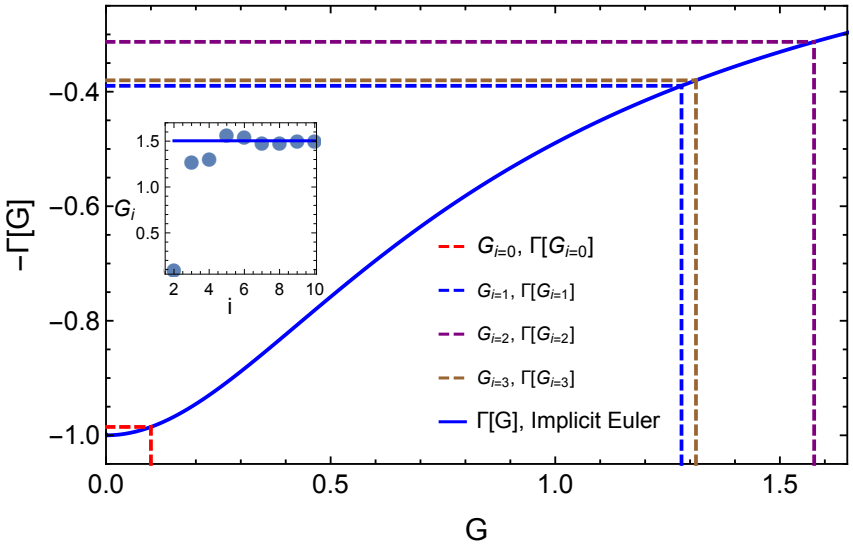

Figure 5.5.: The universal function $\Gamma[G]$ for $\lambda = 1$ is obtained by solving the DE (5.56) with the implicit Euler method. The vertical and horizontal lines illustrate the evaluation of $\Gamma[G]$ in the self-consistency loop of Fig. 5.4. We initialize the self-consistency by setting $G_{i=0} = 0.1$ (red) where i denotes the loop index and consequently use the evaluation $\Gamma[G_{i=0}]$ in the auxiliary problem (5.57) to obtain $G_{i=1}$ (blue). This procedure is repeated until the self-consistency converges which is demonstrated for $k = 0.1$ in the inset.

to obtain G_i. The self-consistency loop is illustrated in Fig. 5.4.
Implementing the protocol for the 0D toy model is straightforward. The ODE is solved using an implicit Euler method [103] starting from $\Gamma[0] = \lambda$, i.e., in this case "Solver I" is just the implicit Euler method.
The solution of the differential equation for $\lambda = 1$ is shown in Fig. 5.5. The universal functional $\Gamma[G]$ for the 0D toy model can also be obtained from its functional integral representation by first calculating G and Γ for arbitrary k, i.e., $G[k]$ and $\Gamma[k]$, and afterwards plugging the inverse $k[G]$ into $\Gamma[k[G]]$. The result for $\Gamma[G]$ agrees with the one found from the solution of the ODE (5.56) but, as we will see later, calculating the inverse even for the 0D toy model adds some extra complications and obviously can not be generalized to a FT.
Equipped with the solution $\Gamma[G]$ we now discuss the self-consistency for the example of the physical parameters $k = 0.1$, $\lambda = 1$ illustrated in Fig. 5.5. We initialize the self-consistency at step $i = 1$ with $G_{i=0} = 0.1$. This is indicated as the vertical red line in Fig. 5.5. The horizontal red line in Fig. 5.4 illustrates the evaluation of the universal functional $\Gamma[G]$, which is found with the help of "Solver I", at $G_{i=0}$. Thereafter we solve the auxiliary problem (5.57) with $\Gamma[\tilde{G}] = \Gamma[G_{i=0}]$ to obtain the approximation of the two-point correlation function $G_{i=1}$ at step $i = 1$, cf. the vertical blue line in Fig. 5.5. For the 0D toy model the auxiliary problem (5.57) is a root finding problem for a polynomial of degree 4 and can be solved by elementary algebra. This completes the first iteration step and we can repeat the above procedure until the self-consistency converges, cf. the inset in Fig. 5.5. Therefore, we have determined the two-point correlation function and the four-point vertex function for the physical parameters $k = 0.1$, $\lambda = 1$. This completes the numerical solution of the 0D toy model.
In order to use the self-consistency loop for a realistic FT we have to generalize the following steps. Most obvious, in the case where the ODE turns into a functional integro-differential equation the solution $\Gamma[G]$ can not be simply found by integrating the differential equation with the implicit Euler method. Moreover, if we assume that we can construct the solution $\Gamma[G]$ we

still have to evaluate the functional at each iteration step and store the approximation to the four-point vertex function obtained from this evaluation for later use in the auxiliary problem. The evaluation and storage is a formidable problem as the vertex function is a rank-4D or rank-4$(D+1)$ tensor for a classical or quantum field theory, respectively. Finally, we have to introduce a method to find the solution of the auxiliary problem, which turns for a realistic FT into an integral equation. Fortunately, as integral equations are closely related to differential equations, we can use the same method introduced for the functional integro-differential equation to solve the auxiliary problem.
In the following we first introduce a semi-analytic method, the homotopy analysis method (HAM), to solve the ODE (5.56) for the 0D toy model. We will show in later sections that the HAM can be generalized to functional integro-diferential equations. Before discussing this generalization, we develop in the next section a stochastic interpretation for the HAM to evaluate $\Gamma[G]$ and use the obtained approximation for the four-point vertex function in the auxiliary problem without explicitly storing the high-dimensional objects.

The homotopy analysis method is a semi-analytic method developed to solve non-linear integral or differential equations. Ref. [104] and [105] gives detailed introductions to the method including the discussion of various applications in basic science, finance, fluid dynamics and engineering. Here, we only introduce the method briefly and apply it to the differential equation defining $\Gamma[G]$. The starting point is the construction of the homotopy

$$\mathcal{H}[\Phi[G,q]] = (1-q)\mathcal{L}\left[\Phi[G,q] - u_{\Gamma,0}[G]\right] + qc_0\mathcal{N}\left[\Phi[G,q]\right] = 0 \tag{5.59}$$

for the differential equation (5.56). We have defined the non-linear operator

$$\mathcal{N}\left[\Gamma[G]\right] = \Gamma - \lambda + \frac{3\lambda}{2}G^2\Gamma - \frac{\lambda}{2}G^4\Gamma^2 + \frac{\lambda}{3}G^3\Gamma' - \frac{\lambda}{6}G^5\Gamma'\Gamma \tag{5.60}$$

and an auxiliary operator $\mathcal{L}$. The auxiliary operator $\mathcal{L}$ is an arbitrary operator with the property $\mathcal{L}[0] = 0$ and will be specified later. The homotopy (5.59) includes the deformation parameter $q \in [0,1]$ which deforms the solution of $\mathcal{L}$ from $\Phi[G,0] = u_{\Gamma,0}[G]$ at $q=0$ to the solution of the differential equation (5.56), $\Phi[G,1] = \Gamma[G]$, at $q=1$. $u_{\Gamma,0}[G]$ is the initial guess for the solution of $\mathcal{N}\left[\Gamma[G]\right] = 0$. The HAM attempts to construct the solution of (5.59) through a power series expansion in q,

$$\Phi[G,q] = u_{\Gamma,0}[G] + \sum_{m=1} u_{\Gamma,m}[G]\, q^m. \tag{5.61}$$

The expansion coefficients are given by

$$u_{\Gamma,m}[G] = \frac{1}{m!}\Phi^{(m)}[G, q=0] \tag{5.62}$$

and can be obtained by the m-th derivative of (5.59). Therefore, the HAM yields a series solution of the differential equation (5.56) in terms of the deformation coefficients $u_{\Gamma,m}[G]$,

$$\Gamma[G] = u_{\Gamma,0}[G] + \lim_{M\to\infty}\sum_{m=1}^{M} u_{\Gamma,m}[G]. \tag{5.63}$$

In order to show the power and flexibility of the HAM we first discuss the solution of a truncated version of the vertex equation. We define the truncation

$$\mathcal{N}_{\text{truncI}}\left[\Gamma[G]\right] = \Gamma - \lambda + \frac{3\lambda}{2}G^2\Gamma - \frac{\lambda}{2}G^4\Gamma^2. \tag{5.64}$$

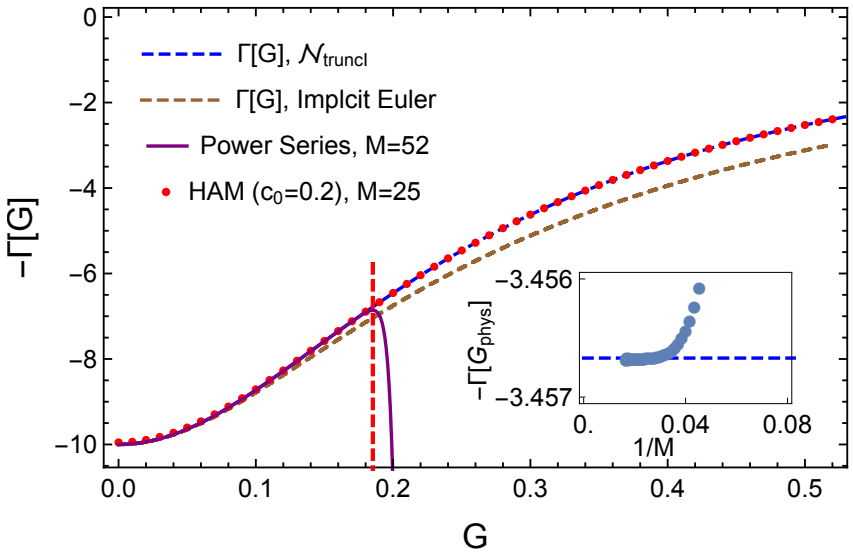

Figure 5.6.: The universal functional $\Gamma[G]$ obtained from the truncation $\mathcal{N}_{\text{truncI}}$, which neglects higher order n-point vertex corrections with $n > 4$, for $\lambda = 10$. The result of the truncation is compared with the exact solution of (5.56) obtained by the implicit Euler method. The analytic structure of the truncated functional $\Gamma[G]$ is such that the power series solution of $\mathcal{N}_{\text{truncI}}[\Gamma[G]] = 0$ has a finite convergence radius indicated by the vertical dashed line. The HAM series solution yields a convergent series solution beyond the convergence radius of the power series. The convergence of the HAM series solution at $G_{\text{phys}} = G[k = 1]$ is demonstrated in the inset as a function of the inverse of the maximal expansion order M.

The truncation completely neglects the derivatives and turns the problem from a differential equation to an algebraic equation. The above problem is a common approximation. It neglects the contributions coming from higher order n-point vertex functions with $n > 4$, cf. (5.13). It should be noted that this truncation is not completely equivalent to setting $\Gamma^{(6)} = 0$ in the infinite tower (5.13) as the multiplicity of the last term is different. For a realistic FT solving the truncated equation - which in this case is an integral equation for the rank-4D or rank-4$(D+1)$ object - without further truncation of the momentum or frequency dependence would already establish the state of the art for the self-consistent solution of the DSE. We will show later how to solve this formidable problem as a preliminary step before obtaining the full solution of the functional integro-differential equation.
The solution of $\mathcal{N}_{\text{truncI}}[\Gamma[G]] = 0$ which is regular at $G = 0$ is given by

$$\Gamma[G] = \frac{-1 - \frac{3\lambda}{2}G^2 + \sqrt{1 + 3\lambda G^2 + \frac{\lambda^2}{4}G^4}}{\lambda G^4} \tag{5.65}$$

and is shown for $\lambda = 10$ in Fig. 5.6. It has branch point singularities in the complex plane where the singularities closest to the origin are given by

$$G_{\text{s}} = \pm i\sqrt{\frac{6 - 4\sqrt{2}}{\lambda}}. \tag{5.66}$$

As already discussed these singularities determine the convergence radius of the power series solution in G, i.e.,

$$\Gamma[G] = \lim_{M\to\infty} \sum_{m=0}^{M} b_m G^m. \tag{5.67}$$

Fig. 5.6 indicates the convergence radius of the power series solution as the vertical dashed line. The power series solution indeed converges up to that point and starts to diverge afterwards. The divergence is regularized due to the finite amount of coefficients b_m used to approximate the functional.
The HAM provides a more powerful series solution technique. The simplest possible operator $\mathcal{L}\left[\Phi[G,q] - u_{\Gamma,0}[G]\right] = \Phi[G,q]$ already yields interesting results. We have set $u_{\Gamma,0}[G] = 0$. For that operator the m-th order deformation in the HAM series solution is given by the recursion relation

$$u_{\Gamma,m} = (1-\delta_{m,1})u_{\Gamma,m-1} - c_0\left[u_{\Gamma,m-1} - \lambda\delta_{m,1} + \frac{3\lambda}{2}G^2 u_{\Gamma,m-1} - \frac{\lambda}{2}G^4 \sum_{k=0}^{m-1} u_{\Gamma,m-1-k}u_{\Gamma,k}\right]. \tag{5.68}$$

Fig. 5.6 shows that the series of deformations continuous the power series solution beyond the convergence radius.

Understanding the convergence of the HAM series solution in general, i.e., deriving definite theorems about convergence properties is a complicated task and not fully understood. In the general setup, these properties have to be deduced either from the homotopy itself or equivalently from the recursion relation of the deformation coefficients. While the former amounts to a research direction similar to the study of the analytic properties of the path integral in the coupling constant, cf. the discussion in Ref. [96, 97] and Ch. 4, the latter is similar to the study of the large order behaviour of perturbation theory. Due to the theorems of complex analysis there is a direct equivalence between these two approaches.
Nevertheless, the homotopy approach is fundamentally different from the perturbation theory approach, i.e., different from calculating a power series in a formal coupling constant parameter. In order to illustrate this we take a shortcut and discuss the convergence of the HAM series for our particular analytically solvable truncation.
As a first step we consider an even simpler problem obtained by truncating (5.64) further. We introduce $x = \lambda G^2$, $y(x) = \Gamma[G]/\lambda$ and study the problem

$$\mathcal{N}_{\text{truncII}}\left[y(x)\right] = y(x) - 1 + \frac{3}{2}xy(x) \tag{5.69}$$

which is obtained by neglecting the non-linear term in (5.64). The solution of

$$\mathcal{N}_{\text{truncII}}\left[y(x)\right] = 0 \tag{5.70}$$

is given by

$$y(x) = \frac{1}{1+\frac{3}{2}x} \tag{5.71}$$

and has a single singular point at

$$x_s^{\text{II}} = -\frac{2}{3}. \tag{5.72}$$

Therefore, the convergence radius of the power series solution around $x = 0$ is given by $R = |x_s^{\text{II}}|$. We are interested to study the convergence properties of the HAM series solution with respect to the homotopy

$$\mathcal{H}_{\text{truncII}}[g(x,q)] = (1-q)g(x,q) + c_0 q\mathcal{N}_{\text{truncII}}\left[g(x,q)\right] = 0. \tag{5.73}$$

Due to its simplicity the homotopy can be solved in closed form

$$g(x,q) = \frac{qc_0}{1-q+qc_0+\frac{3}{2}qc_0x} \tag{5.74}$$

and, as expected,

$$y(x) = g(x,1). \tag{5.75}$$

The convergence properties of the HAM series solution can be determined by the analytic properties of the function $g(x,q)$. We are interested in the convergence of the power series

$$g(x,q) = \sum_m u_m(x)q^m \tag{5.76}$$

at $q=1$. Its convergence radius may depend on x and the convergence control parameter c_0. If $g(x,q)$ has no singularity inside the unit disc $|q| \leq 1$, $q \in \mathbb{C}$, we know that the HAM series solution for $y(x)$ converges. In the above simple case the singularity of $g(x,q)$ is determined by

$$1-q+qc_0+\frac{3}{2}qc_0x = 0 \rightarrow q_c(x,c_0) = \frac{2}{2-2c_0-3xc_0} \tag{5.77}$$

which leads to the convergence condition of the HAM series solution

$$|q_c(x,c_0)| > 1. \tag{5.78}$$

Therefore, the HAM series solution for $x \in \mathbb{R}$ converges in the open interval $x \in]-2/3, 2(2-c_0)/3c_0[$. Thus, for the case $c_0 = 1$ the HAM series solution convergence inside the convergence radius of the power series of $y(x)$ and constructing the homotopy brings no advantages. But for $c_0 \rightarrow 0$ the convergence region of the HAM series solution has been enlarged to $x \in]-2/3, \infty[$. As expected, it is possible to understand the convergence of the HAM series solution from the knowledge of the solution of the homotopy, $g(x,q)$, in $q \in \mathbb{C}$ with $|q| \leq 1$. Unfortunately, as we have already argued, this is of little practical use as in all interesting cases we construct the homotopy exactly because $\mathcal{N}[y] = 0$ can not be solved analytically and consequently the solution of the even harder problem $\mathcal{H}[g] = 0$ can not be obtained in closed form.
For a class of operators $\mathcal{L}$ a more practical argument was put forward [106, 107, 108] which uses only the information about the actual form of the recursion relation for the m-th order deformation coefficients to understand the convergence properties. On the basis of our particular example we show that this argument can not be used in general. The argument links the convergence of the HAM series solution to the convergence of the power series solution of $y(x)$. In case the operator $\mathcal{L}$ is picked in such a way that the deformation coefficients are in simple powers of the unknown variable the HAM series solution corresponds to a rearrangement of a power series solution centered around some c_0 dependent point. We will show in a first step that this is indeed the case for the truncation $\mathcal{N}_{\text{truncII}}$. In a second step we analyse this proposition in a more abstract form and show that, in general, it relies on mathematically ill-defined operations which casts doubt on the correctness of the proposition. For the example of the previously introduced truncation, $\mathcal{N}_{\text{truncI}}$, we show explicitly that even though the deformation coefficients are given in simple powers of the unknown x the convergence properties can not be understood from the analytic properties of $y(x)$ and therefore the proposition does not hold in general.
We consider again the homotopy $\mathcal{H}_{\text{truncII}}$ constructed for the truncation $\mathcal{N}_{\text{truncII}}$. The HAM series solution is given by the deformation coefficients satisfying the recursion relation

$$u_{\Gamma,m} = (1-\delta_{m,1})u_{\Gamma,m-1} - c_0\left[u_{\Gamma,m-1} - \delta_{m,1} + \frac{3}{2}xu_{\Gamma,m-1}\right]. \tag{5.79}$$

Therefore, the m-th order deformation is in simple powers of the unknown x. As we have seen the convergence of the HAM series is guaranteed inside the interval $x \in]-2/3, 2/3(2-c_0)/c_0[$. If the HAM series is just a rearrangement of the power series of $y(x)$ centered around some c_0 dependent point this point has to be the center of the convergence interval. In this case the convergence interval of the HAM series is in correspondence to the convergence radius of the power series of $y(x)$ centered around $\tilde{x}(c_0)$, $|x - \tilde{x}(c_0)| < R$. We find

$$\tilde{x}(c_0) = \frac{2}{3}\frac{1-c_0}{c_0}. \tag{5.80}$$

As we know $y(x)$ and $g(x,q)$ in closed form we can check this statement easily by comparing the power series expansion of $y(x)$ around $\tilde{x}(c_0)$ with the power series expansion of $g(x,q)$ in q evaluated at $q=1$,

$$\begin{aligned} g(x,q=1) &= c_0 \sum_m (-1)^m \left(c_0 - 1 + \frac{3}{2}c_0 x\right)^m = c_0 \sum_m (-1)^m (\frac{3}{2}c_0)^m (x - \tilde{x}(c_0))^m \\ y(x) &= \frac{1}{1+\frac{3}{2}x} = \frac{1}{1+\frac{3}{2}\tilde{x}(c_0) - \frac{3}{2}\tilde{x}(c_0) + \frac{3}{2}x} = c_0 \sum_m (-1)^m (\frac{3}{2}c_0)^m (x - \tilde{x}(c_0))^m. \end{aligned} \tag{5.81}$$

We have shown that the HAM series solution in this case is indeed a rearrangement of the power series solution of $y(x)$ centered around $\tilde{x}(c_0)$.
We discuss this proposition in more general terms. We assume that the deformation coefficients u_m (neglecting the subscript Γ for the moment) are given in simple powers of the unknown x, i.e.,

$$u_m(x) = \sum_{k=0}^{h(m)} u_{m,k} x^k \tag{5.82}$$

The maximal power of x for the m-th deformation is given by the function $h(m)$ which we assume to be monotonically increasing such that h^{-1} exists. With this we can write the HAM series solution as a formal power series in x,

$$g(x,1) = \lim_{M\to\infty} \sum_{m=0}^{M} \left[\sum_{k=0}^{h(m)} u_{m,k} x^k\right] = \lim_{M\to\infty} \sum_{k=0}^{M} \left[\sum_{m=h^{-1}(k)}^{M} u_{m,k}\right] x^k. \tag{5.83}$$

The interchange of the summation order may only hold formally and therefore has to be done with care if definite statements should be made. The power series of $y(x)$ around $\tilde{x}$ can be formally written as

$$\begin{aligned} y(x) &= \lim_{M\to\infty} \sum_{m=0}^{M} y_m(\tilde{x})\,(x-\tilde{x})^m = \lim_{M\to\infty} \sum_{m=0}^{M} y_m(\tilde{x}) \sum_{k=0}^{m} \binom{m}{k} x^k (-\tilde{x})^{m-k} \\ &= \lim_{M\to\infty} \sum_{k=0}^{M} \left[\sum_{m=k}^{M} \binom{m}{k} y_m(\tilde{x}) (-\tilde{x})^{m-k}\right] x^k \end{aligned} \tag{5.84}$$

where we have denoted $y_m(\tilde{x}) = \frac{1}{m!}\frac{\mathrm{d}^m y}{\mathrm{d}x^m}(\tilde{x})$. The last equality has been obtained by exchanging the summation orders. Therefore, we formally find

$$\lim_{M\to\infty} \sum_{k=0}^{M} \left[\sum_{m=k}^{M} \binom{m}{k} y_m(\tilde{x})(-\tilde{x})^{m-k}\right] x^k = y(x) = g(x,1) = \lim_{M\to\infty} \sum_{k=0}^{M} \left[\sum_{m=h^{-1}(k)}^{M} u_{m,k}\right] x^k. \tag{5.85}$$

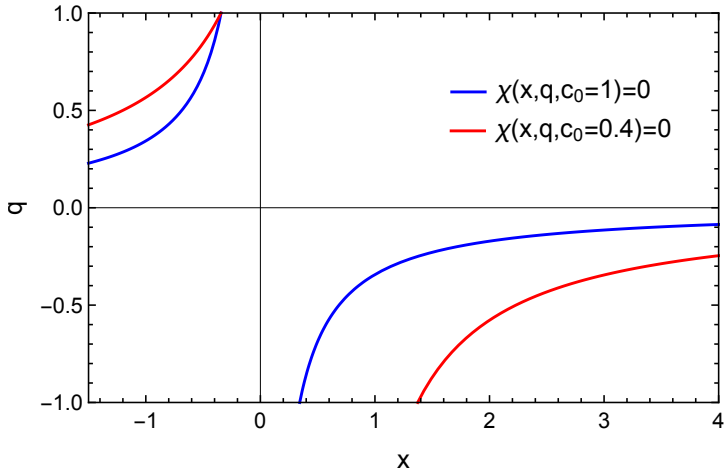

Figure 5.7.: The singularities of the solution to the homotopy $\mathcal{N}_{\text{truncI}}$, $g(x,q)$, which determine the convergence radius of a power series in x or q around $x=0$ or $q=0$, respectively. The position of the singularities, determined by the condition $\chi(x,q,c_0)=0$, depend in general on the auxiliary parameter c_0. The singularity at $\chi(x,1,c_0)=0$ is fixed and does not depend on c_0 by the construction of the homotopy.

Using the uniqueness theorem of the power series representation it is often argued that there is a direct relation between $y_m(\tilde{x})$ and $u_{m,k}$ and therefore the HAM series solution is just a reordering of the power series of $y(x)$. In contrast, from the above equation, assuming that the exchange of summation order holds, together with the uniqueness of the power series representation a much weak statement follows,

$$\lim_{M\to\infty}\sum_{m=k}^{M}\binom{m}{k}y_m(\tilde{x})(-\tilde{x})^{m-k}=\lim_{M\to\infty}\sum_{m=h^{-1}(k)}^{M}u_{m,k}=y_k(0)=\frac{1}{k!}\frac{\mathrm{d}^k y}{\mathrm{d}x^k}(0). \tag{5.86}$$

The first equality is due to the above equation and the second equality due to the uniqueness theorem. Assuming that the summation orders can not be exchanged not even this formal statement is guaranteed to hold.
For the truncation $\mathcal{N}_{\text{truncII}}$ we have found that the HAM series solution is indeed corresponding to the power series expansion of $y(x)$ centered around a c_0 dependent point. This result can be compared to the above general discussion. From (5.81) we see that the identification of the HAM series solution with the power series centered around $\tilde{x}(c_0)$ is obtained before the dangerous exchange of summation limits has to be performed. Thus, this example is just a simplification of the general case.
For the more complicated truncation $\mathcal{N}_{\text{truncI}}$ we have explicitly shown numerically in Fig. 5.6 that the HAM series solution has a larger convergence interval compared to the convergence radius of the power series solution around $x=\lambda G^2=0$. We will show that this is an example where the HAM series solution can be understood as a power series of $y(x)$ centered around a c_0 dependent point even tough the m-th order deformation is given in powers of the unknown x.
In terms of the variables $x=\lambda G^2$ and $y(x)=\Gamma[G]/\lambda$ the truncation (5.64) is given by

$$\mathcal{N}_{\text{truncI}}\left[y(x)\right]=y(x)-1+\frac{3}{2}xy(x)-\frac{1}{2}x^2y(x)^2 \tag{5.87}$$

and the solution of $\mathcal{N}_{\text{truncI}}[y(x)] = 0$ which is regular at $x = 0$ is

$$y(x) = \frac{1 + \frac{3}{2}x - \sqrt{1 + 3x + \frac{1}{4}x^2}}{x^2}. \tag{5.88}$$

The closest singularity to the origin is at $x_s^{\text{I}} = 2(2\sqrt{2} - 3)$. The corresponding homotopy

$$\mathcal{H}_{\text{truncI}}[g(x,q)] = (1-q)g(x,q) + c_0 q \mathcal{N}_{\text{truncI}}[g(x,q)] = 0 \tag{5.89}$$

can be also solved in closed form,

$$g(x,q) = \frac{1 - q + qc_0 + \frac{3}{2}qxc_0 - \sqrt{(q - 1 - qc_0 - \frac{3}{2}qxc_0)^2 - 2q^2x^2c_0^2}}{qc_0x^2}. \tag{5.90}$$

The HAM series converges if $g(x,q)$ has no singularities inside the unit disc. For $g(x,q)$ the singularities are determined by

$$\chi(q,x,c_0) = (q - 1 - qc_0 - \frac{3}{2}qxc_0)^2 - 2q^2x^2c_0^2 = 0. \tag{5.91}$$

Fig. 5.7 shows the position of the closest singularities to the origin depending on c_0 in the (q,x) plane. The relevant singularities $q_s(x,c_0)$ as a function of x are given by

$$q_s(x,c_0) = \frac{2(2 - 2c_0 - (3 - 2\sqrt{2})xc_0)}{4 - 8c_0 + 4c_0^2 - 12xc_0 + 12xc_0^2 + x^2c_0^2}. \tag{5.92}$$

Consequently, we find that $g(x,q)$ has no singularities in $|q| \leq 1$ for $x \in]x_s^{\text{I}}, x_{\max}[$ where

$$x_{\max} = \frac{2(6 - 4\sqrt{2} - 3c_0 + 2\sqrt{2}c_0)}{c_0}. \tag{5.93}$$

Thus, the HAM series solution converges in the above interval which for $c_0 \to 0$ extends to $x_{\max} \to \infty$.

In contrast to the simpler truncation $\mathcal{N}_{\text{truncII}}$ it can be checked numerically that the HAM series solution for $c_0 < 1$ does not correspond to the power series expansion around the midpoint of the convergence interval although the deformations u_m are given in simple powers of the unknown x. In the following we show that, for $c_0 < 1$, no expansion point exists such that the HAM series solution of the homotopy $\mathcal{H}_{\text{truncI}}$ can not be understood in terms of a power series solution of $y(x)$ around that point. For $c_0 = 1$ the HAM series solution is equivalent to the power series expansion of $y(x)$ around $x = 0$.

First we show that there is no $\tilde{x}$ such that $u_{m+1}(x) = y_m(\tilde{x})(x - \tilde{x})^m$ for all $m \geq 0$. We have to consider $u_{m+1}(x)$ because the maximal power in the unknown x is in this case m, i.e., $h(m) = m - 1$. Therefore, as we already discussed previously, in order to identify the power series solution centered around some c_0 dependent point with the HAM series solution we have to interchange the order of summation. In a second step we show that it is not allowed to interchange the summation orders and consequently the HAM series solution is not equivalent to the power series solution of $y(x)$ around a c_0 dependent point.

From the recursion relation of $u_m(x)$ the first non-vanishing deformation coefficients are

$$g(x,q) = u_1(x)q + u_2(x)q^2 + \mathcal{O}(q^3) = c_0 + (c_0 - c_0^2 - \frac{3}{2}xc_0^2)q^2 + \mathcal{O}(q^3). \tag{5.94}$$

However, there is no $\tilde{x}$ such that

$$\begin{aligned} c_0 &= y(\tilde{x}), \\ c_0 - c_0^2 - \frac{3}{2} x c_0^2 &= y_1(\tilde{x})(x - \tilde{x}) \end{aligned} \tag{5.95}$$

simultaneously holds for $c_0 < 1$.
Now we show that

$$\lim_{M\to\infty} \sum_{m=0}^{M} \left[\sum_{k=0}^{h(m)} u_{m,k} x^k \right] \neq \lim_{M\to\infty} \sum_{k=0}^{M} \left[\sum_{m=h^{-1}(k)}^{M} u_{m,k} \right] x^k. \tag{5.96}$$

This follows from the simple observation that $g(x,q)$ can be formally written as

$$g(x,q) = \sum_m u_m(x) q^m \tag{5.97}$$

$$g(x,q) = \sum_m v_m(q) x^m. \tag{5.98}$$

Whereas, as we have shown, for every $x > |x_s^{\mathrm{I}}|$ there exists a c_0 such that the power series in (5.97) converges at $q = 1$ the power series in (5.98) diverges for $x > |x_s^{\mathrm{I}}|$ at $q = 1$. This can be simply seen from

$$\lim_{q\to 1} \sum_m v_m(q) x^m = \sum_m v_m(1) x^m = \sum_m y_m x^m. \tag{5.99}$$

The interchange of the limit and the sum in the first equality is allowed due to the uniform convergence theorem in combination with the continuity of $v_m(q)$ and the last equality follows from $y(x) = g(x,1)$ and the uniqueness of the power series representation of $y(x)$. Alternatively, we can observe this order of limits from the location of the singularities in the (q,x) plane shown in Fig. 5.7. The singularity at $\chi(x, q = 1, c_0) = 0$ does not move by tuning c_0 because, by construction of the homotopy, $y(x) = g(x,1)$ for every c_0. Expanding $g(x,q)$ in a power series in q we have to ask for which x the singularities lie outside of $|q| < 1$. We see that only the lower limit of the convergence interval in x is determined by the fixed singularity. Expanding $g(x,q)$ in a power series in x we have to consider the (x,q) plane and ask what is the maximal $|x|$, $|x_m|$, such that there is no singularity inside $|x| < |x_m|$ if $g(x,q)$ is evaluated at $q = 1$. In this case the convergence interval in x is always determined by the fixed singularity.

From both considerations we see that it is not allowed to interchange the summation orders and therefore the HAM series solution can not be interpreted as a simple power series of $y(x)$ around a c_0 dependent point.

Although from discussing the truncations $\mathcal{N}_{\mathrm{truncI,II}}$, we have not found a general statement about the convergence properties of the HAM series solution we have established that, in general, there is no simple connection between the analytic structure of $y(x)$ and the convergence properties of the HAM series solution. Even if the deformation coefficients are given in simple powers of the unknown x, there is no direct relation to the power series expansion of $y(x)$. Consequently, without definite convergence theorems, it is necessary to assess the properties of the HAM series for each construction of the homotopy under consideration separately.

In the following we study the semi-analytic solution of the full problem (5.56). Unfortunately, the analytic structure of the full functional $\Gamma[G]$ is more complicated than for the truncated versions studied previously. The power series expansion (5.67) has zero convergence radius [109, 110]: Bringing (5.56) into the form of $\Gamma'[G] = F[G, \Gamma[G]]$ we find that F is not holomorphic at $G = 0$, $\Gamma = \lambda$ and therefore belongs to the set of potential fixed singularities of the solution to the

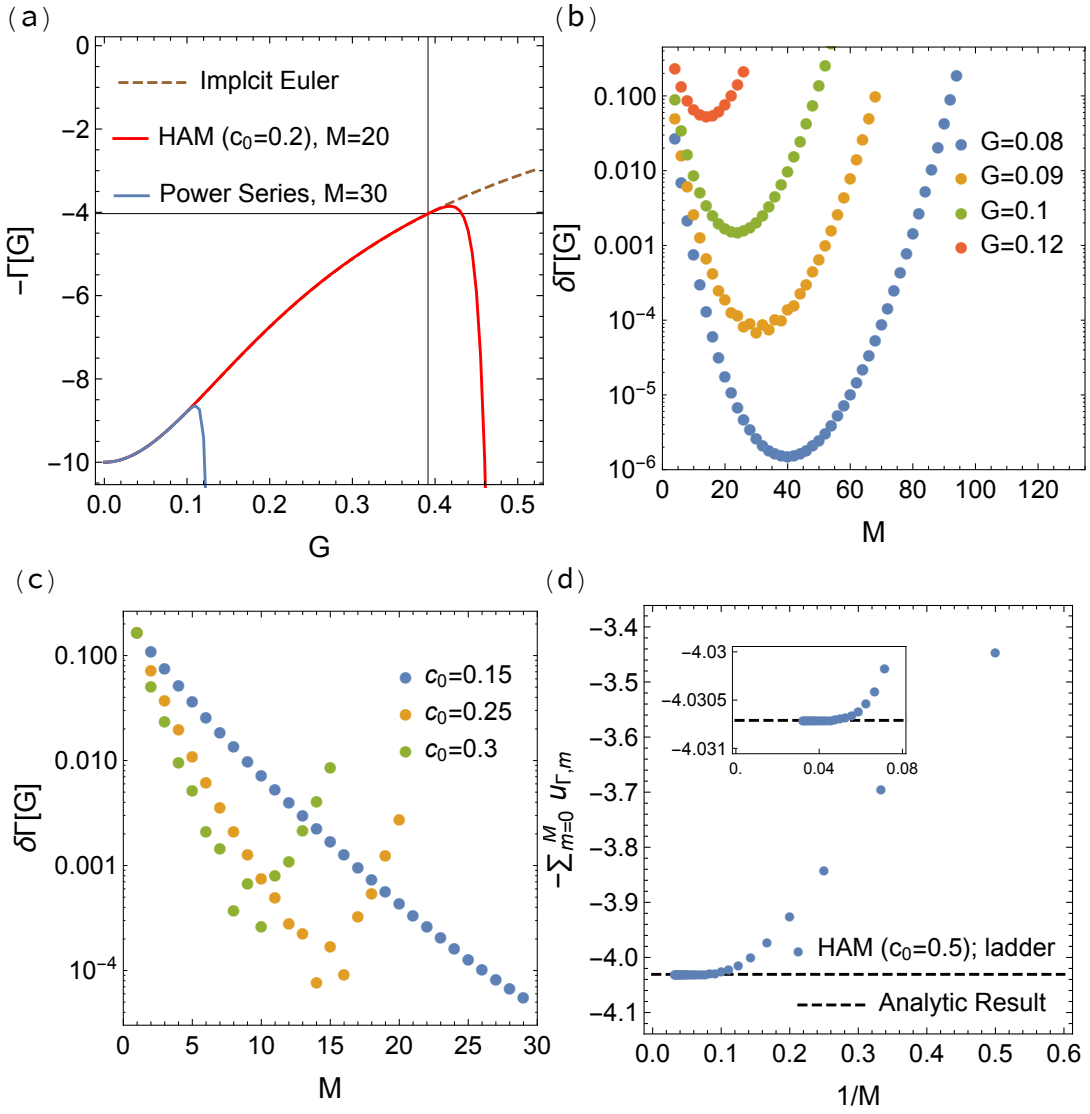

Figure 5.8.: (a) $\Gamma[G]$ at coupling $\lambda = 10$ obtained by the implicit Euler algorithm, a power series (asymptotic), and the HAM (asymptotic). The thin grid lines show the evaluation for the physical G, Γ for $k = 1$. (b) The relative error $\delta\Gamma[G]$ of a power series solution at small G shows the behaviour of an asymptotic series in the maximal expansion order M. (c) The relative error $\delta\Gamma[G]$ of the HAM series solution constructed with the operator $\mathcal{L} = \mathrm{id}$ for $G = 0.3$ shows the behaviour of an asymptotic series in the deformation order M controlled by the convergence control parameter c_0. (d) The convergence of the HAM series of deformations, $\sum_{m=0}^{M} u_{\Gamma,m}[G]$ with respect to a linear operator $\mathcal{L}_{\text{ladder}}[\Gamma[G]] = \Gamma[G] - \lambda + \frac{3\lambda}{2} G^2 \Gamma[G]$, the ladder approximation to the vertex equation (5.56). The functional $\Gamma[G]$ is evaluated at the physical G for $k = 1$. The inset shows the convergence of the main plot on a much finer scale.

differential equation. We discuss the analytic structure of $\Gamma[G]$ in the complex G plane in more detail in App. C. This result can be easily anticipated from the fact that the expansion around $G = 0$ corresponds to approaching the non-interacting limit by fixing λ and taking $k \to \infty$, i.e.,

$$Gk = \frac{1}{Z}\int \mathrm{d}\phi\ \phi^2\, e^{-\frac{1}{2}\phi^2 - \frac{\lambda}{4!k^2}\phi^4} \overset{k\to\infty}{=} 1. \tag{5.100}$$

We have shown in the previous chapter that the expansion around the non-interacting limit is an asymptotic series. Fig. 5.8(a) shows that the power series solution gives a good approximation for small values of G before it starts to diverge. In contrast to the truncated functional the convergence radius is indeed zero and the power series is an asymptotic expansion, i.e., for every small G there exists an optimal truncation order M such that the truncated power series asymptotically approaches the exact answer with exponential accuracy. This is shown in Fig. 5.8(b) where we plot the truncation error $\delta\Gamma[G] = \left|\sum_{m=0}^{M} b_m G^m - \Gamma[G]\right| / \Gamma[G]$ over the maximal expansion order M for various values of G on a semi-log scale.
We now use the HAM to solve the differential equation. At a first step the auxiliary operator $\mathcal{L}\left[\Phi[G,q] - u_{\Gamma,0}[G]\right] = \Phi[G,q] - u_{\Gamma,0}[G]$ is used, i.e., $\mathcal{L} = \mathrm{id}$. In this case the m-th order deformation can be computed from the following recursion relation,

$$\begin{aligned} u_{\Gamma,m} \;=\; & (1-\delta_{m,1})u_{\Gamma,m-1} - c_0\,[u_{\Gamma,m-1} - \lambda\delta_{m,1} \\ & + \frac{3\lambda}{2}G^2 u_{\Gamma,m-1} - \frac{\lambda}{2}G^4 \sum_{k=0}^{m-1} u_{\Gamma,k}u_{\Gamma,m-1-k} \\ & + \frac{\lambda}{3}G^3\frac{\mathrm{d}u_{\Gamma,m-1}}{\mathrm{d}G} - \frac{\lambda}{6}G^5 \sum_{k=0}^{m-1}\frac{\mathrm{d}u_{\Gamma,k}}{\mathrm{d}G}u_{\Gamma,m-1-k}], \end{aligned} \tag{5.101}$$

resulting in a HAM series solution in which the m-th order deformation is given in simple powers of G and additionally depend on the auxiliary parameter c_0.
Picking the identity operator, $\mathcal{L} = \mathrm{id}$, is a too simplistic choice and does not lead to a convergent HAM series solution. Nevertheless, the homotopy introduces additional degrees of freedom such that it overcomes the limitations of the standard power series approach. Fig. 5.8(a) shows the resulting HAM series solution. It approximates the functional well up to some point where it starts to diverge. We see that whereas it is not possible to construct $\Gamma[G]$ as a power series at values of G corresponding to the considered model parameters $k = 1$, $\lambda = 10$ it is possible to obtain controlled results from the HAM series solution. However, as expected, this is not due to a finite convergence interval for the HAM series solution but it is due to the control of the expansion introduced by the auxiliary parameter c_0. The HAM convergence parameter c_0 gives us additional freedom since the effective parameter $c_0 G$ can always be made small as long as G remains finite. As is illustrated in Figs. 5.8(a) and (c), the asymptotic nature can then be postponed to larger expansion orders for smaller c_0 but with larger deviations from the exact result at low expansion orders. In the following sections this approach will be generalized to realistic field theories in which case $c_0||G||$ can be chosen to be small where $||G||$ denotes the L^p-norm of the two-point correlation function. We will show numerically that this holds for a generic FT and that it is possible to get accurate results even close to a 2nd order phase-transition at which $||G||$ gets unbounded.

Before extending this approach to a realistic FT we like to emphasise the great potential and novelty of the Dyson-Schwinger and homotopy approach to FT. Instead of constructing the HAM series expansion around the non-interacting limit, $G = 0$, we can use the linear operator $\mathcal{L} = \mathcal{L}_{\text{ladder}}$ to construct a homotopy with respect to the analytically solvable ladder approximation, $\mathcal{L}_{\text{ladder}}[\Gamma[G]] = \Gamma[G] - \lambda + \frac{3\lambda}{2}G^2\Gamma[G]$. In a FT the term $\frac{3\lambda}{2}G^2\Gamma[G]$ sums up all

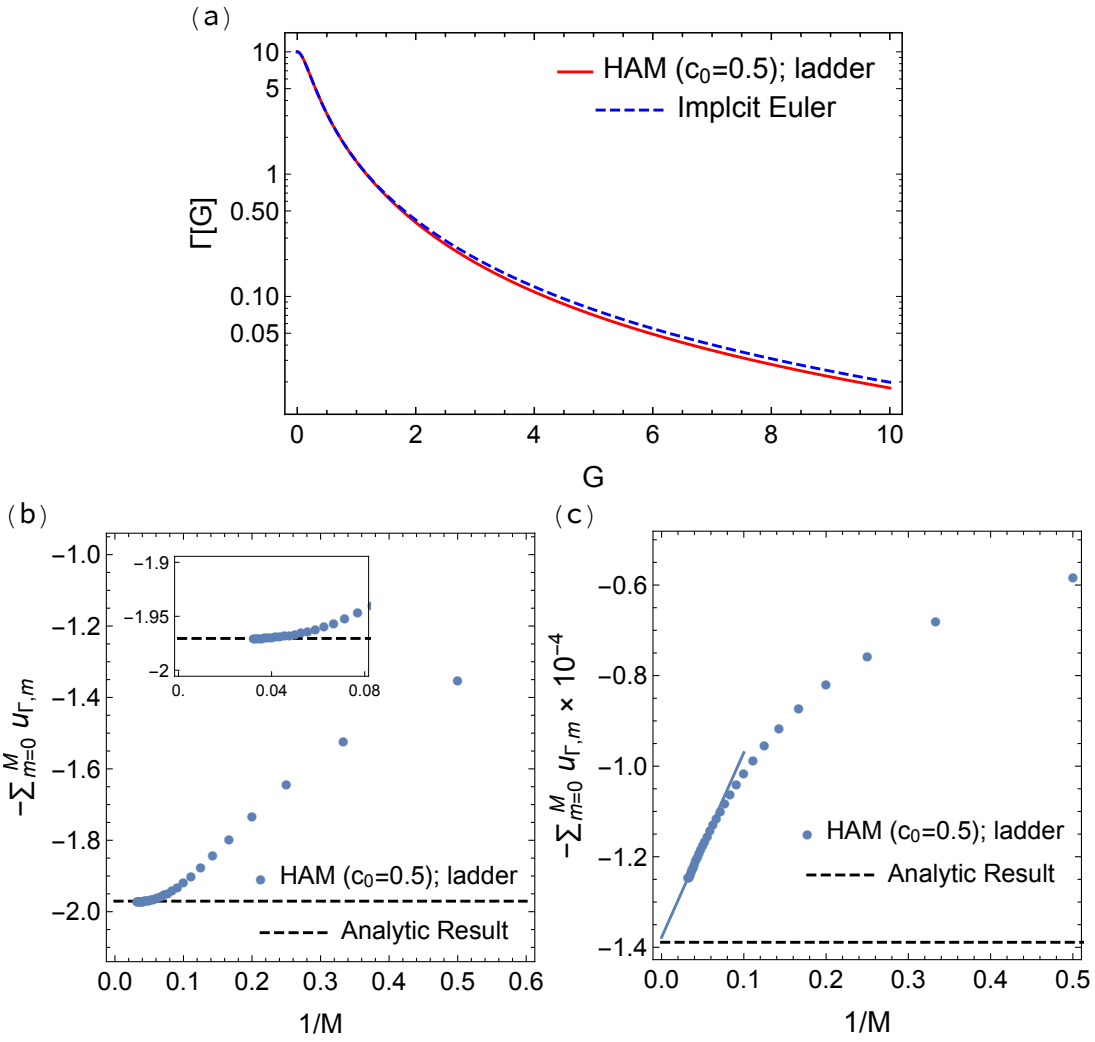

Figure 5.9.: a) The approximation to the HAM series solution $\Gamma[G] = \lim_{m\to\infty} \sum_m^M u_{\Gamma,m}$ with $M = 30$ on a semi-log scale. The HAM series converges globally, i.e., it is not limited to a finite, c_0-dependent convergence interval. Therefore, convergence can be achieved for large values of G corresponding to $G[k]$, $k < 0$. The truncation of the series solution at $M = 30$ already gives decent results for large G without extrapolating the series solution. The convergence of the HAM series solution is explicitly demonstrated in (b) and (c). Without tuning the convergence control parameter c_0, convergence can be observed both for small ((b) $G[k = -1] \approx 0.73$) and large ((c) $G[k = -100] \approx 12$) G.

RPA-ladder diagrams. The resulting homotopy can be written as,

$$\begin{aligned}\Gamma_q[G] &= \lambda - \frac{3\lambda}{2}G^2\Gamma_q + \frac{\tilde{\lambda}(q,c_0)}{2}G^4\Gamma_q^2 \\ &\quad -\frac{\tilde{\lambda}(q,c_0)}{3}G^3\Gamma_q' + \frac{\tilde{\lambda}(q,c_0)}{6}G^5\Gamma_q'\Gamma_q \\ \text{where} \qquad &\tilde{\lambda}(q,c_0) = \frac{c_0 q}{1-q+c_0 q}\lambda.\end{aligned} \tag{5.102}$$

This should be compared to the closed DSE (5.56). Taking into account the equivalence between the functional integral and the functional integro-differential approach, an important question is if (5.102) can be related back to an auxiliary action such as $S(q) = S_0(q) + qS_{\text{int}}$ which has been considered in variational perturbation theory approaches [111, 112, 113, 114] or shifted action approaches [115]. $S_0(q)$ is some quadratic auxiliary action and S_{int} is the interaction part such that $S(q=1) = S$ with S the physical action of the theory under consideration. A general feature of DSEs is that each term on the right hand side of (5.56) contributes exactly with one factor of the bare coupling constant. In contrary, for the homotopy (5.102), there are terms contributing with a modified bare coupling constant $\tilde{\lambda}$ and therefore (5.102) can not be associated with the closed DSE of an auxiliary action.
In conclusion we see that the HAM series solution is effectively an expansion with respect to the truncated interacting ladder model which has no correspondence in a functional integral representation and can only be written down in the equations of motion approach. Fig. 5.8(d) shows that the HAM series with respect to the ladder approximation yields a convergent HAM series solution. Moreover, as demonstrated in Fig. 5.9(a), the HAM series solution is globally convergent, i.e., it is not restricted by a finite, c_0-dependent convergence interval. Therefore, we also find a convergent solution for values of G which correspond to $G[k]$ with $k < 0$, cf. Figs. 5.9(b) and (c). In this parameter regime the action (5.1) has degenerate minima and the standard perturbative series for the vertex function is not Boreal summable [116].

5.4. Homotopy analysis method for integral equations in high dimensions

In the last section we showed how to compute the 2-point correlation function and the 4-point vertex function for the 0D toy model. The closed DSE for the vertex function was solved using the HAM and the solution of the coupled system of DSEs was obtained by fixed point iteration. There are two open problems we still have to solve in order to generalize the introduced approach to a realistic field theory.
We have seen that the HAM gives us a series solution in terms of the deformations $u_{\Gamma,m}[G]$, which are calculated from a recursion relation. In order to apply the recursion relation we have to take the derivative - a functional derivative for a realistic field theory - of lower order deformations with respect to G. Therefore, we have to show how these functional derivatives can be implemented in an actual computation. Moreover, as we have already mentioned, the four-point vertex function is itself a high dimensional tensor, which without truncation, e.g., of the momentum dependence, can not be stored and manipulated on present days computers.
The aim of this section is to work out a diagrammatic language and with that a closely connected stochastic interpretation of the HAM in order to solve this storage problem. In the following section we will see that the developed diagrammatic language will also allow for a natural interpretation of the functional derivatives.

In this section we neglect the functional derivatives for a moment and go back to the truncation $\mathcal{N}_{\text{truncI}}$ in (5.64) and repeated here for convenience,

$$\mathcal{N}_{\text{truncI}}\left[\Gamma[G]\right] = \Gamma - \lambda + \frac{3\lambda}{2}G^2\Gamma - \frac{\lambda}{2}G^4\Gamma^2. \tag{5.103}$$

We already discussed in detail how to solve $\mathcal{N}_{\text{truncI}}[\Gamma] = 0$ using the HAM. The recursion relation for the deformations $u_{\Gamma,m}$ is given for $m > 1$ by

$$u_{\Gamma,m} = (1-c_0)u_{\Gamma,m-1} - \frac{3c_0\lambda}{2}G^2 u_{\Gamma,m-1} + \frac{c_0\lambda}{2}G^4\sum_{k=0}^{m-1} u_{\Gamma,m-1-k}u_{\Gamma,k}. \tag{5.104}$$

The numerical implementation of this recursion relation is trivial in the 0D case as $u_{\Gamma,m}$ for a fixed G is just a number and consequently only M numbers have to be stored in order to calculate the HAM series expansion to order M at a given G. For a realistic field theory the four-point vertex function and consequently also the deformations depend on four external indices where each index separately is a D-dimensional vector, e.g., a continuous momentum variable in the first Brillouin zone. Calculating and storing just the first deformation without truncation, e.g., of the momentum dependence, is for $D > 1$ already an impossible task.
An easy solution circumventing the storage and manipulation at intermediate steps is to use the recursion relation (5.104) again on its right hand side to formally eliminate the dependence on the deformation of order $m-1$,

$$\begin{aligned}
u_{\Gamma,m} &= (1-c_0)u_{\Gamma,m-1} - \frac{3c_0\lambda}{2}G^2 u_{\Gamma,m-1} + \frac{c_0\lambda}{2}G^4\sum_{k=0}^{m-1} u_{\Gamma,m-1-k}u_{\Gamma,k} \\
&= (1-c_0)\left[(1-c_0)u_{\Gamma,m-2} - \frac{3c_0\lambda}{2}G^2 u_{\Gamma,m-2} + \frac{c_0\lambda}{2}G^4\sum_{k=0}^{m-2} u_{\Gamma,m-2-k}u_{\Gamma,k}\right] \\
&\quad - \frac{3c_0\lambda}{2}G^2\left[(1-c_0)u_{\Gamma,m-2} - \frac{3c_0\lambda}{2}G^2 u_{\Gamma,m-2} + \frac{c_0\lambda}{2}G^4\sum_{k=0}^{m-2} u_{\Gamma,m-2-k}u_{\Gamma,k}\right] \\
&\quad + \frac{c_0\lambda}{2}G^4\sum_{k=0}^{m-1}\left[(1-c_0)u_{\Gamma,m-2-k} - \frac{3c_0\lambda}{2}G^2 u_{\Gamma,m-2-k} + \frac{c_0\lambda}{2}G^4\sum_{k'=0}^{m-2-k} u_{\Gamma,m-2-k-k'}u_{\Gamma,k'}\right] \\
&\qquad\qquad \times\left[(1-c_0)u_{\Gamma,k-1} - \frac{3c_0\lambda}{2}G^2 u_{\Gamma,k-1} + \frac{c_0\lambda}{2}G^4\sum_{k''=0}^{k-1} u_{\Gamma,k-1-k''}u_{\Gamma,k''}\right] \\
&= \cdots = F^{\text{tree}}(u_{\Gamma,0}).
\end{aligned} \tag{5.105}$$

This procedure is repeated recursively until all dependence on all lower order deformations is eliminated. The result is a complicated expression, the tree expansion F^{tree}. Therefore, we have replaced the problem of explicitly storing and manipulating the deformations with the problem of calculating F^{tree}, which requires keeping track and summing all the terms generated in the tree expansion to all orders in the recursion. The diagrammatic language developed in this section is the bookkeeping tool which makes it possible to generate and sum all the terms in F^{tree}.
For a realistic field theory the truncation $\mathcal{N}_{\text{truncI}} = 0$ is a non-linear integral equation in 4D or 4(D+1) dimensions. Before jumping to this complicated problem we develop the diagrammatic language of rooted trees for a much simpler non-linear integral equation and only in a consecutive section use the introduced tools for the truncation $\mathcal{N}_{\text{truncI}}$.

In the following we consider a non-linear integral equation in the form

$$f(x) = c(x) + \int_a^b \mathrm{d}t\; K(x,t)\; n(f(t))\,, \tag{5.106}$$

with given functions c, n and the kernel of the integration K. Furthermore, for the purpose of demonstration and to benchmark the results we take $x \in \mathbb{R}$. The performance of the developed algorithm will not rely on the fact that x is not a high dimensional vector.

5.4.1. Tree expansion for the homotopy analysis method

We are interested to solve the non-linear integral equation defined by the operator $\mathcal{N}$,

$$\mathcal{N}[f] = f(x) - c(x) - \int_a^b \mathrm{d}t\; K(x,t)\; n(f(t)) = 0. \tag{5.107}$$

For that we construct, as in the previous section, the homotopy

$$(1-q)\mathcal{L}[\phi(x,q) - u_{f,0}] + qc_0\mathcal{N}[\phi(x,q)] = 0. \tag{5.108}$$

Again, $\mathcal{L}$ is an arbitrary linear operator with $\mathcal{L}[0] = 0$. The solution of the homotopy is written as a Taylor expansion in q,

$$\phi(x,q) = \sum_m \frac{1}{m!}\frac{\mathrm{d}^m}{\mathrm{dq}^m}\phi(x,q)\Big|_{q=0} q^m. \tag{5.109}$$

Therefore,

$$\begin{aligned} f(x) = \phi(x, q=1) &= \sum_m u_{f,m}(x) \\ \text{with} \quad u_{f,m}(x) &= \frac{1}{m!}\frac{\mathrm{d}^m}{\mathrm{dq}^m}\phi(x,q)\Big|_{q=0}. \end{aligned} \tag{5.110}$$

The Taylor coefficients $u_{f,m}$ can be obtained by differentiating the 0th order deformation equation m times with respect to q and setting $q = 0$ afterwards. This can be done analytically yielding a recursive relation for the deformations $u_{f,m}$. We show how to represent the tree expansion of this recursion relation with the help of diagrams.
We choose the HAM convergence parameters $c_0 = 1$ and the linear operator $\mathcal{L}$ as the identity operator. Taking the derivative with respect to q m times in the 0th order deformation equation and setting $q = 0$ afterwards gives an equation for $u_{f,m}$. For $m \geq 2$ we have

$$u_{f,m}(x) = \frac{1}{(m-1)!}\,\frac{\mathrm{d}^{m-1}}{\mathrm{dq}^{m-1}}\int_a^b K(x,t) n(\phi(t,q))\mathrm{d}t\Big|_{q=0}. \tag{5.111}$$

The above equation can be written without specifying the non-linear function n,

$$\begin{aligned} u_{f,m}(x) =& \frac{1}{(m-1)!}\int_a^b \mathrm{d}t\; K(x,t)\; \frac{\mathrm{d}^{m-1} n(\phi(t,q))}{\mathrm{dq}^{m-1}}\Big|_{q=0} \\ =& \frac{1}{(m-1)!}\int_a^b \mathrm{d}t\; K(x,t) \sum_{k=1}^{m-1} n^{(k)}(\phi(t,q)) \\ & \times B_{m-1,k}\left(\phi(t,q)', \ldots, \phi(t,q)^{(m-k-1)}\right)\Big|_{q=0} \end{aligned} \tag{5.112}$$

$$= \frac{1}{(m-1)!} \int_a^b \mathrm{d}t\; K(x,t) \sum_{k=1}^{m-1} n^{(k)}(u_0(t)) \times B_{m-1,k}\left(u_{f,1}(t), \ldots, (m-k-1)! u_{f,m-k-1}(t)\right).$$

Here, $B_{m-1,k}$ are the Bell polynomials of the second kind [117] encoding the combinatorial coefficients produced by the action of the derivative $\frac{\mathrm{d}^{m-1}}{\mathrm{d}q^{m-1}}$ on $n(\phi(t,q))$. It can be checked that for the initial guess of the root finding $f_0(x) = u_{f,0}(x) = c(x)$ Eq. (5.112) also holds for $m = 1$. This is the starting point for the tree expansion. We are interested to calculate the HAM series up to order M, thus all references to the lower order deformations $u_{f,m}$, $m < M$ should be eliminated in the recursion relation Eq. (5.112) by using Eq. (5.112) iteratively for every $u_{f,m}$, $m \neq 0$, on the right hand side, cf. 5.105.

In the sequel we restrict the discussion to the specific non-linear function $n(x) = x^2$, which reduces the sum over k in Eq. (5.112) to $k_{\max} = 2$ as $n''' = 0$.
Let us take $m = 6$ to set the ideas for the diagrammatic representation. The recursion relation for $u_{f,6}$ involves the Bell polynomials $B_{5,1}$ and $B_{5,2}$ given by

$$\begin{aligned} B_{5,1}(x_1, x_2, x_3, x_4, x_5) &= x_5 \\ B_{5,2}(x_1, x_2, x_3, x_4) &= 10 x_2 x_3 + 5 x_1 x_4, \end{aligned} \tag{5.113}$$

or $B_{m,k} = \sum_{n=1}^{n_{m,k}} b_n$, where $n_{m,k}$ is the number of monomials b_n for the polynomial $B_{m,k}$. In this notation Eq. (5.112) can be written as

$$\begin{aligned} u_{f,6} = &\frac{1}{5!} \int_a^b \mathrm{d}t\; K(x,t) \sum_{k=1}^{2} \sum_{n}^{n_{m-1,k}} n^{(k)}(u_0(t)) \times \\ &b_n\left(u_{f,1}(t), \ldots, (m-k-1)! u_{f,m-k-1}(t)\right). \end{aligned} \tag{5.114}$$

In this form it is evident that all terms in the expansion can be obtained by writing down all possible configurations of (k, n). For example, choosing the configuration $(k = 2, n = 1)$ yields the term

$$\frac{1}{5!} \int_a^b \mathrm{d}t\; K(x,t)\, 20\; (2! u_{f,2}(t))\, (3! u_{f,3}(t)) \tag{5.115}$$

by considering the first monomial of $B_{5,2}$ and $n'' = 2$. What we achieved so far is just the first step in obtaining a single term in the tree expansion since $u_2(t)$ and $u_3(t)$ have to be expanded further. Writing down Eq. (5.114) for $u_2(t)$ and $u_3(t)$ and choosing for each a new configuration (k, n) eliminates $u_{f,2}$ and $u_{f,3}$ from (5.115). To be concrete, choosing $(k = 1, n = 1)$ for $u_{f,2}(t)$ and $(k = 2, n = 1)$ for $u_{f,3}(t)$ yields

$$\begin{aligned} \frac{1}{5!} \int_a^b \mathrm{d}t\; K(x,t)\, 20\; 2! \left(\int_a^b K(t,t') 2\, u_{f,0}(t')\; u_{f,1}(t') u_1(t') dt' \right) \\ \times 3! \left(\frac{1}{2!} \int_a^b K(t,t'') 2 u_{f,1}(t'')\, u_{f,1}(t'') dt'' \right). \end{aligned} \tag{5.116}$$

At this point only $u_{f,1}$ remains to be eliminated, for which there is only one possibility,

$$u_{f,1}(x) = \int_a^b \mathrm{d}t\; K(x,t)\, u_{f,0}(t)\, u_{f,0}(t). \tag{5.117}$$

Graphically, this elimination procedure is depicted by rooted trees where the basic elements, see Fig. 5.10, are the roots and leafs of the tree which are connected by branches. One term in the

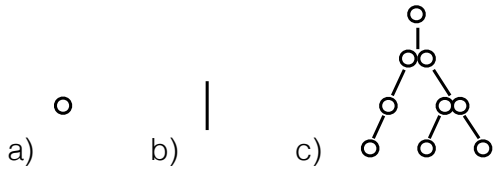

Figure 5.10.: The basic elements of the rooted trees. a) The roots and leafs are drawn as open circles and depict the different deformations $u_{f,m}$. b) Branches are connecting the roots with the leafs. The branches growing from the root or sub-roots, $u_{f,m}$, graphically represent the integral kernels in the definition of the deformation $u_{f,m}$. c) A set consisting of a root, leafs and branches constitutes a rooted tree.

tree expansion corresponds to a fully grown rooted tree. A random term in the tree expansion is picked by growing a random rooted tree in the following way:

1. Select a random integer m for the root.
2. Grow a branch from the root according to some random integer k, which fixes the Bell polynomial $B_{m-1,k}$.
3. Grow leafs from this branch according to some random integer n, corresponding to the monomials of the Bell polynomials $B_{m-1,k}$.
4. Regard every leaf of the branch of $B_{m-1,k}$ as a new root and go back to step 2 if $m > 1$ or finish the recursion by using Eq. (5.117) if $m = 1$.

Applied to the example discussed above (see also Fig. 5.11), the root is $m = 6$ which has two different branch types k where $k = 2$ is picked. By selecting $n = 2$ two leafs are grown on this branch (cf. Eq. 5.116), and the decomposition ends by invoking Eq. (5.117). In order to associate to each fully grown rooted tree a term in the tree expansion each element in the rooted tree must correspond to an element in expression (5.116) according to the following rules:

1. For each branch from a root with given m
   a) there is a factor $\frac{1}{(m-1)!}$.
   b) there is a factor $2u_0(t)$ if $k = 1$ or 2 if $k = 2$.
   c) there is the prefactor from the randomly picked monomial of $B_{m-1,k}$.
   d) there is an integration over a new variable t and a factor $K(x,t)$.
2. For each new leaf with label $m \neq 0$ there is a factor $m!$.
3. For each new leaf with label $m = 0$ there is a factor $u_0(t)$.

Fig. 5.12 shows the fully grown, labelled tree, from which the integral can be read off,

$$\begin{aligned}\int dt_1 dt_2 dt_3 dt_4 dt_5 dt_6 \, &\frac{1}{5!} K(x,t_1) 20 \times \\ &2! K(t_1,t_3)\, 2\, u_0(t_3)\, K(t_3,t_4)\, 2\, u_0(t_4) u_0(t_4) \times \\ &\frac{3!}{2!} K(t_1,t_2)\, 2\, K(t_2,t_5)\, 2\, u_0(t_5) u_0(t_5) \times \\ &K(t_2,t_6)\, 2\, u_0(t_6) u_0(t_6).\end{aligned} \tag{5.118}$$

It corresponds to a single term in the tree expansion of the HAM.

The solution of the integral equation is given by the HAM series to M-th order, $\sum_{m=0}^{M} u_{f,m}$,

1. Choose a random m for the root.

2. Grow a branch with random k.

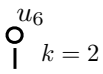

3. Grow leafs according to a random monomial of $B_{6,2}$.

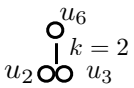

4. Regard the leafs as new roots and start again with Step 2 for each new root.

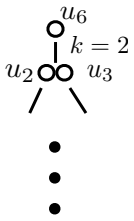

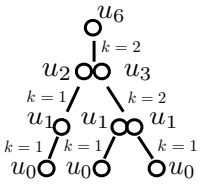

Figure 5.11.: The construction of a rooted tree with height $m = 6$. A fully grown rooted tree corresponds to a single term in the tree expansion which is constructed by iteratively applying the recursion relation Eq. (5.112) on its right hand side.

and therefore the tree expansion consists of generating and evaluating all integral expressions corresponding to all possible rooted trees. As the final answer is given by the sum over all deformations $u_{f,m}$ trees with variable height have to be considered.
In principle this expansion can be done explicitly by drawing and calculating each diagram. But already for moderate M the exponential growth in the number of diagrams renders this approach impractical. Therefore only a stochastic evaluation of the sum $\sum_{m=0}^{M} u_{f,m}$ is feasible.

5.4.2. Update structure for the Diagrammatic Monte Carlo sampling of rooted trees

This section introduces the Monte Carlo updates to stochastically sum the tree expansion of the HAM for the above example where $n(x) = x^2$. The core of the diagrammatic Monte Carlo algorithm is a Markov Chain which changes the topologies and integration variables of the diagrams according to their respective weights. The weight of a diagram is given by the integration kernel of the integral expression corresponding to the diagram. The rooted tree in

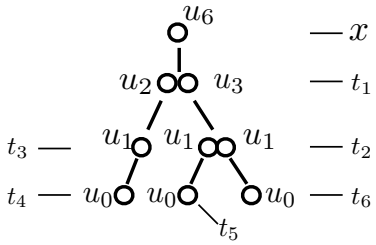

Figure 5.12.: Each fully grown rooted tree corresponds to an integral expression, e.g. Eq. (5.118), in the tree expansion which can be read off from the labeled rooted tree.

Fig. 5.12 corresponds to the integral expression (5.118) and therefore its weight is

$$\begin{aligned}&\mathrm{d}t_1\mathrm{d}t_2\mathrm{d}t_3\mathrm{d}t_4\mathrm{d}t_5\mathrm{d}t_6\, 32\, K(x,t_1)K(t_1,t_3)K(t_3,t_4)\times\\ &\times K(t_1,t_2)K(t_2,t_5)K(t_2,t_6)u_0(t_3)u_0(t_4)^2u_0(t_5)^2u_0(t_6)^2.\end{aligned}$$

Furthermore, we have shown that the integral expression can be read off from the rooted tree diagram by using a set of rules which associate to each elementary diagram element, Fig. 5.10, an analytic expression. With this set of rules changes in the topology and integration variables of a diagram by introducing or removing elementary diagram elements can be related to changes of the weight of the diagram. In the following a set of updates is introduced which generates a Markov Chain Monte Carlo in the space of all possible rooted trees and therefore stochastically sums the tree expansion of the HAM. The updates to calculate $\sum_{m=0}^{M} u_{f,m}(x)$ for a fixed external variable x are:

1. change integration variable: This update performs a shift of the internal integration variables. It picks one of the internal integration variables and updates the variable according to standard detailed balance rules. As this update is balanced with itself and does not change the diagram structure only the weights of the diagrams have to be taken into account. For the above example the update is schematically depicted in Fig. 5.13.

2. shrink-tree/expand-tree: This update is changing the height of the rooted tree.
   a) expand-tree: A new root with $m+1$ will be introduced. From this new root a branch with $k=1$ will be grown and the leaf of this branch is the old root. Furthermore a new integration variable t_{new} will be seeded according to some probability density function $P(t_{new})$ and assigned to the old root.
   b) shrink-tree: This update can only be performed if the branch growing from the root has $k=1$. The root of the rooted tree is deleted and the leaf of the root is assigned to be the new root. The acceptance ratio is the inverse of the expand-tree update.

3. shrink-tree-cluster/expand-tree-cluster: This is almost the same update pair as the update

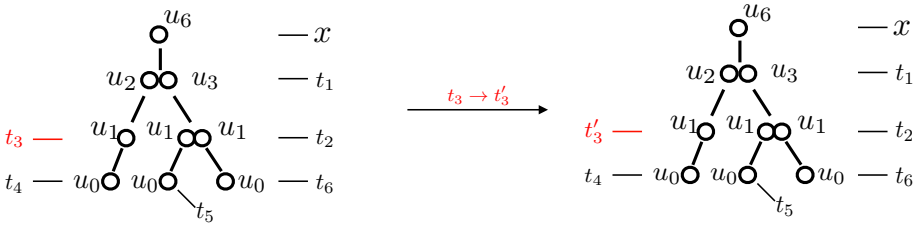

Figure 5.13.: The update to change an integration variable. The acceptance ratio is only determined by the different weights of the rooted tree.

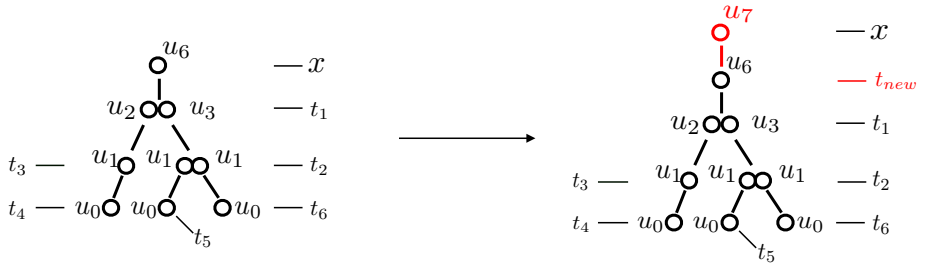

Figure 5.14.: The update to change the height of a rooted tree by a branch with $k = 1$.

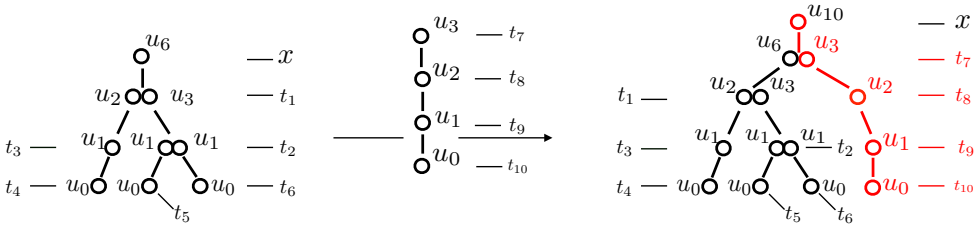

Figure 5.15.: The update to change the height of a rooted tree by a branch with $k = 2$.

shrink-tree/expand-tree. Instead of introducing a new root with a new branch in the $k = 1$ configuration a branch in the $k = 2$ configuration is grown. As can be seen in Fig. 5.15 this can be done by first growing a new random rooted tree with random height and afterwards glue this tree to the root of the current random tree. These two roots can be regarded as the leafs of a $k = 2$ branch grown from the new root of the combined rooted tree.

4. change-subtree: A random leaf of the rooted tree is chosen from which, regarded as a sub-root, a new subtree is grown. When accepted, the old subtree is deleted and replaced by the new subtree. This update is shown in Fig. 5.16.

5.4.3. Results

We illustrate the above algorithm for the non-linear integral equation,

$$f(x) = c(x) + \int_0^1 \mathrm{d}t\; K(x,t)\; n(f(t)). \tag{5.119}$$

The kernel of the integration is $K(x,t) = (x - t)$ and $n(x) = x^2$. The function $c(x)$ is picked in such a way that the solution of Eq. (5.119) is given by $f(x) = \log(x + 1)$. It can be checked that $c(x) = \log(x + 1) + 2\log(2) - 2x(\log(2) - 1)(\log(2) - 1) - \frac{5}{4}$ satisfies this condition. The initial approximation of the root is $u_0(x) = c(x)$ and $c_0 = 1$. As is shown in Fig. 5.17 the result $f(x) \approx f_M(x) = \sum_{m=0}^{M} u_m(x)$ quickly converges to the correct answer as a function of maximum

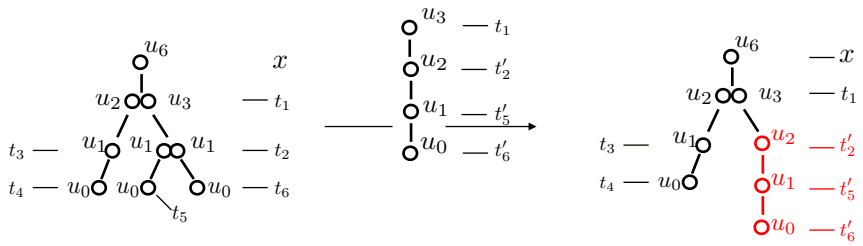

Figure 5.16.: The update to change a random subtree of a rooted tree.

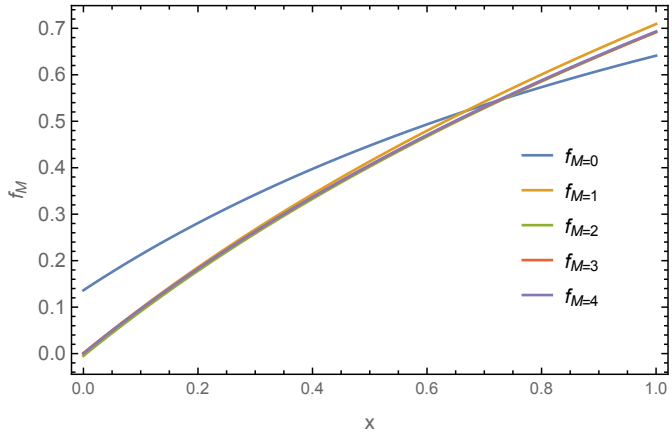

Figure 5.17.: The successive approximations $f_M(x) = \sum_{m=0}^{M} u_m(x)$ to the non-linear integral equation Eq. (5.119) with $n(x) = x^2$ and $K(x,t) = (x-t)$. The initial guess $u_0(x) = c(x)$ for the solution of the integral equation converges to the correct solution already for low M ≈ 4 iteration steps in the HAM.

m	$u_m(x = 0.5)$	$u_m(x = 0.5)$ (diagMC)	p
1	-0.0339665		
2	-0.0112517	-0.01127 ± 0.00004	0.587
3	0.00292815	0.00293 ± 0.00001	0.247
4	0.000486724	0.000488 ± 5e-06	0.096
5	-0.000359147	-0.000359 ± 5e-06	0.041
6	-2.77262e-06	-2.6 e-06 ± 3.6e-06	0.019
7	4.24149e-05	4.2e-05 ± 3e-06	0.009

Table 5.1.: Comparing the tree expansion sampled with diagMC to the exact answer where every $u_m(x)$ is calculated and stored on an external $x \in [0,1]$ grid. The last column indicates the probability p of reaching the expansion order m.

deformation order M. The results of the diagMC calculation of the tree expansion at $x = 0.5$ are given in Table 5.1 and compared with the exact answer. As the expansion of u_1 into u_0 is immediate it has not been included into the diagMC sampling.
The 4-th column in Table 5.1 shows the probability p to reach deformation order m, indicating the convergence of the HAM series solution as $p \to 0$ for larger m.

This completes the discussion of the stochastic interpretation of the HAM developed in order to solve non-linear integral equations in high dimensions. We have shown how the recursion relation for the deformations of the HAM series solution can be interpreted as the tree expansion and that each term in this expansion can be depicted in terms of rooted tree diagrams which are amenable to a systematic Monte Carlo sampling. Therefore, we can circumvent any direct storage or manipulation of the deformations $u_{f,m}$ and have direct access to the HAM series solution via the sampling of the rooted tree diagrams.

5.5. Solution of the Dyson-Schwinger equation for ϕ^4 theory in 2D

In this section we will move on and apply the newly developed computational techniques to the more challenging case of the $\mathcal{Z}_2$-symmetric ϕ^4 theory on a 2D square lattice with action

$$S[\phi] = \frac{1}{2}\sum_{i,j}\phi_i G^{-1}_{0;i,j}\phi_j + \frac{\lambda}{4!}\sum \phi_i^4. \tag{5.120}$$

The inverse non-interacting two-point correlation function is given by $G^{-1}_{0;i,j} = -\Box_{i,j} + m^2\delta_{i,j}$ where $\Box_{i,j}$ denotes the discretized Laplace operator in 2D. In momentum space $G_0(\mathbf{p})$ is given by

$$G_0(\mathbf{p}) = \left(4\sum_{\mu=1}^{D}\sin^2(\frac{p_\mu}{2}) + m^2\right)^{-1} \tag{5.121}$$

where $\mathbf{p}$ is a momentum variable restricted to the first Brillouin zone, $p_\mu \in [-\pi, \pi]$ with $\mu \in \{x, y\}$ and we measure distances in units of the lattice constant set to unity. For $m^2 < 0$, i.e., for the case the potential energy has degenerate minima, the theory undergoes a second order phase transition at some non-trivial coupling $\lambda_c(m^2)$ from an ordered phase $0 \leq \lambda < \lambda_c(m^2)$ to an unordered phase $\lambda > \lambda_c(m^2)$. The phase transition, belonging to the universality class of the Ising model, is signalled by the divergence of the magnetic susceptibility $\chi = G(p = 0)$. In our simulation we use $m^2 = -0.5$ which corresponds to $\lambda_c(m^2) \sim 2$.
The classical Worm algorithm is one of the most efficient classical Monte Carlo algorithms to compute the two-point correlation function G for model (5.120) in the functional integral representation. In this section we use this results to benchmark our functional integro-differential approach in the strongly correlated regime of model (5.120), i.e., close to its second order phase transition. The closed set of equations defining our model in this representation were derived in Sec. 5.2 and are given by Eq. (5.53), (5.54) and are depicted in Fig. 5.3. For convenience, we repeat the coupled set of equations for model (5.120) in this section,

$$G^{-1}_{1,2} = G^{-1}_{0;1,2} + \frac{1}{2}V_{1,2,3,4}G_{4,3} - \frac{1}{6}V_{1,3,4,5}G_{5,6}G_{4,7}G_{3,8}\Gamma_{6,7,8,2}, \tag{5.122}$$

$$\begin{aligned}
\Gamma_{1,2,3,4} = {} & V_{1,2,3,4} - \frac{1}{2}V_{1,2,5,6}G_{5,8}G_{6,7}\Gamma_{7,8,3,4} \\
& - \frac{1}{2}V_{1,3,5,6}G_{5,8}G_{6,7}\Gamma_{7,8,2,4} \\
& - \frac{1}{2}V_{1,4,5,6}G_{5,8}G_{6,7}\Gamma_{7,8,3,2} \\
& + \frac{1}{6}V_{1,5,6,7}G_{7,10}\Gamma_{10,12,3,4}G_{12,11}G_{5,8}G_{6,9}\Gamma_{8,2,11,9} \\
& + \frac{1}{6}V_{1,5,6,7}G_{7,10}\Gamma_{10,12,2,4}G_{12,11}G_{5,8}G_{6,9}\Gamma_{8,3,11,9} \\
& + \frac{1}{6}V_{1,5,6,7}G_{7,10}\Gamma_{10,12,3,2}G_{12,11}G_{5,8}G_{6,9}\Gamma_{8,4,11,9} \\
& - \frac{1}{3}V_{1,5,6,7}G_{5,8}G_{6,9}G_{7,10}\frac{\delta\Gamma_{8,2,3,4}}{\delta G_{9,10}} \\
& + \frac{1}{6}V_{1,5,6,7}G_{5,8}G_{6,11}G_{7,14}\Gamma_{11,12,13,14}G_{12,9}G_{13,10}\frac{\delta\Gamma_{8,2,3,4}}{\delta G_{9,10}}.
\end{aligned} \tag{5.123}$$

The collective indices i consist in the present case just of the labels of the lattices sites and is denoted by $i_k = k$ and summation over repeated indices is assumed. The interaction is given by $V_{1,2,3,4} = \lambda\delta_{1,2}\delta_{1,3}\delta_{1,4}$.
We approach the full solution by first studying various truncations of increasing complexity in the same fashion as already considered for the 0D toy-model in Sec. 5.3. Afterwards we will discuss the full solution of the coupled set of closed DSEs. To set the stage we will in a first step solve the mean field or Hartree-Fock approximation obtained by setting $\Gamma = 0$ resulting in a simple algebraic equation for G. In a next step we take into account the vertex corrections at zero momentum given by the ladder approximation. To solve the resulting coupled set of equations we use the self-consistency loop introduced in Sec. 5.3 and depicted in Fig. 5.4 with a truncated functional $\Gamma[G]$. The auxiliary problem (5.57), an algebraic equation for the 0D toy-model, turns into an integral equation for G. The HAM will be used to solve the auxiliary problem in each self-consistency step. No diagrammatic Monte Carlo sampling is needed at this level of complexity because the ladder approximation can be solved analytically and the HAM for the auxiliary problem can still be implemented on a momentum grid since G depends only on a single external momentum variable. The most complex truncation considered, before discussing the solution of the full integro-differential equation, is the generalization of the truncation $\mathcal{N}_{\text{truncI}}$ to the 2D model. In this case already the full machinery developed in the previous section will be needed in combination with the self-consistency loop. This will give an approximation to the solution of the DSE without neglecting any momentum dependence of the four-point vertex function and already establishes the state of the art for such self-consistent methods.
In a final step we introduce to the language of rooted trees the functional derivative terms in order to solve the DSE without any truncation. Further refinements of the algorithm discussed in the previous section will be introduced in order to make the rooted tree diagrams with functional derivative terms amenable to diagrammatic Monte Carlo sampling.

5.5.1. Truncations of the Dyson-Schwinger equation

Before discussing results for the full solution of the coupled DSEs (5.122), (5.123) we introduce various truncations of $\Gamma[G]$ in order to solve the coupled set of closed DSEs. The DSE for the two-point correlation function (5.122) is given in momentum space by

$$\Gamma^{(2)}(\mathbf{p}) - G_0^{-1}(\mathbf{p}) - \frac{\lambda}{2}\int_k \frac{1}{\Gamma^{(2)}(\mathbf{k})} + \frac{\lambda}{6}\int_{k,q} \frac{\Gamma(\mathbf{p}-\mathbf{k}-\mathbf{q},\mathbf{q},\mathbf{k},-\mathbf{p})}{\Gamma^{(2)}(\mathbf{k})\Gamma^{(2)}(\mathbf{q})\Gamma^{(2)}(\mathbf{p}-\mathbf{k}-\mathbf{q})} = 0, \tag{5.124}$$

where we introduced the inverse of G, $\Gamma^{(2)} = G^{-1}$ and denote here and in the following the integration over the first Brillouin zone as

$$\int_k = \int_{-\pi}^{\pi} \frac{\mathrm{d}k_x}{2\pi} \int_{-\pi}^{\pi} \frac{\mathrm{d}k_y}{2\pi}. \tag{5.125}$$

Setting $\Gamma = 0$ in Eq. (5.124) transforms the non-linear integral equation into a non-linear algebraic equation,

$$\begin{aligned} m_R^2 - m^2 - \frac{\lambda}{2}\int_k \frac{1}{\Gamma^{(2)}(\mathbf{k})} &= 0 \\ \Gamma^{(2)}(\mathbf{k}) = 4\sum_{\mu=1}^{2} \sin(\frac{k_\mu}{2})^2 + m_R^2, & \end{aligned} \tag{5.126}$$

for the renormalized mass m_R. This equation can be easily solved by tabulating the integral for different m_R and using standard numerical methods for solving algebraic non-linear equations.

We will discuss the results of the mean field approximation in the following subsection.

Another simple truncation is to take $\Gamma = \text{const.} \neq 0$ in momentum space. In order to find a non-trivial fixed point the dimensionless renormalized coupling constant in 2D, $\tilde{\lambda}_R = \Gamma(0,0,0)m_R^{-2}$, has to approach a non-trivial value if the system is tuned close to the phase transition. The next to leading order truncation to the coupled system of DSEs satisfying this condition is to use the ladder approximation $\mathcal{N}_{\text{truncII}}$ for $\Gamma[G]$ already discussed for the 0D toy-model,

$$\begin{aligned}\Gamma^{(2)}(\mathbf{p}) &= G_0^{-1}(\mathbf{p}) + \frac{\lambda}{2}\int_k \frac{1}{\Gamma^{(2)}(\mathbf{k})} - \frac{\lambda}{6}\int_{k,q} \frac{g_R[\Gamma^{(2)}]}{\Gamma^{(2)}(\mathbf{k})\Gamma^{(2)}(\mathbf{q})\Gamma^{(2)}(\mathbf{p}-\mathbf{k}-\mathbf{q})},\\ g_R[\Gamma^{(2)}] &= \frac{\lambda}{1+\frac{3}{2}\lambda\int_k \left(\frac{1}{\Gamma^{(2)}(\mathbf{k})}\right)^2}.\end{aligned} \tag{5.127}$$

The latter equation corresponds to the analytic solution of the resummed ladder expansion at zero external momentum.
The set of equations can be solved either by further approximating $\Gamma^{(2)}(\mathbf{p}) = 4\sum_{\mu=1}^{2}\sin(\frac{p_\mu}{2})^2 + m_R^2$, yielding a set of non-linear algebraic equations for m_R and g_R, or without further approximations by using the self-consistency loop, Fig. 5.4. The auxiliary problem which has to be solved at each iteration step i for a new approximation $\Gamma^{(2),(i)}$ to the inverse two-point correlation function is

$$\Gamma^{(2),(i)}(\mathbf{p}) = G_0^{-1}(\mathbf{p}) - \frac{\lambda}{2}\int_k \frac{1}{\Gamma^{(2),(i)}(\mathbf{k})} + \frac{\lambda}{6}\int_{k,q} \frac{g_R[\Gamma^{(2),(i-1)}]}{\Gamma^{(2),(i)}(\mathbf{k})\Gamma^{(2),(i)}(\mathbf{q})\Gamma^{(2),(i)}(\mathbf{p}-\mathbf{k}-\mathbf{q})}. \tag{5.128}$$

We use the HAM to solve this non-linear integral equation. The HAM series solution is given by

$$\Gamma^{(2),(i)} = u_{\Gamma^{(2),(i)},0} + \lim_{M\to\infty}\sum_{m=1}^{M} u_{\Gamma^{(2),(i)},m} \tag{5.129}$$

where the deformations coefficient are obtained from the recursion relation

$$\begin{aligned}u_{\Gamma^{(2),(i)},m}(\mathbf{p}) =& \chi_m u_{\Gamma^{(2),(i)},m-1}(\mathbf{p}) - c_0\Big[u_{\Gamma^{(2),(i)},m-1}(\mathbf{p})\\ &- \tilde{\chi}_m G_0^{-1}(\mathbf{p}) + \frac{\lambda}{2}H[u_{\Gamma^{(2),(i)}},m] - \frac{\lambda}{6}S_R[u_{\Gamma^{(2),(i)}},m](\mathbf{p})\Big].\end{aligned} \tag{5.130}$$

We use the identity as the linear operator $\mathcal{L}$ to construct the homotopy and introduced the functions

$$\begin{aligned}H[u_{\Gamma^{(2),(i)}},m] &= \frac{1}{(m-1)!}\int_k \frac{\mathrm{d}^{m-1}}{\mathrm{dq}^{m-1}}\frac{1}{\phi(\mathbf{k},q)}\bigg|_{q=0},\\ S_R[u_{\Gamma^{(2),(i)}},m](\mathbf{p}) &= \frac{g_R[\Gamma^{(2),(i-1)}]}{(m-1)!}\int_{k,l}\frac{\mathrm{d}^{m-1}}{\mathrm{dq}^{m-1}}\frac{1}{\phi(\mathbf{k},q)\phi(\mathbf{l},q)\phi(\mathbf{p}+\mathbf{k}+\mathbf{l},q)}\bigg|_{q=0}\\ &= g_R[\Gamma^{(2)}_{i-1}]\int_{k,l} W[u_{\Gamma^{(2),(i)}},m]\,(\mathbf{p},\mathbf{k},\mathbf{l}),\\ \text{where}\quad u_{\Gamma^{(2),(i)},m}(\mathbf{p}) &= \frac{1}{m!}\frac{\mathrm{d}^m}{\mathrm{dq}^m}\phi(\mathbf{p},q)\bigg|_{q=0}.\end{aligned} \tag{5.131}$$

Here and in the following the self-consistency loop is initialized by setting $\Gamma^{(2),(i)}(\mathbf{p}) = \Gamma^{(2)}(\mathbf{p})$, i.e., we use the exact two-point correlation function as a starting point for the solution of the coupled system of DSEs. The exact two-point correlation function $G_{i,j}$ in coordinate space is obtained from classical Monte Carlo simulations by the Worm algorithm [77] for lattice sizes

much bigger than the correlation length. The obtained result is Fourier transformed and inverted to obtain $\hat{\Gamma}^{(2)}(\mathbf{p})$, the discrete values of $\Gamma^{(2)}$ on a 2D momentum grid in the first Brillouin zone. $\Gamma^{(2)}(\mathbf{p})$ can then be approximated by using bilinear interpolation. In the following it is assumed that all functions depending on just a single momentum variable are represented in its discretized form. It should be noted that this starting point does not simplify the calculations for the truncation under consideration. We observe for other starting points, e.g., the mean field approximation, that approximately the same number of self-consistency steps are needed for the self-consistency to converge. Nevertheless, the obtained correlation functions from more complex truncations are already in good agreement with the exact results and therefore choosing this starting point will speed up the benchmarking because a lower number of self-consistency steps are needed. This speed up is only linear in the number of self-consistency steps and therefore it does not affect the generality of the obtained results.
In each step we first calculate g_R with respect to the previously found approximation to $\Gamma^{(2)}$. Since we know the analytic solution of the ladder approximation "Solver I" is made up of just numerically evaluating the integral

$$\int_k \left(\frac{1}{\Gamma^{(2)}_{i-1}(\mathbf{k})} \right)^2 , \tag{5.132}$$

which can be done by elementary means.
'Solver II" is given by the HAM series solution of the auxiliary problem. The deformation coefficients are obtained by directly applying the recursion relation (5.130). The most expensive operation in calculating a new deformation from the recursion relation is the numerical evaluation of the integral over two internal momentum variables in S_R for each external momentum grid point,

$$\int_{k,l} W[u_{\Gamma^{(2)}}, m]\,(\mathbf{p}, \mathbf{k}, \mathbf{l}). \tag{5.133}$$

This completes a single self-consistency step and we obtain a new approximation $\Gamma^{(2),(i)}(\mathbf{p})$. The procedure is repeated until the self-consistency converges. We will discuss the results in the following subsection.

The most complex approximation we consider is the truncation $\mathcal{N}_{\text{truncI}}$. It completely neglects the functional derivative terms in (5.123) but takes the complete momentum dependence of the four-point vertex function into account. The coupled set of equations in momentum space

is given in this truncation by

$$\begin{aligned}
\Gamma^{(2)}(\mathbf{p}) &= G_0^{-1}(\mathbf{p}) + \frac{\lambda}{2}\int_k \frac{1}{\Gamma^{(2)}(\mathbf{k})} - \frac{\lambda}{6}\int_{k,q} \frac{\Gamma(\mathbf{p}-\mathbf{k}-\mathbf{q},\mathbf{q},\mathbf{k},-\mathbf{p})}{\Gamma^{(2)}(\mathbf{k})\Gamma^{(2)}(\mathbf{q})\Gamma^{(2)}(\mathbf{p}-\mathbf{k}-\mathbf{q})}, \\
\Gamma(\mathbf{p}_1,\mathbf{p}_2,\mathbf{p}_3,\mathbf{p}_4) &= \lambda - \frac{\lambda}{2}\int_k G(\mathbf{k})G(\mathbf{p}_1+\mathbf{p}_2-\mathbf{k})\Gamma(\mathbf{p}_1+\mathbf{p}_2-\mathbf{k},\mathbf{k},\mathbf{p}_3,\mathbf{p}_4) \\
&\quad - \frac{\lambda}{2}\int_k G(\mathbf{k})G(\mathbf{p}_1+\mathbf{p}_3-\mathbf{k})\Gamma(\mathbf{p}_1+\mathbf{p}_3-\mathbf{k},\mathbf{k},\mathbf{p}_2,\mathbf{p}_4) \\
&\quad - \frac{\lambda}{2}\int_k G(\mathbf{k})G(\mathbf{p}_1+\mathbf{p}_4-\mathbf{k})\Gamma(\mathbf{p}_1+\mathbf{p}_4-\mathbf{k},\mathbf{k},\mathbf{p}_3,\mathbf{p}_2) \\
&\quad + \frac{\lambda}{6}\int_{k,q} G(\mathbf{k})G(\mathbf{q})G(-\mathbf{p}_2+\mathbf{k}-\mathbf{q})G(\mathbf{p}_1+\mathbf{p}_2-\mathbf{k})\times \\
&\qquad \Gamma(\mathbf{q},\mathbf{p}_2,-\mathbf{k},-\mathbf{p}_2+\mathbf{k}-\mathbf{q})\Gamma(\mathbf{p}_1+\mathbf{p}_2-\mathbf{k},\mathbf{k},\mathbf{p}_3,\mathbf{p}_4) \\
&\quad + \frac{\lambda}{6}\int_{k,q} G(\mathbf{k})G(\mathbf{q})G(-\mathbf{p}_3+\mathbf{k}-\mathbf{q})G(\mathbf{p}_1+\mathbf{p}_3-\mathbf{k})\times \\
&\qquad \Gamma(\mathbf{q},\mathbf{p}_3,-\mathbf{k},-\mathbf{p}_3+\mathbf{k}-\mathbf{q})\Gamma(\mathbf{p}_1+\mathbf{p}_3-\mathbf{k},\mathbf{k},\mathbf{p}_2,\mathbf{p}_4) \\
&\quad + \frac{\lambda}{6}\int_{k,q} G(\mathbf{k})G(\mathbf{q})G(-\mathbf{p}_4+\mathbf{k}-\mathbf{q})G(\mathbf{p}_1+\mathbf{p}_4-\mathbf{k})\times \\
&\qquad \Gamma(\mathbf{q},\mathbf{p}_4,-\mathbf{k},-\mathbf{p}_4+\mathbf{k}-\mathbf{q})\Gamma(\mathbf{p}_1+\mathbf{p}_4-\mathbf{k},\mathbf{k},\mathbf{p}_3,\mathbf{p}_2).
\end{aligned} \tag{5.134}$$

Due to momentum conservation $\mathbf{p}_4 = -\mathbf{p}_1 - \mathbf{p}_2 - \mathbf{p}_3$.
The second equation is a non-linear integral equation for the high dimensional four-point vertex function Γ. The numerical solution for the coupled set of equations (5.134) is obtained by incorporating the diagrammatic Monte Carlo sampling of rooted tree diagrams into the self-consistency introduced for the ladder approximation. The HAM is used for "Solver I" to obtain a series representation of the non-linear integral equation defining a truncated functional $\Gamma[G]$,

$$\Gamma[G] = u_{\Gamma,0}[G] + \lim_{M\to\infty}\sum_{m=1}^{M} u_{\Gamma,m}[G]. \tag{5.135}$$

The homotopy is constructed with respect to the identity operator $\mathcal{L} = \mathrm{id}$ and the initial guess for the zeroth order deformation is taken to be the result of the ladder approximation at zero external momentum, $u_{\Gamma,0}[G] = g_R[G]$. We like to note that, although the solution of the ladder approximation is taken for $u_{\Gamma,0}$, this has little to do with constructing the homotopy around the ladder approximation as discussed for the 0D toy model in Sec. 5.3.

The self-consistency is then applied as in the previously discussed ladder truncation with the difference that now in each iteration step we have to solve the auxiliary problem

$$\Gamma^{(2),(i)}(\mathbf{p}) = G_0^{-1}(\mathbf{p}) - \frac{\lambda}{2}\int_k \frac{1}{\Gamma^{(2),(i)}(\mathbf{k})} + \frac{\lambda}{6}\int_{k,q} \frac{\Gamma[G^{(i-1)}](\mathbf{p}-\mathbf{k}-\mathbf{q},\mathbf{q},\mathbf{k},-\mathbf{p})}{\Gamma^{(2),(i)}(\mathbf{k})\Gamma^{(2),(i)}(\mathbf{q})\Gamma^{(2),(i)}(\mathbf{p}-\mathbf{k}-\mathbf{q})}, \tag{5.136}$$

where ${G^{(i)}}^{-1} = \Gamma^{(2),(i)}$. The HAM is used to obtain a series representation of the solution,

$$\Gamma^{(2),(i)} = u_{\Gamma^{(2),(i)},0} + \lim_{M\to\infty}\sum_{m=1}^{M} u_{\Gamma^{(2),(i)},m}, \tag{5.137}$$

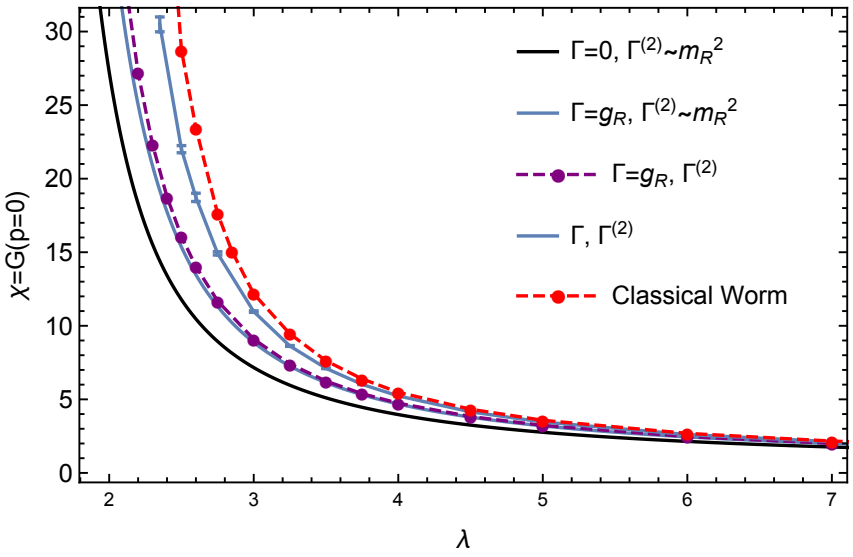

Figure 5.18.: The results from various approximations to the coupled DSEs (5.53), (5.54) compared to the classical worm algorithm.

where the deformation coefficients are calculated from the recursion relation in the same way as for the ladder approximation at zero external momentum,

$$\begin{aligned} u_{\Gamma^{(2),(i)},m}(\mathbf{p}) =& \chi_m u_{\Gamma^{(2),(i)},m-1}(\mathbf{p}) - c_0 \Big[u_{\Gamma^{(2),(i)},m-1}(\mathbf{p}) \\ & - \tilde{\chi}_m G_0^{-1}(\mathbf{p}) + \frac{\lambda}{2} H[u_{\Gamma^{(2),(i)}}, m] - \frac{\lambda}{6} S[u_{\Gamma^{(2),(i)}}, m](\mathbf{p}) \Big]. \end{aligned} \tag{5.138}$$

The only difference is that now we have to calculate at each self-consistency step,

$$\begin{aligned} S[u_{\Gamma^{(2),(i)}}, m](\mathbf{p}) =& \int_{k,q} W[u_{\Gamma^{(2)}}, m]\,(\mathbf{p},\mathbf{k},\mathbf{q}) \Gamma[G^{(i-1)}](\mathbf{p}-\mathbf{k}-\mathbf{q},\mathbf{q},\mathbf{k},-\mathbf{p}) \\ =& \int_{k,q} W[u_{\Gamma^{(2),(i)}}, m]\,(\mathbf{p},\mathbf{k},\mathbf{q}) \lim_{M\to\infty} \sum_{m=0}^{M} u_{\Gamma,m}[G^{(i-1)}](\mathbf{p}-\mathbf{k}-\mathbf{q},\mathbf{q},\mathbf{k},-\mathbf{p}) \\ =& S_R[u_{\Gamma^{(2),(i)}}, m](\mathbf{p}) + S_\Gamma[u_{\Gamma^{(2),(i)}}, m](\mathbf{p}), \\ S_\Gamma[u_{\Gamma^{(2),(i)}}, m](\mathbf{p}) =& \lim_{M\to\infty} \sum_{m=1}^{M} \int_{k,q} W[u_{\Gamma^{(2),(i)}}, m]\,(\mathbf{p},\mathbf{k},\mathbf{q}) u_{\Gamma,m}[G^{(i-1)}](\mathbf{p}-\mathbf{k}-\mathbf{q},\mathbf{q},\mathbf{k},-\mathbf{p}). \end{aligned} \tag{5.139}$$

The function $S_\Gamma(\mathbf{p})$ is calculated by applying the Markov chain Monte Carlo algorithm of Sec. 5.4 to sum up all possible rooted tree diagrams with variable heights and variable external momentum. The external momentas of the rooted tree diagrams are updated by importance sampling of the variables $\mathbf{p}$, $\mathbf{k}$, and $\mathbf{q}$ with respect to the integral weight $W[u_{\Gamma^{(2),(i)}}, m]\,(\mathbf{p},\mathbf{k},\mathbf{q})$ and histograms are taken for the discrete external momentum grid points $\mathbf{p}_i$. These histograms are normalized and stored giving a discretized function $S_\Gamma(\mathbf{p})$ which is used to compute $u_{\Gamma^{(2),(i)},m}(\mathbf{p})$ on the same momentum grid. For calculating the j-th order deformation $u_{\Gamma^{(2),(i)},j}$ the deformations $u_{\Gamma^{(2),(i)},m}$ with $m < j$ are needed which can be retrieved by bilinear interpolation of their discretized counterparts. H is calculated in the same way as for the ladder truncation.

Results and numerical sign problem

In order to compare the quality of the truncations in the strongly correlated regime the susceptibility $\chi = 1/\Gamma^{(2)}(\mathbf{p}=0) = G(0)$ is calculated in each setup from the obtained two-point correlation function and compared to the results from the classical worm algorithm [77]. As the worm algorithm works only on a finite lattice one must ensure that the system size is much larger than the correlation length. The results are shown in Fig. 5.18. The quality of the truncation increases smoothly with the number of terms in the functional integro-differential equation for $\Gamma[G]$ taken exactly into account. Deviations from the exact result obtained from the classical Worm algorithm remain nevertheless visible in the strongly correlated regime, which is attributed to the the omission of higher order vertices such as $\Gamma^{(6)}$.
In order to obtain controlled diagMC simulation results to the coupled integral equations of the truncation $\mathcal{N}_{\text{truncI}}$ (5.134), the following issues have to be taken into account. To determine the maximal order of the tree expansion $\sum_{m=0}^{M} u_{\Gamma,m}$ we calculate $u_{\Gamma^{(2),(i=1)},1}(\mathbf{p}=0)$, cf. Eq. (5.138), for different expansion orders M and various convergence control parameters c_0. Examples of these calculations are shown in Fig. 5.19. The convergence control parameter must be chosen such that the convergence is as fast as possible, i.e., the expansion order is as low as possible. For $\lambda = 7$ the choice $c_0 = 0.4$ is optimal while a higher value $c_0 = 0.6$ leads to an oscillating solution with high error bars. If c_0 is set to too small values (like for the $\lambda = 2.5$, $c_0 = 0.1$ case) systematic errors in the calculation of the deformations of $\Gamma^{(2)}$ are introduced through the omission of higher order deformations and extrapolations have to be used in order to obtain the results for $M \to \infty$.

The average sign $\langle s \rangle$ of the diagMC integration also depends on the convergence control parameter. While for $\lambda = 7$, $c_0 = 0.3$, $\langle s \rangle = -0.18$, it goes down to $\langle s \rangle = -0.09$ for $c_0 = 0.4$ and drops further to $\langle s \rangle = -0.03$ for $c_0 = 0.6$ in the case of an oscillating convergence. The sign problem originates from the different signs in front of the linear and quadratic term with respect to Γ in the DSE for the vertex function, cf. Eq (5.134), and therefore all rooted tree diagrams can be classified by having either a positive or negative contribution to $S(\mathbf{p}) = S^{+}(\mathbf{p}) - |S^{-}(\mathbf{p})|$ in Eq. (5.138). Note that $\Gamma^{(2)}(\mathbf{p})$ is positive definite. The number of rooted tree diagrams in order m grows exponentially with m. Therefore, without the weights of the rooted tree diagrams cancelling this exponential growth,

$$\left|S_m^{\pm}(\mathbf{p})\right| = \int_{k,q} W[u_{\Gamma^{(2)}}, m]\,(\mathbf{p},\mathbf{k},\mathbf{q}) \left|u_{\Gamma,m}^{\pm}(\mathbf{p}-\mathbf{k}-\mathbf{q},\mathbf{q},\mathbf{k},-\mathbf{p})\right| \tag{5.140}$$

will grow exponentially. Here, $u_{\Gamma,m}^{\pm}$ denotes the sum of all rooted tree diagrams contributing with a positive (negative) sign in the tree expansion of $u_{\Gamma,m}$. Assuming convergence in the form $S_m(\mathbf{p}) \to 0$ for $m \to \infty$ while $S_m(\mathbf{p})$ having a definite sign for all m, which is actually the case for a carefully chosen c_0 as can be deduced from Fig. 5.19, both exponentially growing numbers $S_m^{\pm}(\mathbf{p})$ have to be computed to very high precision in order for their difference to have a high precision. This also explains the fact why $\langle s \rangle$ is smaller for $c_0 = 0.4$ compared to $c_0 = 0.35$ as convergence sets in faster for $c_0 = 0.4$. Thus, with carefully chosen simulation parameters it is possible to extract meaningful results before the statistical errors become too large due to the numerical sign problem. If one has oscillating convergence the sign problem makes it, as expected, impossible to extract controlled results in a realistic simulation time.
Apart from the cancellation of terms in the calculation of $S(\mathbf{p})$ more cancellations occur in the calculation of the deformations $u_{\Gamma^{(2),(i)},m}$. Assuming convergence of the self-consistency loop, i.e., $\Gamma^{(2),(i-1)} \approx \Gamma^{(2),(i)}$, it follows that $u_{\Gamma^{(2),(i)},1} \approx 0$. But $u_{\Gamma^{(2),(i)},1} \approx 0$ is obtained by an almost perfect cancellation of the individual contributions in (5.138) and clearly the absolute error $\Delta u_{\Gamma^{(2),(i)},1}$ is given by the statistical error of the diagMC calculation of $S(\mathbf{p})$. As this statistical error is almost constant with respect to the self-consistency loop index i the relative

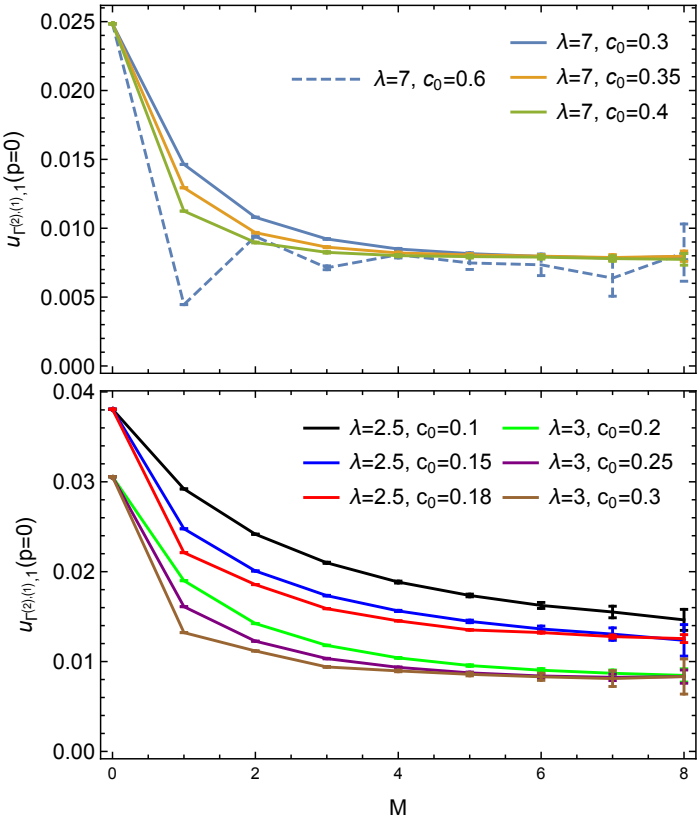

Figure 5.19.: The first deformation of $\Gamma^{(2)}$ in the first self-consistency loop at zero external momentum for different truncation orders in the tree expansion of $\sum_{m=0}^{M} u_{\Gamma,m}$. Choosing c_0 carefully makes it possible to let the expansion converge in few orders and preventing a systematic error from the expansion order cutoff. While for $\lambda = 7$ the tree expansion can already be truncated at $M = 4$ for $\lambda = 2.5$ the tree expansion has to be considered up to order $M = 8$.

error $\delta u_{\Gamma^{(2),(i)},1} = \Delta u_{\Gamma^{(2),(i)},1} / u_{\Gamma^{(2),(i)},1}$ diverges. It is hence the sign problem that poses the strongest limitation on approaching the critical point more closely.

5.5.2. Full and unbiased solution of the Dyson-Schwinger equation in the functional integro-differential representation

In this subsection we finally discuss the full and unbiased solution of the functional integro-differential equation (5.54) defining the universal functional $\Gamma[G]$. For that we first discuss how the diagrammatic language of rooted trees is used to naturally include the functional derivative terms.

We consider the construction of the universal functional $\Gamma[G]$ through the solution of (5.123) in momentum space. In the following the momentum variables are denoted by $\mathbf{p}_i = i$ and the linear combination of momentum variables by, e.g., $\mathbf{p}_i + \mathbf{p}_j = i + j$ moreover the integration over the first Brillouin zone is denoted by $\sum_5 = \int_{p_5}$. In this representation the integro-differential equation in (5.123) can be written as

$$\begin{aligned}\Gamma_{1,2,3,4} &= \lambda\delta(\mathbf{p}) - \frac{\lambda}{2}\sum_{5,6,7} G_{5,6}\left[G_{1+2-5,7}\Gamma_{-7,-6,3,4} + G_{1+3-5,7}\Gamma_{-7,-6,2,4} + G_{1+4-5,7}\Gamma_{-7,-6,3,2}\right] + \\ &\frac{\lambda}{6}\sum_{5,\ldots,12} G_{1-5-7,11}G_{5,6}G_{7,8}G_{9,10}\times \\ &\quad\left[\Gamma_{-6,2,-9,-8}\Gamma_{-11,-10,3,4} + \Gamma_{-6,3,-9,-8}\Gamma_{-11,-10,2,4} + \Gamma_{-6,4,-9,-8}\Gamma_{-11,-10,3,2}\right] - \\ &\frac{\lambda}{3}\sum_{5,\ldots,9} G_{1-5-6,7}G_{5,8}G_{6,9}\frac{\delta\Gamma_{-7,2,3,4}}{\delta G_{8,9}} + \\ &\frac{\lambda}{6}\sum_{5,\ldots,13} G_{1-5-6,7}G_{5,8}G_{6,9}\Gamma_{-8,-11,-13,-9}G_{10,11}G_{12,13}\frac{\delta\Gamma_{-7,2,3,4}}{\delta G_{10,12}},\end{aligned} \tag{5.141}$$

where $\delta(\mathbf{p}) = \delta_{1+2+3,-4}$ denotes the momentum conservation at the bare vertex. The universal functional $\Gamma[G]$ has to be constructed as the solution of (5.141) for arbitrary $G \in \mathbb{R}^{L\times L}$, i.e., not restricted to the subspace of physical correlation functions which satisfy translational symmetry. Thus, going into the momentum representation does not diagonalize the two-point correlation function, $G(1,2) \neq G(1)\delta_{1,-2}$ and also $\Gamma(1,2,3,4) \neq \Gamma(1,2,3,-1-2-3)\delta_{4,-1-2-3}$. Only the evaluation of $\Gamma[G]$ in the physical subspace of translational invariant solutions will give a translational invariant four-point vertex function $\Gamma(1,2,3,4) = \Gamma(1,2,3,-1-2-3)\delta_{4,-1-2-3}$. We show in the following that it is possible to construct the solution in the absence of translational symmetry and simultaneously evaluate the solution $\Gamma[G]$ only in the restricted physical subspace of translational invariant G.

Homotopy analysis method for functional integro-differential equations

We use the HAM to solve the functional integro-differential equation (5.141). As discussed in Sec. 5.3 the starting point of the HAM is the construction of the homotopy

$$(1-q)\mathcal{L}\left[\phi[G,q] - u_{\Gamma,0}[G]\right] + qc_0\mathcal{N}\left[\phi[G,q]\right] = 0. \tag{5.142}$$

$\mathcal{N}\left[\Gamma[G]\right] = 0$ is the non-linear differential operator defining (5.141) and $\mathcal{L}$ is an arbitrary linear operator with the property $\mathcal{L}[0] = 0$. The homotopy (5.142) includes the deformation parameter $q \in [0,1]$ which deforms the solution of $\mathcal{L}$, $\phi[G,0] = u_{\Gamma,0}[G]$, at $q = 0$ to the solution of the differential equation (5.141), $\phi[G,1] = \Gamma[G]$, at $q = 1$. In the following we use the easiest possible linear operator $\mathcal{L}\left[\phi[G,q] - u_{\Gamma,0}[G]\right] = \phi[G,q] - u_{\Gamma,0}[G]$. $u_{\Gamma,0}[G]$ is the initial guess for the solution of $\mathcal{N}\left[\Gamma[G]\right] = 0$. We use, as for the truncation $\mathcal{N}_{\text{truncI}}$, $u_{\Gamma,0}[G] = g_R[G]$. The convergence control parameter c_0 controls the rate at which the deformation takes place. The HAM gives a series solution of the functional integro-differential equation (5.141) in terms of the deformation coefficients $u_{\Gamma,m}[G]$,

$$\Gamma[G] = u_{\Gamma,0}[G] + \sum_{m=1} u_{\Gamma,m}[G]. \tag{5.143}$$

Differentiating (5.141) m times with respect to q and setting $q = 0$ yields the recursion relation for the mth order deformation equation,

$$\begin{aligned}u_{\Gamma,m}(\mathbf{p}) &= \chi_m u_{\Gamma,m-1}(\mathbf{p}) - c_0\left[u_{\Gamma,m-1}(\mathbf{p}) - \lambda\delta(\mathbf{p})\tilde{\chi}_m + \right. \\ &\left.\frac{\lambda}{2}\sum_c\sum_{5,6,7} K_c^{(1)}(\mathbf{p}_c,5,6,7)u_{\Gamma,m-1}(-7,-6,\mathbf{p}_{\bar{c}}) - \right.\end{aligned}$$

$$\frac{\lambda}{6}\sum_c \sum_{5,\ldots,11} K_c^{(2)}(\mathbf{p}_c,5,\ldots,11)\sum_{k=0}^{m-1} u_{\Gamma,k}(-11,-10,\mathbf{p}_{\bar{c}})\,u_{\Gamma,m-1-k}(-6,p_c,-9,-8)+$$
$$\frac{\lambda}{3}\sum_{5,\ldots,9} K^{(3)}(1,5,\ldots,9)\frac{\delta u_{\Gamma,m-1}(-7,2,3,4)}{\delta G_{8,9}}- \tag{5.144}$$
$$\frac{\lambda}{6}\sum_{5,\ldots,13} K^{(4)}(1,5,\ldots,13)\sum_{k}^{m-1} u_{\Gamma,m-1-k}(-8,-11,-13,-9)\frac{\delta u_{\Gamma,k}(-7,2,3,4)}{\delta G_{10,12}}\Bigg].$$

We have introduced the following notations:

1. $u_{\Gamma,m}(\mathbf{p})$ denotes the deformation $u_{\Gamma,m}[G]$ at external variables $\mathbf{p}=(1,2,3,4)$.
2. The sum $\sum_c$ runs over the three possible permutations of external legs, cf. Eq. (5.141). We introduce the following abbreviations for the permutations: s = {1,2,3,4}, t={1,3,2,4}, u={1,4,3,2}.
3. The contributions coming from G in (5.141) are collected in the kernel functions $K_c^{(i)}$, $i\in\{1,2\}$ and $K^{(3)}$, $K^{(4)}$. The various kernel functions are explicitly summarized in App. D.
4. The projection of the 4D vector of external variables $\mathbf{p}$ onto a 2D subspace and its complement is denoted by $\mathbf{p}_c$, $\mathbf{p}_{\bar{c}}$, respectively: $\mathbf{p}_{c=s}=(1,2)$, $\mathbf{p}_{\bar{c}=\bar{s}}=(3,4)$; $\mathbf{p}_{c=t}=(1,3)$, $\mathbf{p}_{\bar{c}=\bar{t}}=(2,4)$; $\mathbf{p}_{c=u}=(1,4)$, $\mathbf{p}_{\bar{c}=\bar{u}}=(3,2)$.
5. The projection of the 4D vector of external variables $\mathbf{p}$ onto a D dimensional vector is denoted by p_c: $p_{c=s}=2$; $p_{c=t}=3$; $p_{c=u}=4$.
6. $\chi_m=1-\delta_{m,1}$ and $\tilde{\chi}_m=\delta_{m,1}$.
7. $\delta(\mathbf{p})=\delta_{4,-1-2-3}$ denotes the momentum conservation at the bare vertex.

The recursion relation for the mth order deformation equation is the starting point for the tree expansion developed in Sec. 5.4 for simple integral equation and already used in Sec. 5.5.1 for a truncated functional $\Gamma[G]$. In the following we will extend these ideas to account for the functional derivatives in (5.144).

Tree expansion

The mth order deformation equation (5.144) gives the mth term in the series solution (5.143) of the HAM. In order to calculate the mth deformation all previous deformations and their functional derivatives have to be known. As already discussed in pervious section already the full storage of a single deformation is a formidable task as the deformations themselves depend on 4 external indices which are D-dimensional vectors, i.e., $u_{\Gamma,m}(\mathbf{p})$ is a rank-4D tensor. Including the functional derivatives seems to make a numerical calculation of (5.144) an impossible task. The tree expansion developed in Sec. 5.4 solves this apparently impossible task by a stochastic interpretation. The basic idea of the tree expansion is that in order to calculate the mth order deformation by the recursion relation (5.144), (5.144) is used again on the right hand side to get rid off the explicit dependence of all deformations and functional derivatives with $k<m$. This procedure is recursively repeated until all deformations $u_{\Gamma,k}$ with $k>0$ are eliminated on the right hand side. The result is a complicated expression, the tree expansion, which only depends explicitly on the deformation $u_{\Gamma,0}$. We will develop an extension to the diagrammatic language of rooted trees which captures all possible terms in the tree expansion including the functional derivative terms and introduce a Monte Carlo algorithm to stochastically sum all terms.

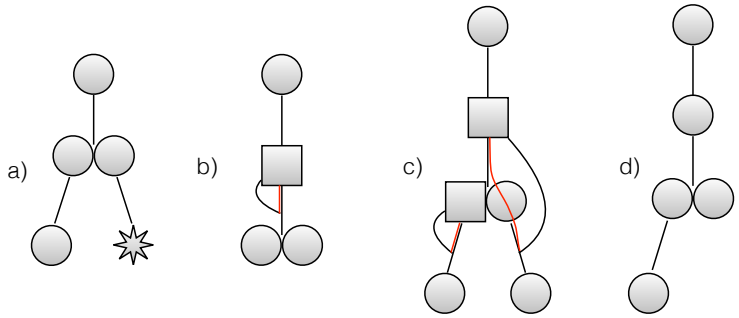

Figure 5.20.: Examples of rooted tree diagrams which are constructed by expanding the HAM in the tree expansion. The different diagrammatic elements are explained in the main text and listed in Fig. 5.21. The rooted tree diagrams in a) and d) do not include functional derivatives. The rooted trees in b) and c) include functional derivatives which are indicated by the arc lines closing on a branch. The additional red line is introduced for the bookkeeping of excess momenta carried by the functional derivative. The different stages in the tree expansion leading to the rooted trees in a)-d) are explained in the main text.

We start the discussion with the rooted tree diagram in Fig. 5.20 a). It corresponds to a single term in the tree expansion. For the moment we are neglecting the labeling of the rooted tree and consider only the overall structure of the tree and its corresponding analytic expression. After the general structure is introduced we discuss its labeling, i.e., how momentum variables and additional labels, e.g., external leg permutations, are taken into account. The rooted tree and the structure of the corresponding analytic expression are obtained from the following procedure. The uppermost circle, the root of the rooted tree, corresponds to the left hand side of (5.144). In the case of Fig. 5.20 a) $u_{\Gamma,3}$ should be expanded. The branch, indicated by a straight line, growing from the root leading to two leafs, represented by the circles, diagrammatically depicts that $u_{\Gamma,3}$ is expanded in the first stage with respect to the third line in (5.144), i.e.,

$$K_c^{(2)} \sum_{k=0}^{m-1} u_{\Gamma,k} u_{\Gamma,m-1-k}. \tag{5.145}$$

Thus, the branch corresponds to the integral kernel $K_c^{(2)}$ and the two leafs corresponds to the product of deformations $u_{\Gamma,k} u_{\Gamma,m-1-k}$. A single term in the sum over deformations is chosen. In Fig. 5.20 a) $k = 1$ has been picked leading to $u_{\Gamma,1} u_{\Gamma,1}$. In the second stage the above procedure is repeated by considering each leaf as a new individual root. In case of Fig. 5.20 a) the left leaf has been expanded with respect to the second line in (5.144), i.e.,

$$K_c^{(1)} u_{\Gamma,0}. \tag{5.146}$$

and the right leaf corresponds to the first line, i.e.,

$$\chi_1 u_{\Gamma,0} - c_0 \left[u_{\Gamma,0} - \lambda \tilde{\chi}_1 \right] = -c_0 \left[u_{\Gamma,0} - \lambda \right]. \tag{5.147}$$

For that case there is no contribution from an integral kernel. This is indicated by drawing the leaf as a star instead of a circle. Gathering all contributions the structure of the analytic expression corresponding to the rooted tree in the example of Fig. 5.20 a) is

$$K_c^{(2)} K_c^{(1)} u_{\Gamma,0} \left(-c_0 \left[u_{\Gamma,0} - \lambda \right] \right). \tag{5.148}$$

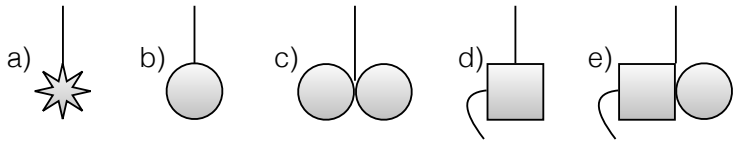

Figure 5.21.: The possible branch types of the rooted trees. Each branch type corresponds to a single line on the right hand side of (5.144). The straight line, the branch itself, represents the corresponding kernel function $K_c^{(i)}$, $i \in \{1,2\}$ or $K^{(i)}$, $i \in \{3,4\}$ for the respective branch type. The star, circle and box indicate the leaf grown from the branch. They represent the contribution from the deformation, $u_{\Gamma,m}$, for the specific branch type. The star contributes no integration variable to the tree, cf. first line in (5.144). The box corresponds to a leaf at which a functional derivative is introduced. The branch type can be read off from the combination of leafs grown on the lower end of the branch. The leaf types c), e) consists of two individual single leafs because each can be individually expanded further in the tree expansion. The dangling lines on the leafs of d), e) are representing the not yet completed action of the functional derivative on a consecutive branch.

This is a single term in the tree expansion and illustrates that the rooted trees depend explicitly only on the kernel functions and on the initial guess $u_{\Gamma,0}$ which is the starting point of the series solution (5.143). The discussion also shows that in (5.144) there are 5 different possibilities to expand $u_{\Gamma,m}$ which lead to the 5 different branch types. All branch types with their respective leafs are shown in Fig. 5.21. In the diagrammatic expressions the branch type is determined by the leafs on the lower end of the branch. The branch type in Fig. 5.21 d), e) correspond to the expansion with respect to the functional derivative terms. The leafs with functional derivatives are drawn by boxes and the additional dangling line is introduced. It indicates the action of the functional derivative on a consecutive element in the rooted tree.
On the basis of Fig. 5.20 c) we discuss the structure of the analytic expression corresponding to a rooted tree with functional derivatives. In the first stage of the tree expansion the root, $u_{\Gamma,4}$, is expanded with respect to the branch type Fig. 5.21 d) which includes a single leaf with a functional derivative. The structure of the analytic expression in this expansion stage is given by,

$$K^{(3)} \frac{\delta u_{\Gamma,3}}{\delta G}. \tag{5.149}$$

In the next stage $u_{\Gamma,3}$ is expanded with respect to the branch type Fig. 5.21 e). This gives the analytic expression

$$K^{(3)} \frac{\delta}{\delta G} \left(K^{(4)} \frac{\delta u_{\Gamma,1}}{\delta G} u_{\Gamma,1} \right). \tag{5.150}$$

Due to the product rule of functional derivatives there are three possibilities for the action of the outer functional derivative. The first possibility is that the functional derivative is acting on the kernel function of the second expansion stage, i.e., the branch directly after the deformation $u_{\Gamma,3}$ is differentiated. The second possibility is that the outer derivative is acting on the leaf with the functional derivative and therefore a second order functional derivative is produced. The third possibility is that it acts on the deformation $u_{\Gamma,1}$. From Fig. 5.20 c) we see that the dangling line is completed to an arc line which indicates that the derivative introduced in the first stage of the tree expansion is differentiating a branch grown after the leaf without a functional derivative. Therefore, the third possibility is represented by the rooted tree in Fig. 5.20 c) and the analytic expression for the rooted tree in this expansion stage is

$$K^{(3)} K^{(4)} \frac{\delta u_{\Gamma,1}}{\delta G} \frac{\delta u_{\Gamma,1}}{\delta G}. \tag{5.151}$$

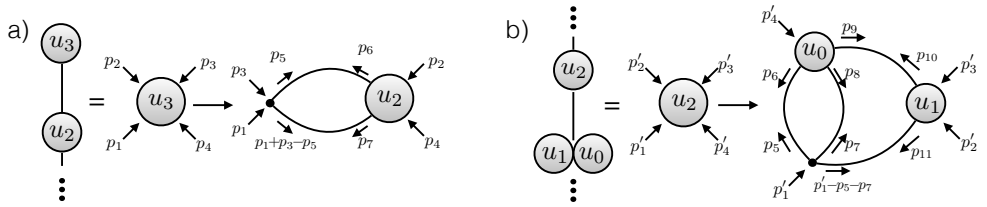

Figure 5.22.: Two consecutive stages of expansions in the tree expansion leading to the full rooted tree in Fig. 5.20 d). The two-point correlation functions contribution to the kernel are not yet evaluated in the physical, translational invariant subspace. Therefore, G still depends on two momentum variables which are indicated by two arrows on top of the G-lines. The new external momentum carried by the leafs is determined by the kernel functions in (5.144) and the specific random permutation of external legs picked for this expansion stage. Diagrammatically the contributing kernel functions together with the respective deformations are depicted on the right hand side of the arrow. a) The deformation $u_{\Gamma,3}$ is expanded with respect to the second line in (5.144) leading to a new leaf, $u_{\Gamma,2}$. The branch corresponds to the kernel function depending on two two-point correlation functions which lead to an evaluation of the lower order deformation at a new external momentum. In this example the t-channel is considered. b) In the next expansion stage the leaf, $u_{\Gamma,2}$, is expanded further with respect to the third line in (5.144) in the u-permutation. In this case the kernel function depends on four two-point correlation functions and the leafs corresponds to two lower order deformations each evaluated at a new external momentum.

In the next two expansion stages the deformations $u_{\Gamma,1}$ are further expanded. In both cases with respect to the branch type Fig. 5.21 b). This gives the analytic expression

$$K^{(3)}K^{(4)}\frac{\delta}{\delta G}\left(K_c^{(1)}u_{\Gamma,0}\right)\frac{\delta}{\delta G}\left(K_c^{(1)}u_{\Gamma,0}\right). \tag{5.152}$$

Here and in the following we consider only initial guesses $u_{\Gamma,0}$ which have no explicit G dependence, i.e.,

$$\frac{\delta u_{\Gamma,0}}{\delta G} = 0. \tag{5.153}$$

Taking this into account the structure of the analytic expression corresponding to the fully grown root tree in Fig. 5.20 c) is given by

$$K^{(3)}K^{(4)}\frac{\delta K_c^{(1)}}{\delta G}u_{\Gamma,0}\frac{\delta K_c^{(1)}}{\delta G}u_{\Gamma,0}. \tag{5.154}$$

From this discussion we see that functional derivatives can only act on the branches of a fully grown rooted tree. Nevertheless, in intermediate stages of the tree expansion the functional derivatives can act on the deformations with $u_{\Gamma,m}$, $m > 0$. These have to be expanded further in later stages of the tree expansion and therefore the analytic expression corresponding to a fully grown rooted tree involves only $u_{\Gamma,0}$, kernel functions and functional derivatives of the kernel functions. Moreover, as we see from the above discussion the derivatives can only act on branches which are grown from a leaf consecutive to a functional derivative leaf. Examples of valid rooted trees with functional derivatives are shown in Fig. 5.20 b), c). In these fully grown rooted trees the dangling lines which indicate the action of the functional derivative form closed arc lines connecting a functional derivative leaf to a branch. This denotes which branch is differentiated by the functional derivative. We will see later that each branch can only be differentiated a finite

amount of times and therefore all possible functional derivatives on all possible branches can be tabulated, cf. App. E.

We have introduced the general structure of the rooted trees in the framework of the tree expansion on the basis of the examples in Fig. 5.20. In the following we discuss the labeling and the specific analytic expressions of the diagrammatic elements in the rooted tree diagrams. The universal functional $\Gamma[G]$ is a functional with respect to an arbitrary $G \in \mathbb{R}^{L\times L}$ which is not necessary defined inside the physical, translational invariant subspace. Nevertheless, we finally want to evaluate $\Gamma[G]$ in the subspace of physical G. We showed that $\Gamma[G]$ can be constructed by drawing all possible rooted tree diagrams in the tree expansion of the HAM. Therefore, in order to evaluate $\Gamma[G]$ at a physical G the diagrammatic elements of the rooted tree diagrams, i.e., the kernel functions and their derivatives have to be build up from the physical, translational invariant two-point correlation functions. In the following we show how this leads to the correct labeling of the rooted tree diagrams.
Consider the rooted tree diagram in the tree expansion for $u_{\Gamma,3}$ depicted in Fig. 5.20 d). We fix the external momentum of the root, $u_{\Gamma,3}(\mathbf{p})$, to be $\mathbf{p} = (p_1, p_2, p_3, -p_1 - p_2 - p_3)$, i.e., the rooted tree diagram is evaluated inside the translational invariant subspace. The first stage in the tree expansion for the rooted tree in Fig. 5.20 d) is graphically illustrated in Fig. 5.22 a). In the example the expansion is performed in the t-permutation channel, cf. (5.144). The analytic expression corresponding to this expansion stage is diagrammatically illustrated on the right hand side of the arrow in Fig. 5.22 a) and can be read off as

$$\begin{aligned}
&\sum_{5,6,7} K^{(1)}_{c=t}(\mathbf{p}_{c=t}, 5, 6, 7) u_{\Gamma,2}(-7, -6, \mathbf{p}_{\bar{c}=\bar{t}}) \\
&= G_{5,6} G_{1+3-5,7}\; u_{\Gamma,2}(-7, -6, 2, 4) \overset{G=G_{\text{phys}}}{=} G_5 G_{1+3-5} u_{\Gamma,2}(\mathbf{p}'). \qquad (5.155)
\end{aligned}$$

Here and in the following summation over repeated indices is assumed implicitly. Obviously, the kernel function can be evaluated in the physical subspace of translational invariant G, $G_{\text{phys},1,2} = G_1 \delta_{1,-2}$. Consequently, the new external momentum for $u_{\Gamma,2}(\mathbf{p}')$ is $\mathbf{p}' = (p'_1, p'_2, p'_3, p'_4) = (p_1 + p_3 - p_5, p_5, p_2, -p_1 - p_2 - p_3)$ and therefore momentum conservation is fulfilled and the procedure of the tree expansion can be recursively repeated without leaving the physical subspace. The same holds for the expansion with respect to the branch type Fig. 5.21 c). For the example of Fig. 5.20 d) the second stage of the tree expansion is illustrated in Fig. 5.22 b). In this case, assuming that the u-permutation has been chosen,

$$\begin{aligned}
&\sum_{5,\ldots,11} K^{(2)}_{u}(\mathbf{p}'_{c=u}, 5, \ldots, 11) u_{\Gamma,1}(-11, -10, \mathbf{p}'_{\bar{c}=\bar{u}}) \\
&\qquad \times u_{\Gamma,0}(-6, p_{c=u}, -9, -8) \qquad (5.156) \\
&= G_{1'-5-7,11} G_{5,6} G_{7,8} G_{9,10} u_{\Gamma,1}(-11, -10, 3', 2') \\
&\qquad \times u_{\Gamma,0}(-6, 4', -9, -8) \\
&\overset{G=G_{\text{phys}}}{=} G_5 G_6 G_{-4'-5+6} G_{1'+4'-6} u_{\Gamma,0}(\mathbf{p}'') u_{\Gamma,1}(\mathbf{p}''').
\end{aligned}$$

The external momentum variables for the leafs $u_{\Gamma,0}(\mathbf{p}'')$ and $u_{\Gamma,1}(\mathbf{p}''')$ are after the evaluation of G in the physical subspace, $\mathbf{p}'' = (p_5, p'_4, -p_6, -p'_4 - p_5 + p_6)$ and $\mathbf{p}''' = (p'_1 + p'_4 - p_6, p_6, p'_3, p'_2)$. Therefore, the evaluation of the deformations $u_{\Gamma,0}$, $u_{\Gamma,1}$ is again in the physical subspace. We are choosing the convention that the leaf on the left hand side of the grown branch of type Fig. 5.21 c) corresponds to the deformation depending on two external variables. In the example the deformation $u_{\Gamma,1}$, depending on two external variables, is represented by the left leaf whereas $u_{\Gamma,0}$, depending on one external variables, is represented by the right leaf, cf. Fig. 5.22 b).
In conclusion we see from this example that there are no further complications in evaluating the

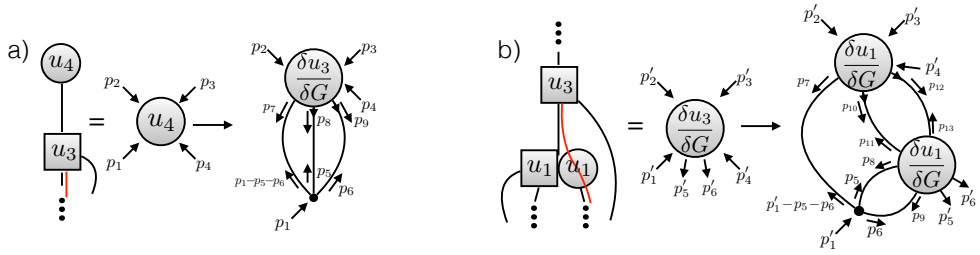

Figure 5.23.: Two consecutive stages in the tree expansion leading to the full rooted tree in Fig. 5.20 c). In this case both expansion stages involve functional derivatives. In order to indicate the correct momentum conservation (5.159) the legs of the leaf corresponding to the momentum variables of the functional derivatives carry additional arrows. a) The first stage of the expansion of $u_{\Gamma,4}$ is carried out with respect to the fourth line in (5.144). The dangling line on the leaf indicates the functional derivative whereas the red line indicates the bookkeeping of excess momentum carried by the derivative as discussed in the main text. b) In the second stage of the tree expansion $u_{\Gamma,3}$ is expanded with respect to the fifth line. The dangling functional derivative is not directly acting on the newly grown branch. Therefore, the red bookkeeping line goes straight through the leaf. In the diagrammatic expansion for the kernel this is indicated as an additional derivative for the leaf on the lower right hand side, cf. the fifth line in (5.144) which includes only the derivative of the upper leaf.

rooted tree diagram at $G = G_{\text{phys}}$ if the diagram contains no elements with functional derivatives. In this case the only information needed in each expansion stage is:

1. The external momentum variables of the leaf which is expanded.
2. The branch type into which the leaf is expanded.
3. The internal momentum variables over which is integrated.

This provides enough information to compute in each expansion stage the new external momentum variables for the newly grown leafs and therefore the tree expansion can be carried out recursively. Rooted tree diagrams with elements of type Fig. 5.21 d), e) need some further consideration. As an example consider Fig. 5.20 b) which contains a functional derivative.
As in the previous example the rooted tree is evaluated in the physical subspace by fixing the external momentum of the root to be $\mathbf{p} = (p_1, p_2, p_3, -p_1 - p_2 - p_3)$ and evaluate the kernel function corresponding to the branch of the corresponding branch type, Fig. 5.21 d), at translational invariant G. This is illustrated in Fig. 5.23 a).

$$\sum_{5,\dots,9} K^{(3)}(1,5,\dots,9)\frac{\delta u_{\Gamma,1}(-7,2,3,4)}{\delta G_{8,9}} = \tag{5.157}$$
$$G_{1-5-6,7}G_{5,8}G_{6,9}\frac{\delta u_{\Gamma,1}(-7,2,3,-1-2-3)}{\delta G_{8,9}} \overset{G=G_{\text{phys}}}{=}$$
$$G_{1-5-6}G_5G_6\frac{\delta u_{\Gamma,1}(\mathbf{p}')}{\delta G_{-5,-6}}.$$

The additional arrowheads on the two-point correlation function lines in Fig. 5.23 a) are indicating the connection to the functional derivative. Note that only the G-lines contributing to the kernel function are evaluated in the physical subspace. The functional derivative still depends on two momentum variables. We will show later how this has to be understood by considering the

differentiation of a kernel function. The G-lines without additional arrowheads are connected to the deformation such that the momentum carried by this line is contributing to the new external momentum of the newly grown leaf. In contrast to the previous examples without functional derivatives the external momentum $\mathbf{p}' = (p'_1, p'_2, p'_3, p'_4) = (1{-}5{-}6, 2, 3, {-}1{-}2{-}3)$ for $u_{\Gamma,1}$ does not automatically satisfy momentum conservation after the kernel function has been evaluated in the physical subspace of translational invariant G. There is an excess momentum carried by the functional derivative. Only if this excess momentum is taken correctly into account the momentum variables sum up to zero. The correct momentum conservation at the functional derivative terms can be found from the following argument.
The functional derivative of the four-point vertex function with respect to G gives a term which account for correlation functions on the 6-point level. We write this as

$$\begin{aligned} &\mathcal{O}_{\Gamma^{(6)}}(i_1, i_2, i_3, i_4; i_5, i_6) \equiv \frac{\delta\Gamma(i_1, i_2, i_3, i_4)}{\delta G(i_5, i_6)} \\ &= \frac{\delta\Gamma(p_1, p_2, p_3, p_4)}{\delta G(p_5, p_6)} e^{-i\sum_{n=1}^{4} p_n i_n} e^{i\sum_{n=5}^{6} p_n i_n}. \end{aligned} \tag{5.158}$$

In the subspace of physical correlation functions $\mathcal{O}_{\Gamma^{(6)}}$ depends only on the relative distances between the lattice sites $i_1, \ldots, i_6$. Therefore, in order to evaluate rooted trees with functional derivatives in the translational invariant subspace the correct momentum conservation at the functional derivative is $\delta(p_1 + p_2 + p_3 + p_4 - p_5 - p_6)$. We will also need the more general result for the momentum conservation with multiple functional derivatives

$$\begin{aligned} &\mathcal{O}_{\Gamma^{(4+N)}}(p_1, p_2, p_3, p_4; l_0, l_1, \ldots, l_{2N}, l_{2N-1}) \\ &= \frac{\delta\Gamma(p_1, p_2, p_3, p_4)}{\delta G(l_0, l_1) \ldots G(l_{2N}, l_{2N-1})} \times \\ &\qquad \delta(p_1 + p_2 + p_3 + p_4 - \sum_{n=0}^{2N-1} l_n). \end{aligned} \tag{5.159}$$

The functional derivative terms explicitly break momentum conservation on the four-point level but on a higher correlation function level it must always be satisfied with respect to the extended momentum conservation rule (5.159). The additional arrowheads on the G-lines, cf. Fig. 5.23 a), can also be viewed as indicating that these momenta are contributing with a minus sign in the extended momentum conservation rule. This consideration shows that (5.157) is a valid projection into the physical subspace and the tree expansion can now be carried on if the momentum conservation rule (5.159) is taken into account.
Diagrammatically the excess momenta carried by the functional derivatives are depicted as the previously introduced additional arcs which originate from leafs with functional derivatives and close on a branch, cf. Fig. 5.20 c).
We show in the following that once an arc closes on a branch, i.e., after the functional derivative acted on a kernel function, momentum conservation will be automatically restored on the four-point level.
We consider the example in Fig. 5.20 c). The analytic expression obtained in the first stage of the expansion of $u_{\Gamma,4}$ at fixed external momentum variables compatible with translational invariance $\mathbf{p} = (p_1, p_2, p_3, -p_1 - p_2 - p_3)$ is already given in (5.157) and illustrated in Fig. 5.23 a). In the second stage in Fig. 5.20 c) the leaf $u_{\Gamma,3}$ is further expanded with respect to the branch of type Fig. 5.21 e). This expansion process is illustrated in Fig. 5.23 b). The external momentum variables for $u_{\Gamma,3}(\mathbf{p}')$ are given by $\mathbf{p}' = (p'_1, p'_2, p'_3, p'_4) = (1{-}5{-}6, 2, 3, {-}1{-}2{-}3)$. The functional derivative with respect to the momentum variable $(p'_5, p'_6) = (-p_5, -p_6)$ does not act directly on the branch grown after the leaf with the functional derivative, $u_{\Gamma,3}$, but it acts on a branch grown from a

consecutive leaf. If the functional derivative would act on the branch grown from the functional derivative leaf, represented by the box, it would yield a second order functional derivative. But from Fig. 5.20 c) we see that it acts on the branch grown from the leaf without functional derivative. Therefore, we obtain an expression with two first order functional derivatives which is diagrammatically depicted in Fig. 5.23 b). The functional derivative with respect to $G(p_{10}, p_{12})$ originates from $u_{\Gamma,1}$, i.e., from the current branch type, whereas the derivative with respect to $G(p'_5, p'_6)$ originates from $u_{\Gamma,3}$. We consider the extended momentum conservation rule (5.159). The analytic expression corresponding to this expansion step is given by

$$\begin{aligned}
&\sum_{5,\ldots,13} K^{(4)}(1,5,\ldots,13)\frac{\delta u_{\Gamma,1}(-8,-11,-13,-9)}{G_{5',6'}} \\
&\qquad\times\frac{\delta u_{\Gamma,1}(-7,2',3',4')}{\delta G_{10,12}} \\
&= G_{1'-5-6,7}G_{10,11}G_{12,13}G_{5,8}G_{6,9}\frac{\delta u_{\Gamma,1}(-7,2',3',4')}{\delta G_{10,12}} \\
&\qquad\times\frac{\delta u_{\Gamma,1}(-8,-11,-13,-9)}{\delta G_{5',6'}} \\
&\overset{G=G_{\text{phys}}}{=} G_{1'-7-8}G_9G_{1'+2'+3'+4'-7-8-9}G_7G_8 \\
&\qquad\times\frac{\delta u_{\Gamma,1}(7,9,1'+2'+3'+4'-7-8-9,8)}{\delta G_{5',6'}} \\
&\qquad\times\frac{\delta u_{\Gamma,1}(1'-7-8,2',3',4')}{\delta G_{9,1'+2'+3'+4'-7-8-9}},
\end{aligned} \tag{5.160}$$

where we have established the generalized momentum conservation rule for $p_{12} = p'_1 + p'_2 + p'_3 + p'_4 - p_5 - p_6 - p_{10}$ and renamed in the last equality the integration variables in order to distinguish them from the integration variables of the previous expansion stage. This example shows that even though the functional derivative with respect to $G(5', 6')$ only acts on a branch consecutive to the leaf $u_{\Gamma,1}$ which for itself is not a leaf with a functional derivative the information about the excess momentum running over this leaf has to be stored. Therefore, an additional line through the rooted tree is drawn which indicates that the excess momentum has to be accounted for on the intermediate leafs by using the extended momentum conservation (5.159). The excess momentum is removed if the arc line meets the additional line. This additional diagrammatic element is shown as the red line in Fig. 5.20 b), c) and Fig. 5.23 a), b).
Finally, in the next two expansion stages the functional derivatives act on the branches. The functional derivative acting on a branch can be graphically depicted as just cutting out one of the two-point correlation function lines. This is shown in Fig. 5.24 for a particular example. It corresponds to the last expansion stage in Fig. 5.20 c) where the right leaf, $u_{\Gamma,1}$, is expanded. It is assumed that the t-permutation channel is picked. The external momentum of the leaf $u_{\Gamma,1}(\mathbf{p}'')$ is $\mathbf{p}'' = (7, 9, 1' + 2' + 3' + 4' - 7 - 8 - 9, 8)$. The analytic expression for the differentiated branch is given by

$$\left(\frac{\delta}{\delta G(5',6')}G_{5,6}G_{1+3-5,7}\right)u_{\Gamma,0}(-6,-7,2'',4'') \overset{G=G_{\text{phys}}}{=} G_{1''+3''-5'}u_{\Gamma,0}(\mathbf{p}'''). \tag{5.161}$$

The new external variable for the leaf grown from the differentiated branch, $u_{\Gamma,0}(\mathbf{p}''')$, is $\mathbf{p}''' = (-6', 1'' + 3'' - 10, 2'', 4'')$. Inserting the expression for the primed variables we find that $u_{\Gamma,0}$ is evaluated at $\mathbf{p}''' = (6,-6-8-9, 9, 8)$. Therefore, after the functional derivative has acted on the branch the excess momentum is annihilated and momentum conservation at the four-point level is restored.

The discussion of the examples in Fig. 5.20 provides enough information to write down a set of rules to construct and label all possible rooted trees. A second set of rules assigns to each diagrammatic element in a rooted tree an analytic weight. This makes it possible to design a Monte Carlo algorithm in the space of rooted trees which directly evaluates $\Gamma[G]$ in the subspace of translational invariant G. In the following we first write down the set of rules to construct and label a random rooted tree. The complete list of diagrammatic elements with their respective weights are tabulated in App. D and E.
We would also like to note that the above examples only discuss the case where the physical subspace is defined by translational invariance. With the same line of arguments it is possible to obtain the construction and evaluation of $\Gamma[G]$ in a physical subspace for general symmetries defined by the collective index space, cf. (5.32), (5.122), and (5.123).
The HAM gives a series solution for $\Gamma[G]$ which sums over all deformations $u_{\Gamma,m}$. Thus rooted trees of arbitrary expansion order m have to be considered.

The rules to generate a random rooted tree in the tree expansion of an arbitrary $u_{\Gamma,m}$ with external momentum variables $\mathbf{p}$ are.

1. Grow a random branch from the root, i.e., select the expansion of the root into one of the branch types in Fig. 5.21. For this choice we assign the labels (k,b,d). The label k stands for the number of leafs grown from the branch, k=1,2. The label b = bare, bold for whether the analytic expression for the branch involves contributions from two-point correlation functions and d = True, False whether one of the leafs is a functional derivative. Thus the respective labeling for the branch types in Fig. 5.21 are a): (1,bare,False), b) (1,bold,False), c) (2,bold,False), d) (1,bold,True), e) (2,bold,True). The probability to select the chosen (k,b,d) is stored in $\mathrm{p}_{\text{a-priori}}$ in order to obtain the a-priori probability for the fully grown rooted tree which is needed for the Monte Carlo process.

2. According to the randomly picked branch type add the respective number of leafs with their given type to the tree.
   If a branch type with k=2 was picked one term in the sum $\sum_{i=0}^{m-1}$ has to be chosen randomly, cf. (5.144), and the probability for that choice is multiplied to $\mathrm{p}_{\text{a-priori}}$.
   If a branch type with b=bold and d = False was pick one channel of external leg permutations in the sum $\sum_c$ has to be chosen randomly, cf. (5.144), and the probability for that choice is multiplied to $\mathrm{p}_{\text{a-priori}}$.
   Depending on the branch type new momentum variables have to be seeded randomly. These are D-dimensional random vectors in the first Brillouin zone. The number of new momentum variables for the possible types are: a) 0, b) 1, c) 2, d) 2, e) 3. The probability

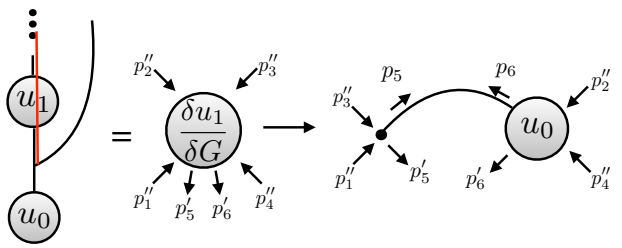

Figure 5.24.: A functional derivative is acting on a branch. In this stage of the tree expansion the grown branch corresponds to the second line in (5.144). Therefore, the functional derivative can act on one of the two G lines which is equivalent to cutting out one of them. The momentum carried by the functional derivative is assigned to the open ends produced in that way.

for the choice of momentum variables is multiplied to $\mathrm{p}_{\text{a-priori}}$.
For the branch type c), e) there are two newly grown leafs. For c) there are two new momentum variables. We assign the left leaf to represent the deformation evaluated at two external momentum variables and the right leaf depending on only one. We choose the convention that the first of the two momentum variable is assigned to the left leaf whereas the right leaf depends on both variables.
For e) there are three momentum variables. The leaf with the functional derivative depends only on two of the three randomly seeded momentum variables. We choose the convention that the the first two of these variables are assigned to the functional derivative leaf and the right leaf depends on all three variables.

3. For each of the new leafs, $u_{\Gamma,m'}$, if $m' > 0$ consider this leaf as a new root and go to 1. If $m' = 0$ a new branch can not be grown.

4. Start a search through the fully grown rooted tree. For each functional derivative encountered choose randomly a branch consecutive to the functional derivative leaf. This branch will be differentiated by the functional derivative and therefore the additional bookkeeping line is established. The probability for each choice is multiplied to $\mathrm{p}_{\text{a-priori}}$.

5. Start a search through the fully grown rooted tree. If a differentiated branch is encountered pick randomly a term in the respective list of differentiated kernel functions, cf. App. E. Correspondingly, reduce the number of momentum variables of the differentiated branch. The probability for each choice is multiplied to $\mathrm{p}_{\text{a-priori}}$.

6. Start a search through the fully grown rooted tree. For each expansion stage determine the new external momentum variables of the leafs grown in this expansion stage. This is done with respect to the extended momentum conservation rule (5.159), cf. also App. D, E.

7. Start a search through the fully grown rooted tree. As the momentum variables are now correctly assigned the complete weight of the rooted tree can be determined by multiplying the contributions from the kernel functions and from $u_{\Gamma,0}$ at each expansion into a variable w_{tree}.

Therefore, after having applied the above rules a randomly grown rooted tree is obtained with a corresponding weight w_{tree}. Together with the a-priori generation probability $\mathrm{p}_{\text{a-priori}}$ this is sufficient to perform a direct sampling of the tree expansion by the rules of detailed balance. Therefore, we obtain a stochastic summation of the HAM series solution for the functional integro-differential equation defining $\Gamma[G]$.
We find it convenient to extend the direct sampling of diagram topologies with a Markov chain sampling of the integration variables. For that we randomly pick a single integration variable of a rooted tree and suggest to update this integration variable by adding a random shift in that momentum variable. After the integration variable has been changed we start from step 6 in the above set of rules to generate a new weight for the tree with the new integration variable. Together with detailed balance this is used to perform a Markov chain sampling of the integration variables. In order to achieve good acceptance ratios for the direct sampling of rooted tree topologies we restrict the randomly seeded integration variables in each stage of the tree expansion to belong to a small region around zero momentum. Therefore, we rely on the Markov chain sampling of integration variables to obtain the integration over the complete first Brillouin zone. This leads to sampling problems for higher deformation orders because the sampling can get stuck in a random rooted tree topology. A Markov chain Monte Carlo algorithm has to be used which also samples diagram topologies and not only integration variables. Therefore, a better starting point to include the functional derivatives, compared to randomly suggesting a rooted tree, is the algorithm developed in Sec. 5.4.

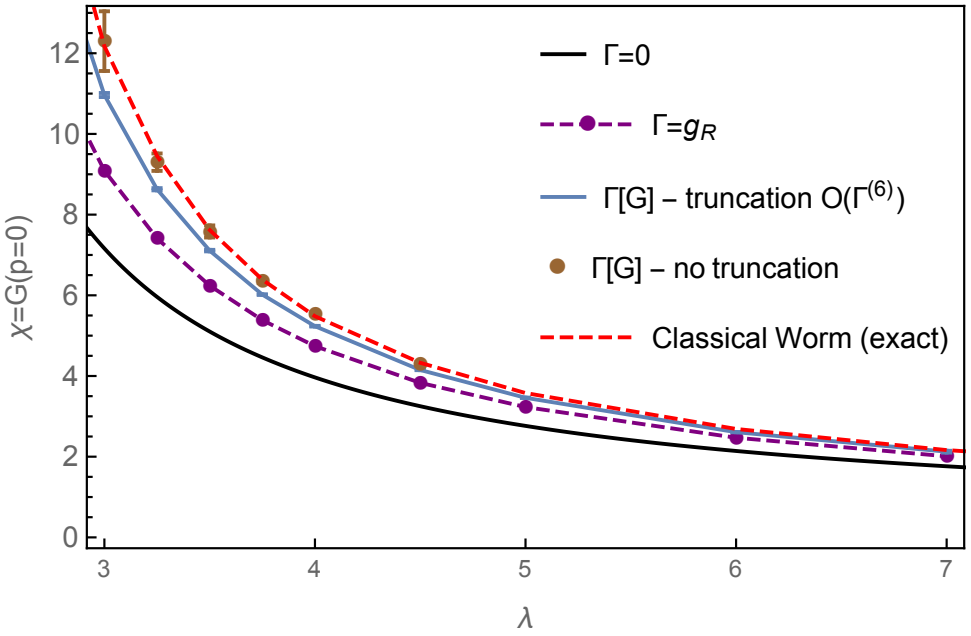

Figure 5.25.: The development of the divergence of the susceptibility $\chi = G(p = 0)$ close to the phase transition for the model (5.120). Various approximations of the universal functional $\Gamma[G]$ yield systematic, quantitative errors whereas the full solution captures the correct quantitative behavior. The black, dashed purple and blue lines were obtained in the previous subsection and correspond to different truncations of the functional $\Gamma[G]$. The black approximation corresponds to $\Gamma[G] = 0$, the dashed purple line to $\Gamma[G] = g_R = \lambda \left(1 + 3\lambda/2 \int_p G(p)^2\right)^{-1}$ and the blue line to the truncation of $\Gamma[G]$ which takes in account only the first three diagram elements on the right hand side of Fig. 5.3 in the functional integro-differential equation for $\Gamma[G]$ i.e. corrections of the order of the 6-point vertex function $\Gamma^{(6)}$ are neglected.

Results

Fig. 5.25 shows the result for the divergence of the susceptibility χ for successive approximations of $\Gamma[G]$ and for the full solution of the functional integro-differential equation. It should be pointed out that the coupled set of equations, Fig. 5.3, are defining the FT (5.120) directly in the thermodynamic limit, i.e., results obtained by our method are for infinite system sizes. The results are compared to the numerically exact simulation of model (5.120) with the classical Worm algorithm [77] on system sizes which are much larger than the correlation length. We find that it is possible to obtain controlled results with our current Monte Carlo algorithm up to $\chi \sim 10$ which corresponds to a correlation length of $\xi \sim 3$. Our diagrammatic Monte Carlo sampling is based on a direct sampling of all topologies of rooted tree diagrams at a given order. This naive approach leads to sampling problems at higher deformation orders and restricts the order to 5-6. Due to the sign alternation between the linear and quadratic terms in the vertex equation the sampling suffers from a sign problem discussed in the previous subsection for the case of the stochastic construction of a truncated functional. We find no qualitative difference if the functional derivative terms are added. We performed extensive Monte Carlo simulations such that the error bars are exclusively determined by the extrapolation of the lowest deformation orders as is shown in Fig. 5.26. It is only possible to extrapolate the inverse of the two-point correlation function and therefore the error introduced through the extrapolation is growing rapidly as the susceptibility diverges, cf. Fig. 5.25. It should be pointed out that we have no global excess to $\Gamma[G]$ but only to a stochastic, local evaluation of the universal functional through

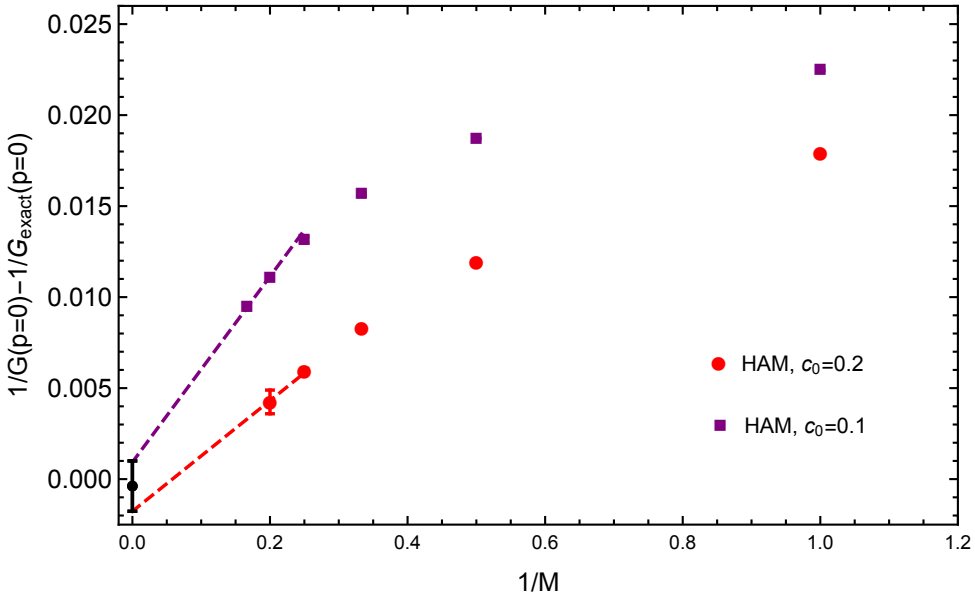

Figure 5.26.: In order to obtain an error estimate for the extrapolation of the homotopy series we use a linear extrapolation for different deformation parameters c_0. We make sure within errorbars that results extrapolate to the same value for different c_0. The plot shows the results for $\lambda = 3.5$ where the correlation length is already large enough such that there are considerable deviation from the exact result if only a truncated functional $\Gamma[G]$ has been considered, cf. Fig. 5.25.

the diagrammatic Monte Carlo sampling of the HAM series solution in terms of rooted tree diagrams. In order to obtain the results in Fig. 5.25 through this evaluation of $\Gamma[G]$ we simplified the calculation by starting the fixed point iteration for the coupled system in Fig. 5.3 at the numerically exact two-point correlation function. This reduces the computational time as we have to perform only a single fixed point iteration step. For more general starting points of the fixed point iteration we refer to the previous subsection. Figs. 5.25 and 5.26 show that, although there is no single physical small parameter close to the phase transition, we obtain controlled results as we can construct the homotopy (5.59) always with respect to a small enough c_0. In the vicinity of the second order phase transition, $||G|| \to \infty$ implies that $c_0 \to 0$ but in order to get meaningful results, the number of required deformations increases rapidly. Therefore, due to the limited number of deformations which can be computed with our algorithm we can not go closer to the phase transition. For transitions where $||G||$ remains finite (the divergence may then occur in the four-point vertex function), this argument is not applicable.

Although the approach to FT introduced in this work is illustrated for the simple though representative case of ϕ^4-theory, models with arbitrary 2-body interactions in its symmetric phase can be tackled on the same footing. As shown in Sec. 5.2 the transition from the functional integral representation for general models to functional integro-differential equations yields exactly the same set of equations as depicted in Fig. 5.3. The only difference is that the convolution of indices in the diagrams representing the functional integro-differential equation is with respect to a collective index i which summarizes all possible field labels of the considered model. The statistics of fermionic fields translate into additional signs for the permutations of external indices in the diagrams of Fig. 5.3 and into sign alternating two-point correlation functions.

5.5.3. Semi-analytic solution of the Dyson-Schwinger equation in the functional integro-differential representation

Up to now we used the HAM for the 2D ϕ^4 model to construct a series representation of the universal function $\Gamma[G]$ around the non-interacting limit. We showed how to obtain controlled results, even in the strongly correlated regime, by introducing the auxiliary convergence control parameter c_0. In this section we will discuss the extension of the construction of the homotopy around the analytic solvable ladder approximation from the 0D toy model to a realistic field theory.
In order to solve the functional integro-differential equation (5.141) for ϕ^4 theory in 2D we consider the homotopy

$$\mathcal{H}[\phi[G,q]] = (1-q)\mathcal{L}_{\text{ladder}}[\phi[G,q]] + c_0 q \mathcal{N}[\phi[G,q]] = 0. \tag{5.162}$$

Again, $\mathcal{N}$ is the non-linear operator defining (5.141) and now $\mathcal{L} = \mathcal{L}_{\text{ladder}}$ is given by

$$\mathcal{L}_{\text{ladder}}[\Gamma[G]] = \Gamma_{1,2,3,4} - \lambda\delta_{1+2+3,-4} + \frac{\lambda}{2}\sum_{5,6,7} G_{5,6}G_{1+2-5,7}\Gamma_{-7,-6,3,4}. \tag{5.163}$$

The HAM series solution,

$$\Gamma[G] = u_{\Gamma,0}[G] + \lim_{M\to\infty}\sum_{m=1}^{M} u_{\Gamma,m}[G] = \phi[G,0] + \lim_{M\to\infty}\sum_{m=1}^{M}\frac{1}{m!}\frac{\mathrm{d}^m\phi[G,q]}{\mathrm{d}q^m}\bigg|_{q=0}, \tag{5.164}$$

is given by the HAM series coefficients $u_{\Gamma,m}$ satisfying for $m \geq 1$,

$$\begin{aligned}
u_{\Gamma,m}(1,2,3,4) &= f_m(1,2,3,4) - \frac{\lambda}{2}\sum_{5,6,7} G_{5,6}G_{1+2-5,7}u_{\Gamma,m}(-7,-6,3,4),\\
f_m(\mathbf{p}) &= (1-c_0)\left[u_{\Gamma,m-1}(\mathbf{p}) - \lambda\delta(\mathbf{p})\delta_{m,1} + \frac{\lambda}{2}\sum_{5,6,7} G_{5,6}G_{1+2-5,7}u_{\Gamma,m-1}(-7,-6,3,4)\right]\\
&\quad - c_0\left[\frac{\lambda}{2}\sum_{c\in\{u,t\}}\sum_{5,6,7} K_c^{(1)}(\mathbf{p}_c,5,6,7)u_{\Gamma,m-1}(-7,-6,\mathbf{p}_{\bar{c}})\right.\\
&\quad - \frac{\lambda}{6}\sum_{c}\sum_{5,\ldots,11} K_c^{(2)}(\mathbf{p}_c,5,\ldots,11)\sum_{k=0}^{m-1} u_{\Gamma,k}(-11,-10,\mathbf{p}_{\bar{c}})\,u_{\Gamma,m-1-k}(-6,p_c,-9,-8)\\
&\quad + \frac{\lambda}{3}\sum_{5,\ldots,9} K^{(3)}(1,5,\ldots,9)\frac{\delta u_{\Gamma,m-1}(-7,2,3,4)}{\delta G_{8,9}} -\\
&\quad \left. - \frac{\lambda}{6}\sum_{5,\ldots,13} K^{(4)}(1,5,\ldots,13)\sum_{k}^{m-1} u_{\Gamma,m-1-k}(-8,-11,-13,-9)\frac{\delta u_{\Gamma,k}(-7,2,3,4)}{\delta G_{10,12}}\right].
\end{aligned} \tag{5.165}$$

We we use the notations of (5.144) in the above equation and

$$u_{\Gamma,0}(1,2,3,4) = \lambda\delta_{1+2+3,-4} - \frac{\lambda}{2}\sum_{5,6,7} G_{5,6}G_{1+2-5,7}u_{\Gamma,0}(-7,-6,3,4). \tag{5.166}$$

In order to obtain a recursion relation for the HAM series coefficients we have to solve the above Bethe-Salper-like equation. Without assuming translational symmetry the solution is formally

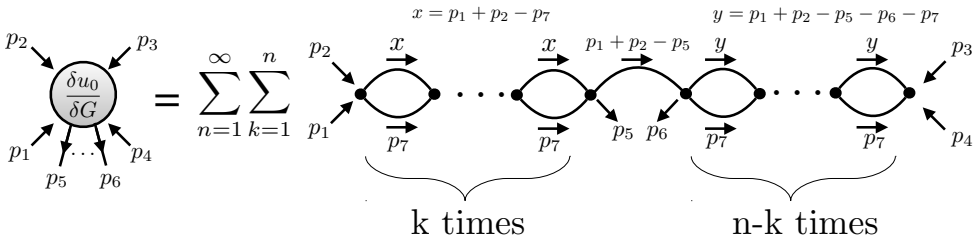

Figure 5.27.: The power series representation of the functional derivative of the zeroth order deformation $u_{\Gamma,0}(1,2,3,4)$ with respect to $G(5,6)$ in the case the homotopy is constructed around the ladder truncation.

given by,

$$\begin{aligned} u_{\Gamma,m}(1,2,3,4) =& f_m(1,2,3,4) - \frac{\lambda}{2}\sum_{5,6,7} G_{5,6}G_{1+2-5,7}f_m(-7,-6,3,4) \\ &+ \left(\frac{\lambda}{2}\right)^2 \frac{\lambda}{2}\sum_{5,6,7,5',6',7'} G_{5,6}G_{1+2-5,7}G_{5',6'}G_{-6-7-5',7'}u_{\Gamma,m}(-7',-6',3,4) \\ =& f_m(1,2,3,4) + \sum_{n=1}^{\infty}\left(-\frac{\lambda}{2}\right)^n \sum_{5^{(1)},6^{(1)},7^{(1)},\ldots,5^{(n)},6^{(n)},7^{(n)}} \\ &\times \prod_{i=1}^{n} G_{5^{(i)},6^{(i)}}G_{-6^{(i-1)}-7^{(i-1)}-5^{(i)},7^{(i)}}f_m(-7^{(n)},-6^{(n)},3,4), \end{aligned} \tag{5.167}$$

where we denote $1 = -6^{(0)}$, $2 = -7^{(0)}$. For the translational invariant case, $G(1,2) = G(1)\delta_{1,-2}$, this complicated expression, after evaluating the delta functions due to translational invariance, has a closed form solution,

$$\begin{aligned} u_{\Gamma,m}(1,2,3,4) \overset{G=G_{\text{phys}}}{=}& f_m(1,2,3,4) + \sum_{n=1}^{\infty}\left(-\frac{\lambda}{2}\sum_5 G_5 G_{1+2-5}\right)^{n-1} \\ &\times\left(-\frac{\lambda}{2}\sum_5 G_5 G_{1+2-5}f_m(1+2-5,5,3,4)\right) \\ =& f_m(1,2,3,4) - \frac{\frac{\lambda}{2}\sum_5 G_{1+2-5}G_5 f_m(1+2-5,5,3,4)}{1+\frac{\lambda}{2}\sum_5 G_{1+2-5}G_5}, \end{aligned} \tag{5.168}$$

which is the desired recursion relation for the HAM series coefficients lending itself to a statistical interpretation as we showed in the previous sections. Nevertheless, as we also discussed in the previous section, we have to know, at least formally, the solution in absence of any symmetry in order to take the functional derivative before restoring the respective symmetries. In particular, consider the example of the functional derivative of the zeroth order deformation,

$$\begin{aligned} \frac{\delta u_{\Gamma,0}(1,2,3,4)}{\delta G(5,6)} =& \lambda\sum_{n=1}^{\infty}\sum_{k=0}^{n-1}\sum_{5^{(1)},\ldots,7^{(n)}}\left(-\frac{\lambda}{2}\right)^k\prod_{i=1}^{k}G_{5^{(i)},6^{(i)}}G_{-6^{(i-1)}-7^{(i-1)}-5^{(i)},7^{(i)}} \\ &\times(-\lambda)G_{-6^{(k)}-7^{(k)}-5,7^{(k+1)}}\delta_{6,6^{(k+1)}} \\ &\times\left(-\frac{\lambda}{2}\right)^{n-1-k}\prod_{i=k+2}^{n}G_{5^{(i)},6^{(i)}}G_{-6^{(i-1)}-7^{(i-1)}-5^{(i)},7^{(i)}}\delta_{7^{(n)},3+4-6^{(n)}} \end{aligned}$$

$$
\begin{aligned}
\overset{G=G_{\text{phys}}}{=} \quad & -\lambda^2 G_{1+2-5} \sum_{n=1}^{\infty} \sum_{k=1}^{n} \left(-\frac{\lambda}{2} \sum_{7} G_7 G_{1+2-7} \right)^{k-1} \\
& \times \left(-\frac{\lambda}{2} \sum_{7} G_7 G_{1+2-5-6-7} \right)^{n-k} \\
= \quad & -\frac{\lambda^2 G_{1+2-5}}{\left(1 + \frac{\lambda}{2} \sum_7 G_7 G_{1+2-7}\right) \left(1 + \frac{\lambda}{2} \sum_7 G_7 G_{1+2-5-6-7}\right)}.
\end{aligned}
\tag{5.169}
$$

Fig. 5.27 illustrates this result in diagrammatic language. Moreover, the result can be used to calculate the functional derivative of the denominator in (5.168). The functional derivative of the numerator f_m was already discussed in great detail in the previous section. Therefore, with this result we can generalize the expansion of the HAM in terms of rooted tree diagrams and consequently the associated Monte Carlo algorithm. In general, we see that it is possible to construct homotopies around (truncated) quantum field theories where an analytic solution can be written down. Although in this work we have not yet presented the detailed numerical implementation of the homotopy series around such analytic solutions we have worked out all the necessary analytical and technical building blocks. With this we conclude the discussion of the homotopy approach to quantum field theoretic calculations of many-body systems. Although we have not yet applied this new approach to the model systems driving our research we worked out all the basic techniques and have laid the foundations of a novel and powerful approach beyond perturbative techniques.

6

Conclusion and Outlook

This thesis deals with various computational and analytical aspects of the study of strongly correlated systems. In the first part of the thesis we used the renormalization group approach together with first-principles classical Monte Carlo simulations to investigate the strong disorder regime of systems allowing for a two-dimensional (2D) hydrodynamic description, e.g., for one-dimensional interacting quantum systems. We unambiguously demonstrated the existence of a new universality class - the scratched-XY universality class - in the strong disorder regime. This criticality describes the destruction of the low temperature critical superfluid phase by a mechanism fundamentally different from the proliferation of topological defects. In order to show that, we studied the finite-temperature superfluid transition in the scratched-XY model, a modified two-dimensional XY model with power-law distributed "scratch"-like bond disorder. The disorder grows stronger as Γ, characterizing the exponent $1/\Gamma - 1$ of its power law disorder distribution, decreases. We used the asymptotically exact semi-renormalization group theory introduced by Pollet et al. [65, 66, 67], which was previously developed in the context of the superfluid-insulator transition in one-dimensional disordered quantum systems, to analytically obtain the renormalization group flow of the superfluid stiffness. This theory predicts the slow renormalization of the superfluid stiffness due to the collective effect of the Kane-Fisher physics [63, 64] of scale-dependent scratches over several length scales, which eventually leads to a phase transition in the strong disorder regime. The hallmark of this new criticality is that the microscopic, irrenormalizable parameter $\zeta = 1 - \Gamma$ enters the equations and determines the non-universal jump of the superfluid stiffness Λ_c at the transition point, $K_c = 1/\zeta$ in contrast to $K_c = 2$ for the BKT universality. Classical Monte Carlo simulations are used to numerically obtain the renormalization group flow of the superfluid stiffness with system size. We found that this flow is perfectly described by the one analytically obtained from the theory of Pollet et al. and therefore, these results unambiguously demonstrated the existence of the scratched-XY universality class. At a temperature $T = 0.2$, we obtained $K_c = 4.24(4)$, where $K_c = \pi\Lambda_c/T$ and Λ_c is the superfluid stiffness at criticality, consistent with the strong disorder scenario $K_c > 2$. One of the key insights, which brought the necessary analytic control and made a solid numerical proof of the scratched-XY universality feasible, is equally well important for the design of possible experimental systems realizing this universality class. The disorder must couple directly through a power law to the phase fluctuations of the effective bosonic degrees of freedom because otherwise this power law has to be determined from measurements of a large collection of samples.
From the theoretical side, an interesting question is how the scratched-XY universality class is connected to the BKT universality class at weak disorder. We have established the nature of the finite-temperature phase transition in the strong disorder regime, which deep in the strong disorder regime happens at low temperatures and large values of K. Therefore, the renormalization of the superfluid stiffness by thermally excited vortex–anti-vortex pairs, which drive the transition at weak disorder, can be neglected. At intermediate strength of disorder, where $K_c \gtrapprox 2$, this renormalization due to vortex–anti-vortex pairs has to be taken into account on the same footing as the renormalization from scale dependent scratches. Due to the extent of

the vortex–anti-vortex pairs in two dimensions - in contrast to the "vertical" vortex–anti-vortex-pairs in disordered one-dimensional quantum systems [54, 58] - this may not simply result in a superposition of both mechanisms.

In the second part of the thesis we introduced a new computational approach for the study of strongly correlated systems. We first argued that the flexibility of perturbative series expansion techniques in the quantum field theoretic description of strongly correlated systems is the key to overcome the limitations of existing computational techniques. However, the power of this approach crucially hinges upon the convergence properties of the perturbative series. In general, perturbative series expansions around exactly solvable non-interacting theories have zero or finite convergence radius and are not valid in the strongly correlated regime. In the second part of this thesis we proposed to set up series expansion techniques not in a functional integral formulation but in the language of functional integro-differential equations. The functional closure of the Dyson-Schwinger equation is introduced in order to obtain a functional integro-differential equation, which defines a universal functional $\Gamma[G]$. Evaluating this functional at the physical two-point correlation function G yields the physical four-point vertex function Γ. A self-consistent iteration scheme can be devised that uses the functional $\Gamma[G]$ such that upon convergence of the self-consistency, the physical two-point correlation function and consequently the physical four-point vertex function are calculated. The universal functional $\Gamma[G]$ is constructed through the solution of the functional integro-differential equation defining $\Gamma[G]$ beyond any truncation scheme. This solution is obtained by introducing a homotopy approach, the homotopy analysis method, which provides a series expansion scheme more powerful than perturbative series expansion techniques already for the simplest case where the homotopy is constructed around the non-interacting limit. Moreover, we showed that, in general, the homotopy can be constructed around truncated though analytic solvable interacting field theories and in that way overcomes the usual paradigms of perturbative field theory. In order to evaluate the resulting homotopy series at larger orders, we first developed the diagrammatic language of rooted tree diagrams and afterwards introduced a Monte Carlo sampling to stochastically sum up all rooted tree diagrams contributing to the series. Using these newly developed techniques, we provided a full and unbiased solution to the Dyson-Schwinger equation beyond any truncation scheme illustrated for ϕ^4 theory on a 2D square lattice in its strongly correlated regime close to a second-order phase transition. These results should be considered as a solid numerical benchmark for the validity of the introduced approach. In future work we first will have to focus on the extension of the present numerical implementation to numerically construct the functional $\Gamma[G]$ with respect to the homotopy around the ladder summation. We derived the resulting homotopy series in Sec. 5.5.3 but have not yet presented the numerical results for the homotopy construction around the ladder summation. With that adaptation it may be possible, without further improvements, to study the strongly correlated regime of the $O(2)$ symmetric ϕ^4 model in 2D, which undergoes a BKT transition but, contrary to the simpler classical XY model, takes into account density and phase fluctuations on equal footing. This would be a striking demonstration of the power of the homotopy approach as it would constitute a first-principles quantum field theoretic series expansion technique which can generically deal with non-Borel resummable, non-perturbative features such as the vortices driving the BKT transition. These results may then serve as the starting point for the study of more challenging bosonic lattice models in 2D where standard quantum Monte Carlo approaches suffer from a prohibitive sign problem. Moreover, we are confident that the results carry over to interacting fermionic systems, where in a first step the existing numerical implementation can be adapted to obtain the benchmark for the Anderson impurity model or Hubbard atom. This benchmark is of even more fundamental interest as it has been shown [119] that self-consistent approaches relying on the perturbative construction of the two-particle irreducible Luttinger-Ward functional $\Phi[G]$ can converge to wrong answers.

Therefore, it is necessary and interesting to show that our newly developed self-consistent approach, which relies on the one-particle irreducible functional $\Gamma[G]$, does not run into this kind of problems. Moreover, the developed approach is perfectly adapted to the phenomenology of the pseudogap regime of the Hubbard model [120, 30], which is signaled by strong non-perturbative features on the single particle level [121] arising out of short range antiferromagnetic fluctuations [122, 123, 124].

Appendix

A

The superfluid stiffness in the presence of a single weak barrier

We consider the continuum model

$$\begin{aligned} Z &= \int \mathrm{d}(\theta_i)\, e^{-S[\theta_i]} \qquad \text{where} \\ S[\theta_i] &= \sum_i \frac{\Lambda}{2T} \int_{-L}^{L} \mathrm{d}x\mathrm{d}y\, (\nabla\theta_i(\mathbf{r}))^2 - \frac{t}{T} \int_{-L}^{L} \mathrm{d}y\, \cos(\theta_+(y) - \theta_-(y)) \end{aligned} \tag{A.1}$$

in a finite box of linear size $2L$ and $\Lambda = \Lambda_\mu(L, 2L)$, $\mu \in \{x, y\}$ is the microscopic superfluid stiffness of the homogenous system of size $L_x = L$, $L_y = 2L$ in μ-direction. The measure of the functional integral over θ_i is denoted by $\mathrm{d}(\theta_i)$, $\mathbf{r} = (x, y)$, and θ_-, θ_+ are the values of the left and right phase field at $x = 0$, i.e., $\theta_-(y) = \theta_1(0, y)$ and $\theta_+(y) = \theta_2(0, y)$.
We calculate the superfluid stiffness in x-direction for the whole system in the limit of large β. The superfluid stiffness in x-direction is defined by

$$\Lambda_x = 2\frac{L_x}{L_y} \frac{[F_{L_x,L_y}(\phi) - F_{L_x,L_y}(0)]}{\phi^2}, \tag{A.2}$$

where $F(L_x, L_y)(\phi)$ is the free energy $F = -T \ln Z$ of a system of size L_μ in μ-direction in the presence of a phase twist ϕ. At $T = 0$ one can simply minimize $TS_{2L,2L}(\phi)$, where $S_{2L,2L}(\phi)$ is the action of a system of linear size $2L$ with fixed finite phase twist $\theta = \phi\, x/2L$,

$$\begin{aligned} TS_{2L,2L}(\phi) &= \frac{1}{2}\Lambda_x(2L, 2L)\phi^2 \\ &= \frac{1}{2}\frac{2L}{L}\Lambda_x(L, 2L)\phi_1^2 + \frac{t2L}{2}\phi_{1,2}^2 + \frac{1}{2}\frac{2L}{L}\Lambda_x(L, 2L)\phi_2^2 \\ &= 2\Lambda_x(L, 2L)\phi_1^2 + \frac{t2L}{2}\phi_{1,2}^2 \approx 2\Lambda_x(L, L)\phi_1^2 + \frac{t2L}{2}\phi_{1,2}^2, \end{aligned} \tag{A.3}$$

where $\phi = \phi_1 + \phi_{1,2} + \phi_2$ and $\phi_1 = \phi_2$. The minimum for a given fixed phase twist ϕ is reached for

$$\phi_1 = \frac{t\ 2L}{2\Lambda_x(L, L) + 2t\ 2L}\phi \tag{A.4}$$

which leads to

$$\Lambda_x(2L, 2L)^{-1} = \Lambda_x(L, L)^{-1} + ((2L)t)^{-1}. \tag{A.5}$$

For a infinite system Λ_x is not renormalized by a single barrier in accordance with the result of Kane and Fisher [63, 64]. For finite but large β the free energy can be evaluated by the method of steepest decent around the saddle point solution found for $T = 0$.

B

Perturbative calculation of the beta function

In this section we review the perturbative calculation of the beta function for the $\mathcal{Z}_2$ symmetric ϕ^4 model

$$\begin{aligned} Z &= \int \mathrm{d}(\phi) e^{-S[\phi]} \quad \text{where} \\ S[\phi] &= \int \mathrm{d}^D x \, \frac{1}{2}(\nabla\phi_B)^2 + \frac{m_B^2}{2}\phi_B^2 + \frac{\lambda_B}{4!}\phi_B^4, \end{aligned} \tag{B.1}$$

A regularization by a large momentum cutoff Λ is assumed to make the functional integral, denoted by its measure $\mathrm{d}(\phi)$, a well defined mathematical object. The continuum limit, $\Lambda \to \infty$, in $2D$ can be taken by introducing the counterterm δm_I^2 in a reparametrization

$$\phi_B = \phi_I \tag{B.2}$$

$$\lambda_B = 6 m_I^{4-D} \lambda_I \tag{B.3}$$

$$m_B^2 = m_I^2 + \delta m_I^2 \tag{B.4}$$

$$\text{where} \quad \delta m_I^2 = -\frac{\lambda_I}{2} \int_\Lambda \mathrm{d}^2\mathbf{p} \, G_0(\mathbf{p}). \tag{B.5}$$

The non-interacting 2-point correlation function is given by

$$G_0(\mathbf{p}) = (\mathbf{p}^2 + m_I^2)^{-1}. \tag{B.6}$$

The perturbative expansion of the n-point correlation function $G^{(n)}(x_1, \ldots, x_n)$ is given by

$$\begin{aligned} G^{(n)}(x_1, \ldots, x_n) &= \frac{1}{Z} \int \mathrm{d}(\phi) e^{-S[\phi]} \phi(x_1) \ldots \phi(x_n) \\ &= \lim_{M\to\infty} \sum_{m=0}^{M} \frac{(-1)^m}{m!} \int \mathrm{d}y_1 \ldots \mathrm{d}y_m \\ &\quad \times \langle \phi(x_1) \ldots \phi(x_n) \prod_{i=0}^{m} \left(\frac{\delta m_I}{2} \phi_I^2(y_i) + \frac{m_I^{4-D}}{4} \lambda_I \phi^4(y_i) \right) \rangle_0 \end{aligned} \tag{B.7}$$

and we denote $G^{(2)} = G$ as usual and

$$\langle \ldots \rangle_0 = \frac{1}{Z} \int \mathrm{d}(\phi) e^{-S_0[\phi]} \ldots \, . \tag{B.8}$$

The average $\langle \ldots \rangle_0$ is evaluated using Wicks theorem [91] where each generated term in this evaluation can be diagrammatically represented by standard Feynman diagrams with respect to the non-interacting 2-point correlation function G_0. Since the normalization of the functional

integral in $\langle \dots \rangle_0$ is with respect to the full partition function Z all Feynman diagrams including vacuum bubbles are set to zero. The introduced counterterm δm_I^2 sets all Feynman diagrams including tadpole subdiagrams to zero and therefore the theory is free of any divergencies in the limit $\Lambda \to \infty$. The connected 4-point correlation function is given by

$$\begin{aligned} G_c^{(4)}(x_1,x_2,x_3,x_4) = G^{(4)}(x_1,x_2,x_3,x_4) \\ - G(x_1,x_2)G(x_3,x_4) - G(x_1,x_3)G(x_2,x_4) - G(x_1,x_4)G(x_2,x_3) \end{aligned} \tag{B.9}$$

and we introduce the one-particle irreducible objects $\Gamma^{(2)}$, the inverse of the 2-point correlation function and Γ, the 4-point vertex function,

$$\begin{aligned} \int \mathrm{d}^D x_3 \Gamma^{(2)}(x_1,x_3)G(x_3,x_2) &= \delta(x_1-x_2) \\ G_c^{(4)}(x_1,x_2,x_3,x_4) &= \int \mathrm{d}^D x_5 \dots \mathrm{d}^D x_8 \; G(x_1,x_5)G(x_2,x_6)G(x_3,x_7)G(x_4,x_8) \\ &\quad \times \Gamma(x_5,x_6,x_7,x_8). \end{aligned} \tag{B.10}$$

The perturbative series expansion of this objects at selected external momentum points are given by [92]

$$\begin{aligned} \frac{\Gamma^{(2)}(0)}{m_I^2} &= 1 - 1.4249247346311\lambda_I^2 + 3.7798975113\lambda_I^3 - 13.1529123(81)\lambda_I^4 \\ &\quad +57.50923(15)\lambda_I^5 - 295.3633(20)\lambda_I^6 + 1723.533(29)\lambda_I^7 \end{aligned} \tag{B.11}$$

$$\begin{aligned} \frac{\partial_{p^2}\Gamma^{(2)}(\mathbf{p})\big|_{p=0}}{m_I^2} &= 1 - 0.069690176974\lambda_I^2 + 3.7798975113\lambda_I^3 - 13.1529123(81)\lambda_I^4 \\ &\quad +57.50923(15)\lambda_I^5 - 295.3633(20)\lambda_I^6 + 1723.533(29)\lambda_I^7 \end{aligned} \tag{B.12}$$

$$\begin{aligned} \frac{\Gamma(0,0,0,0)}{m_I^2} &= 24\lambda_I - \frac{216}{\pi}\lambda_I^2 + 270.8452888\lambda_I^3 - 1403.66817(58)\lambda_I^4 \\ &\quad +8341.758(61)\lambda_I^5 - 54808.87(32)\lambda_I^6 + 392070.3(6.4)\lambda_I^7. \end{aligned} \tag{B.13}$$

These perturbative expansions can be used in a renormalization group treatment.
From simple power counting it follows that there are only three relevant operators $(\nabla\phi)^2$, ϕ^2, ϕ^4. Therefore, we define the three renormalized coupling constants Z_ϕ, m_R, λ_R associated with that operators as

$$\Gamma_R^{(n)} = Z_\phi^{n/2}\Gamma^{(n)} \tag{B.14}$$

$$\Gamma_R^{(2)}(0) = m_R^2 \tag{B.15}$$

$$\partial_{p^2}\Gamma_R^{(2)}(\mathbf{p})\big|_{p=0} = 1 \tag{B.16}$$

$$\Gamma_R^{(4)}(0,0,0,0) = \lambda_R m_R^{D-4}. \tag{B.17}$$

In terms of the perturbative series expansions (B.11), (B.12), (B.13) the renormalized coupling constants are given by

$$Z_\phi = \left(\partial_{p^2}\Gamma^{(2)}(\mathbf{p})\big|_{p=0}\right)^{-1} \tag{B.18}$$

$$m_R^2 = \Gamma^{(2)}(0)\left(\partial_{p^2}\Gamma^{(2)}(\mathbf{p})\big|_{p=0}\right)^{-1} \tag{B.19}$$

$$\lambda_R \;=\; \Gamma^{(4)}(0,0,0,0)\left(\Gamma^{(2)}(0)\right)^{-1/2}\left(\partial_{p^2}\Gamma^{(2)}(\mathbf{p})\Big|_{p=0}\right)^{-D/2}. \tag{B.20}$$

The beta function describing the renormalization group flow of the renormalized coupling constant is defined by

$$\beta(\lambda_R) = D_m\left[\lambda_R\right] = m_R\frac{\mathrm{d}\lambda_R}{\mathrm{d}m_R}. \tag{B.21}$$

For a perturbative expansion of $\beta(\lambda_R)$ in terms of λ_R we use (B.18), (B.19), (B.20) to first calculate $\beta(\lambda_I)$ in a power series in λ_I and afterwards invert the series $\lambda_R(\lambda_I)$ to arrive at $\beta(\lambda_I(\lambda_R))$. Using the chain rule for the definition of the beta function we have

$$\beta(\lambda_R) = D_m\left[\lambda_I\right]\frac{\partial\lambda_R}{\partial\lambda_I}. \tag{B.22}$$

The second term can be easily calculated from (B.20) and the first term needs some further consideration. We have defined $\lambda_B = m_I^{4-D}\lambda_I$ and therefore $m_I D_m\left[\lambda_I\right] = (D-4)\lambda_I D_m[m_I]$ and together with the identity [91]

$$\frac{D_m[m_I]}{m_I} = 1 - \frac{1}{2}D_m\log\frac{m_R^2}{m_I^2} = 1 - \frac{1}{2}D_M(\lambda_I)\frac{\partial\log\frac{m_R^2}{m_I^2}}{\partial\lambda_I} \tag{B.23}$$

we find

$$D_m\left[\lambda_I\right] = (D-4)\lambda_I\left(1 + \frac{D-4}{2}\lambda_I\frac{\partial\log\frac{m_R^2}{m_I^2}}{\partial\lambda_I}\right)^{-1}. \tag{B.24}$$

With this we can easily compute $\beta(\lambda_I)$ as a power series in λ_I and plugging in the inverted series $\lambda_R(\lambda_I)$ we obtain

$$\begin{aligned}\frac{\beta(v)}{2} =& -v + v^2 - 0.7161736v^3 + 0.930768(3)v^4 \\ &- 1.5824(2)v^5 + 3.2591(9)v^6 - 7.711(5)v^7,\end{aligned} \tag{B.25}$$

where $v = \frac{3}{8\pi}\lambda_R$.

C

Analytic structure of the universal functional $\Gamma[G]$

In order to obtain the analytic structure of $\Gamma[G]$ near $G = 0$ we first consider the analytic solution to the integral

$$Z = \int \mathrm{d}\phi \, e^{-S[\phi]} \text{ with } S[\phi] = \frac{1}{2}k\phi^2 + \frac{\lambda}{4!}\phi^4. \tag{C.1}$$

The analytic solution to this integral for $k \in \mathbb{C}$ with fixed $\lambda \in \mathbb{R}^+$ is given as

$$\begin{aligned} Z[k] &= e^{\frac{3k^2}{4\lambda}} \\ &\times \begin{cases} \sqrt{3}\sqrt{\frac{k}{\lambda}} K_{\frac{1}{4}}\left(\frac{3k^2}{4\lambda}\right) & \mathrm{Re}(k) > 0 \\ \sqrt{\frac{3}{2}}\pi\sqrt{-\frac{k}{\lambda}}\left(I_{\frac{1}{4}}\left(\frac{3k^2}{4\lambda}\right) + I_{-\frac{1}{4}}\left(\frac{3k^2}{4\lambda}\right)\right) & \mathrm{Re}(k) < 0. \end{cases} \end{aligned} \tag{C.2}$$

Here $I_n(z)/K_n(z)$ are the modified Bessel functions of the first/second kind and $Z[k = 0] = (3/2\lambda)^{1/4}\Gamma(1/4)$ where $\Gamma(x)$ is the Gamma function. The integral (C.1) can be regarded as an integral representation of the function Z defined in (C.2). The same holds for the 2-point correlation function $G[k]$ which we do not show here. The important point is that both $Z[k]$ and $G[k]$ are piecewise-defined functions in k which can be represented by a single integral expression. There exists also a differential equation equivalent to the integral representation of the function $Z[k]$ or $G[k]$. For $G[k]$ this is the coupled system of differential equations,

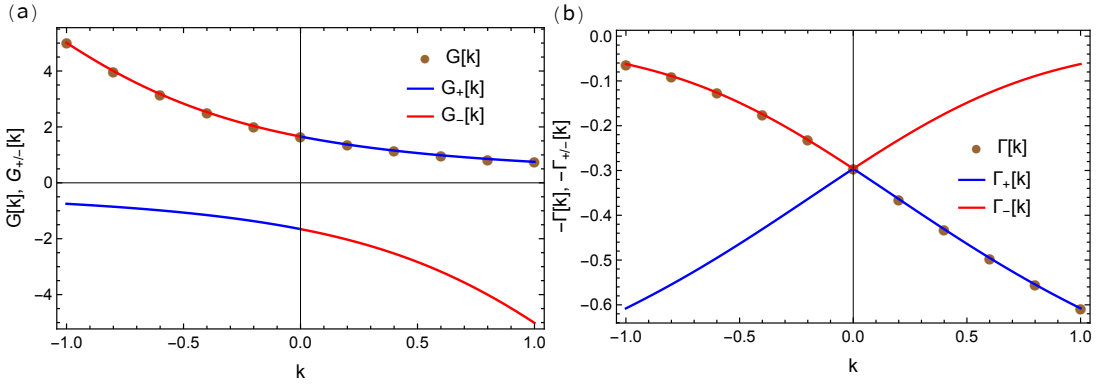

Figure C.1.: The two solutions for $G(\Gamma)_\pm[k]$ of (C.3) on the real axis for $\lambda = 1$. The physical solution $G(\Gamma)[k]$ corresponds to the solution $G(\Gamma)_+[k]$ for $k > 0$ and $G(\Gamma)_-[k]$ for $k < 0$ cf. (C.2).

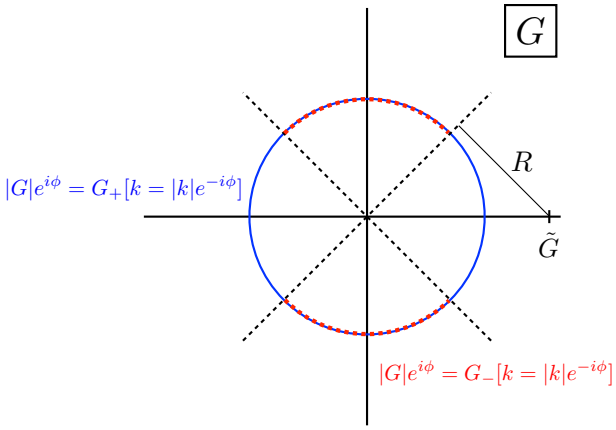

Figure C.2.: The elements of the images of $G_\pm[k]$ onto the circle $|G|e^{i\phi}$ for $|G| \to 0$. For $\phi \in [\frac{\pi}{4}, \frac{3\pi}{4}]$ and $[\frac{5\pi}{4}, \frac{7\pi}{4}]$ $G_\pm$ map onto the same G. Therefore, $\Gamma[G]$ has to be single valued on $\phi \in [-\frac{\pi}{4}, \frac{\pi}{4}]$ and $[\frac{3\pi}{4}, \frac{5\pi}{4}]$ and multi-valued on $\phi \in [\frac{\pi}{4}, \frac{3\pi}{4}]$ and $[\frac{5\pi}{4}, \frac{7\pi}{4}]$. The Taylor series of $\Gamma[G]$ around $\tilde{G} \in \mathbb{R}^+$ has the convergence radius $R = \sin(\frac{\pi}{4})\tilde{G}$.

$$
\begin{aligned}
G_\pm[k]^{-1} - k &= \frac{\lambda}{2} G_\pm[k] - \frac{\lambda}{6} G_\pm[k]^3 \Gamma_\pm^{(4)}[k] \\
\Gamma_\pm[k] &= \lambda - \frac{3\lambda}{2} G_\pm[k]^2 \Gamma_\pm[k] + \frac{\lambda}{2} G[k]_\pm^4 \left[\Gamma_\pm^{(4)}\right]^2 \\
&\quad + \frac{\lambda}{6} G_\pm[k] \frac{\mathrm{d}\Gamma_\pm^{(4)}}{\mathrm{d}k}.
\end{aligned}
\tag{C.3}
$$

There are two independent solutions to this equation for G and, consequently, also for Γ denoted as $G_\pm[k]$ and $\Gamma_\pm[k]$, respectively. While (C.1) is single-valued, the solution to the system of equations (C.3) in principle leads to two independent solutions. They are shown for $G_\pm[k]$, $\Gamma_\pm[k]$ on the real axis in Fig. C.1. We will show in the following that the analytic structure of $\Gamma[G]$ near $G = 0$ can be understood from the existence of the two independent solutions to (C.3). Formally, $\Gamma[G]$ can be obtained from $\Gamma_\pm[k]$ by inverting the relation $G = G_\pm[k]$. There are two independent solutions which for some k satisfy $G = G_+[k_1] = G_-[k_2]$. This leads to two branches for $\Gamma[G]$ where $\Gamma[G]$ must evaluate to $\Gamma_+^{(4)}[k_1]$ on the first branch and to $\Gamma_-^{(4)}[k_2]$ on the second branch. In order to obtain the analytic structure of $\Gamma[G]$ near $|G| = 0$ it is necessary to study the intersection of the images of $G_\pm$ for elements which satisfy $|G| \to 0$. The complete circle in the complex G plane $|G|e^{i\phi}$, $\phi \in [0, 2\pi]$ for $|G| \to 0$ in Fig. C.2 is included in the image

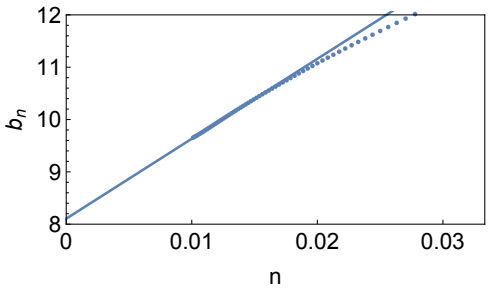

Figure C.3.: The linear extrapolation of the large order asymptotic $b_n^2 = \frac{c_{n+1}c_{n-1} - c_n^2}{c_n c_{n-2} - c_{n-1}^2}$ yields a convergence radius $R \approx \frac{1}{8.105} = 0.123$ which can be compared to the expected convergence radius of $R = \sin(\frac{\pi}{4})0.172 = 0.122$. Here $\tilde{G} = G_+[k = 5] = 0.172$ has been considered.

of $G_+[k]$ and can be obtained by the parametrization $k = |k|e^{-i\phi}$ where $|k| \to \infty$. On the other hand, the image of $G_-[k]$ includes two segments of the circle $|G|e^{i\phi}$ namely with $\phi \in [\frac{\pi}{4}, \frac{3\pi}{4}]$ and $\phi \in [\frac{5\pi}{4}, \frac{7\pi}{4}]$ and can also be obtained by the parametrization $k = |k|e^{-i\phi}$. Therefore there are branch cuts starting from $G = 0$ cutting the complex G plane in the $\pm\frac{\pi}{4}$ direction.
According to the above result a power series solution around $\tilde{G} \in \mathbb{R}^+$, should have convergence radius $R = \sin(\frac{\pi}{4})\tilde{G}$. The convergence radius can also be determined numerically by considering the coefficients c_n in the power series $\Gamma[G] = \sum_n c_n(G - \tilde{G})^n$. The power series can be obtained by using the analytically known result for $\Gamma_+^{(4)}[G_+[k]]$ on the real axis i.e. $c_0 = \Gamma[\tilde{G}]$. As shown in Fig. C.3 the numerically obtained convergence radius from the large order behavior of the coefficients c_n agrees with the expected convergence radius.

D

Kernel Functions

In this section we list the analytic expressions for the different branch types and the new external momentum variables for the corresponding leafs grown from these branches. The analytic expressions give directly the projection into the physical subspace of translational invariant G. We denote the external momentum variables at the leaf from which the branch is grown as $\mathbf{p} = (p_1, p_2, p_3, p_4)$ and assume that this leaf corresponds to a deformation $u_{\Gamma,m}$. We again use the shorthand notation $p_i = i$ and $p_i + p_j = i + j$ and implicitly assume summation over repeated indices.
Fig. 5.21 lists all possible branch types where each branch type accounts for a single line in (5.144). Furthermore, we consider functional derivatives in intermediate stages which directly act on the leafs and which have to be accounted for by the momentum conservation rule (5.159). These additional functional derivatives are highlighted by the momentum labels l_i. Diagrammatically the branch types are depicted in Figs. D.1, D.2. The analytic expressions for the different branch types, including the intermediate functional derivatives, are given by:

a) The analytic expression for the branch type in Fig. 5.21 a):

i) $m \neq 1$

$$(1 - c_0) \frac{\delta^p u_{\Gamma,m-1}(1,2,3,4)}{\delta G(l_0, l_1) \dots \delta G(l_{2p-2}, l_{2p-1})} \tag{D.1}$$

ii) $m = 1$

$$- c_0 \left(u_0(1,2,3,4) - \lambda\right) \tag{D.2}$$

In this case, by definition, there are no intermediate functional derivatives which directly act on the leaf because $\frac{\delta u_{\Gamma,0}}{\delta G} = 0$.

b) The analytic expression for the branch type in Fig. 5.21 b):

i) c = s

$$K^{(1)}_{c=s}(\mathbf{p}_{c=s}, 5, 6, 7) = G(1 + 2 - 5, 7) G(5, 6) \tag{D.3}$$

Therefore, at $G(1,2) = G(1)\delta_{1,-2}$:

$$\begin{aligned} &\sum_{5,6,7} K^{(1)}_{c=s}(\mathbf{p}_{c=s}, 5, 6, 7) \frac{\delta^p u_{\Gamma,m-1}(-7, -6, \mathbf{p}_{\bar{c}=\bar{s}})}{\delta G(l_0, l_1) \dots \delta G(l_{2p-2}, l_{2p-1})} \overset{G=G_{\text{phys}}}{=} \\ &\sum_{5} G(5) G(1+2-5) \frac{\delta^p u_{\Gamma,m-1}(1+2-5, 5, 3, 4)}{\delta G(l_0, l_1) \dots \delta G(l_{2p-2}, l_{2p-1})}. \end{aligned} \tag{D.4}$$

ii) c = t
$2 \leftrightarrow 3$

iii) c = u
$2 \leftrightarrow 4$

c) The analytic expression for the branch type in Fig. 5.21 c):

i) c = s

$$K^{(2)}_{c=s}(\mathbf{p}_{c=s}, 5, \ldots, 11) = G(1-5-7,11)G(5,6)G(7,8)G(9,10) \tag{D.5}$$

Therefore, at $G(1,2) = G(1)\delta_{1,-2}$ and taking into account the extended momentum conservation (5.159) at $u_{\Gamma,k}$:

$$\begin{aligned}
&\sum_{5,\ldots,11} K^{(2)}_{c=s}(\mathbf{p}_{c=s}, 5, \ldots, 11) \frac{\delta^r u_{\Gamma,s}(-6,-8,p_{c=s},-9)}{\delta G(l_{2q}, l_{2q+1}) \ldots \delta G(l_{2p-2}, l_{2p-1})} \\
&\qquad \times \frac{\delta^q u_{\Gamma,k}(-11,-10,\mathbf{p}_{\bar{c}=\bar{s}})}{\delta G(l_0, l_1) \ldots \delta G(l_{2q-2}, l_{2q-1})} \overset{G=G_{\text{phys}}}{=} \\
&\sum_{5,9} \quad G(5)G(9)G(x)G(1-5-x) \\
&\qquad \times \frac{\delta^r u_{\Gamma,s}(5,2,-9,x)}{\delta G(l_{2q}, l_{2q+1}) \ldots \delta G(l_{2p-2}, l_{2p-1})} \frac{\delta^q u_{\Gamma,k}(1-5-x,9,3,4)}{\delta G(l_0, l_1) \ldots \delta G(l_{2q-2}, l_{2q-1})}.
\end{aligned} \tag{D.6}$$

Where

$$x = -p_2 - p_5 + p_9 + \sum_{i=2q}^{2p-1} l_i. \tag{D.7}$$

ii) c = t
$2 \leftrightarrow 3$

iii) c = u
$2 \leftrightarrow 4$

Where $s = m - 1 - k$ with $k \in \{0, \ldots, m-1\}$ and $r + q = p$ with $q \in \{0, \ldots, p\}$.

d) The analytic expression for the branch type in Fig. 5.21 d):

$$K^{(3)}(1, 5, \ldots, 9) = G(1-5-6,7)G(5,8)G(6,9) \tag{D.8}$$

Therefore, evaluating the kernel function at $G(1,2) = G(1)\delta_{1,-2}$:

$$\begin{aligned}
&\sum_{5,\ldots,9} K^{(3)}(1, 5, \ldots, 9) \frac{\delta^{p+1} u_{\Gamma,m-1}(-7,2,3,4)}{\delta G(8,9)\delta G(l_0, l_1) \ldots G(l_{2p-2}, l_{2p-1})} \overset{G=G_{\text{phys}}}{=} \\
&\sum_{5,6} G(1-5-6)G(5)G(6) \frac{\delta^{p+1} u_{\Gamma,m-1}(1-5-6,2,3,4)}{\delta G(-5,-6)\delta G(l_0, l_1) \ldots G(l_{2p-2}, l_{2p-1})}.
\end{aligned} \tag{D.9}$$

e) The analytic expression for the branch type in Fig. 5.21 e):

$$K^{(4)}(1, 5, \ldots, 13) = G(1-5-6,7)G(5,8)G(6,9)G(10,11)G(12,13) \tag{D.10}$$

Therefore, evaluating the kernel function at $G(1,2) = G(1)\delta_{1,-2}$:

$$\begin{aligned}
&\sum_{5,\dots,13} K^{(4)}(1,5,\dots,13)\frac{\delta^{r+1}u_{\Gamma,k}(-7,2,3,4)}{\delta G(10,12)\delta G(l_{2q},l_{2q+1})\dots G(l_{2p-2},l_{2p-1})} \\
&\qquad\times \frac{\delta^{q}u_{\Gamma,s}(-8,-11,-13,-9)}{\delta G(l_0,l_1)\dots G(l_{2q-2},l_{2q-1})} \overset{G=G_{\text{phys}}}{=} \\
&\sum_{5,6,10} G(1-5-6)G(5)G(6)G(10)G(x)\frac{\delta^{r+1}u_{\Gamma,k}(1-5-6,2,3,4)}{\delta G(10,x)\delta G(l_{2q},l_{2q+1})\dots G(l_{2p-2},l_{2p-1})} \\
&\qquad\times \frac{\delta^{q}u_{\Gamma,s}(5,10,x,6)}{\delta G(l_0,l_1)\dots G(l_{2q-2},l_{2q-1})}.
\end{aligned} \tag{D.11}$$

Where

$$x = \sum_{i=1}^{4} p_i - p_5 - p_6 - p_{10} - \sum_{i=2q}^{2p-1} l_i \tag{D.12}$$

and $s = m-1-k$ with $k \in \{0,\dots,m-1\}$, $r+q=p$ with $q \in \{0,\dots,p\}$.

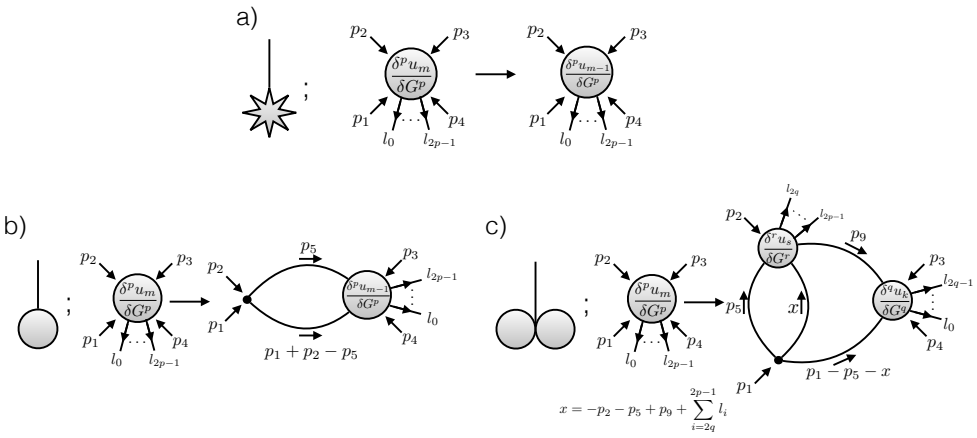

Figure D.1.: The diagrammatic expressions for the kernel functions corresponding to the first three branch types in Fig. 5.21 in the presence of p intermediate derivatives. In the diagrammatic expressions the lines correspond to 2-point correlation functions with momentum labeled by the arrow. The analytic expression for the contributing kernel function for each branch type can be read off by standard diagrammatic rules. The new external momentum at the newly grown leafs can also be read off by standard diagrammatic rules and taking the extended momentum conservation rule (5.159) into account as explained in the main text. The dot represents a bare vertex and therefore ordinary momentum conservation at the 4-point level holds there. The momentum variables for the p intermediate derivatives are indicated by l, i.e. $G(l_{2i}, l_{2i+1})$ with $i \in \{0, \dots, p-1\}$. These intermediate derivatives are diagrammatically depicted as the additional lines with arrows on the lines. These arrows indicate that the respective momentum on that line has to be taken into account with an additional minus sign in the extended momentum conservation rule. a) The branch corresponds to the expansion with respect to the first line in (5.144). It contributes with a trivial factor to the rooted tree expansion and does not introduce new integration variables. Therefore, the external momentum variables stay the same and the deformation order is reduced from m to $m-1$. b) The branch corresponds to the expansion with respect to the second line in (5.144) and an external leg permutation has to be chosen. In this example the s-channel is chosen. Due to the momentum conservation at the bare vertex the internal momentum variables for the 2-point correlation functions are independent of the momentum variables contributing from the intermediate derivatives. c) The branch corresponds to the expansion with respect to the third line in (5.144) and a external leg permutation has to be chosen. In this example the s-channel is chosen. For that branch type the internal lines depend on the momentum variables of the intermediate derivatives. The convention is picked such that the extended momentum conservation is taken at u_s. In this case there are two newly grown leafs which can be expanded further and therefore the p intermediate derivatives are distributed randomly such that $r + q = p$.

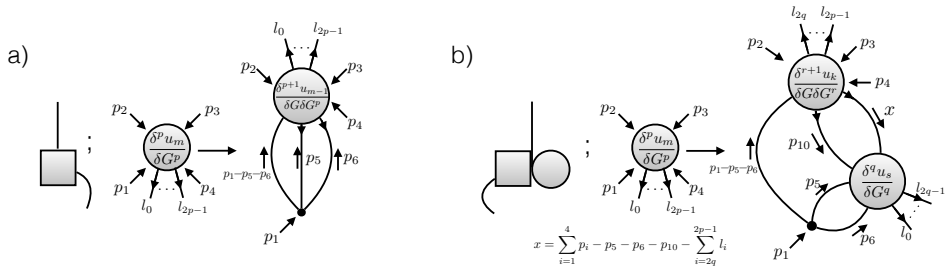

Figure D.2.: The diagrammatic expressions for the kernel functions corresponding to the last two branch types in Fig. 5.21 in the presence of p intermediate derivatives. In the diagrammatic expressions the lines correspond to 2-point correlation functions with momentum labeled by the arrow. The analytic expression for the contributing kernel function for each branch type can be read off by standard diagrammatic rules. The new external momentum at the newly grown leafs can also be read off by standard diagrammatic rules and taking the extended momentum conservation (5.159) rule into account as explained in the main text. The dot represents a bare vertex and therefore ordinary momentum conservation at the 4-point level holds there. The momentum variables for the p intermediate derivatives are indicated by l, i.e. $G(l_{2i}, l_{2i+1})$ with $i \in \{0, \ldots, p-1\}$. These intermediate derivatives are diagrammatically depicted as the additional lines with arrows on the lines. These arrows indicate that the respective momentum on that line has to be taken into account with an additional minus sign in the extended momentum conservation rule. a) The branch corresponds to the expansion with respect to the fourth line in (5.144) and contributes an additional functional derivative. b) The branch corresponds to the expansion with respect to the fourth line in (5.144) and contributes an additional functional derivative on the leaf connected to 3 external lines. For that branch type the internal lines depend on the momentum variables of the intermediate derivatives. The convention is picked such that the extended momentum conservation is taken at u_k. In this case there are two newly grown leafs which can be expanded further and therefore the p intermediate derivatives are distributed randomly such that $r + q = p$.

E

Functional Derivatives of Kernel Functions

In this section we list the analytic expressions for the functional derivative of the different branch types and the resulting new external momentum variables for the corresponding leafs grown from these differentiated branches in the presence of intermediate functional derivatives. The momentum variables of the functional derivative differentiating the considered branch are denoted by l_0, l_1 if there is a single derivative acting on the branch and $l_0, \ldots, l_3$ if there are two derivatives. Further p intermediate derivatives are labeled with consecutive numbers $l_2, \ldots, l_{2p+1}$ and $l_4, \ldots, l_{2p+3}$, respectively. During the Monte Carlo run we measure the average number of functional derivatives. We find that this number is around unity for the parameter range considered in Fig. 5.25 and the maximal expansion order $m = 6$ reached in our Monte Carlo algorithm. Therefore, we list here the kernel functions up to second order derivatives for the branch types Fig. 5.21 b), c) which contribute itself no functional derivative and up to first order for the branch types Fig. 5.21 d), e) which contribute itself a functional derivative to the rooted tree. We note that we do not restrict the maximal number of functional derivative in a rooted tree but only the number of derivative which can act on a single branch. Bookkeeping of higher order derivatives of the kernel function, i.e., up to a maximum of 5 for Fig. 5.21 e) will become increasingly difficult.
The analytic expressions for the derivatives of the various branches are:

a) This branch contributes with a trivial factor and therefore can not be differentiated, i.e., the derivative on that branch yields a zero contribution.

b) The diagrammatic expression for the first and second derivative are shown in Fig. E.1.

1.

i. c=s

$$\sum_{5,6,7} \left(\frac{\delta}{\delta G(l_0, l_1)} K^{(1)}_{c=s}(\mathbf{p}_{c=s}, 5, 6, 7) \right) \frac{\delta^p u_{\Gamma, m-1}(-7, -6, \mathbf{p}_{\bar{c}=\bar{s}})}{\delta G(l_2, l_3) \ldots \delta G(l_{2p}, l_{2p+1})} \overset{G=G_{\text{phys}}}{=} 2G(1 + 2 - l_0) \frac{\delta^p u_{m-1}(-l_1, 1 + 2 - l_0, 3, 4)}{\delta G(l_2, l_3) \ldots \delta G(l_{2p}, l_{2p+1})}. \tag{E.1}$$

ii. c=t
$2 \leftrightarrow 3$

iii. c=u
$2 \leftrightarrow 4$

2.

i. c=s

$$\sum_{5,6,7}\left(\frac{\delta}{\delta G(l_0,l_1)\delta G(l_2,l_3)}K^{(1)}_{c=s}(\mathbf{p}_{c=s},5,6,7)\right)\frac{\delta^p u_{\Gamma,m-1}(-7,-6,\mathbf{p}_{\bar{c}=\bar{s}})}{\delta G(l_4,l_5)\dots\delta G(l_{2p+1},l_{2p+3})}$$
$$\overset{G=G_{\text{phys}}}{=} 2\delta(1+2-l_0-l_2)\frac{\delta^p u_{\Gamma,m-1}(-l_1,-l_3,3,4)}{\delta G(l_4,l_5)\dots\delta G(l_{2p+1},l_{2p+3})}. \tag{E.2}$$

ii. c=t
$2 \leftrightarrow 3$

iii. c=u
$2 \leftrightarrow 4$

c) The diagrammatic expression for the first and second derivative are shown in Fig. E.2 and Fig. E.3. Due to the product rule the differentiation of the branch yields 4 possible terms where 2 are symmetric to each other. A random rooted tree corresponds to the random choice of a single term.

1.

i. c=s

$$\begin{aligned}
&\sum_{5,\dots,11}\left(\frac{\delta}{\delta G(l_0,l_1)}K^{(2)}_{c=s}(\mathbf{p}_{c=s},5,\dots,11)\right)\frac{\delta^r u_{\Gamma,s}(-6,p_{c=s},-9,-8)}{\delta G(l_{2q+2},l_{2q+3})\dots\delta G(l_{2p},l_{2p+1})}\\
&\qquad\times\frac{\delta^q u_{\Gamma,k}(-11,-10,\mathbf{p}_{\bar{c}=\bar{s}})}{\delta G(l_2,l_3)\dots\delta G(l_{2q},l_{2q+1})}\overset{G=G_{\text{phys}}}{=}\\
&\sum_5 G(5)G(x)G(1-l_0-x)\frac{\delta^r u_{\Gamma,s}(-l_1,2,-5,1-l_0-x)}{\delta G(l_{2q+2},l_{2q+3})\dots\delta G(l_{2p},l_{2p+1})}\\
&\qquad\times\frac{\delta^q u_{\Gamma,k}(x,5,3,4)}{\delta G(l_2,l_3)\dots\delta G(l_{2q},l_{2q+1})}+\\
&\sum_5 G(5)G(y)G(\alpha)\frac{\delta^r u_{\Gamma,s}(5,2,-\alpha,y)}{\delta G(l_{2q+2},l_{2q+3})\dots\delta G(l_{2p},l_{2p+1})}\\
&\qquad\times\frac{\delta^q u_{\Gamma,k}(l_1,\alpha,3,4)}{\delta G(l_2,l_3)\dots\delta G(l_{2q},l_{2q+1})}+\\
&\sum_5 G(5)G(z)G(1-5-z)\frac{\delta^r u_{\Gamma,s}(-l_1,2,-5,1-l_0-x)}{\delta G(l_{2q+2},l_{2q+3})\dots\delta G(l_{2p},l_{2p+1})}\\
&\qquad\frac{\delta^q u_{\Gamma,k}(x,5,3,4)}{\delta G(l_2,l_3)\dots\delta G(l_{2q},l_{2q+1})}.
\end{aligned} \tag{E.3}$$

Where

$$\begin{aligned} x &= -p_3 - p_4 - p_5 + \sum_{i=2}^{2q+1} l_i, \\ y &= p_1 - l_0 - p_5, \\ z &= -p_4 - p_5 + l_0 + \sum_{i=2q+2}^{2p+1} l_i, \\ \alpha &= p_2 + p_5 + y - \sum_{i=2q+2}^{2p+1} l_i. \end{aligned} \tag{E.4}$$

ii. c=t
$2 \leftrightarrow 3$

iii. c=u
$2 \leftrightarrow 4$

Where $s = m - 1 - k$ with $k \in \{0, \ldots, m-1\}$ and $r + q = p$ with $q \in \{0, \ldots, p\}$.

2.

i. c=s

$$\begin{aligned} &\sum_{5,\ldots,11} \left(\frac{\delta}{\delta G(l_0, l_1)\delta G(l_2, l_3)} K^{(2)}_{c=s}(\mathbf{p}_{c=s}, 5, \ldots, 11) \right) \\ &\qquad \times \frac{\delta^r u_{\Gamma,s}(-6, p_{c=s}, -9, -8)}{\delta G(l_{2q+4}, l_{2q+5}) \ldots \delta G(l_{2p+2}, l_{2p+3})} \frac{\delta^q u_{\Gamma,k}(-11, -10, \mathbf{p}_{\bar{c}=\bar{s}})}{\delta G(l_4, l_5) \ldots \delta G(l_{2q+2}, l_{2q+3})} \\ &\overset{G=G_{\text{phys}}}{=} 2G(1 - l_0 - l_2)G(x) \frac{\delta^r u_{\Gamma,s}(-l_1, 2, -x, p_1 - l_0 - x)}{\delta G(l_{2q+4}, l_{2q+5}) \ldots \delta G(l_{2p+2}, l_{2p+3})} \\ &\qquad \times \frac{\delta^q u_{\Gamma,k}(1 - l_0 - l_2, x, 3, 4)}{\delta G(l_4, l_5) \ldots \delta G(l_{2q+2}, l_{2q+3})} \\ &\quad + 4G(y)G(z) \frac{\delta^r u_{\Gamma,s}(-l_3, 2, -z, y)}{\delta G(l_{2q+4}, l_{2q+5}) \ldots \delta G(l_{2p+2}, l_{2p+3})} \\ &\qquad \times \frac{\delta^q u_{\Gamma,k}(-l_1, z, 3, 4)}{\delta G(l_4, l_5) \ldots \delta G(l_{2q+2}, l_{2q+3})} \\ &\quad + 4G(\alpha)G(\beta) \frac{\delta^r u_{\Gamma,s}(-l_3, 2, -l_0, \alpha)}{\delta G(l_{2q+4}, l_{2q+5}) \ldots \delta G(l_{2p+2}, l_{2p+3})} \\ &\qquad \times \frac{\delta^q u_{\Gamma,k}(\beta, -l_1, 3, 4)}{\delta G(l_4, l_5) \ldots \delta G(l_{2q+2}, l_{2q+3})} \\ &\quad + 2 \sum_5 G(5)G(\gamma) \frac{\delta^r u_{\Gamma,s}(5, 2, -l_2, \gamma)}{\delta G(l_{2q+4}, l_{2q+5}) \ldots \delta G(l_{2p+2}, l_{2p+3})} \\ &\qquad \times \frac{\delta^q u_{\Gamma,k}(-l_1, -l_3, 3, 4)}{\delta G(l_4, l_5) \ldots \delta G(l_{2q+2}, l_{2q+3})} \delta(p_3 + p_4 - l_1 - l_3 - \sum_{i=4}^{2q+3} l_i). \end{aligned} \tag{E.5}$$

Where

$$\begin{aligned} x &= p_2 - l_1 - l_3 - \sum_{i=2q+4}^{2p+3} l_i, \\ y &= p_1 - l_0 - l_2, \\ z &= -p_3 - p_4 + l_1 + \sum_{i=4}^{2q+3} l_i, \\ \alpha &= p_1 - \beta - l_2, \\ \beta &= -p_3 - p_4 + l_1 + \sum_{i=4}^{2q+3} l_i, \\ \gamma &= p_1 - l_0 - p_5. \end{aligned} \tag{E.6}$$

ii. c=t
$2 \leftrightarrow 3$

iii. c=u
$2 \leftrightarrow 4$

Where $s = m - 1 - k$ with $k \in \{0, \ldots, m-1\}$ and $r + q = p$ with $q \in \{0, \ldots, p\}$.

d) The diagrammatic expression for the first derivative is shown in Fig. E.4.

1.

$$\begin{aligned} &\sum_{5,\ldots,9} \left(\frac{\delta}{\delta G(l_0, l_1)} K^{(3)}(1, 5, \ldots, 9) \right) \frac{\delta^{p+1} u_{\Gamma, m-1}(-7, 2, 3, 4)}{\delta G(8,9) \delta G(l_2, l_3) \ldots G(l_{2p}, l_{2p+1})} \\ &\overset{G=G_{\text{phys}}}{=} \sum_{5} G(5) G(1 - 5 - l_0) \frac{\delta^{p+1} u_{m-1}(l_1, 2, 3, 4)}{\delta G(-5, -1 + 5 + l_0) \delta G(l_2, l_3) \ldots G(l_{2p}, l_{2p+1})} \\ &\quad + 2 \sum_{5} G(5) G(1 - 5 - l_0) \frac{\delta^{p+1} u_{m-1}(1 - 5 - l_0, 2, 3, 4)}{\delta G(-5, l_1) \delta G(l_2, l_3) \ldots G(l_{2p}, l_{2p+1})}. \end{aligned} \tag{E.7}$$

e) The diagrammatic expression for the first derivative is shown in Fig. E.5.

1.

$$
\begin{aligned}
&\sum_{5,\dots,13}\left(\frac{\delta}{\delta G(l_0,l_1)}K^{(4)}(1,5,\dots,13)\right)\frac{\delta^q u_{\Gamma,s}(-8,-11,-13,-9)}{\delta G(l_2,l_3)\dots G(l_{2q},l_{2q+1})}\\
&\qquad\times\frac{\delta^{r+1}u_{\Gamma,k}(-7,2,3,4)}{\delta G(10,12)\delta G(l_{2q+2},l_{2q+3})\dots G(l_{2p},l_{2p+1})}\\
&\overset{G=G_{\text{phys}}}{=}\sum_{5,7}G(5)G(7)G(1-5-l_0)G(x)\frac{\delta^q u_{\Gamma,s}(5,7,x,1-5-l_0)}{\delta G(l_2,l_3)\dots G(l_{2p},l_{2p+1})}\\
&\qquad\times\frac{\delta^{r+1}u_{\Gamma,k}(-l_1,2,3,4)}{\delta G(7,x)\delta G(l_{2q+2},l_{2q+3})\dots G(l_{2p},l_{2p+1})}\\
&\quad+2\sum_{5,7}G(5)G(7)G(y)G(z)\frac{\delta^q u_{\Gamma,s}(5,7,z,-l_1)}{\delta G(l_2,l_3)\dots G(l_{2p},l_{2p+1})}\\
&\qquad\times\frac{\delta^{r+1}u_{\Gamma,k}(y,2,3,4)}{\delta G(7,z)\delta G(l_{2q+2},l_{2q+3})\dots G(l_{2p},l_{2p+1})}\\
&\quad+2\sum_{5,6}G(5)G(6)G(\alpha)G(\beta)\frac{\delta^q u_{\Gamma,s}(5,\beta,-l_0,6)}{\delta G(l_2,l_3)\dots G(l_{2p},l_{2p+1})}\\
&\qquad\times\frac{\delta^{r+1}u_{\Gamma,k}(y,2,3,4)}{\delta G(\beta,l_1)\delta G(l_{2q+2},l_{2q+3})\dots G(l_{2p},l_{2p+1})}.
\end{aligned}
\tag{E.8}
$$

Where

$$
\begin{aligned}
x&=-p_1-p_7+l_0+\sum_{i=2}^{2q+1}l_i,\\
y&=p_1-p_5-l_0,\\
z&=-p_1-p_7+l_0+\sum_{i=2}^{2q+1}l_i,\\
\alpha&=p_1-p_5-p_6,\\
\beta&=-p_5-p_6+l_0+\sum_{i=2}^{2q+1}l_i.
\end{aligned}
\tag{E.9}
$$

Where $s=m-1-k$ with $k\in\{0,\dots,m-1\}$ and $r+q=p$ with $q\in\{0,\dots,p\}$.

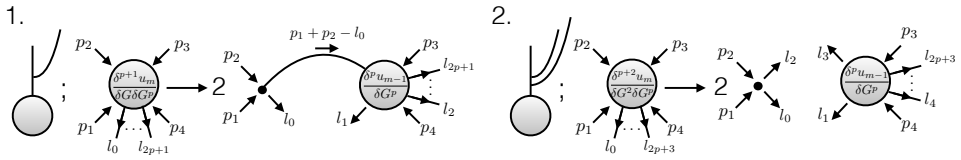

Figure E.1.: The first and second functional derivative of the branch Fig. 5.21b) with respect to $G(l_0, l_1)$ and $G(l_0, l_1)G(l_2, l_3)$, respectively. Whereas the first derivative eliminates the integration variable of the differentiated branch the second derivate contributes a delta function. Therefore, the integration variable of the branch on which l_0 or l_2 depends has to be changed such that the delta constrain is satisfied. Alternatively, the integration variable of the branch on which l_1 or l_3 depends can be changed such that the extended momentum conservation rule (5.159) is satisfied at the new leaf. In this case also the constrain by the delta function is met automatically.

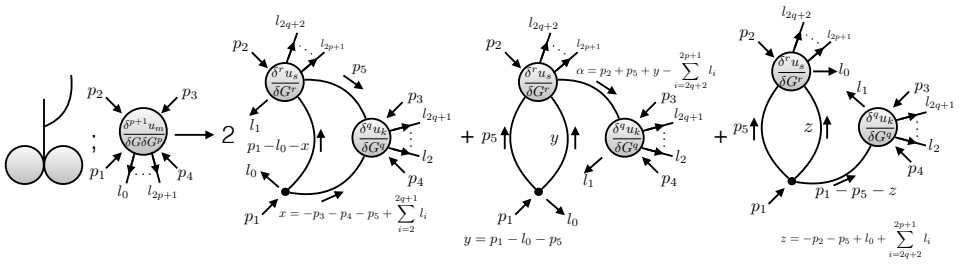

Figure E.2.: The first functional derivative of the branch Fig. 5.21c) with respect to $G(l_0, l_1)$. Due to the product rule of functional derivatives the differentiation of the branch yields 4 terms. As 2 of the terms are symmetric to each other 3 distinct terms are generated.

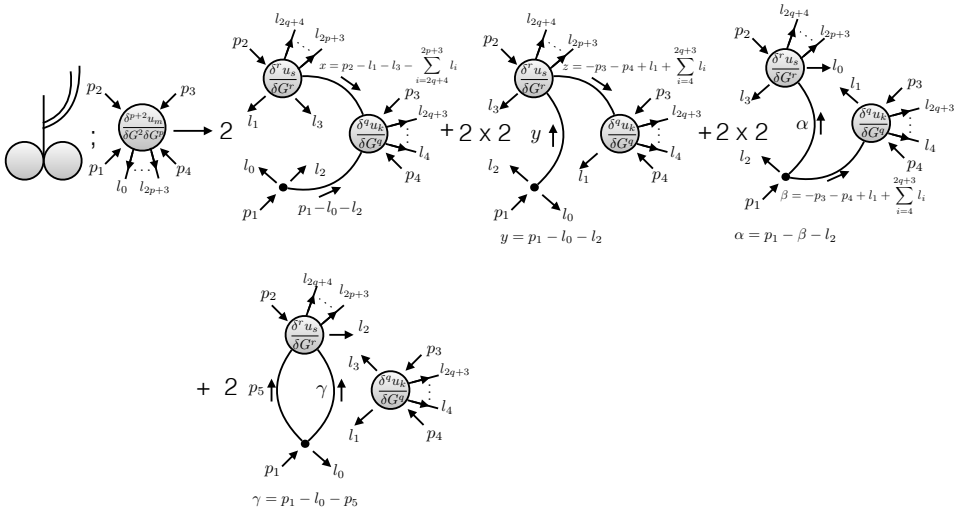

Figure E.3.: The second functional derivative of the branch Fig. 5.21c) with respect to $G(l_0, l_1)G(l_2, l_3)$. Due to the product rule of functional derivatives the differentiation of the branch yields 12 terms. Due to symmetry considerations there are only 4 distinct terms. Additional factors of 2 in the least three terms are due to the fact that second order derivatives commute.

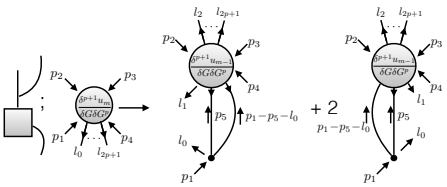

Figure E.4.: The first functional derivative of the branch Fig. 5.21 d) with respect to $G(l_0, l_1)$. This branch type contributes itself a further functional derivative.

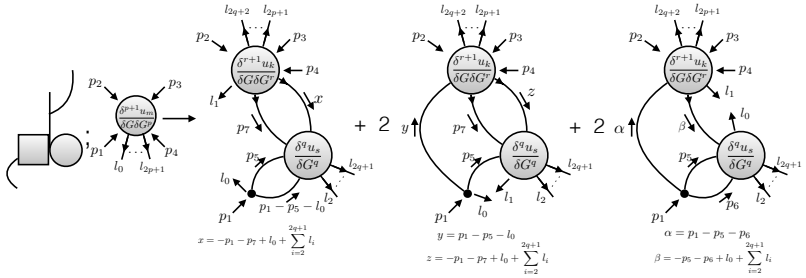

Figure E.5.: The first functional derivative of the branch Fig. 5.21 e) with respect to $G(l_0, l_1)$. This branch type contributes itself a further functional derivative.

Bibliography

[1] Pfeffer T and Pollet L 2017 *New Journal of Physics* **1**9 043005

[2] Pfeffer T and Pollet L 2018 *Phys. Rev. B* **9**8(19) 195104

[3] van Delft D and Kes P 2010 *Physics Today* **6**3(9) 38

[4] Kapitza P 1938 *Nature* **1**41 74

[5] Allen J F and Misner A D 1938 *Nature* **1**41 75

[6] Landau L D 1937 *Zh. Eksp. Teor. Fiz.* **7** 19

[7] Bogoliubov N 1947 *J. Phys. USSR* **1**1 23

[8] Bardeen J, Cooper L N and Schrieffer J R 1957 *Phys. Rev.* **1**06(1) 162–164

[9] Wilson K G 1971 *Phys. Rev. B* **4**(9) 3174–3183

[10] Wilson K G 1971 *Phys. Rev. B* **4**(9) 3184–3205

[11] Wilson K G and Fisher M E 1972 *Phys. Rev. Lett.* **2**8(4) 240–243

[12] Berezinskii V 1971 *Sov. Phys. JETP* **3**2 907

[13] Berezinskii V 1972 *Sov. Phys. JETP* **3**4 610

[14] Kosterlitz J M and Thouless D J 1973 *Journal of Physics C: Solid State Physics* **6** 1181

[15] Berthold J E, Bishop D J and Reppy J D 1977 *Phys. Rev. Lett.* **3**9(6) 348–352

[16] Bishop D J and Reppy J D 1978 *Phys. Rev. Lett.* **4**0(26) 1727–1730

[17] Resnick D J, Garland J C, Boyd J T, Shoemaker S and Newrock R S 1981 *Phys. Rev. Lett.* **4**7(21) 1542–1545

[18] Hadzibabic Z, Krüger P, Cheneau M, Battelier B and Dalibard J 2006 *Nature* **4**41 1118

[19] Mondal M, Kumar S, Chand M, Kamlapure A, Saraswat G, Seibold G, Benfatto L and Raychaudhuri P 2011 *Phys. Rev. Lett.* **1**07(21) 217003

[20] Kosterlitz J M 1974 *Journal of Physics C: Solid State Physics* **7** 1046

[21] Tsui D C, Stormer H L and Gossard A C 1982 *Phys. Rev. Lett.* **4**8(22) 1559–1562

[22] Laughlin R B 1983 *Phys. Rev. Lett.* **5**0(18) 1395–1398

[23] Kitaev A and Preskill J 2006 *Phys. Rev. Lett.* **9**6(11) 110404

[24] Levin M and Wen X G 2006 *Phys. Rev. Lett.* **9**6(11) 110405

[25] Anderson P 1973 *Materials Research Bulletin* **8** 153 – 160

[26] Coldea R, Tennant D A, Tsvelik A M and Tylczynski Z 2001 *Phys. Rev. Lett.* **8**6(7) 1335–1338

[27] Pilon D V, Lui C H, Han T H, Shrekenhamer D, Frenzel A J, Padilla W J, Lee Y S and Gedik N 2013 *Phys. Rev. Lett.* **1**11(12) 127401

[28] Fu M, Imai T, Han T H and Lee Y S 2015 *Science* **3**50 655–658

[29] Bednorz J G and Müller K A 1986 *Zeitschrift für Physik B Condensed Matter* **6**4 189–193

[30] Renner C, Revaz B, Genoud J Y, Kadowaki K and Fischer O 1998 *Phys. Rev. Lett.* **8**0(1) 149–152

[31] Varma C M, Littlewood P B, Schmitt-Rink S, Abrahams E and Ruckenstein A E 1989 *Phys. Rev. Lett.* **6**3(18) 1996–1999

[32] Pollet L 2012 *Reports on Progress in Physics* **7**5 094501

[33] Trotzky S, Pollet L, Gerbier F, Schnorrberger U, Bloch I, Prokof'ev N V, Svistunov B and Troyer M 2010 *Nature Physics* **6** 998

[34] Pollet L and Prokof'ev N 2012 *Phys. Rev. Lett.* **1**09(1) 010401

[35] Boninsegni M, Kuklov A B, Pollet L, Prokof'ev N V, Svistunov B V and Troyer M 2006 *Phys. Rev. Lett.* **9**7(8) 080401

[36] Pollet L, Boninsegni M, Kuklov A B, Prokof'ev N V, Svistunov B V and Troyer M 2007 *Phys. Rev. Lett.* **9**8(13) 135301

[37] Scalapino D J and Sugar R L 1981 *Phys. Rev. Lett.* **4**6(8) 519–521

[38] Blankenbecler R, Scalapino D J and Sugar R L 1981 *Phys. Rev. D* **2**4(8) 2278–2286

[39] Rubtsov A N, Savkin V V and Lichtenstein A I 2005 *Phys. Rev. B* **7**2(3) 035122

[40] Prokof'ev N V and Svistunov B V 1998 *Phys. Rev. Lett.* **8**1(12) 2514–2517

[41] Mishchenko A S, Prokof'ev N V, Sakamoto A and Svistunov B V 2000 *Phys. Rev. B* **6**2(10) 6317–6336

[42] Georges A, Kotliar G, Krauth W and Rozenberg M J 1996 *Rev. Mod. Phys.* **6**8(1) 13–125

[43] Kotliar G, Savrasov S Y, Haule K, Oudovenko V S, Parcollet O and Marianetti C A 2006 *Rev. Mod. Phys.* **7**8(3) 865–951

[44] Hettler M H, Mukherjee M, Jarrell M and Krishnamurthy H R 2000 *Phys. Rev. B* **6**1(19) 12739–12756

[45] Toschi A, Katanin A A and Held K 2007 *Phys. Rev. B* **7**5(4) 045118

[46] Brezin E, Guillou J L, Zinn-Justin J and Nickel B 1973 *Physics Letters A* **4**4 227 – 228

[47] Le Guillou J C and Zinn-Justin J 1980 *Phys. Rev. B* **2**1(9) 3976–3998

[48] Wetterich C 1993 *Physics Letters B* **3**01 90 – 94

[49] White S R 1992 *Phys. Rev. Lett.* **6**9(19) 2863–2866

[50] Schollwöck U 2011 *Annals of Physics* **3**26 96 – 192 january 2011 Special Issue

[51] Verstraete F, Murg V and Cirac J 2008 *Advances in Physics* **5**7 143–224

[52] Vidal G 2008 *Phys. Rev. Lett.* **1**01(11) 110501

[53] Mermin N D and Wagner H 1966 *Phys. Rev. Lett.* **1**7(22) 1133–1136

[54] Giamarchi T and Schulz H J 1987 *EPL (Europhysics Letters)* **3** 1287

[55] Giamarchi T and Schulz H J 1988 *Phys. Rev. B* **3**7(1) 325–340

[56] Ristivojevic Z, Petković A, Le Doussal P and Giamarchi T 2014 *Phys. Rev. B* **9**0(12) 125144

[57] Kashurnikov V A, Podlivaev A I, Prokof'ev N V and Svistunov B V 1996 *Phys. Rev. B* **5**3(19) 13091–13105

[58] Svistunov B V 1996 *Phys. Rev. B* **5**4(22) 16131–16134

[59] Altman E, Kafri Y, Polkovnikov A and Refael G 2004 *Phys. Rev. Lett.* **9**3(15) 150402

[60] Altman E, Kafri Y, Polkovnikov A and Refael G 2008 *Phys. Rev. Lett.* **1**00(17) 170402

[61] Altman E, Kafri Y, Polkovnikov A and Refael G 2010 *Phys. Rev. B* **8**1(17) 174528

[62] Pielawa S and Altman E 2013 *Phys. Rev. B* **8**8(22) 224201

[63] Kane C L and Fisher M P A 1992 *Phys. Rev. Lett.* **6**8(8) 1220–1223

[64] Kane C L and Fisher M P A 1992 *Phys. Rev. B* **4**6(23) 15233–15262

[65] Pollet L, Prokof'ev N V and Svistunov B V 2013 *Phys. Rev. B* **8**7(14) 144203

[66] Pollet L, Prokof'ev N V and Svistunov B V 2014 *Phys. Rev. B* **8**9(5) 054204

[67] Yao Z, Pollet L, Prokof'ev N and Svistunov B 2016 *New Journal of Physics* **1**8 045018

[68] Gerster M, Rizzi M, Tschirsich F, Silvi P, Fazio R and Montangero S 2016 *New Journal of Physics* **1**8 015015

[69] Hrahsheh F and Vojta T 2012 *Phys. Rev. Lett.* **1**09(26) 265303

[70] Doggen E V H, Lemarié G, Capponi S and Laflorencie N 2017 *Phys. Rev. B* **9**6(18) 180202

[71] Kardar M 2007 *Statistical Physics of Fields* (Cambridge University Press)

[72] Nelson D R and Kosterlitz J M 1977 *Phys. Rev. Lett.* **3**9(19) 1201–1205

[73] Svistunov B, Babaev E and Prokof'ev N 2015 *Superfluid States of Matter* (Taylor & Francis)

[74] Harris A B 1974 *Journal of Physics C: Solid State Physics* **7** 1671

[75] Vojta T 2013 *Phases and Phase Transitions in Disordered Quantum Systems* (AIP, Melville, NY)

[76] Pollock E L and Ceperley D M 1987 *Phys. Rev. B* **3**6(16) 8343–8352

[77] Prokof'ev N and Svistunov B 2001 *Phys. Rev. Lett.* **8**7(16) 160601

[78] Weber H and Minnhagen P 1988 *Phys. Rev. B* **3**7(10) 5986–5989

[79] Hsieh Y D, Kao Y J and Sandvik A W 2013 *Journal of Statistical Mechanics: Theory and Experiment* **2**013 P09001

[80] Hasenbusch M 2008 *Journal of Statistical Mechanics: Theory and Experiment* **2**008 P08003

[81] Pelissetto A and Vicari E 2013 *Phys. Rev. E* **8**7(3) 032105

[82] Fisher M P A and Zwerger W 1985 *Phys. Rev. B* **3**2(10) 6190–6206

[83] Altland A and Simons B D 2010 *Condensed Matter Field Theory* 2nd ed (Cambridge University Press)

[84] Giamarchi T 2003 *Quantum Physics in One Dimension* International Series of Monographs on Physics (Clarendon Press)

[85] McCoy B M and Wu T T 1968 *Phys. Rev.* **1**76(2) 631–643

[86] Sachdev S 1999 *Quantum Phase Transitions* (Cambridge University Press)

[87] Prokof'ev N V and Svistunov B V 2000 *Phys. Rev. B* **6**1(17) 11282–11284

[88] Troyer M and Wiese U J 2005 *Phys. Rev. Lett.* **9**4(17) 170201

[89] Rossi R, Prokof'ev N, Svistunov B, Houcke K V and Werner F 2017 *EPL (Europhysics Letters)* **1**18 10004

[90] Orrick W P, Nickel B G, Guttmann A J and Perk J H H 2001 *Phys. Rev. Lett.* **8**6(18) 4120–4123

[91] Zinn-Justin J 2002 *Quantum Field Theory and Critical Phenomena* International series of monographs on physics (Clarendon Press)

[92] Serone M, Spada G and Villadoro G 2018 *Journal of High Energy Physics* **2**018 148

[93] Parisi G 1980 *Journal of Statistical Physics* **2**3 49–82

[94] Dyson F J 1952 *Phys. Rev.* **8**5(4) 631–632

[95] Benfatto G, Giuliani A and Mastropietro V 2006 *Annales Henri Poincaré* **7** 809–898

[96] Bender C M and Wu T T 1969 *Phys. Rev.* **1**84(5) 1231–1260

[97] Bender C M and Wu T T 1973 *Phys. Rev. D* **7**(6) 1620–1636

[98] Brézin E and Parisi G 1978 *Journal of Statistical Physics* **1**9 269–292

[99] Schulte-Frohlinde V and Kleinert H 2001 *Critical properties of phi4-theories* (World Scientific Publishing Company)

[100] Pelissetto A and Vicari E 2002 *Physics Reports* **3**68 549 – 727

[101] Rivers R J 1987 *Path Integral Methods in Quantum Field Theory* Cambridge Monographs on Mathematical Physics (Cambridge University Press)

[102] Freericks J K and Zlatić V 2003 *Rev. Mod. Phys.* **7**5(4) 1333–1382

[103] Press W H, Teukolsky S A, Vetterling W T and Flannery B P 2007 *Numerical Recipes 3rd Edition: The Art of Scientific Computing* 3rd ed (New York, NY, USA: Cambridge University Press)

[104] Liao S 2012 *Homotopy Analysis Method in Nonlinear Differential Equations* (Springer Berlin Heidelberg)

[105] Vajravelu K and Van Gorder R 2013 *Nonlinear Flow Phenomena and Homotopy Analysis: Fluid Flow and Heat Transfer* (Springer Berlin Heidelberg)

[106] Liu C 2010 *Applied Mathematics and Computation* **2**16 1299 – 1303

[107] Liu C 2011 *Communications in Nonlinear Science and Numerical Simulation* **1**6 1254 – 1262

[108] Gorder R A V 2017 *Numerical Algorithms* **7**6 151–162

[109] Hille E 1997 *Ordinary Differential Equations in the Complex Domain* Dover books on mathematics (Dover Publications)

[110] Bender C and Orszag S 1999 *Advanced Mathematical Methods for Scientists and Engineers I: Asymptotic Methods and Perturbation Theory* Advanced Mathematical Methods for Scientists and Engineers (Springer)

[111] Stevenson P M 1984 *Phys. Rev. D* **3**0(8) 1712–1726

[112] Buckley I R C, Duncan A and Jones H F 1993 *Phys. Rev. D* **4**7(6) 2554–2559

[113] Kleinert H 1993 *Physics Letters A* **1**73 332 – 342

[114] Kleinert H 2009 *Path Integrals in Quantum Mechanics, Statistics, Polymer Physics, and Financial Markets* EBL-Schweitzer (World Scientific)

[115] Rossi R, Werner F, Prokof'ev N and Svistunov B 2016 *Phys. Rev. B* **9**3(16) 161102

[116] Serone M, Spada G and Villadoro G 2017 *Journal of High Energy Physics* **2**017 56

[117] Riordan J 2014 *An Introduction to Combinatorial Analysis* Princeton Legacy Library (Princeton University Press)

[118] Josephson B 1962 *Physics Letters* **1** 251 – 253

[119] Kozik E, Ferrero M and Georges A 2015 *Phys. Rev. Lett.* **1**14(15) 156402

[120] Alloul H, Ohno T and Mendels P 1989 *Phys. Rev. Lett.* **6**3(16) 1700–1703

[121] Norman M R, Pines D and Kallin C 2005 *Advances in Physics* **5**4 715–733

[122] Ferrero M, Cornaglia P S, De Leo L, Parcollet O, Kotliar G and Georges A 2009 *Phys. Rev. B* **8**0(6) 064501

[123] Gull E, Parcollet O, Werner P and Millis A J 2009 *Phys. Rev. B* **8**0(24) 245102

[124] Gunnarsson O, Schäfer T, LeBlanc J P F, Gull E, Merino J, Sangiovanni G, Rohringer G and Toschi A 2015 *Phys. Rev. Lett.* **1**14(23) 236402

Acknowledgements

This PhD thesis would not have been possible and such a valuable experience without the support of the people I list below, to whom I want to direct my deepest gratitude:

... my supervisor **Lode Pollet** who has the largest share in making this thesis possible. I really appreciate his advice, patience and trust in my work, which enabled me to grow intellectually as well as personally during the last years. This would not have been possible without the freedom and the support he provided.

... **Uli Schollwöck** for a great time during our stay at the Flatiron Institute, interesting discussions, and valuable support.

... **Matthias Punk** for examining this thesis and being part of my PhD commission.

... **Joachim Rädler** and **Ivo Sachs** for being part of my PhD commission.

... **Boris Svistunov** for the invitation to present our work at the Simons foundation summer school of the Many Electron Collaboration as well as for valuable discussions.

... **Zhiyuan Yao** for illustrating the basic ideas of papers performing RG calculations in exotic conventions.

... **Peter Kroiss** for introducing me to "Hello World" and Monte Carlo methods. We had a great time together during and after work.

... **Dario Hügel** for sharing my interests in and beyond physics and for proof reading the thesis. I will miss our many discussions during and after work.

... **Sebastian Schulteß** for being a great office mate and valuable discussion partner.

... **Jens Grimm** for your warm welcome to the office on my first day and for not even trying to pretend to be professional.

... **Sam Mardazad** for explaining me how things are really supposed to be and for proof reading parts of the thesis.

... **Tuomas Vanhala** for being a valuable discussion partner and for proof reading parts of the thesis.

... **Ke Liu** for your refreshing way of thinking. After attending the APS meeting we realized that, after all, it is not too bad to be a scientist.

... **Jacopo Nespolo** for the daily coffee breaks at the secret coffee machine and for bringing some breath of fresh air to our group.

... **Andrew Hayward**, **Jan Stolpp**, **Carlos Velasco**, **Ines de Vega**, **Nils-Oliver Linden**, **Carlos Parra** and many others. Our joint lunches were welcoming breaks of any workday.

... **Cordula Weber** for all the perfect administrative support and for always being patient with me having missed various deadlines.

... **Raphael Goll** for proof reading the thesis and for always being a motivated climbing partner. I am still convinced that in the end it boils down to finger strength.

... last but not least to **Marina** and **my family**.